Experimental characterization of the underwater pulsed electric discharge

Tetiana Tmenova

THÈSE

En vue de l'obtention du

DOCTORAT DE L'UNIVERSITÉ DE TOULOUSE

Délivré par l'Université Toulouse 3 - Paul Sabatier

Cotutelle internationale : Université nationale Taras-Chevtchenko de Kiev

Présentée et soutenue par

Tetiana TMENOVA

Le 28 novembre 2019

Étude expérimentale de la décharge électrique pulsée dans l'eau

Ecole doctorale : **GEET - Génie Electrique Electronique et Télécommunications : du système au nanosystème**

Spécialité : **Ingénierie des Plasmas**

Unité de recherche :
LAPLACE - Laboratoire PLAsma et Conversion d'Énergie - CNRS-UPS-INPT

Thèse dirigée par
Yann CRESSAULT et Anatoly VEKLICH

Jury

M. Stephane PELLERIN, Rapporteur
M. Vyacheslav TSIOLKO, Rapporteur
M. Igor ANISIMOV, Examinateur
Mme Catherine ROND, Examinatrice
M. Yann CRESSAULT, Directeur de thèse
M. Anatoly VEKLICH, Co-directeur de thèse

To my grandparents,
parents,
and Eduardo.

Acknowledgements

First and foremost, I thank my dissertation advisors, professors Yann Cressault and Anatoly Veklich, for bringing the idea of joint French-Ukrainian thesis supervision into life, for assigning me this pioneering role, and for their valuable guidance and support.

I would like to express special gratitude to my French co-supervisor, M. Flavien Valensi, for his endless patience and motivation, direction and articulation throughout the course of this work. His interest in this work and his style of advising has motivated me to put in my best effort. I would also like to thank my committee members Prof. Pellerin, Prof. Anisimov, Mme Rond and M. Tsiolko for serving on my committee.

I would also like to thank my Ukrainian co-supervisor, M. Viacheslav Boretskij, for his valuable practical inputs regarding the research, equipment and spectroscopy in general.

Special thanks to all my colleagues from Kiev and Toulouse, both inside and outside the lab. Many of them have become much more than that.

I would like to acknowledge the support of the Prof. Lopatko from the National University of Life and Environmental Sciences of Ukraine. I would never have gone this far without him teaching me how to run a synthesis reactor and sharing many of interesting ideas.

Last but not the least, I want to thank my family and friends for supporting my PhD endeavor. Thanks to my parents, my sisters and my very special "new" family for their encouragement, motivation and support in the moments of need.

Abstract

Although electric spark dispersion processes have been known for a while, the plasma created during this process is not well-studied and understood. The complexity of the phenomena occurring during the underwater electric discharges brings additional obstacles to experimental characterization of such plasmas imposed by as small sizes of plasma and their often-short duration, difficult environment of the discharge, its stochastic nature and poor reproducibility.

The main objective of this thesis was set on the investigation of the plasma occurring during the synthesis of metal colloids by an electrospark dispersion generator. The first success of this work was simply to show the applicability of optical emission spectroscopy diagnostics to such discharges. The efforts made for the development of the effective experimental approach in order to meet this research objective have been well rewarded. The results obtained in this work allow to draw interesting conclusions about the physical properties of the underwater pulsed electric discharge plasma of the considered configuration.

Discharge ignites from the short circuit and molten bridge mechanism. Ignition of the arc is characterized by formation of bubble resulting from a pressure shockwave. High-speed imaging allowed to distinguish two phases in the discharge lifetime: plasma in water, and plasma in bubble formed afterwards. From the vapor condensation point of view, these two phases presumably lead to different quenching conditions, and, consequently, to the different synthesis conditions. In the case of discharge generated between molybdenum electrodes, there is a slowly-decaying light emission after the end of the discharge which can be attributed to the ejection of eroded metallic particles. The energy dissipation on the electrodes was found to be different for copper and molybdenum: due to the lower thermal conductivity of molybdenum, smaller portion of energy transferred to the electrodes results in higher energy input into the arc column. Spectroscopic measurements allowed to establish that plasma density (~ 10^{17} cm^{-3}) and moderate temperature (0.6 – 0.95 eV) correspond to a pressure greater than 1 bar. Moreover, plasma presents several non-ideal effects, such as broadening and the asymmetrical shape of the H_α line and absence of H_β line. In general, plasma properties were found to be relatively insensitive to most of the discharge parameters, such as the discharge current or the type of liquid

with the main differences being associated to the used electrodes material.

Key words: electric discharge, plasma in liquid, emission spectroscopy

Résumé

Bien que le procède de dispersion par arc électrique soit connu depuis un certain temps, le plasma formé durant ce procédé est encore peu étudié et compris. La complexité des phénomènes se produisant durant les décharges immergées génèrent de nouveaux obstacles à la caractérisation de tels plasmas, du fait de la faible taille et de la durée souvent très courte, les difficultés liées à l'environnement de la décharge, leur nature stochastique et la faible reproductibilité.

Le principal objectif de cette thèse est l'étude du plasma se formant lors de la synthèse de colloïdes métalliques par un générateur de dispersion par étincelle électrique. Le premier résultat concluant de ce travail a été de démontrer la faisabilité de la spectroscopie optique d'émission pour le diagnostic de telles décharges. Les efforts réalisés pour le développement d'une approche expérimentale ont permis d'atteindre les objectifs de recherche. Les résultats obtenus au cours de ce travail permettent de tirer des conclusions intéressantes sur les propriétés physiques des plasmas de décharge électrique pulsée dans la configuration étudiée.

La décharge est créée à partir d'un court-circuit et d'un amorçage par pont fondu. L'allumage de l'arc est caractérisé par la formation d'une bulle causée par une onde de choc de pression. L'imagerie rapide a permis de distinguer deux phases dans la durée de vie de la décharge : d'abord un plasma dans l'eau, puis un plasma à l'intérieur d'une bulle de gaz formée par la suite. Du point de vue de la condensation de la matière vaporisée, on peut s'attendre à ce que ces deux phases conduisent à des conditions de trempe différentes, et en conséquence des conditions de synthèse différentes. Dans le cas d'une décharge générée entre des électrodes en molybdène, une émission de lumière décroissant lentement après la fin de la décharge se produit, ce qui peut être attribué à l'éjection de particules métalliques érodées. La dissipation de l'énergie aux électrodes s'est avérée être différente pour le cuivre et le molybdène : du fait d'une conductivité thermique plus faible pour le molybdène, une part plus faible de l'énergie transférée aux électrodes conduit à une part plus importante de l'énergie fournie à la colonne d'arc. Les mesure par spectroscopie optique d'émission ont permis d'établir que la densité ($\sim 10^{17}\,\mathrm{cm}^{-3}$) et la température modérée ($0.6 - 0.95\,\mathrm{eV}$) du plasma correspondent à une pression supérieure à 1 bar. Il présente donc

quelques effets non-idéaux, tels que l'élargissement et la forme asymétrique de la raie H_α et l'absence de la raie H_β. En général, les paramètres du plasma se sont avérés être relativement insensibles à la plupart des paramètres de la décharge, tels que le courant de décharge ou le type d'eau, les principales différences étant liées aux matériaux des électrodes utilisées.

Mots-clés : décharge électrique, plasma immergé, spectroscopie d'émission

Table of Contents

List of figures

List of tables

CHAPTER I
INTRODUCTION

1. Introduction

1.1 Context and motivation

Studies of the electric spark dispersion processes have been in the focus of attention for a while. Significant contribution into development of pulse engineering and technology was made by researchers of the Institute of Electrodynamics of National Academy of Sciences of Ukraine (Shcherba A. A., Zakharchenko S. N. et al.) [1]–[4]. Modern technological units with stabilization of impulse parameters allow to achieve desirable process efficiency [5]. However, implementation of a complex physical phenomenon such as underwater electric discharge requires both, the corresponding equipment and the detailed investigation of the process itself.

Electric spark dispersion of conducting materials in liquid media have been extensively studied by the research group of Lopatko K. G. from the National University of Life and Environmental Sciences of Ukraine [6], [7]. Specifics of this process lies in the possibility of a direct synthesis of colloidal solutions with potential to control the degree of nanomaterials' dispersion. A colloidal solution, sometimes also known as a colloidal suspension, is a solution in which a material is evenly suspended in a liquid. In other words, a colloid is a microscopically small substance that is equally dispersed throughout another material, wherein the dispersed-phase particles have a diameter between approximately 1 and 1000 nanometers. Nevertheless, due to the physical reasons, the dispersed matter tends to consolidate, which doesn't allow the dispersed powders to remain isolated. Colloidal solutions, in turn, don't have this disadvantage. In case of their inherent stability, colloids ensure the dispersed-isolated state of a solid phase.

Colloidal solutions as nanofertilizers offer a wide range of promising options for improving the quantities and quality of plants and seeds grown for consumption, reducing the costs of production as well as negative impacts on the environment, to achieve sustainable food development. It is well known that there are about 16 nutrient elements required for growth of plants, i.e., carbon (C), oxygen (O), hydrogen (H), nitrogen (N), potassium (K), phosphorus (P), calcium (Ca), magnesium (Mg), sulfur (S), iron (Fe), manganese (Mn), boron (B), zinc (Zn), copper (Cu), molybdenum (Mo), and chlorine (Cl), as the main elements [8]. In addition, there are seven other elements—nickel (Ni), selenium (Se), vanadium (V), sodium (Na), silicon (Si), cobalt (Co), and aluminum (Al)—that are important elements for plants [8]; they increase plant growth as micronutrients and perform special functions as cofactors for enzymes. Of

course, depending on the plant species, they may not require all of these elements and the necessary quantities may also vary.

Because of the small size and physicochemical characteristics of nanoparticles (NPs) such as shape, surface chemistry, electrical charge, and agglomeration, NPs can be synthesized depending on the requirements and needs of each crop. The main characteristics of NPs are their size, shape, superficial charge, chemical composition, concentration, stability, and availability. These characteristics have effects on the properties of the NPs, i.e., they should be taken into account in the exact applications and various uses of NPs. For example, with regard to size, some studies of (spherical shaped) Ag NPs have shown that particles measuring <40 nm can penetrate the skin, with a critical size of 70 nm, so bigger particles have been shown to be less toxic and cause less damage to the skin than smaller particles [9]. Such results suggest size-dependent toxicity and reactivity of smaller NPs. With regard to shape, Pal et al. [10], studied different shapes of Ag NPs with equal surface areas and found that truncated triangular nanoplates with a {111} lattice plane as the basal plane had higher reactivity than NPs with fewer facets, such as spherical or rod-shaped particles. With regard to surface charge, according to [11], a positive charge in NPs may produce severe effects such as cytotoxicity, genotoxicity, and mutagenicity. Abdelmonem et al. [12] stated that NPs with a positive charge are more toxic than negatively charged ones. Therefore, this must be taken into consideration as an important factor when NPs are released into the environment.

Plasma as a research object has been in the spot of the scientific attention for almost a century, ever since Irving Langmuir provided the world with his iconic description of this fourth state of the matter in 1928 [13]. While it still generates a never-ending scatter of the challenges to attract investigators, the scope of this work lies within the frame of relatively new sub-category of the plasma physics: plasmas in and in contact with liquids. Over the past decades, worldwide community of scientists have made numerous contributions into better understanding of the plasma-liquid interactions and all the subsequent phenomena. A vast base of theoretical works and topical reviews has been created focusing on classification of plasma discharges in and in contact with liquids depending on their configuration, type of the liquid media, specifics of chemical and physical processes occurring in the plasma-liquid interface, etc. Such global interest is explained by the variety of practical applications and emerging technological opportunities for the plasma community.

Intense UV radiation, electric field, shock waves and active species (OH radicals, atomic oxygen, hydrogen peroxide, etc.) generated in plasma-liquid systems are effective agents against many biological and chemical matter which makes liquid plasmas particularly suitable for

decontamination and sterilization purposes. Studies of the environmental and biotechnological applications of pulsed discharges in water conducted by Sato and his colleagues [14] have demonstrated that bubbling of oxygen through a hollow needle electrode in a point-to-plane electrode system is an effective way to decompose organic materials due to the active species originating from oxygen gas. A unique method for deactivation of microorganisms by means of microplasmas generation in saline solution has been presented by Graves and his colleagues at the University of California, Berkeley [15]. They employed *E. coli* to bacteria to investigate the disinfection efficiency of the developed approach. More than 99.5% of *E. coli* was deactivated in 180 seconds as a result of electrolysis in NaCl aqueous solution. Locke and his colleagues at Florida State University have qualitatively studied the production of reductive species by high-voltage electric discharges in water [16] and their effectiveness for water purification. It was shown that the rate of the formation of reductive species in the pulsed streamer discharge increased as the input power to the system increased, offering a possibility that in a mixture of aqueous contaminants some pollutants or a component of certain pollutants could degrade by reductive mechanisms, thereby increasing the degradation efficiency of the process.

On the other hand, another major application of plasmas in and in contact with liquids is NM synthesis through plasma-liquid interactions that represents a separate research branch. Commonly being referred in the literature as “novel” area of study, it actually can be traced back to Swedish scientist Theodor Svedberg when in 1922 he used arc discharge immersed in liquid to synthesize high-dispersed particles [17]. At present, immersed arc discharge presents one of the most common approaches to NPs synthesis. Otherwise known as the electrical condensation method, it has been further developed, and, almost one century after its discovery, it has been successfully used to synthesize carbon nanostructures from nanotubes to complex structures with embedded metals. It was a famous work on synthesis of carbon ‘onions’ in water [18] that served as a starting point to investigate the possibilities of application of an immersed electric discharge for generation of non-carbon structures, including metals [19], silicon [20], oxides [21], and carbides [22].

While application of plasma-liquid interface for water purification has longer history compared to its use in NM synthesis, some of the reactor configurations reviewed in [23], [24] and [25] can be as well applicable for NM generation. Additionally, a substantial number of reviews on NM synthesis by using in-liquid plasma techniques has been published recently. These works mostly focus on certain types of plasma, namely, microplasmas, electric arc discharge in liquids, glow discharge plasma electrolysis, and atmospheric pressure plasma-liquid interactions. These reports, in combination with general reviews covering a variety of plasma

types, provide in-depth information about each plasma type. For instance, Graham and Stalder have presented a summary of plasma-in-liquid systems from the standpoint of nanoscience [26]. General review by Chen et al. [27] focuses specifically on plasma-liquid interactions for NM synthesis.

Another commonly used technique for synthesis of metallic NPs is the laser ablation method. It utilizes laser as an energy source for ablating solid target materials, and allows for production of high-quality metal colloids. In this process, extremely high energy is concentrated at a specific point on a solid surface to evaporate light-absorbing material. High-purity NPs can be generated by laser ablation because the purity of the particles is basically determined by the purity of the target and ambient media (liquid) without contamination from the reactor. However, it is difficult to control size distribution, agglomeration, and crystal structure in the conventional laser ablation process since nanoparticles are built by random (Brownian) motion of molecules. The required laser equipment and considerable power are also expensive. Moreover, some of the liquid media used in the laser ablation systems, such as acetone [28] or copper chloride [29] are hazardous irritants that may lead to hepatotoxic effects (causing liver damage).

Electrochemical method has also been widely applied for the synthesis of metal NPs. Electrochemical deposition (ECD) occurs at the interface of an electrolyte solution containing the metal to be deposited and an electrically conductive metal substrate. For example, in [30] authors used inexpensive conventional two-electrode system for the electrochemical synthesis of Ag NPs. The advantage of this technique over other bottom-up approaches lies in the purity of the obtained NMs. Since the electrochemical method is flexible, the particle size can be improved by controlling the reaction parameters such as electrolytic concentration and the applied current density. This technique is eco-friendly, time- and cost-efficient. The key to the success of ECD methods is the right choice of the chemical agents and the process conditions. However, as pointed out by Rodríguez-Sánchez et al. [31], the method has its limitations, since the deposition of silver on the cathode during the electrochemical process diminishes the effective surface. As the entire cathode surface gets covered with the silver electrodeposits, the particle production comes to a halt altogether. Another important issue is finding ways to avoid the use of stabilizing agents in the EDC processes.

Apart from the laser ablation and ECD techniques, the chemical vapor deposition (CVD) has been recently gaining an increased attention as a promising method to grow NPs in a controlled manner [32]. The mild deposition rate of CVD makes it possible to control the particle growth on the support material. Moreover, since all byproducts are gaseous, there is no subsequent poisoning by residues; also, it minimizes any

environmentally hazardous byproducts. However, the often quite expensive precursors are a challenge for CVD methods. Reagents are mostly air/moisture sensitive and flammable, which makes their handling difficult. Since typical CVD reactions are not selective and self-limiting, the controlled deposition of metallic and bimetallic NPs remains challenging [33].

The arc discharge method in liquid, on the other hand, simply requires a DC power supply and an open vessel full of deionized water, alcohol or other liquid of a choice. It does not require vacuum equipment, reactive gas, a high temperature furnace, or a heat exchanging system. Consequently, such approach is extremely simple and cheap. Application of an electric discharge in liquid can be characterized by high productivity, relatively low costs, possibility of scaling and performing one-stage synthesis of NMs. However, one of the disadvantages of the electrical condensation method is a generation of NPs with a broad size distribution. At the same time, it is possible to carry out directed synthesis of a variety of NMs by regulating the process of interaction between the medium and the particles formed under the influence of the arc discharge. Moreover, the simplicity of this method allows scaling up for mass production of NPs.

The electrical condensation method is the main topic of this thesis. More specifically, the pulsed low-voltage electric discharge immersed in water used for synthesis of metal colloidal solutions. This configuration has been chosen at the beginning of this PhD thesis on the basis of preliminary results and prospects of successful application of the obtained colloidal solutions in the field of biology and agriculture.

This constitutes the main motivation for this thesis: since main properties of the obtained NPs are formed on the stage of their synthesis, it is reasonable to study the qualitative and quantitative correlations between parameters of the electric discharge plasma and resulting NMs.

1.2 Objectives and structure of the thesis

The main objective of this thesis is the investigation of the plasma produced by an underwater low-voltage microsecond pulsed DC discharge. These studies were initiated to bring better understanding of physical processes occurring during the synthesis of metal colloids by an electrospark dispersion generator [34] specially designed in the National University of Life and Environmental Sciences of Ukraine. The operation of this generator is based on volumetric plasma-assisted destruction of a liquid-immersed layer of metal granules via simultaneous formation of spark channels in contact points between the granules as a result of pulse energy input from the generator. More specifically, this thesis deals with a pulsed low-voltage electric discharges immersed in water, where “low-voltage” corresponds to the values of voltage below 1 kV.

For the purposes of appropriate positioning of the present study, it is crucial to define the frame of the available literature on diagnostics of the immersed electric discharges. As it is shown in Chapter 2, none of the relevant existing research works are comparable enough to fully represent all points of the scientific interest this thesis pursues. Nevertheless, some aspects of resemblance between the experimental arrangement employed in the present study (see Chapter 3) and other configurations found in the literature should be considered. It can refer to, for instance, electrical parameters and electrode configurations of the discharge reactors. Analysis of the available research in the domain of pulsed low-voltage electric discharges in water has shown that their presence in the literature mostly occurs in the form of the electric discharge machining (EDM) process. What makes the EDM electric discharges relevant for the scope of this thesis is that, according to Descoeudres [35], OES, high-speed imaging and electrical parameter measurements are some of the very few methods capable to provide information on such plasmas. Hence, studies of the EDM electric discharges fit into the context of this work not only from the perspective of in-liquid plasma.

The choice of the electrode materials used in this work was motivated by the following considerations: variety of colloidal solutions previously synthesized and tested by the team of the National University of Life and Environmental Sciences of Ukraine, and the prospects of their applications for biological and agricultural purposes. Most of the results presented in this thesis are obtained from the experiments involving Cu and Mo electrodes.

Copper is a very important micronutrient, which regulates the rate of many biochemical reactions in plants. Like Zn, Cu is an essential element for enzymatic activity. It also participates in chlorophyll synthesis, as well as in the production of seeds. For instance, Taran et al. have demonstrated in [36] that colloidal solutions of Cu and Zn NPs had a positive effect on pro-oxidative/antioxidative balance and content of photosynthetic pigments and leaf area of winter wheat plants and decreased the negative effect of drought action upon the wheat seedlings.

The role of molybdenum in plants is to fix nitrogen through bacteria found in plant roots. Mo is also required for the synthesis of an enzyme called nitrate reductase, which reduces nitrate to nitrite. This process is crucial for protein synthesis in plants. Up to date, there have been no short- or long-term studies reported on the use of Mo-NP as a fertilizer. However, Taran et al. reported use of Mo NPs in the studies of their effects on metabolic processes in plants [7]. The obtained results point to the indirect effect of molybdenum NPs upon the metabolic processes that lead to activation of antioxidant enzymes and reduction of oxidative processes, thus promoting adaptation of plants. This is probably due to the fact that metal NPs have excess energy; they are highly reactive and can engage

in the process of aggregation. In addition, they can bind to different organelles in cytoplasm thus changing intracellular and physiological features.

The path that this thesis follows consists in the characterization of the plasma at different operating conditions, in order to deduce their influence. Experimental characterization of the immersed electric discharge plasma is lacking. Some spectroscopic studies have already been performed but remain very incomplete [37]. This is mostly because plasma in water is experimentally difficult to investigate with classical plasma diagnostics, due to its small size, short duration, and often poor reproducibility. In this work, the plasma is investigated with high-speed imaging and with spatially-resolved optical emission spectroscopy (OES). OES allows to determine such parameters as temperature, electron number density, and composition of plasma in order to improve the understanding of its complex basic physics.

While the focus of the thesis is set on plasma diagnostics, other aspects of the underwater electric discharge characterization are also important in the context of their further correlation with the properties of NMs. The unique feature of the present study is the simultaneity of spectroscopic, electric and imaging measurements. The readings of oscilloscope combined with registered spectra and discharge visualization allow to obtain clear understanding about the arc configuration during the period corresponding to the spectroscopic data acquisition.

This thesis is divided into 5 chapters. Chapters from two to four have a short introduction and the main findings are summarized in a conclusions section of chapters 2 and 3. Chapter 2 describes the physics of the cold plasmas typically encountered in the immersed electric discharges, and forms the theoretical basis for the rest of the thesis.

Chapter 3 describes the experimental approach developed in order to successfully achieve the research objectives and explains the principles of the plasma diagnostics used.

Chapter 4 presents the experimental investigations of the underwater multiple- and the single-pulse discharge configurations. The electric and optical diagnostics of the plasma is performed to determine the main characteristics of the discharge. Variation of parameters such as the type of electrode material, liquid and voltage is performed and analyzed (presents the detailed analysis of the high-speed imaging of a single-pulse discharge. Results reflect the correlation between the discharge radius, size of the bubble surrounding it, and electric pulse parameters).

Chapter 5 summarizes the findings and conclusions of the thesis and proposes future investigations.

References to chapter I

[1] A. A. Shcherba and N. I. Suprunovska, “Cyclic transients in the circuits of electric discharge installations taking into account the influence of magnitude and rate of discharge currents rise on resistance of electric spark load,” *Tech. Electrodyn.*, no. 2, pp. 3–10, 2018.
[2] A. A. Shcherba, N. I. Suprunovskaya, and D. S. Ivashchenko, “Modeling of nonlinear resistance of electro-spark load for synthesis of discharge circuit of capacitor by time parameters,” *Tech. Electrodyn.*, no. 3, pp. 12–18, 2014.
[3] A. A. Shcherba, A. D. Podoltsev, S. N. Zakharchenko, I. N. Kucheryavaya, N. I. Shevchenko, and N. I. Suprunovskaya, “Progress in spark-eroded particle production: Development of technological system for high-yield electrical-spark dispersion of metal granules in liquid,” *Tech. Electrodyn.*, no. 6, pp. 3–13, 2005.
[4] A. A. Shcherba, S. N. Zakharchenko, N. I. Suprunovskaya, and N. I. Shevchenko, “The influence of repetition rate of discharge pulses on electrical resistance of current-conducting granular layer during its electric-spark treatment,” *Tech. Electrodyn.*, no. 2, pp. 10–14, 2006.
[5] A. E. Berkowitz *et al.*, “Amorphous soft magnetic particles produced by spark erosion,” *J. Magn. Magn. Mater.*, vol. 254, pp. 1–6, 2003.
[6] K. G. Lopatko *et al.*, “Obtaining of metallic nanoparticles by plasma-erosion electrical discharges in liquid mediums for biological application,” *Ann. Wars. Univ. Life Sci. - SGGW Agric.*, no. 61, pp. 105–115, 2013.
[7] N. Taran *et al.*, “Colloidal Nanomolybdenum Influence upon the Antioxidative Reaction of Chickpea Plants (Cicer arietinum L.),” *Nanoscale Res. Lett.*, vol. 11, no. 1, p. 476, Dec. 2016.
[8] F. Fernández-Luqueño, F. López-Valdez, and M. F. Rodríguez, “Mineral fertilizers, bio-fertilizers and PGPRs: Advantages and disadvantages of its implementation,” in *Fertilizer Technology II, Biofertilizers.*, New Delhi: Studium Press, 2015, pp. 277–294.
[9] F. L. Filon, M. Mauro, G. Adami, M. Bovenzi, and M. Crosera, “Nanoparticles skin absorption: New aspects for a safety profile evaluation,” *Regul. Toxicol. Pharmacol.*, vol. 72, no. 2, pp. 310–322, 2015.
[10] S. Pal, Y. K. Tak, and J. M. Song, “Does the antibacterial activity of silver nanoparticles depend on the shape of the nanoparticle? A study of the gram-negative bacterium Escherichia coli,” *Appl Env. Microbiol*, vol. 73, no. 6, pp. 1712–1720, 2007.
[11] A. Huk *et al.*, “Impact of nanosilver on various DNA lesions and HPRT gene mutations–effects of charge and surface coating,” *Part. Fibre Toxicol.*, vol. 12, no. 1, p. 25, 2015.
[12] A. M. Abdelmonem, B. Pelaz, K. Kantner, N. C. Bigall, P. del Pino, and W. J. Parak, “Charge and agglomeration dependent in vitro uptake

and cytotoxicity of zinc oxide nanoparticles," *J. Inorg. Biochem.*, vol. 153, pp. 334–338, 2015.
[13] I. Langmuir, "Oscillations in Ionized Gases," *Proc. Natl. Acad. Sci. U. S. A.*, vol. 14, no. 8, pp. 627–637, 1928.
[14] K. Sato, K. Yasuoka, and S. Ishii, "Water treatment with pulsed discharges generated inside bubbles," *Electr. Eng. Jpn.*, vol. 170, no. 1, pp. 1–7, Jan. 2010.
[15] Y. Sakiyama, T. Tomai, M. Miyano, and D. B. Graves, "Disinfection of *E. coli* by nonthermal microplasma electrolysis in normal saline solution," *Appl. Phys. Lett.*, vol. 94, no. 16, p. 161501, Apr. 2009.
[16] B. R. Locke and S. M. Thagard, "Analysis and Review of Chemical Reactions and Transport Processes in Pulsed Electrical Discharge Plasma Formed Directly in Liquid Water," *Plasma Chem. Plasma Process.*, vol. 32, no. 5, pp. 875–917, Oct. 2012.
[17] T. Svedberg, "Herstellung Kolloider Liisungen Anorganischer Stoffe," *Dresden/Leipzig*, 1922.
[18] A. ChhowallaM and G. A. J. Amaratunga, "Synthesis of carbon 'onions' in water," *Nature*, vol. 414, pp. 506–507, Nov. 2001.
[19] A. Ashkarran, "Synthesis and characterization of gold nanoparticles via submerged arc discharge based on a seed-mediated approach," *J. Theor. Appl. Phys.*, vol. 6, no. 1, p. 14, 2012.
[20] S.-M. Liu, M. Kobayashi, S. Sato, and K. Kimura, "Synthesis of silicon nanowires and nanoparticles by arc-discharge in water," *Chem. Commun.*, no. 37, pp. 4690–4692, 2005.
[21] A. A. Ashkarran, A. Iraji zad, S. M. Mahdavi, and M. M. Ahadian, "ZnO nanoparticles prepared by electrical arc discharge method in water," *Mater. Chem. Phys.*, vol. 118, no. 1, pp. 6–8, Nov. 2009.
[22] N. Parkansky *et al.*, "W-C Synthesis in a Pulsed Arc Submerged in Liquid," *Plasma Chem. Plasma Process.*, vol. 28, no. 3, pp. 365–375, Jun. 2008.
[23] B. R. Locke, M. Sato, P. Sunka, M. R. Hoffmann, and J.-S. Chang, "Electrohydraulic Discharge and Nonthermal Plasma for Water Treatment," *Ind. Eng. Chem. Res.*, vol. 45, no. 3, pp. 882–905, Feb. 2006.
[24] P. Bruggeman and C. Leys, "Non-thermal plasmas in and in contact with liquids," *J. Phys. Appl. Phys.*, vol. 42, no. 5, p. 053001, Mar. 2009.
[25] B. Jiang *et al.*, "Review on electrical discharge plasma technology for wastewater remediation," *Chem. Eng. J.*, vol. 236, pp. 348–368, Jan. 2014.
[26] W. G. Graham and K. R. Stalder, "Plasmas in liquids and some of their applications in nanoscience," *J. Phys. Appl. Phys.*, vol. 44, no. 17, p. 174037, May 2011.
[27] Q. Chen, J. Li, and Y. Li, "A review of plasma–liquid interactions for nanomaterial synthesis," *J. Phys. Appl. Phys.*, vol. 48, no. 42, p. 424005, Oct. 2015.

[28] N. V. Tarasenko, A. V. Butsen, and E. A. Nevar, “Laser-induced modification of metal nanoparticles formed by laser ablation technique in liquids,” *Appl. Surf. Sci.*, vol. 247, no. 1–4, pp. 418–422, Jul. 2005.
[29] V. S. Burakov, N. A. Savastenko, N. V. Tarasenko, and E. A. Nevar, “Laser-induced modification of composite Cu-C nanosized particles synthesized using a pulsed electrical discharge in a liquid,” *J. Appl. Spectrosc.*, vol. 75, no. 3, pp. 394–401, May 2008.
[30] R. Singaravelan and S. Bangaru Sudarsan Alwar, “Electrochemical synthesis, characterisation and phytogenic properties of silver nanoparticles,” *Appl. Nanosci.*, vol. 5, no. 8, pp. 983–991, Nov. 2015.
[31] L. Rodríguez-Sánchez, M. C. Blanco, and M. A. López-Quintela, “Electrochemical Synthesis of Silver Nanoparticles,” *J. Phys. Chem. B*, vol. 104, no. 41, pp. 9683–9688, Oct. 2000.
[32] S. Saedy, D. Palagin, O. Safonova, J. A. van Bokhoven, A. A. Khodadadi, and Y. Mortazavi, “Understanding the mechanism of synthesis of Pt 3 Co intermetallic nanoparticles via preferential chemical vapor deposition,” *J. Mater. Chem. A*, vol. 5, no. 46, pp. 24396–24406, 2017.
[33] P. Piszczek and A. Radtke, “Silver Nanoparticles Fabricated Using Chemical Vapor Deposition and Atomic Layer Deposition Techniques: Properties, Applications and Perspectives: Review,” in *Noble and Precious Metals - Properties, Nanoscale Effects and Applications*, M. S. Seehra and A. D. Bristow, Eds. InTech, 2018.
[34] K. G. Lopatko, E. H. Aftandilyants, A. A. Scherba, S. M. Zakharchenko, and S. A. Yatsuk, “Setup for synthesis of colloidal solutions of ultra-disperse metal powders,” u200810312, 10-Dec-2009.
[35] A. Descoeudres, “Characterization of electrical discharge machining plasmas (Thesis),” EPFL, Lausanne (Switzerland), 2006.
[36] N. Taran, V. Storozhenko, N. Svietlova, L. Batsmanova, V. Shvartau, and M. Kovalenko, “Effect of Zinc and Copper Nanoparticles on Drought Resistance of Wheat Seedlings,” *Nanoscale Res. Lett.*, vol. 12, no. 1, p. 60, Dec. 2017.
[37] P. Bruggeman, D. Schram, M. Á. González, R. Rego, M. G. Kong, and C. Leys, “Characterization of a direct dc-excited discharge in water by optical emission spectroscopy,” *Plasma Sources Sci. Technol.*, vol. 18, no. 2, p. 025017, May 2009.

CHAPTER II
DISCHARGES IN LIQUID: STATE OF THE ART

2. Discharges in liquid: state of the art

2.1 Introduction

As of today, amount of the existing literature dealing with plasmas in and in contact with liquids is simply inconceivable. That created the need to filter and categorize the available information based on practical applications, types of the electric discharges or liquid media, experimental reactor's configurations, parameters of the power input or operation mode, etc. One of the most comprehensible works is the review published by Bruggeman and Leys [1] on atmospheric pressure non-thermal discharges in and in contact with liquids. Authors distinguished three different types of plasmas: direct in-liquid discharges, discharges in gas phase with a liquid electrode, and discharges in bubbles in liquids. From then on, this classification has become generally accepted by plasma community. This chapter will focus exclusively on direct in-liquid electric discharges. The general aim is to present a state-of-the-art experimental characterization of such immersed discharges, emphasizing existing and commonly employed methods for underwater plasma diagnostics.

This chapter provides concepts necessary for the understanding of the plasma diagnostics mainly with the purpose to explain the findings of this thesis and to place them in their context.

The existing classifications of plasma-liquid reactor configurations are presented in section 2.2 while section 2.3 focuses specifically on those cases of plasmas in and in contact with liquid that found their applications in the field of nanoscience. Section 2.4 provides a short overview of the different direct in-liquid discharges generated between two electrodes that are known to be use for synthesis of various nanomaterials. Section 2.5 presents the literature overview on the state-of-the-art experimental results of the low-voltage underwater electric discharge and plasma diagnostics. The last section gives the short summary of the whole chapter.

2.2 The wide variety of plasma-liquid reactors

The visible universe is 99.9999% plasma. At the same time, the planet we live on is for about 71% covered by water. Surprisingly, the interaction of these two states of matter does not occur so often naturally on Earth. Therefore, the importance of plasma physics as a specialized research domain can undoubtedly be proven by the numerous existing and possible future promising applications of plasma-liquid systems. Currently, industrial implementations include high-voltage switching [2],

electric discharge machining [3], chemical analysis [4], and food processing [5]. Apart from that, adaptability of this technology has led to development of numerous reactor types for water treatment [6], shockwave production [7], polymer solution treatment [8], chemical synthesis of H_2 and H_2O_2 [9], NM synthesis [10]–[12], and extraction of biological compounds [13]. Plasma-induced catalysis of germination and enhanced growth of plants resulted in the emerging field of plasma agriculture [14]. Alike, the successful application of plasma for wound healing, skin treatment, dentistry, and cancer treatment has provoked a rapidly growing interest in plasma medicine in recent years [15].

In spite of all the recent progress, a fundamental understanding of the underlying processes in these applications is still missing. Partly, such complexity is caused by the wide variety in plasma-liquid reactors. Classification methods can be based on plasma regime, i.e., corona, glow, arc, or dielectric barrier discharge, on the applied voltage waveform, i.e., DC, AC (low frequency), radio frequency, microwave or pulsed discharge, or on the plasma-liquid phase distribution and electrode configuration. For instance, one popular classification approach starts with a basis of 2 or 3 main plasma–water phase distributions and then subdivides reactors depending on their electrode configuration, as in [1], [6].

In terms of the latter, Vanraes et al. [16] have identified 107 types of different plasma reactors in a literature review of around 300 scientific reports on the water treatment application. Six main classes of reactors have been distinguished, namely, in-liquid discharge, gas phase discharge over a liquid surface, bubble discharge, spray discharge, remote discharge, and hybrid reactors (Fig. 2.1).

This classification is based on the idea that the total plasma–water interface surface presents an important parameter in determining the reactor's energy efficiency. The larger the interface surface, the higher is expected pollutant degradation efficiency [17], [18]. Enlargement of an interface surface can be achieved by generation of plasma in bubbles, by solution spraying through the active plasma zone, and by creating a thin solution flow film along the discharge. It can be enlarged even further by extending the plasma volume, which has led to many possible choices of electrode configurations and geometries. Apart from that, undesired energy loses to, for instance, Joule heating of water can be avoided by introducing dielectric barriers and porous layers in the setup, while enhancing the local electric field for easier breakdown.

According to another popular classification approach [6] for water treatment reactors based on the used discharge regime and applied voltage waveform, the following discharge regimes can be distinguished:

- Corona and streamer discharge;
- Glow discharge;
- Dielectric barrier discharge (DBD);

– Arc discharge.

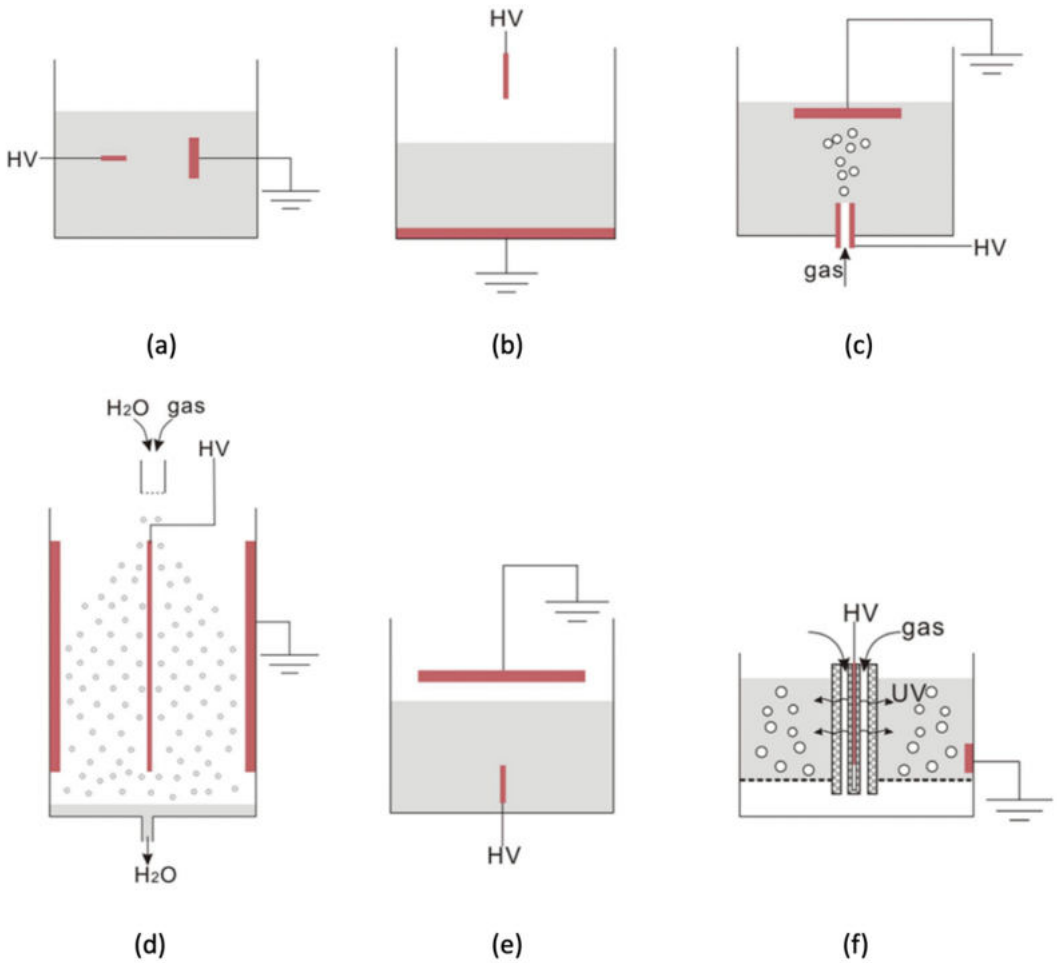

Figure 2.1: The six main plasma-liquid reactor types, according to [16]: (a) in-liquid discharge (here represented with the commonly used pin-to-plate configuration), (b) gas phase discharge over a liquid surface, (c) bubble discharge, (d) spray discharge, (e) hybrid reactors, which combine any of the other types (e.g., in-liquid and gas phase discharge in this scheme), and (f) remote discharge, where plasma is generated not in direct contact with the liquid. HV stands for high voltage and UV for ultraviolet radiation. The liquid phase is represented in grey, the electrodes in red, and dielectric barriers [in (f)] with cross hatching [16].

Spark discharge is considered as a transient form of arc and therefore falls in the fourth category. All listed discharge regimes can be generated both in the gas and liquid phase.

Based on the voltage waveform used, the following discharge types can be identified:

– DC discharge;
– AC (low frequency) discharge;
– Radio frequency (RF) discharge;
– Microwave discharge;
– Monopolar pulsed discharge;
– Bipolar pulsed discharge.

Numerous voltage-related parameters, such as voltage amplitude and polarity, pulse frequency, rise time and width can affect reactor energy efficiency. For instance, Malik, identified 27 different reactor types in his literature study [18]. On the other hand, Locke et al. distinguished following 7 types of reactors [6]:

- Pulsed corona and corona-like electrohydraulic discharge;
- Pulsed spark electrohydraulic discharge;
- Pulsed arc electrohydraulic discharge;
- Pulsed power electrohydraulic discharge;
- Gas phase glow discharge;
- Gas phase pulsed corona discharge;
- Hybrid gas–liquid electric discharge.

In [19], Jiang et al. identify 4 more reactive types:

- DC pulseless corona electrohydraulic discharge;
- Dielectric barrier discharge;
- Gas phase gliding arc discharge;
- DC arc discharge torch.

In the first 3 types of reactors, plasma is generated in or in contact with liquid, while the last type introduces water directly in the torch, where it subsequently vaporizes and becomes the plasma forming gas. Therefore, it can be categorized as a subtype of spray discharge. More summarized information on basic chemistry and physics of the discharge types in this list can be found in [6], [17]. The list shows the subtype division of the 6 main reactor types on the basis of plasma–water phase distribution. More extensively this has been performed by Locke and Shih in their comparative study for the reactor energy efficiency of H_2O_2 production [9], where authors distinguish more than 30 subtypes. This method, however, neglects the influence of reactor design, materials, and working parameters.

2.3 Plasma generation in liquid for nanomaterial synthesis

So far, Section 2.2 has discussed classification of plasma-liquid reactors from the perspective of their application in the water treatment technologies. However, the focus of this work is primarily on yet another major application of plasmas in and in contact with liquids that represents a separate research branch: NM synthesis through plasma-liquid interactions.

As mentioned in Chapter 1, a pioneering work in this domain had been carried out by Theodor Svedberg [20]. In his experiments, a discharge was generated between metal electrodes immersed in liquid and placed in contact with metal powder. The high-frequency alternating current passing through the electrodes led to their rapid melting and

evaporation and subsequent condensation of metal vapors in vapors of the liquid medium. According to Richard Feynman [21], such electrical condensation method represents a “bottom-up” approach to nanofabrication. Its main advantage lies in its versatility with the only fundamental limitation requiring the dispersed material to be electrically conductive.

Over the next decades since the Svedberg’s discovery, various new approaches using in-liquid plasma generation have been successfully developed and applied for synthesis of metal, alloy, oxide, inorganic, carbonaceous, and composite NMs. Such increasing interest can be explained by various advantages of this so-called electrical condensation method, such as, foremost, design simplicity. As a result, numerous works emerged reporting variety of experimental setups [10], [12], [22], [23], differing in such parameters as liquid media, electrode material, electrode configuration, electric power source, etc. Despite of the importance, several significant points are not addressed in these works, including the electrode configuration for NM synthesis, the supply method of the source materials for NMs, and the liquid used. These aspects, as they can be expected to be of a determining role in further development of NM synthesis, have been covered by Saito and Akiyama in [11]. This review presents and categorizes all available plasma in liquid configurations for application in number of fields, such as NM synthesis, analytical optical emission spectrometry, hydrogen production, polymerization, and water treatment.

Based on the electrode configurations and power sources used, four main groups of plasma-liquid discharges can be distinguished [11]:

– Gas discharge between an electrode and the electrolyte surface;

– Direct discharge between two electrodes;

– Contact discharge between an electrode and the surface of surrounding electrolyte;

– Radio frequency (RF) and microwave (MW) generation.

The second group in this list deals with direct plasma discharge between two electrodes and can be referred to as “solution plasma”, “discharge plasma in liquid”, “electric spark discharge”, “arc discharge”, “capillary discharge”, and “streamer discharge”. This group is of the main interest for the scope of this research work, and, therefore, will be regarded in more detail in the Section 2.4.

2.4 Direct in-liquid discharge between two electrodes

Figure 2.2 illustrates the variety of reactor configurations for direct in-liquid plasma discharges, as summarized by authors in [11]. Contrary to gas discharges between an electrode and the electrolyte surface

(where the liquid acts as a second conductive electrode), direct in-liquid discharges are initiated between two electrodes of similar size and shape that are immersed in the liquid at a short distance.

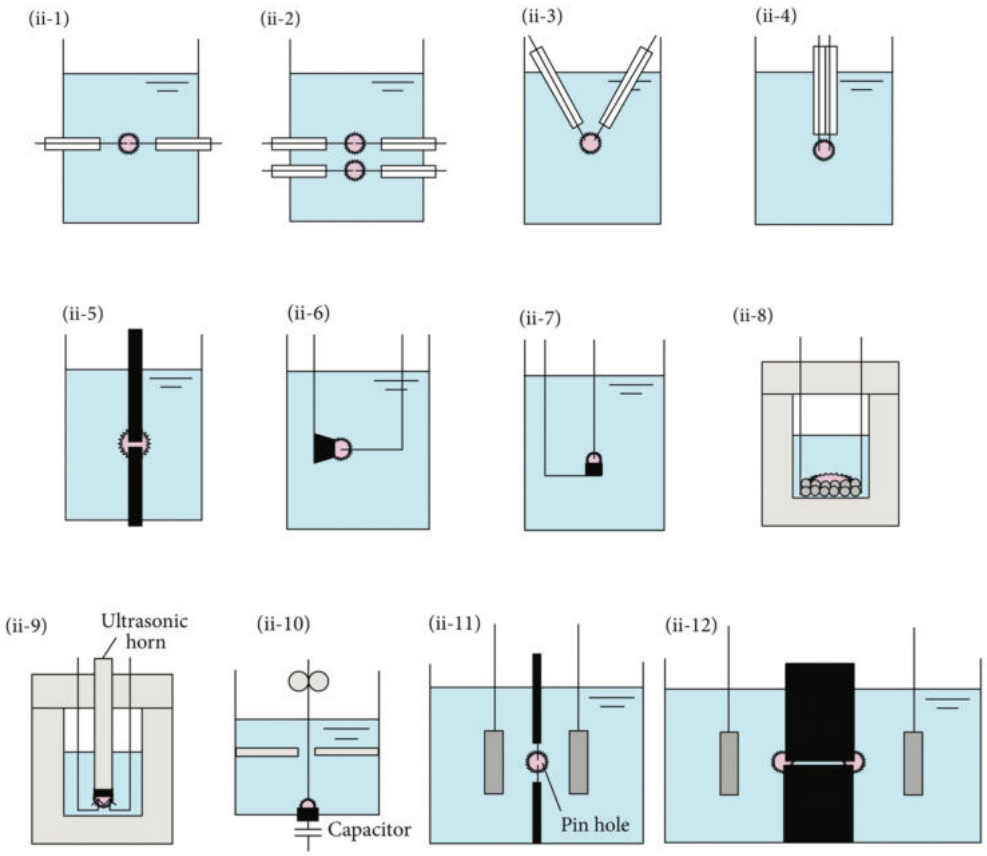

Figure 2.2: Typical electrode configuration for direct discharge between two electrodes [11]: (ii-1) solution plasma; (ii-2) solution plasma with pair electrodes; (ii-3) pulsed plasma in a liquid, arc process, and solution plasma; (ii- 4) solution plasma; (ii-5) arc discharge, submerged arc nanoparticle synthesis system (SANSS), electric spark discharge; (ii-6) arc discharge; (ii-7) arc discharge; (ii-8) spark discharge method in liquid media; (ii-9) electric plasma discharge in an ultrasonic cavitation field; (ii-10) wire explosion process in water; (ii-11) DC diaphragm discharge, and (ii-12) AC capillary discharge.

Direct discharge ensures that most liquids containing conductive electrolytes, such as deionized water, ethanol, and liquid nitrogen can be used for such purposes. In this configuration, both ions in the liquid and electrodes can serve as raw materials for NM formation. For instance, direct in-liquid discharges are used for the synthesis of carbon-based NMs by employing graphite rods or organic solvent as the raw materials. However, in case of the NMs precipitation from the liquid phase, impurities of the electrode origin should be carefully considered.

Originally, a model for a solution plasma was reported by Takai [24]. “Solution plasma processing (SPP)” is referred to as a developed technique for nanoparticles (NP) synthesis, surface modification of

metals, and sterilization of water. Typical setups for solution plasma generation are shown in Figure 2.2 (ii-1) and (ii-2). Figure 2.3 depicts model for a solution plasma proposed in [24]. Plasma is located at the center and is surrounded by a gas phase, which, in term, is surrounded by a liquid phase. Two interfaces are present: plasma/gas and gas/liquid. Since the solution plasma is confined by its condensed state, it displays unique properties and can promote fast reactions that offer a scope for basic studies on the solution plasma, from the viewpoints of both physics and chemistry.

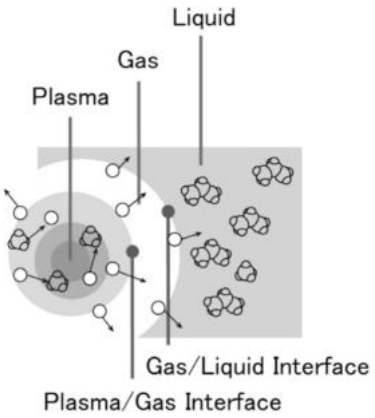

Figure 2.3: Model of the solution plasma proposed by Takai [24].

When the solid electrode is used as a source material of NMs, such process is called “solution plasma sputtering (SPS)”. The typical applied voltages are between 1.6 and 2.4 kV, with pulses at around 15 kHz and pulse widths at 2 μs. SPS has been widely used for synthesis of Au NPs [25], [26], composite Pt-Au and Pt-Au/C NMs using Pt and Au electrodes within the carbon-dispersed solution [27], CuO and ZnO NPs from Cu and Zn electrodes in water [28]. Tarasenko et al. also reported using electric discharge techniques in water for NP synthesis, in which the peak current was 60 A, and AC, DC, and pulsed power sources were used.

The reactor configuration (ii-3) in Figure 2.2 has been used for synthesis of carbon-encapsulated Co, Ni and Fe magnetic NPs [29], spherical ferromagnetic Fe_3O_4 NPs [30], Wurtzite-type ZnMgS [31], and carbon-coated Fe and Ni NPs [32] using pulsed plasma techniques in liquid media, such as ethanol, tap water, water mixture with a cationic surfactant, 1-hexadecylpyridinium bromide mono- hydrate (CPyB), and liquid sulfur. Typically, these systems operate at low voltages and low currents with a discharge duration of around 10 μs. One of the electrodes is kept vibrating in order to keep the discharge process stable. Without vibration of the electrode, the discharge process continues until the electrodes become eroded enough to make the gap between the electrodes larger than the required distance for the breakdown [31].

Tong et al. used the configuration (ii-4) in Figure 2.2 for the cutting of multiwalled carbon nanotubes (MWCNTs) via SPP technique [33]. In a typical cutting process, purified MWCNTs and potassium chloride (KCl) solution are added into a SPP system. After mixing by vigorous stirring, the suspension of MWCNTs with serious aggregation is formed. Then SPP is carried out under exposure to O_2, and the aggregation degree of MWCNTs shows a continual decrease with SPP-treatment time.

Configuration (ii-5) in Figure 2.2 shows the setup of DC or pulsed arc discharge in deionized water. In the arc discharge process at higher currents ($15 \sim 25$ A) and lower voltages, the electrode material is vaporized to form NPs. Lo et al. reported on a synthesis of Cu-based nanofluids through submerged arc nanoparticle synthesis system (SANSS) [34]. Pure copper is selected as both, an electrode material and workpiece. Copper is heated and evaporated by arc sparking between two electrodes being immersed in dielectric liquids, mainly including mixing solutions of deionized water and ethylene glycol. The copper aerosol can be condensed to form NPs immediately by the cooling media. The NPs then dissolve in the which become metal nanofluids. In such a manner, various Cu-based NMs can be synthesized using different dielectric liquids. The same SANSS technique has been applied to synthesize Ag [35], and Au [36] nanofluids. Ashkarran et al. produced Au [37], Ag [38], [39], ZnO [40], WO_3 [41], ZrO_2 [42], and TiO_2 [43] NPs by arc discharge with currents ranging between 10 and 40 A. In the case of using a DC power source for arc discharge in liquid [37], [38], [39], [40], the reaction time was less than 5 minutes. In contrast to the arc discharge with low voltage and high current, high-voltage and low-current plasma was also generated in the liquid.

In works of Sano et al. [44], [45], famous carbon “onions”, as well as other various carbon-based NMs and composite materials were synthesized using submerged arc discharge in water of configurations seen in Figure 2.2 (ii-6) and (ii-7). In these systems, the anode is smaller than the cathode and the gap distance between the two was maintained at less than 1 mm. The small anode is mostly consumed during discharge [44].

Spark discharge method involving a spark discharge reaction conducted in autoclave [46], [47] is depicted in Figure 2.2 (ii-8). The role of the electrodes in such configuration is performed by pure metallic plates, while pure metallic pellets with diameters of 2–6 mm are used as starting materials, and liquid ammonia and n- heptane as dielectric liquid media.

Figure 2.2 (ii-9) presents a typical reactor for electric plasma discharge in an ultrasonic cavitation field. In work of Sergiienko et al. [48], such discharge configuration has been used with an iron tip fixed on top of a titanium ultrasonic horn and two wire electrodes inserted 1 mm away

from the iron tip. Authors explained that due to the radicals and free electrons formed within an ultrasonic cavitation field it enhanced electrical conductivity, which allowed for an electric plasma discharge to be generated at a relatively low electric power.

Wire explosion processes in water [49] can also be included to the group of direct in-liquid discharges between two electrodes, as shown in (ii-10) Figure 2.2. In such configuration, stored electrical energy of a capacitor is released through a triggered spark gap switch to the wire. Due to the fact that resistivity of the wire is very low compared to that of distilled water, the electrical energy mainly dissipates in the wire. Therefore, the part of wire between the electrodes is heated, vaporized, and turned into plasma, that eventually allows for NPs formation.

While for configurations (ii-1) to (ii-10) in Figure 2.2, discharge occurs between two solid electrodes, in the cases of DC diaphragm discharge [50] (ii-11) and AC capillary discharge [51] (ii- 12), the electrode is the electrolyte itself. When a high voltage is applied on electrodes separated by a dielectric barrier (diaphragm) with a small pinhole in it, the discharge is ignited just in this pinhole [50]. In case of the diaphragm discharge, the electrode erosion is minimized and, thus, the electrode lifetime is prolonged, due to the fact that discharge does not reach the electrode surface. However, the material surrounding the pinhole is damaged during discharge. Diaphragm discharge has potential for use in NM synthesis, despite of it mainly being applied to water purification purposes.

It should be mentioned that none of the configurations presented in Fig. 2.2 fully match those employed in this thesis (see Chapter 3 for more detail). Nevertheless, some similarities can be underlined. For instance, in terms of the overall reactor configuration, (ii- 5) and (ii-8) are the closest to the electrode arrangements of interest of this work. However, while works featuring (ii- 5) ([34]–[43]) deal with in-liquid discharges generated at low voltages, there are other aspects that decrease their relevance in the context of present thesis. Namely, the fact that all reactors in [34] – [43] operate at low currents (10 – 40 A), wherein the pulsed electric discharges are addressed only in [34]–[36] with pulse widths well below 20 μs. Moreover, none of these studies cover diagnostics of the electric discharge plasma. Instead, they mainly focus on synthesis process and characterization of obtained NMs.

Reactor configuration (ii-8) was used by Sato et al. in [46] and [47] for synthesis of metal powders by the spark discharge method. In terms of the operating principle, this technique is analogical to that investigated in the present study, and is based on a spark discharge occurring at the contact points of metal pellets dipped in the liquid medium. However, some experimental parameters in [46] and [47] are substantially different,

such as high discharge voltage (from 5 to 11 kV) and choice of the liquid media (liquid ammonia, n-heptane and hydrocarbon).

2.5 Plasma diagnostics of electric discharges in water

Plasma diagnostics techniques allow the determination of plasma parameters such as the temperatures (translational, rotational, vibrational and electronic), the density of species, the electric field, the magnetic field, etc. The techniques available depend largely on the type of plasma, which is characterized mainly by its pressure, the ionization degree, the temperature and its dimensions. Plasmas generated in water usually produce some observable optical emissions, and its diagnostics is a key tool in helping to understand the performance issues. Generally, combination of optical emission spectroscopy (OES), high-speed imaging, and electric parameter measurements are some of the most used methods capable of providing information on the underwater electric discharges. Therefore, this section will be dedicated to general overview of the state-of-the-art experimental characterization of in-liquid plasma by means of OES techniques.

Burakov et al. have performed spectroscopic diagnostics of the electric discharge plasma in liquid used for synthesis of nanosized particles of metals and their compounds [52], [53]. In [52], authors carried out a comparative analysis of the plasma parameters for high-voltage spark and arc discharges in water, ethanol, and air. The electron temperature was calculated from the intensity ratio of the copper lines, while the electron number density was obtained from Stark broadening of the H_α hydrogen line. Authors also estimated the pressure in the discharge channel from the equation of state of an ideal plasma. According to the results, the pressure in the plasma channel in the spark regime in liquid reached ~3×10^8 Pa at T = 18000 K. The fraction of atoms and ions of the electrode material was about 10% for a total concentration of 1×10^{21} cm^{-3}. The assumption was made that a substantial part of the total erosion of the electrode material involved particles in the solid or liquid states. In [53], authors presented a combined gas-liquid interface high-voltage discharge reactor developed for synthesis of colloidal nanoparticles. Their experimental investigations focused on diagnostics of the electric discharge plasma created between Ni–Ni or Ni–graphite (Ni–C) electrodes in distilled H_2O with and without Ar purging into the discharge gap. The recorded Ni lines were poorly suited for determining the plasma temperature. Therefore, the temperature was determined using groups of O spectral lines. The electron number density was derived from the H_α line width. According to the results, the plasma temperature was practically independent of the capacitance of the discharge condenser that was varied in the experiments, regardless of a change of the

discharge energy. However, it depended considerably on the type of working solution and was found to be 1.2 eV for discharge in liquid and ~1.5 eV with Ar purging of the interelectrode gap. The electron number densities were in qualitative agreement with the increasing condenser capacitance for the regime with Ar purging. This suggested that the electron number density had a more sensitive dependence because of the faster rate of ionization–recombination processes than establishment of thermodynamic equilibrium for the neutral atomic states. However, the inverse dependence of electron number density on condenser capacitance was observed without Ar purging.

In contrast to high-voltage discharge reactors in [52] and [53], NMs in [31] were synthesised using low-voltage (220 – 260 V) and low-current (10 – 60 A) pulsed discharge. However, main object of the work was to study the effects of the discharge current and pulse duration on the morphology and phase composition of the synthesized NMs, therefore no plasma diagnostics was performed.

Analysis of the available literature on this subject has brought to the light that the class of pulsed low-voltage electric discharges in water is mostly represented by the electric spark discharge occurring in the electric discharge machining (EDM) process. EDM in liquid dielectric media is a well-stablished manufacturing process widely used to produce injection molds, dies, finished parts, such as cutting tools and items with complex shapes. It will be discussed in more detail in subsection 2.5.1.

The working principles of EDM are based on interactions of electric discharge plasmas with electrodes materials, which is a poorly understood phenomenon. Therefore, optimization of EDM processes is still based on empirical methods and recipes. This explains the high amount of published research works on diagnostics of the EDM electric discharge plasma. The latter, however, impose a number of certain difficulties, such as tiny sizes of the plasma, short duration, weak luminous intensities, poor reproducibility due to continuously evolving electrode surface profiles and dielectric contamination from eroded electrode materials. These aspects make diagnostics of the EDM plasmas a very challenging task.

2.5.1 Electric Discharge Machining (EDM) – a perfect case of a low-voltage underwater electric discharge plasma

EDM is a well-known machining technique since more than fifty years. The principle of EDM is to use the eroding effect of controlled electric spark discharges on the electrodes. It is thus a thermal erosion process. The sparks are created in a dielectric liquid, generally water or oil, between the workpiece and an electrode, which can be considered as the cutting tool. There is no mechanical contact between the electrodes

during the whole process. Since erosion is produced by electric discharges, both electrode and workpiece have to be electrically conductive. Thus, the machining process consists in successively removing small volumes of workpiece material, molten or vaporized during a discharge. The volume removed by a single spark is small, in the range of 10^{-6}–10^{-4} mm^3, but this basic process is repeated typically 10000 times per second.

Figure 2.4 gives a simple explanation of the erosion process due to a single EDM discharge.

First, voltage is applied between the electrodes. This ignition voltage is typically around 200 V. The breakdown of the dielectric is initiated by moving the electrode towards the workpiece. This will increase the electric field in the gap, until it reaches the necessary value for breakdown. The location of breakdown is generally between the closest points of the electrode and of the workpiece, but it will also depend on particles present in the gap. When the breakdown occurs, the voltage falls and a current rise abruptly. The presence of a current is possible at this stage, because the dielectric has been ionized and a plasma channel has been created between the electrodes.

The discharge current is then maintained, assuring a continuous bombardment of ions and electrons on the electrodes. This will cause strong heating of the workpiece material (but also of the electrode material), rapidly creating a small molten metal pool at the surface. A small quantity of metal can even be directly vaporized due to the heating. During the discharge, the plasma channel expands. Therefore, the radius of the molten metal pool increases with time.

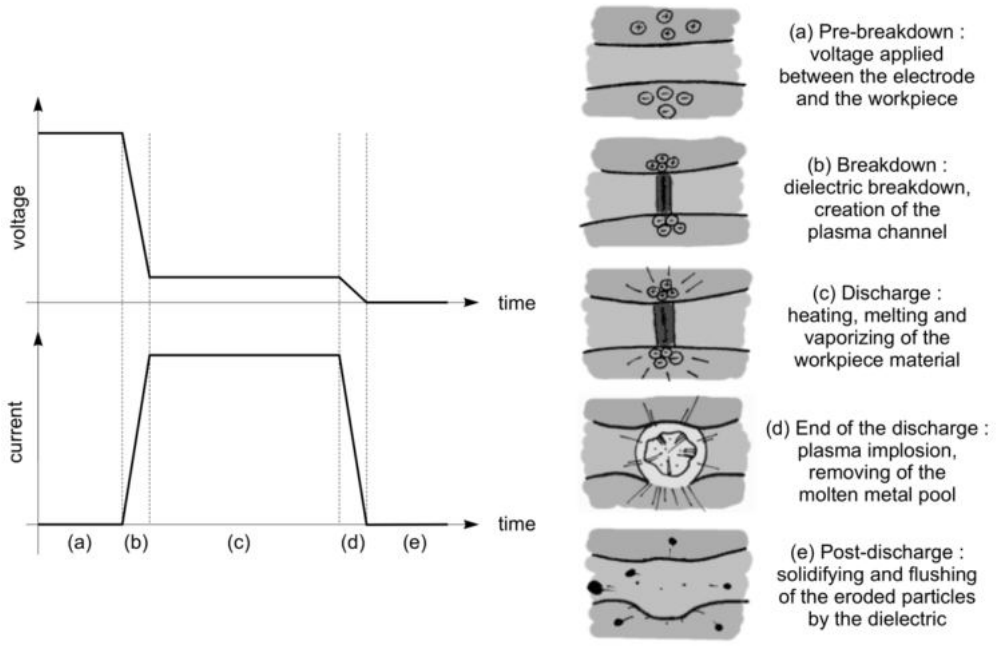

Figure 2.4: Principle of the EDM process [54].

At the end of the discharge, current and voltage are shut down. The plasma implodes under the pressure imposed by the surrounding dielectric. Consequently, the molten metal pool is strongly sucked up into the dielectric, leaving a small crater at the workpiece surface (typically 1−500 μm in diameter, depending on the current).

The liquid dielectric plays a crucial role during the whole process: it cools down the electrodes, it guarantees a high plasma pressure and therefore a high removing force on the molten metal when the plasma collapses, it solidifies the molten metal into small spherical particles, and it also flushes away these particles. The post-discharge is in fact a crucial stage, during which the electrode gap is cleaned of the removed particles for the next discharge. If particles stay in the gap, the electrical conductivity of the dielectric liquid increases, leading to a bad control of the process and poor machining quality. To enhance the flushing of particles, the dielectric is generally flowing through the gap. In addition, the electrode movement can be pulsed, typically every second, performing a large retreat movement. This pulsing movement also enhances the cleaning, on a larger scale, by bringing “fresh” dielectric into the gap.

Typical experimental arrangement for EDM and its diagnostics is shown in Figure 2.5. Underwater EDM basically involves discharge between a tool electrode (cathode) and the job (anode). Typical gap between the electrodes is about few tens of μm and applied voltage across them is several hundreds of volts. Usually, the voltage is applied between the electrodes in the form of pulses with on-time less than 100 μs.

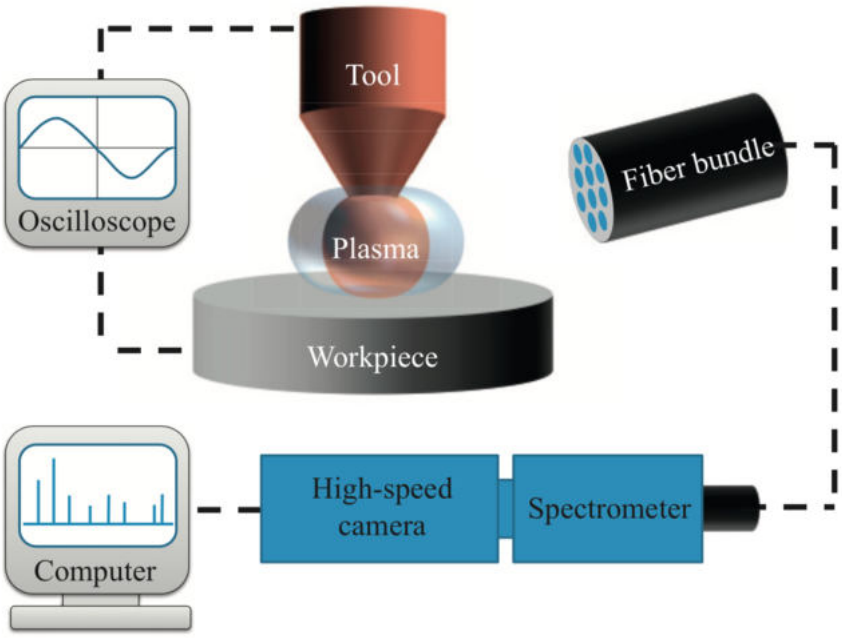

Figure 2.5: Experimental arrangement for EDM and its diagnostics [55].

2.5.2 EDM discharge plasma imaging and visualization

Descoeudres et al. have investigated and presented a spatio-temporal characterization of the EDM plasma with imaging and optical emission spectroscopy [56]. Authors used a standard EDM die-sinking machine, with a copper electrode and a steel workpiece. In order to localize the discharge as much as possible the electrode configuration is point-to-point.

Figure 2.6 shows a typical image of an EDM plasma in oil. The electrodes have been outlined because they are not visible without external lighting. The imaging was made with a 30000-fibre endoscope, directly immersed in the dielectric. The endoscope is equipped with a small lens at its tip, in order to have a magnification of the plasma region. The light emitting region is generally round or oval. Its diameter increases with the discharge current, from 50 to 400 µm for a current increase from 6 to 48 A. But even for the same discharge parameters, plasma images are poorly reproducible. The plasma, and hence the shape and size of the emitting region recorded on the images, depend strongly on the electrode surface state, which is constantly evolving during machining. However, the light mostly originates from a broader region than the gap itself, i.e. the discharge excites a broad volume around the electrode gap.

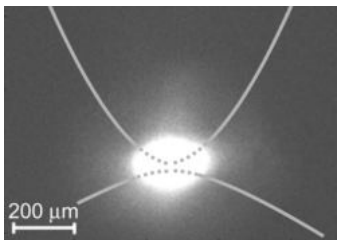

Figure 2.6: Typical plasma image (5 µs exposure, 5 µs delay after breakdown; 24 A, 100 µs, oil) [56].

Figure 2.7 shows plasma images at different stages of the discharge. There is a slight growth of the emitting region, but its size remains fairly constant during the whole discharge.

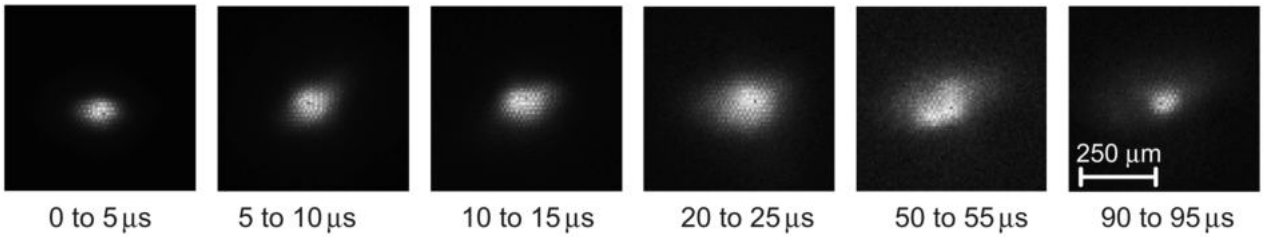

Figure 2.7: Plasma images at different times during the discharge (5 µs exposure, variable delay after breakdown; 24 A, 100 µs, water). The images are normalized in intensity. Each image is obtained during a different discharge [56].

The evolution of the plasma size is a more delicate point. Since the CCD readout time is much longer than the discharge on-time, it was impossible to acquire more than one image during a single discharge. Thus, each image was acquired during a different discharge. Since the discharges were poorly reproducible, the comparison between the images becomes difficult.

Authors have also investigated the afterglow of the discharge. There is still a weak slowly-decaying light emission, typically until 400 µs after the end of the discharge. Figure 2.8(a) shows an image acquired directly after a discharge, and Figure 2.8(b) shows the optical spectrum of the post-discharge light.

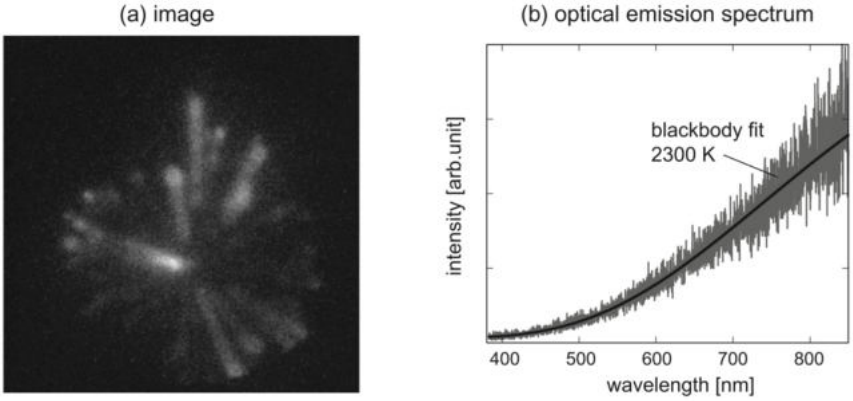

Figure 2.8: Incandescence of the removed particles after a discharge. (a) Image of a single post-discharge (100 µs exposure; 12 A, 50 µs, oil). (b) Optical emission spectrum, with a 2300 K blackbody fit. The light measurement is time integrated over thousands of post-discharges (50 µs exposure, 150 g mm^{-1} grating; 16 A, 50 µs, oil) [56].

As it can be seen in Figure 2.8 (a), the weak light emitted after the discharge is due to particles of heated metal. These particles come from the molten metal pool created in the workpiece during the discharge, and are then removed from the workpiece and ejected in the dielectric when the discharge is shut down. Their path is visible apart from the luminous dots, because they are moving during the camera exposure. Spectroscopy showed that this post-discharge light emission is close to a blackbody radiation, which confirms that the emitters are heated metal particles. The spectrum in Figure 2.8(b) is quite noisy, due to the low intensity of the afterglow emission. The temperature of the emitters was found to be around 2300 K (±100 K) as estimated from the fitting the afterglow spectra with Planck's law. Since the melting point of steel is ~1700 K, the particles are still in a liquid state at the very beginning of the post-discharge. The particle size and speed can also be estimated from the images. Authors found that the largest particles have a diameter of ~ 30 µm and speed of around 3 m s^{-1} [56].

In [57], Bhattacharya et al. have investigated dynamic evolution of the EDM arcs in water using fast photographic camera. The experimental EDM setup employed by authors consisted of a vertical rod type tungsten electrode (diameter 4 mm) with conical tip as cathode and a rectangular anode. Four different anode materials of high technological relevance, namely SS304 (stainless steel), copper, zircaloy, and P91 (reduced activity ferritic martensitic steel) have been used. A pulsed power supply of 10 kHz generating rectangular pulse of 500 V height and maximum current of 2 A was connected to the upper end of the cathode. Bottom part of the cathode and the whole anode were immersed in demineralized water. The gap between the cathode tip and the anode surface, adjusted through an attached micrometer screw, is maintained within 40-50 μm. When voltage between the terminals increased beyond the dielectric breakdown voltage of the demineralized water, arc formed between the cathode tip and the job. The point of connection between the arc and the job is called arc root.

Through numerous observations in the fast-photographic study, authors found that one phenomenon was common with all anode materials: flow in the form of an expanding jet (see Fig. 2.9 (b), and images in Fig. 2.10). This very significant phenomenon has not been considered in any of the earlier theoretical or experimental studies in the context of EDM processes. Nevertheless, it is actually well discussed in thermal plasma literature [58] and termed as “JxB” pumping. When associated current lines in a conducting medium arrange in a vertically diverging configuration, as can be seen in Figure 2.9 (a), the magnetic field at the top is less compared to the same at the bottom (inversely proportional to the radius of the column). Similarly, the current density (J) is also less at the top compared to the same at the bottom (due to larger area of cross-section at the top). As a result, net JxB body force at the top (F_{Btop}) is less compared to the same at the ($F_{Bbottom}$). Therefore, net pressure (P_{top}) in the upper region is the sum of plasma pressure (Nk_BT_{top}) and contribution due to F_{Btop}. The same (P_{bottom}) in the bottom region is the sum of plasma pressure (Nk_BT_{bottom}) and contribution due to $F_{Bbottom}$. Obviously P_{top} is less than P_{bottom}. In such a situation, a gradient in pressure develops in the vertically upward direction:

$$\nabla p \propto (P_{top} - P_{bottom}) \tag{2.1}$$

This is the root cause of formation of an expanding plasma jet propagating in the upward direction. Since associated flow is driven by gradient in pressure and not absolute pressure, even a slightest gradient in the pressure may induce such flow. It may also be noted that the phenomenon may happen with any nonzero current, provided the current configuration is able to produce a pressure difference.

Another commonly observed phenomenon is a curvature in the current path caused by a kink (see Fig. 2.9 (a)). This is due to the higher concentration of magnetic field lines towards the center of the curvature causing the magnetic field inside curvature (B_{in}) greater than that (B_{out}) outside. Naturally, magnetic pressure P_{Bout} is less than P_{Bin}, which leads to development of magnetic pressure gradient in radially outward direction as shown in Fig. 2.9 (a). Higher the degree of curvature, greater is the driving force. This is how “kink induced magnetic pressure driven flow” arises in the present case. It is very obvious, that this phenomenon may happen with any magnitude of current whenever there is a curvature in the current path in the medium. In addition, the arc In Fig. 2.9 (b) does not attach to the tip of the cathode. This shows the strong effect of the magnetic pressure driven flow, that "draws" the arc root away from the electrode tip

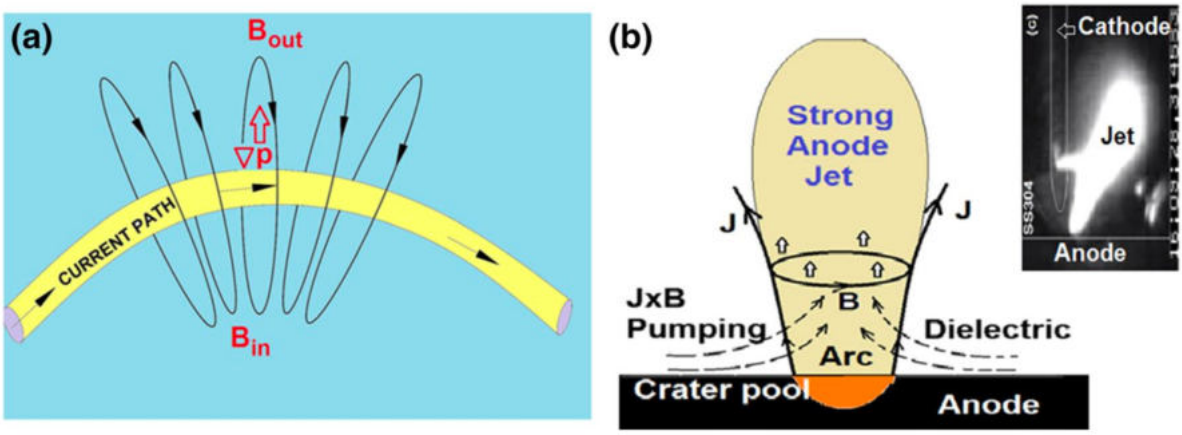

Figure 2.9: (a) Kink induced magnetic pressure driven flow; (b) The mechanism of JxB pumping for removal of anode material and image captured by fast camera as a combined effect of JxB pumping and kink [57].

In [57], authors present visualization of the discharge kinetics and its extensive analysis for all four anode materials. In this review, for the sake of brevity, these findings will be illustrated only for the discharge with P91 anode, which can be seen in Figure 2.10 (a–f).

Two previously discussed important features, namely kink instability and JxB pumping can be clearly observed. The kink in Fig. 2.10 (a) and (e) embodies higher magnetic field in the concave side compared to the same in the convex side. Resulting difference in magnetic pressure causes a strong mass flow across the arc in radially outward direction as observed. Once the flow detaches from the arc, typical movement of the plasma bubble is captured in Fig. 2.10 (f). Figure 2.10 (b) and (c) present observed mass flow related to JxB pumping effect, discussed above. Material from the arc root region flows like an intense expanding jet in the vertically upward direction. On its way, it interacts with the kink induced

magnetic pressure driven force and finally chooses a resultant path slightly inclined with the vertical. The interaction zone and the point of deflections are identifiable.

Due to intensive cooling by the dielectric, the plasma channel becomes thin and current density becomes extremely high. Associated pinching effect leads to another kind of interesting instability in the arc, so-called “sausage type”, as can be observed in Fig. 2.10 (d). It may be emphasized that this transient phenomenon is observed in the zone of dielectric media (water), where temperature is much lower compared to the same in the main arcing zone. The thin filamentary arc transiently passes through such colder zone making it further thinner through thermal pinching. Present observation indicates that the diameter of the EDM plasma channel is thin enough to make self-pinching force greater than the force applied by plasma pressure, a requirement for sausage type instability to occur. The fast-photographic images are the direct proofs that such phenomena happen.

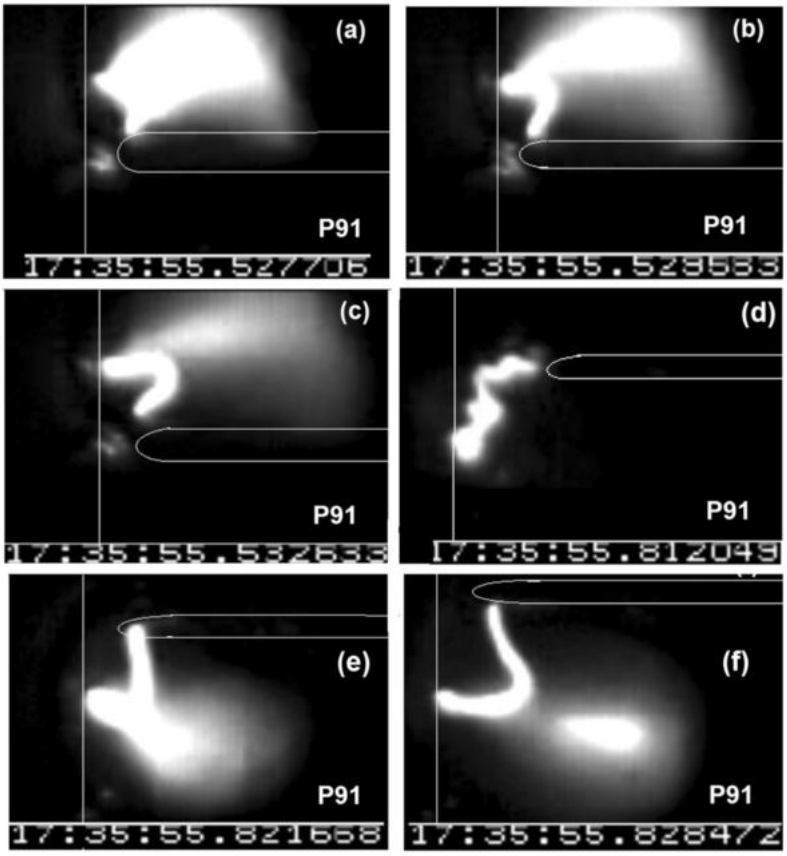

Figure 2.10: Observed evolution of arcs in underwater EDM discharges with P91 as anode material. The cathode is not visible. Approximate location of the cathode (finger shaped) and anode (vertical line) are sketched [57].

Information on time evolution of discharge dynamics and its interaction with the electrodes presented and discussed in [57] is

qualitative but may serve as a good first-hand information for future theoretical modelling and advancement in experimental understanding. Some of the phenomena reported by authors, such as direct observation of simultaneous multiple arc attachments over electrodes (in the case of the SS304 anode) and JxB pumping have not been discussed in any of the previous experimental or theoretical studies. It should be noted that EDM discharges with copper and zircaloy as anode materials exhibited features substantially different from the other two. In all frames highly prominent shock boundaries, indicative of occurrence of high temperature, have been observed. This fact was supported by the spectroscopic measurements, presented in the next subsection of this work.

2.5.3 EDM discharge plasma diagnostics

Descoeudres et al. [56] have performed optical emission spectroscopy of the EDM plasma. In order to have sufficient light intensity for spectroscopy, the light from thousands of discharges was accumulated over several seconds. Figure 2.11 shows spatially-resolved spectra (along a vertical axis) of an interesting spectral region for plasma contamination measurements. Near 520 nm are located three intense lines of neutral chromium (at 520.45, 520.6 and 520.84 nm) and one intense line of neutral copper (at 521.82 nm). Since authors use a copper electrode and a stainless-steel workpiece, the Cu line is emitted by particles coming from the electrode and the Cr lines are emitted by particles coming from the workpiece.

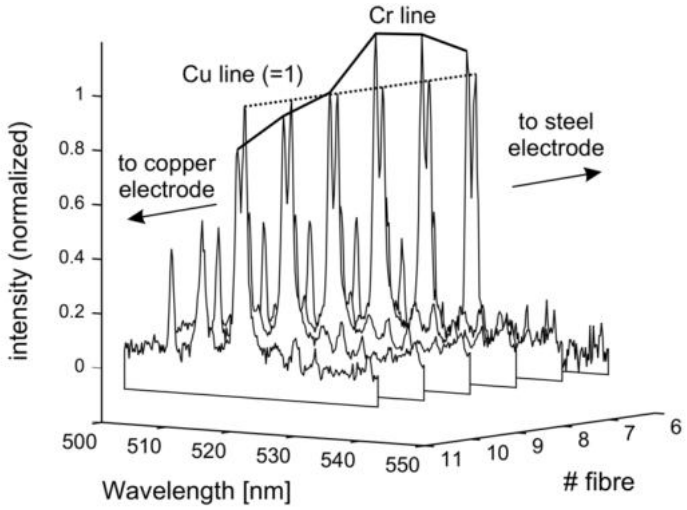

Figure 2.11: Vertical asymmetry of the plasma contamination observed with spatially-resolved spectroscopy. The spectra are normalized to the intensity of the Cu line at 521.8 nm. The light measurement is time integrated over thousands of discharges (6 A, 100 µs, water, 150 g mm^{-1} grating) [56].

It can be clearly seen from Figure 2.11 that plasma contamination is asymmetrical. Near the Cu electrode, the Cu line is more intense than the Cr lines. On the other hand, the Cr lines are more intense than the Cu line near the steel workpiece. Thus, each electrode contaminates the plasma mostly in a region close to itself.

The electron number density was calculated from H_α line broadening measurements. In dense plasmas such as EDM plasma, line broadening is dominated by far by Stark broadening. From H_α full width at half maximum (FWHM) measurements, the electron number density has been determined using the calculations of Gigosos and Cardenoso on hydrogen Stark broadening [59], and was found to be around 5×10^{16} cm^{-3} for a 100 µs discharge. Figure 2.12 shows spatially-resolved H_α spectra, along with the electron number density vertical profile calculated from them. The central spectra have a better signal to noise ratio than the outer ones, because the light intensity is higher in the center. Despite large error bars, the electron number density seems to be slightly higher in the plasma center (i.e. center of the electrode gap).

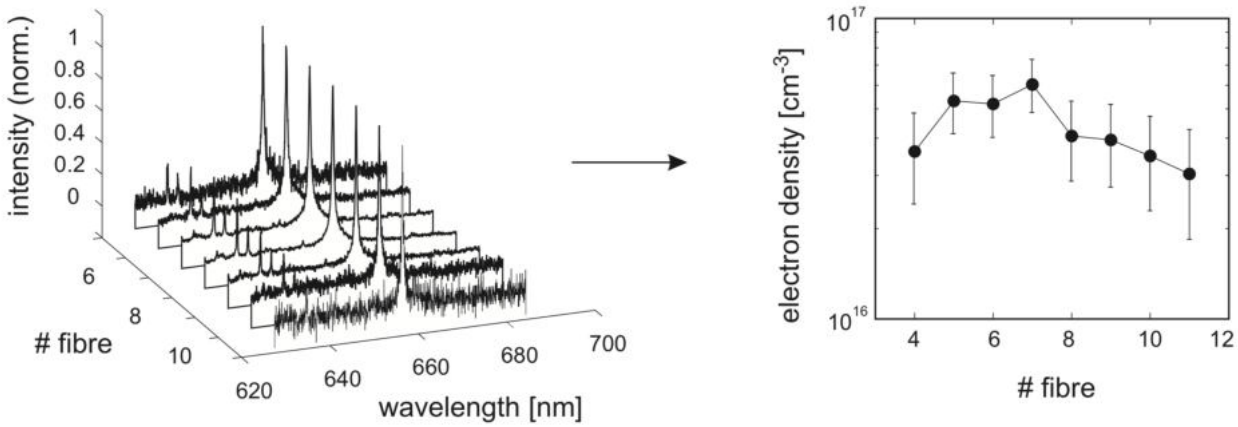

Figure 2.12: Vertical profile of the electron number density calculated from spatially-resolved H_α broadening measurements. The spectra are normalized to the intensity of the H_α line at 656.2 nm. The light measurement is time integrated over thousands of discharges (6 A, 100 µs, water,600 g mm^{-1} grating) [56].

Calculations of the electron temperature were done with the Boltzmann plot method, based on line intensity ratio measurements. Authors have used three lines emitted by neutral copper, at 510.55, 515.32 and 521.82 nm. Since these lines are located in the same spectral region, one can assume that the overall spectral transmission is the same for the three lines. It should be noted that the Boltzmann plot method requires the assumption of a plasma in local thermal equilibrium (LTE). It is not an obvious assumption, especially for non-ideal plasmas like EDM plasmas. However, due to the high plasma density, one can assume that

the numerous collisions between particles thermalize them rapidly. The assumption of LTE can thus reasonably be accepted.

Spatially-resolved spectra of the three Cu lines are shown in Figure 2.13, along with the electron temperature vertical profile. The electron temperature is quite constant over the whole profile. The plasma has thus a homogeneous electron temperature around 0.7 eV (8100 K).

In their later research, Descoeudres et al. [60] have performed time-resolved OES investigation of the EDM plasma. To calculate the evolution and profiles of the electron number density, authors used FWHM and shift measurements from time- and spatially-resolved spectra of the H_α line, shown in Figure 2.14. The FWHM and shift were calculated from a Lorentzian fit of the H_α peak for each spectrum.

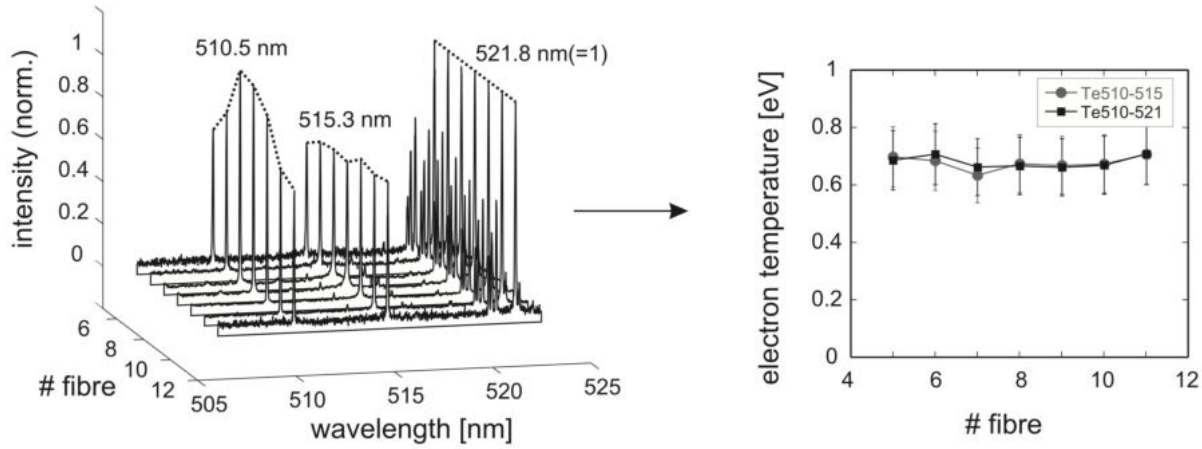

Figure 2.13: Vertical profile of the electron temperature calculated from spatially-resolved Cu lines intensities ratios. The spectra are normalized to the intensity of the Cu line at 521.8 nm. The light measurement is time integrated over thousands of discharges (6 A, 100 µs, water,1800 g mm^{-1} grating) [56].

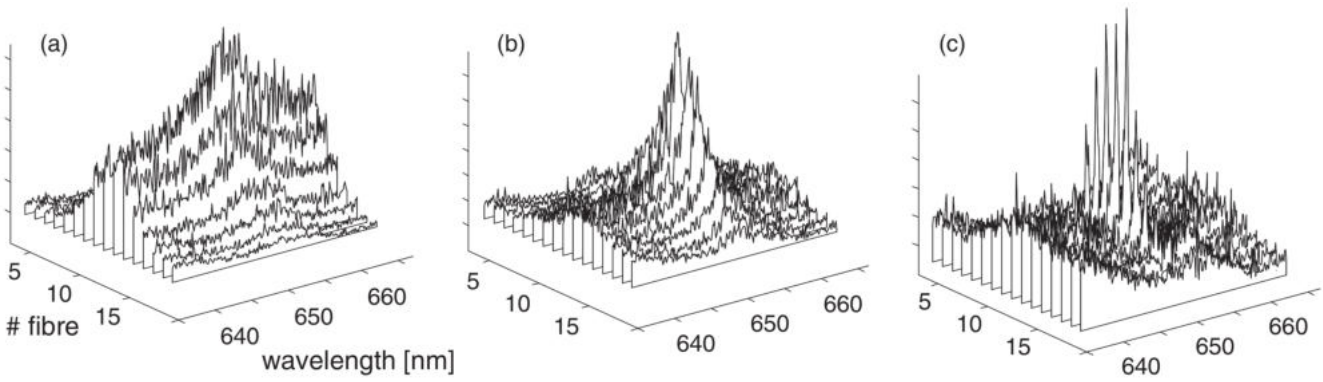

Figure 2.14: Time- and spatially-resolved spectra of the H_α line (Cu/steel, 12 A, 50 µs, water; time resolution 2 µs, 600 g mm^{-1} grating): (a) 0–2 µs; (b) 4–6 µs; (c) 36–38 µs [60].

The FWHM and the shift measurements gave comparable density values and evolution (see Figure 2.15 (a)). The results showed that the

electron number density was extremely high during the first microsecond (above 10^{18} cm^{-3}) and then decreased rapidly with time. The main reason for such high density is the fact that the EDM plasma is created from a liquid, which is a dense medium (~ 3×10^{22} water molecules cm^{-3}, for example). At the very beginning of the discharge, the plasma has to overcome the extreme pressure imposed by the dielectric. Then the plasma expands, which results in a decrease in its density. But during the whole discharge, the density remains high (always above 10^{16} cm^{-3}) due to the constant pressure of the surrounding liquid. The electron number density seems to be slightly higher in the plasma center.

Figure 2.15 (b) shows the evolution of T_e profiles calculated from time- and spatially-resolved spectra of the three Cu lines, analogically to the calculations performed by authors in [56]. The electron temperature was found to be about 0.7 ± 0.15 eV (~ 8100 ± 1750 K). It is slightly higher during the first 10 µs than for the rest of the discharge, being from ~0.8 to 0.7 eV (~9000 – 8000 K). Then it remains rather constant around 0.7 eV within the margin of error, even after 1 ms. The plasma had thus a homogeneous electron temperature.

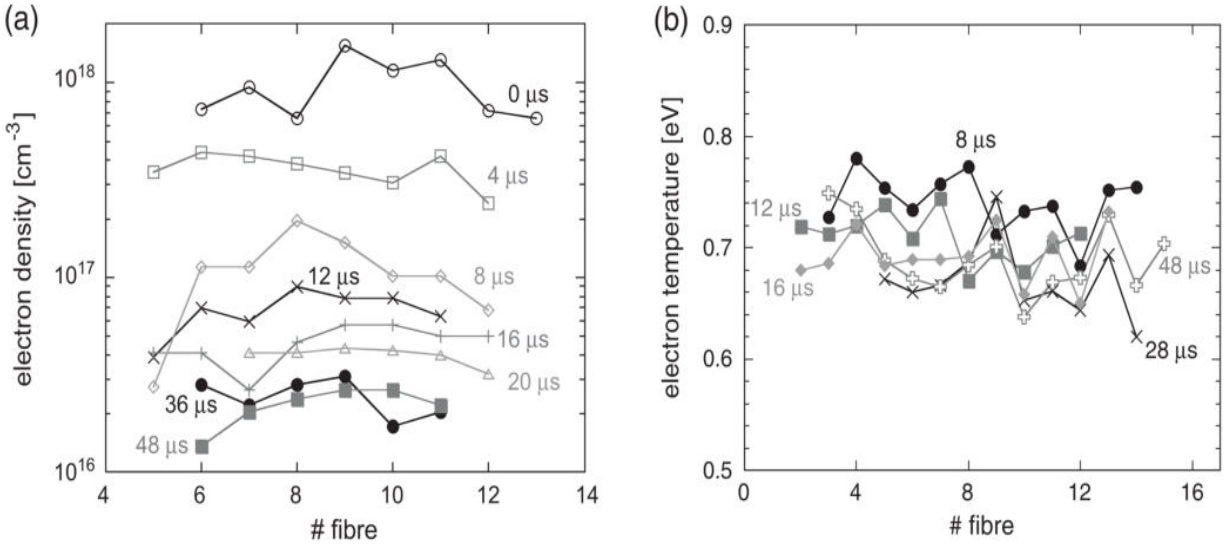

Figure 2.15: Evolution of the electron number density (a) and electron temperature (b) vertical profiles (Cu/steel, 12 A, 50 µs, water, time resolution 2 µs, spatial resolution ~ 20–30 µm/fibre) [60].

In [61], Nagahanumaiah et al. present the spectroscopic measurement of temperature and electron number density in the micro-EDM or µ-EDM process in order to understand the effect of varying process parameters including voltage, current, spark gap and electrode size on the plasma characteristics

In their research, authors used the optical emission spectroscopy technique to record the radiant intensity of light emitted by the impurities removed from the electrode material. Figure 2.16 shows a typical

preprocessed image of the spectrum obtained at one of the test conditions. The enlarged spectrum in the range 370–450 nm is also shown in Figure 2.17.

The emission spectra show a strong underlying continuum at specific wavelengths. However, as can be seen from the spectrum, the H_β (486.13 nm) line is found to be dominant whereas the other Balmer series lines such as H_α (656.28 nm) and H_γ (434.05 nm) are not observed. In addition, the H_β line, which depends strongly on the electron number density, is broadened.

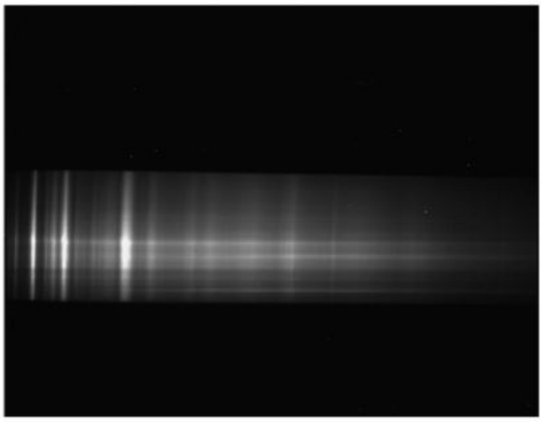

Figure 2.16: Typical preprocessed optical emission image (horizontal axis depicts the spectral coordinate, while vertical axis – radial coordinate) [61].

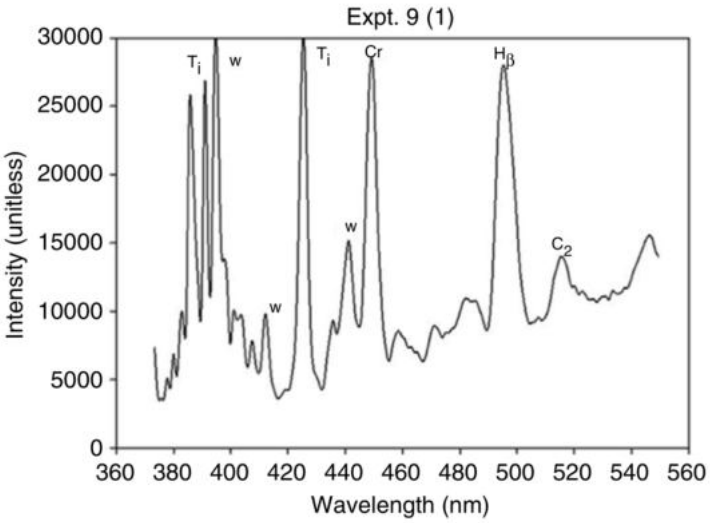

Figure 2.17: Enlarged spectrum in the range 360–560 nm marked with elements emitted in the μ-EDM process [61].

Calculations of the plasma temperature and electron number density were performed using the line pair method and the Stark broadening of the H_β spectral line, and were found to be 6170 K and 3.5×10^{18} cm^{-3} in average, respectively. It was determined that the

electrode size and spark gap play a major role in determining the plasma characteristics in micro-EDM. Smaller electrode size and larger spark gaps produce higher plasma temperature and electron number density.

In [57], Bhattacharya et al. have presented a detailed investigation of the EDM discharge plasma in water. Authors studied discharge evolution of the EDM arcs in water using fast photographic camera, and these results were previously discussed in the subsection 2.5.2 of this work. Apart from the visualization and qualitative analysis of the discharge dynamics, the OES diagnostics was applied in order to determine characteristics of plasma generated between tungsten cathode and P91, Zr, SS304 and Cu anodes. They used a specifically-developed modified Boltzmann plot technique, initially developed by Marotta et al. [62] for determining the axial plasma temperature of the spark EDM discharge.

Reported results confirm that for different anode materials, emission spectra from the discharge were different due to ionic and atomic contribution to the plasma specific to that anode material. Spectra, used in determination of plasma temperature are presented in Figure 2.18. It has been observed that none of the registered experimental spectra showed presence of H_β line while presence of H_α line was observed in every spectrum. Authors identify relatively low temperature (~ eV) and high density as the primary reason for strong Stark broadening of the H_α line and vanishing of the H_β line.

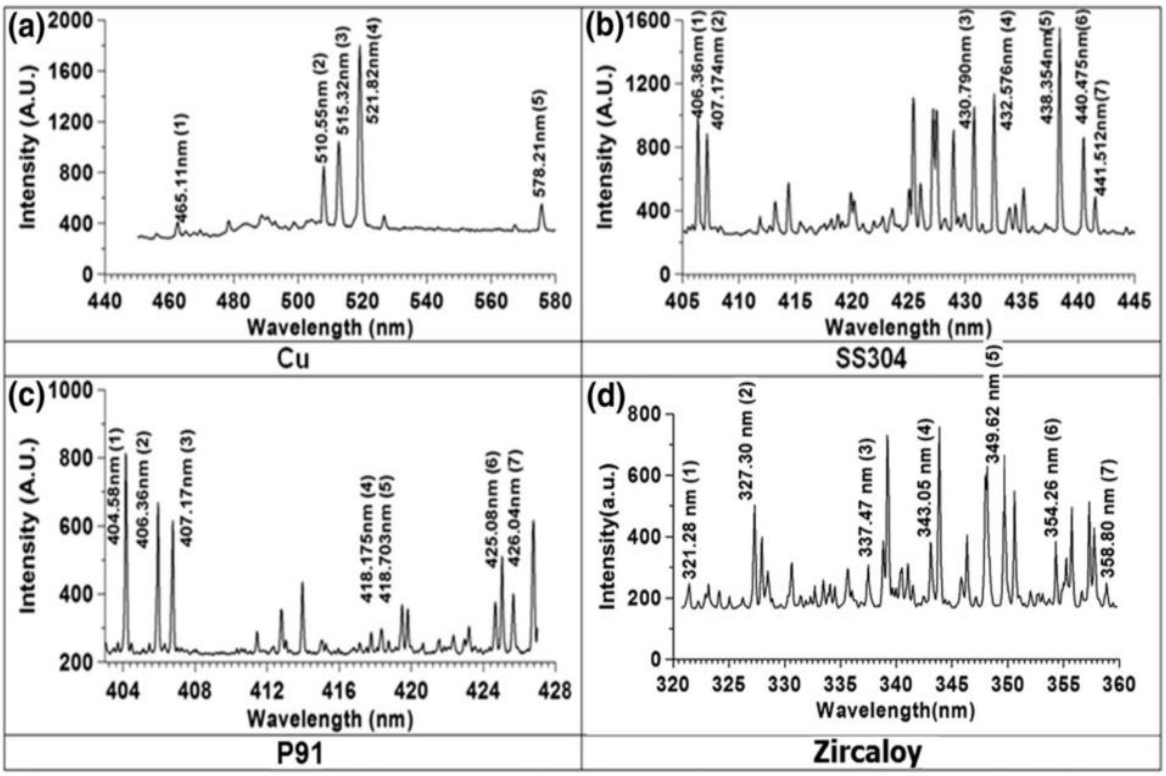

Figure 2.18: Spectra recorded during EDM discharge with different anode materials: (a) Copper; (b) SS304; (c) P91; (d) zircaloy [57].

Typical Boltzmann plots obtained for different anode materials are presented in Figure 2.19. While it is common in the literature to use Boltzmann plot technique for determination of plasma temperature (see eq. (2.2)), it cannot give correct axial temperature for inhomogeneous axisymmetric plasmas without performing the Abel inversion, in the case of spatially integrated line intensity measurements. In [57], authors have used a formula suitable for finding the central axis temperatures in inhomogeneous, axisymmetric, optically thin, LTE plasmas having strong gradient Gaussian temperature profile. Specialty of the method is that it avoids the necessity of Abel inversion. Due to its integral features, it is well suited for rapid monitoring of spatially unstable arc discharges and pulsating arcs.

The formula used in the present study differs from the usual expression (2.2)

$$\ln\left(\frac{I_{ui}\lambda_{ui}}{g_u A_{ui}}\right) = -\frac{E_u}{k_B T} + C, \tag{2.2}$$

where k_B is the Boltzmann constant, A_{ui} is the 'transition probability' for the specific transition. E_u and g_u are the excitation energy and statistical weight factors of the upper level.

The logarithmic part and may be expressed as [62]:

$$\ln\left(\frac{I_{ui}E_u\lambda_{ui}}{g_u A_{ui}}\right) = -\frac{E_u}{k_B T} + C. \tag{2.3}$$

Axial temperature is determined from the slope of the linear plot similar to (2.2).

Observed good linearity in the plots ensures PLTE among the levels considered. Average axial temperature is determined from independent measurements using the same set of emission lines.

Figure 2.20 presents the axial temperatures of the plasma estimated in discharges with different anodes. Application of Boltzmann plot method to the spectra received from discharge with SS304 anode gave an average axial temperature of 6151 K. Similarly, obtained average axial temperatures with P91 and Cu anodes were respectively 8159 K and 10534 K. However, for zircaloy observed emission was found to be radically different. Unlike the previous three cases where emission lines were primarily from atomic transitions, most of the intense emission lines from discharge with zircaloy anode were found to be from singly ionized Zr (Zr-II). Since first ionization potential (IP) of Cu, Fe and Zr are close to each other (IP_{Cu} = 7.7 eV, IP_{Fe} = 7.9 eV, IP_{Zr} = 6.6 eV), this itself is indicative of existence of higher temperature in the discharge with zircaloy as anode. Slightly lower IP of Zr might have contributed as well to this

effect. Estimated average axial temperature from Boltzmann plot using Zr-II lines is found to be 14525 K which is substantially higher compared to that for other anode materials. The observation is also supported by the pronounced shock boundaries and presence of ionic lines of Zr in recorded spectra.

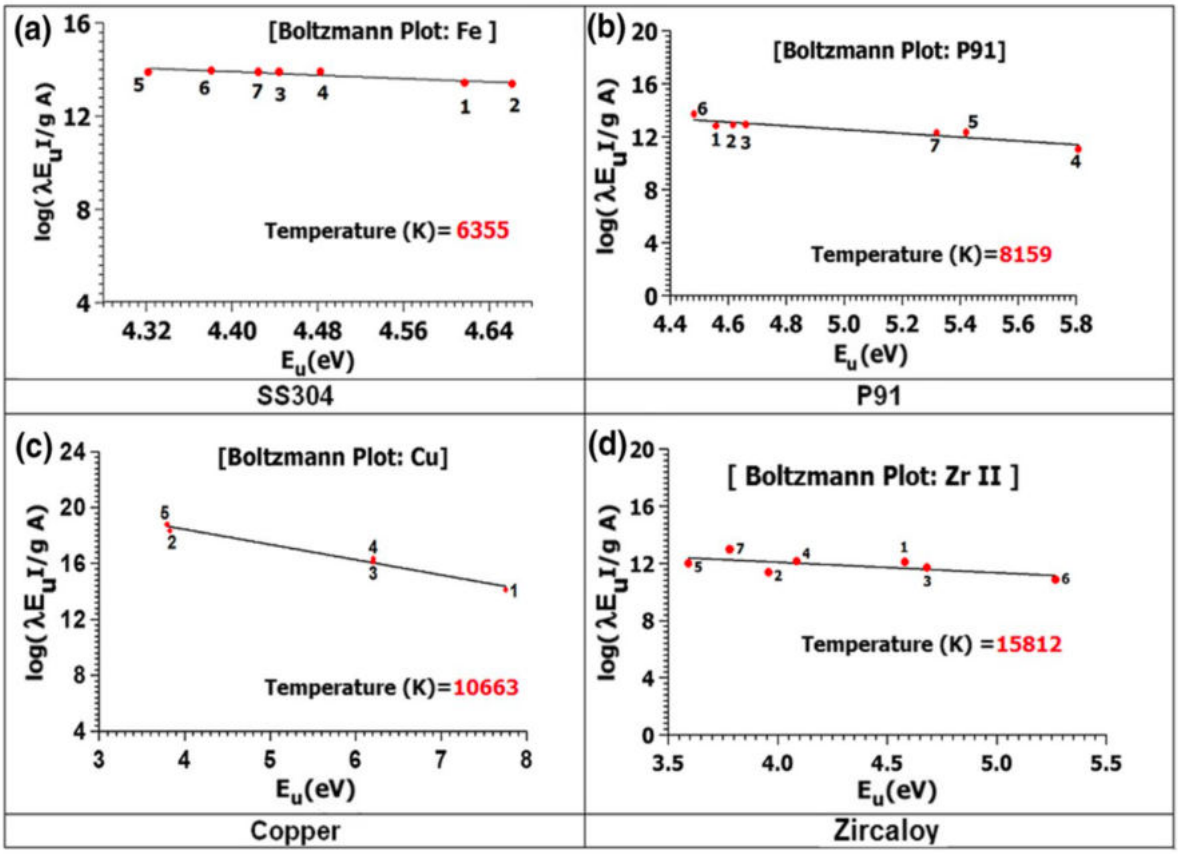

Figure 2.19: Typical Boltzmann plot obtained for discharges with anode material (a) SS304; (b) P91; (c) copper, and (d) zircaloy [57].

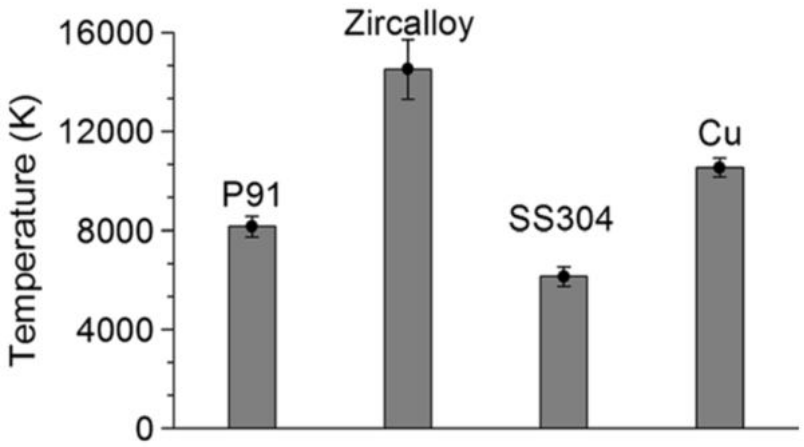

Figure 2.20: Temperatures as obtained from Boltzmann plot for discharges with different anode materials. Bars indicate the typical scatter in the data, estimated over the range of 5 measurements [57].

Electron number density inside the plasma has been determined from the width of Stark broadened Lorentzian profile of H_α line. Recorded H_α line profiles for different anode materials are presented in Figure 2.21. Values of the electron number densities per m^3 in the discharge zone are estimated to be 2.97×10^{23}, 3.76×10^{23}, 0.41×10^{23} and 6.21×10^{23} for P91, Zr, SS304 and Cu anodes, respectively.

Apart from Stark broadening and shift of the line location, authors obtained some other important information about the system from the H_α line. A scrutiny of the recorded H_α profile shape in Figure 2.21 reveals that it is not perfectly symmetric like a Lorentzian profile. Such observed slight asymmetry owes its origin to the interactions between other ions present in the weakly coupled non-ideal EDM plasma and the H_α emitting hydrogen atom.

Another important observation is that the recorded H_α profiles with most of the anode material reveal existence of tiny bumps and dips near their base. According to authors, this can be explained by the resonant interaction between Stark splitting and the ion acoustic turbulence induced oscillating electric field.

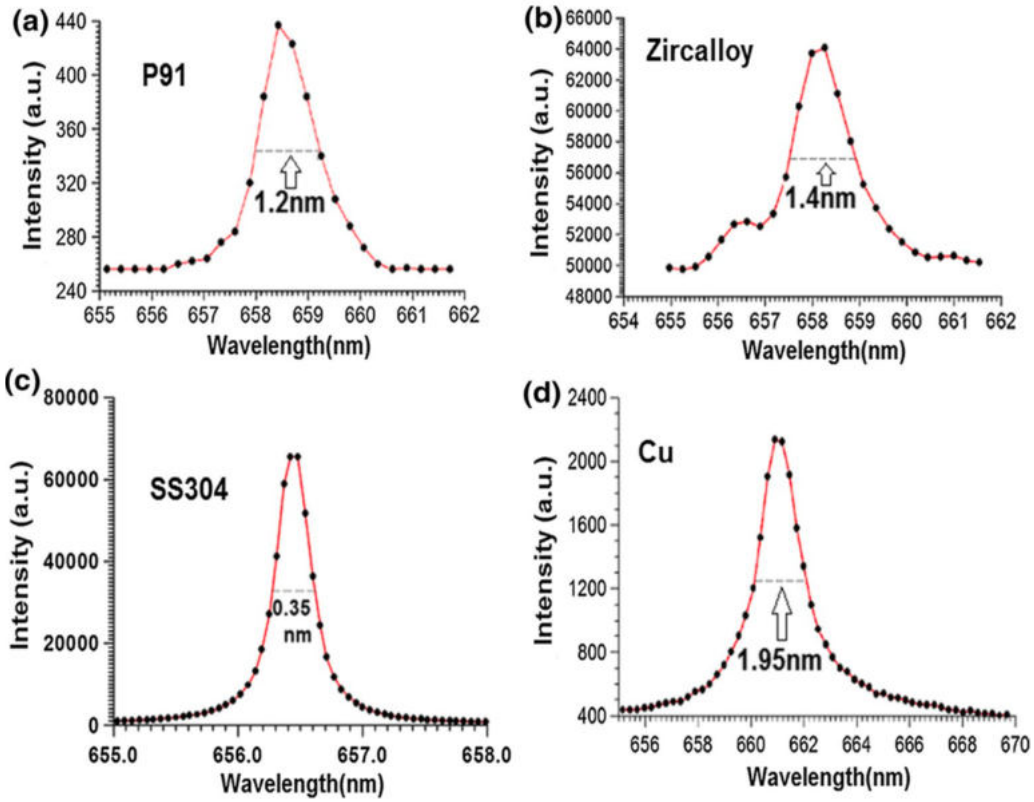

Figure 2.21: Recorded H_α line profiles: (a) P91; (b) zircaloy; (c) SS304, and (d) copper anodes [57].

2.6 Conclusions

This chapter presented a generalized introduction into the research domain of electric discharges in liquid and their most common practical applications. In order to appropriately position this thesis within the framework of the plasma physics discipline and among the available literature on the relevant subject, some of the most popular classification approaches were reviewed in section 2.2. The emphasis was made on application of plasmas in and in contact with liquids as a part of relatively new research branch of nanomaterial synthesis through plasma-liquid interactions. The latter represents the main area of interest of this work. Section 2.3 discussed the first-ever experiments involving electric discharge generation in liquid media, following by categorization of all available plasma-liquid configurations used for NM synthesis.

As the most relevant for the purposes of this research, direct in-liquid plasma discharges and the variety of reactor configurations for their implementation found in the literature were shown in section 2.4. It should be mentioned that none of the configurations presented in this section fully match those employed in this thesis. Still, some resemblances can be distinguished. For instance, some of the reactor configurations are similar in terms of the electrode arrangements, values of the discharge voltage and overall operating principle. However, these comparable aspects do not outweigh the substantial differences in, for instance, experimental parameters and choice of the liquid media. Moreover, none of the reviewed studies cover diagnostics of the electric discharge plasma. Instead, they mainly focus on synthesis process and characterization of obtained NMs.

Section 2.5 discusses the plasma diagnostics of electric discharges in water. The overall objective of plasma diagnostics is to deduce information about the state of the plasma from practical observations of physical processes and their effects. This usually requires a rather elaborate chain of deduction based on an understanding of the physical processes involved.

Optical methods are most often used in plasmas. Optical methods can be either non-intrusive (emission) or slightly intrusive (absorption). Emission techniques are based on the observation of the light naturally emitted by the plasma. They are usually easy to implement depending on the conditions, but the quality of the results obtained depend on the power of the light source investigated. If the source produces sufficient light, the structure of the resulting spectrum can be analyzed using the methods of emission spectroscopy, which relies on the understanding of the internal configuration of the molecules and atoms. Numerous information on the state of the plasma can be inferred from the emission spectroscopy, such as the population density of radiating particles, electron number density,

rotational, vibrational and electronic temperatures (provided some conditions are fulfilled). The main disadvantage of the emission spectroscopy is that it can be applied only if the source emits sufficient light. When the plasma is unexcited, for instance, in regions with low electric fields, it does not emit light and no information on the plasma can be gathered. Absorption-based techniques use a light source which illuminates a section of the plasma. The molecules of the plasma react by absorbing the light or by stimulated emission of a photon (fluorescence). These techniques are similar to emission spectroscopy, as they rely on the understanding of the electronic structure of particles, however, they are usually harder to implement. The main advantage when compared to pure emission spectroscopy is the ability to gather information on the plasma even when it does not radiate by itself and to provide information about the ground states of the molecules and atoms of the gas. The disadvantages apart from their intrusive nature is the implementation and especially the need of a well-defined stable source of light. For this purpose, most techniques use a laser as the light source.

Study of the state-of-the-art research has shown that experimental determination of plasma characteristics in the case of a in-liquid discharge is largely based on optical methods. This is mostly due to the highly transient nature of the plasma investigated, its usually small dimensions, and to the high voltages and currents involved. Moreover, it can be concluded that the class of pulsed low-voltage electric discharges in water is mostly represented by the electric spark discharge occurring in the EDM process. The common feature of the EDM discharge investigations is the use of OES for the characterization of the plasma. Therefore, section 2.5 presents mostly the overview of the EDM discharge plasma diagnostics.

The majority of the investigations of the EDM discharge use the ratio of two-line intensities method (RTLIM) for plasma temperature determination. It should be noted that it gives accurate temperature only in case if the energy levels associated with the chosen lines maintain LTE distribution. Unfortunately, most of the EDM plasmas do not maintain LTE. Rather, they maintain PLTE (Partial Local Thermodynamic Equilibrium), under which few of the energy levels are not populated as per Boltzmann distribution. If any of the chosen lines in the RTLIM arise out of transition involving levels not maintaining LTE, the temperature estimated is bound to be erroneous.

This important aspect has been taken into consideration by authors of [57] (and [62]). The specialty of the method they used is that it avoids the necessity of Abel inversion. Due to its integral features, it is well suited for rapid monitoring of spatially unstable arc discharges and pulsating arcs. However, it should be noted that limitation of this method is that it gives only the value of axial temperature and cannot yield the radial profile. This modified Boltzmann plot technique is unique in the sense that

the whole emission range with specific anode material is first checked to identify the region where large numbers of emission lines are available over a short wavelength range. This ensures nearly similar general absorption features for all the chosen lines. Next, the fact whether the chosen lines follow LTE distribution or not is verified. This is done by simply checking the linearity maintained by the lines in the Boltzmann plot. Any emission line, originating from levels not maintaining LTE does not follow linearity in the plot. Since instead of only two lines (as used in RTLIM), numbers of lines are considered in the determination of temperature and LTE is ensured, the calculated temperature is expected to be reliable and reasonably accurate.

It is important to highlight that the used in [57] method relies on optically thin assumption of the chosen lines. It may also be noted that authors neglect the absorption of electromagnetic radiation by water in the spectral region selected for temperature estimations. This is justified by the fact that absorption by water in the gas phase occurs mainly in three regions: microwave (rotational transitions), infrared (vibrational transitions) and vacuum ultraviolet (electronic transitions) regions. Additionally, careful analysis of line profiles using Fabry–Perot interferometer in short metal arcs [63] revealed absence of self-absorption of atomic lines in the considered wavelength range.

Optical emission spectroscopy is the main tool of investigation used in this thesis, and is further developed in Chapter 3.

References to chapter II

[1] P. Bruggeman and C. Leys, “Non-thermal plasmas in and in contact with liquids,” *J. Phys. Appl. Phys.*, vol. 42, no. 5, p. 053001, Mar. 2009, doi: 10.1088/0022-3727/42/5/053001.
[2] G. A. Mesjac, *Pulsed power*. New York: Kluwer Acad./Plenum Publ, 2005.
[3] S. Kumar, R. Singh, T. P. Singh, and B. L. Sethi, “Surface modification by electrical discharge machining: A review,” *J. Mater. Process. Technol.*, vol. 209, no. 8, pp. 3675–3687, Apr. 2009, doi: 10.1016/j.jmatprotec.2008.09.032.
[4] Q. He, Z. Zhu, and S. Hu, “Flowing and Nonflowing Liquid Electrode Discharge Microplasma for Metal Ion Detection by Optical Emission Spectrometry,” *Appl. Spectrosc. Rev.*, vol. 49, no. 3, pp. 249–269, Apr. 2014, doi: 10.1080/05704928.2013.820195.
[5] S. K. Pankaj and K. M. Keener, “Cold plasma: background, applications and current trends,” *Curr. Opin. Food Sci.*, vol. 16, pp. 49–52, Aug. 2017, doi: 10.1016/j.cofs.2017.07.008.
[6] B. R. Locke, M. Sato, P. Sunka, M. R. Hoffmann, and J.-S. Chang, “Electrohydraulic Discharge and Nonthermal Plasma for Water Treatment,” *Ind. Eng. Chem. Res.*, vol. 45, no. 3, pp. 882–905, Feb. 2006, doi: 10.1021/ie050981u.
[7] D. Oshita, S. H. R. Hosseini, Y. Miyamoto, K. Mawatari, and H. Akiyama, “Study of underwater shock waves and cavitation bubbles generated by pulsed electric discharges,” *IEEE Trans. Dielectr. Electr. Insul.*, vol. 20, no. 4, pp. 1273–1278, Aug. 2013, doi: 10.1109/TDEI.2013.6571444.
[8] Q. Shi *et al.*, “Atmospheric plasma treatment of pre-electrospinning polymer solution: A feasible method to improve electrospinnability,” *J. Polym. Sci. Part B Polym. Phys.*, vol. 49, no. 2, pp. 115–122, Jan. 2011, doi: 10.1002/polb.22157.
[9] B. R. Locke and K.-Y. Shih, “Review of the methods to form hydrogen peroxide in electrical discharge plasma with liquid water,” *Plasma Sources Sci. Technol.*, vol. 20, no. 3, p. 034006, Jun. 2011, doi: 10.1088/0963-0252/20/3/034006.
[10] Q. Chen, J. Li, and Y. Li, “A review of plasma–liquid interactions for nanomaterial synthesis,” *J. Phys. Appl. Phys.*, vol. 48, no. 42, p. 424005, Oct. 2015, doi: 10.1088/0022-3727/48/42/424005.
[11] G. Saito and T. Akiyama, “Nanomaterial Synthesis Using Plasma Generation in Liquid,” *J. Nanomater.*, vol. 2015, pp. 1–21, Sep. 2015, doi: 10.1155/2015/123696.
[12] S. Horikoshi and N. Serpone, “In-liquid plasma: a novel tool in the fabrication of nanomaterials and in the treatment of wastewaters,” *RSC*

Adv, vol. 7, no. 75, pp. 47196–47218, Sep. 2017, doi: 10.1039/C7RA09600C.
[13] N. Boussetta and E. Vorobiev, “Extraction of valuable biocompounds assisted by high voltage electrical discharges: A review,” *Comptes Rendus Chim.*, vol. 17, no. 3, pp. 197–203, Mar. 2014, doi: 10.1016/j.crci.2013.11.011.
[14] N. N. Misra, O. Schlüter, and P. J. Cullen, *Cold plasma in food and agriculture: Fundamentals and applications*. Academic Press, 2016.
[15] A. A. Fridman and G. Friedman, *Plasma medicine*. Chichester, West Sussex, U.K: John Wiley & Sons, 2013.
[16] P. Vanraes, A. Y. Nikiforov, and C. Leys, “Electrical Discharge in Water Treatment Technology for Micropollutant Decomposition,” in *Plasma Science and Technology - Progress in Physical States and Chemical Reactions*, T. Mieno, Ed. InTech, 2016.
[17] P. Bruggeman and B. Locke, “Assessment of Potential Applications of Plasma with Liquid Water,” in *Low Temperature Plasma Technology*, P. Chu and X. Lu, Eds. CRC Press, 2013, pp. 367–399.
[18] M. A. Malik, “Water Purification by Plasmas: Which Reactors are Most Energy Efficient?,” *Plasma Chem. Plasma Process.*, vol. 30, no. 1, pp. 21–31, Feb. 2010, doi: 10.1007/s11090-009-9202-2.
[19] B. Jiang *et al.*, “Review on electrical discharge plasma technology for wastewater remediation,” *Chem. Eng. J.*, vol. 236, pp. 348–368, Jan. 2014, doi: 10.1016/j.cej.2013.09.090.
[20] T. Svedberg, “Herstellung Kolloider Liisungen Anorganischer Stoffe,” *Dresden/Leipzig*, 1922.
[21] R. Feynman, “There’s plenty of room at the bottom, engineering and science,” *Eng. Sci.*, pp. 22–36, 1960.
[22] T. A. Kareem and A. A. Kaliani, “Glow discharge plasma electrolysis for nanoparticles synthesis,” *Ionics*, vol. 18, no. 3, pp. 315–327, Mar. 2012, doi: 10.1007/s11581-011-0639-y.
[23] W. G. Graham and K. R. Stalder, “Plasmas in liquids and some of their applications in nanoscience,” *J. Phys. Appl. Phys.*, vol. 44, no. 17, p. 174037, May 2011, doi: 10.1088/0022-3727/44/17/174037.
[24] O. Takai, “Solution plasma processing (SPP),” *Pure Appl. Chem.*, vol. 80, no. 9, pp. 2003–2011, Jan. 2008, doi: 10.1351/pac200880092003.
[25] S. M. Kim, G. S. Kim, and S. Y. Lee, “Effects of PVP and KCl concentrations on the synthesis of gold nanoparticles using a solution plasma processing,” *Mater. Lett.*, vol. 62, no. 28, pp. 4354–4356, Nov. 2008, doi: 10.1016/j.matlet.2008.07.025.
[26] M. A. Bratescu, S.-P. Cho, O. Takai, and N. Saito, “Size-Controlled Gold Nanoparticles Synthesized in Solution Plasma,” *J. Phys. Chem. C*, vol. 115, no. 50, pp. 24569–24576, Dec. 2011, doi: 10.1021/jp207447c.
[27] X. Hu, X. Shen, O. Takai, and N. Saito, “Facile fabrication of PtAu alloy clusters using solution plasma sputtering and their electrocatalytic

activity," *J. Alloys Compd.*, vol. 552, pp. 351–355, Mar. 2013, doi: 10.1016/j.jallcom.2012.08.033.
[28] X. Hu, X. Zhang, X. Shen, H. Li, O. Takai, and N. Saito, "Plasma-Induced Synthesis of CuO Nanofibers and ZnO Nanoflowers in Water," *Plasma Chem. Plasma Process.*, vol. 34, no. 5, pp. 1129–1139, Sep. 2014, doi: 10.1007/s11090-014-9546-0.
[29] V. S. Burakov, A. A. Nevar, M. I. Nedel'ko, and N. V. Tarasenko, "Formation of Zinc Oxide Nanoparticles during Electric Discharge in Water," *Tech. Phys. Lett.*, vol. 34, no. 8, pp. 679–681, 2008.
[30] N. Tarasenko, A. Nevar, and M. Nedelko, "Properties of zinc-oxide nanoparticles synthesized by electrical-discharge technique in liquids," *Phys. Status Solidi A*, vol. 207, no. 10, pp. 2319–2322, Oct. 2010, doi: 10.1002/pssa.200925635.
[31] V. S. Burakov, N. A. Savastenko, N. V. Tarasenko, and E. A. Nevar, "Synthesis of nanoparticles using a pulsed electrical discharge in a liquid," *J. Appl. Spectrosc.*, vol. 75, no. 1, pp. 114–124, Jan. 2008, doi: 10.1007/s10812-008-9003-z.
[32] Z. Abdullaeva *et al.*, "Onion-like carbon-encapsulated Co, Ni, and Fe magnetic nanoparticles with low cytotoxicity synthesized by a pulsed plasma in a liquid," *Carbon*, vol. 50, no. 5, pp. 1776–1785, Apr. 2012, doi: 10.1016/j.carbon.2011.12.025.
[33] D. G. Tong, Y. Y. Luo, W. Chu, Y. C. Guo, and W. Tian, "Cutting Of Carbon Nanotubes Via Solution Plasma Processing," *Plasma Chem. Plasma Process.*, vol. 30, no. 6, pp. 897–905, Dec. 2010, doi: 10.1007/s11090-010-9262-3.
[34] C.-H. Lo, T.-T. Tsung, and L.-C. Chen, "Shape-controlled synthesis of Cu-based nanofluid using submerged arc nanoparticle synthesis system (SANSS)," *J. Cryst. Growth*, vol. 277, no. 1–4, pp. 636–642, Apr. 2005, doi: 10.1016/j.jcrysgro.2005.01.067.
[35] J.-K. Lung *et al.*, "Preparation of gold nanoparticles by arc discharge in water," *J. Alloys Compd.*, vol. 434, pp. 655–658, 2007.
[36] C.-H. Lo, T.-T. Tsung, and H.-M. Lin, "Preparation of silver nanofluid by the submerged arc nanoparticle synthesis system (SANSS)," *J. Alloys Compd.*, vol. 434–435, pp. 659–662, May 2007, doi: 10.1016/j.jallcom.2006.08.217.
[37] A. A. Ashkarran, A. Iraji zad, S. M. Mahdavi, M. M. Ahadian, and M. R. Hormozi Nezhad, "Rapid and efficient synthesis of colloidal gold nanoparticles by arc discharge method," *Appl. Phys. A*, vol. 96, no. 2, pp. 423–428, Aug. 2009, doi: 10.1007/s00339-009-5288-x.
[38] A. A. Ashkarran, A. Iraji zad, M. M. Ahadian, and M. R. Hormozi Nezhad, "Stability, size and optical properties of colloidal silver nanoparticles prepared by electrical arc discharge in water," *Eur. Phys. J. Appl. Phys.*, vol. 48, no. 1, p. 10601, Oct. 2009, doi: 10.1051/epjap/2009113.

[39] A. A. Ashkarran, “A novel method for synthesis of colloidal silver nanoparticles by arc discharge in liquid,” *Curr. Appl. Phys.*, vol. 10, no. 6, pp. 1442–1447, Nov. 2010, doi: 10.1016/j.cap.2010.05.010.
[40] A. A. Ashkarran, A. Iraji zad, S. M. Mahdavi, and M. M. Ahadian, “ZnO nanoparticles prepared by electrical arc discharge method in water,” *Mater. Chem. Phys.*, vol. 118, no. 1, pp. 6–8, Nov. 2009, doi: 10.1016/j.matchemphys.2009.07.002.
[41] A. A. Ashkarran, A. Iraji zad, M. M. Ahadian, and S. A. Mahdavi Ardakani, “Synthesis and photocatalytic activity of WO_3 nanoparticles prepared by the arc discharge method in deionized water,” *Nanotechnology*, vol. 19, no. 19, p. 195709, May 2008, doi: 10.1088/0957-4484/19/19/195709.
[42] A. A. Ashkarran, S. A. A. Afshar, S. M. Aghigh, and M. kavianipour, “Photocatalytic activity of ZrO2 nanoparticles prepared by electrical arc discharge method in water,” *Polyhedron*, vol. 29, no. 4, pp. 1370–1374, Mar. 2010, doi: 10.1016/j.poly.2010.01.003.
[43] A. A. Ashkarran, M. Kavianipour, S. M. Aghigh, S. A. Ahmadi Afshar, S. Saviz, and A. Iraji Zad, “On the Formation of TiO2 Nanoparticles Via Submerged Arc Discharge Technique: Synthesis, Characterization and Photocatalytic Properties,” *J. Clust. Sci.*, vol. 21, no. 4, pp. 753–766, Dec. 2010, doi: 10.1007/s10876-010-0333-7.
[44] N. Sano *et al.*, “Properties of carbon onions produced by an arc discharge in water,” *J. Appl. Phys.*, vol. 92, no. 5, pp. 2783–2788, Sep. 2002, doi: 10.1063/1.1498884.
[45] I. Alexandrou, H. Wang, N. Sano, and G. A. J. Amaratunga, “Structure of carbon onions and nanotubes formed by arc in liquids,” *J. Chem. Phys.*, vol. 120, no. 2, pp. 1055–1058, Jan. 2004, doi: 10.1063/1.1629274.
[46] T. Sato, K. Usuki, A. Okuwaki, and Y. Goto, “Synthesis of metal nitrides and carbide powders by a spark discharge method in liquid media,” *J. Mater. Sci.*, vol. 27, no. 14, pp. 3879–3882, Jul. 1992, doi: 10.1007/BF00545471.
[47] T. Sato, S. Yasuda, T. Yoshioka, and A. Okuwaki, “Synthesis of y-iron by a spark discharge method in liquid ammonia,” *J. Mater. Sci. Lett.*, vol. 14, pp. 1430–1435, May 1995.
[48] R. Sergiienko, S. Kim, E. Shibata, and T. Nakamura, “Structure of Fe–Pt alloy included carbon nanocapsules synthesized by an electric plasma discharge in an ultrasonic cavitation field of liquid ethanol,” *J. Nanoparticle Res.*, vol. 12, no. 2, pp. 481–491, Feb. 2010, doi: 10.1007/s11051-009-9677-z.
[49] C. Cho, Y. W. Choi, C. Kang, and G. W. Lee, “Effects of the medium on synthesis of nanopowders by wire explosion process,” *Appl. Phys. Lett.*, vol. 91, no. 14, p. 141501, Oct. 2007, doi: 10.1063/1.2794724.

[50] Z. Kozáková, M. Nejezchleb, F. Krčma, I. Halamová, J. Čáslavský, and J. Dolinová, “Removal of organic dye Direct Red 79 from water solutions by DC diaphragm discharge: Analysis of decomposition products,” *Desalination*, vol. 258, no. 1–3, pp. 93–99, Aug. 2010, doi: 10.1016/j.desal.2010.03.038.
[51] F. D. Baerdemaeker, M. Šimek, J. Schmidt, and C. Leys, “Characteristics of ac capillary discharge produced in electrically conductive water solution,” *Plasma Sources Sci. Technol.*, vol. 16, no. 2, pp. 341–354, May 2007, doi: 10.1088/0963-0252/16/2/018.
[52] V. S. Burakov, E. A. Nevar, M. I. Nedel’ko, N. A. Savastenko, and N. V. Tarasenko, “Spectroscopic diagnostics for an electrical discharge plasma in a liquid,” *J. Appl. Spectrosc.*, vol. 76, no. 6, pp. 856–863, Nov. 2009, doi: 10.1007/s10812-010-9274-z.
[53] V. S. Burakov, V. V. Kiris, A. A. Nevar, M. I. Nedelko, and N. V. Tarasenko, “Combined Gas–Liquid Plasma Source for Nanoparticle Synthesis,” *J. Appl. Spectrosc.*, vol. 83, no. 4, pp. 643–649, Sep. 2016, doi: 10.1007/s10812-016-0341-y.
[54] A. Descoeudres, “Characterization of electrical discharge machining plasmas,” EPFL, Lausanne (Switzerland), 2006.
[55] M. Wiessner, F. T. B. Macedo, C. P. Martendal, F. Kuster, and K. Wegener, “Fundamental Investigation of EDM Plasmas, Part I: A Comparison between Electric Discharges in Gaseous and Liquid Dielectric Media,” *Procedia CIRP*, vol. 68, pp. 330–335, Apr. 2018, doi: 10.1016/j.procir.2017.12.073.
[56] A. Descoeudres, C. Hollenstein, G. Wälder, and R. Perez, “Time-resolved imaging and spatially-resolved spectroscopy of electrical discharge machining plasma,” *J. Phys. Appl. Phys.*, vol. 38, no. 22, pp. 4066–4073, Nov. 2005, doi: 10.1088/0022-3727/38/22/009.
[57] S. Bhattacharya, N. Tiwari, A. Mishra, S. Mitra, G. K. Dey, and S. Ghorui, “Underwater Electrical Discharges: Temperature, Density and Basic Instability Features with Different Anode Materials,” *Plasma Chem. Plasma Process.*, pp. 1019–1048, Feb. 2019, doi: 10.1007/s11090-019-09968-7.
[58] E. Pfender, “Energy transport in thermal plasmas,” *Pure Appl. Chem.*, vol. 52, no. 7, pp. 1773–1800, 1980.
[59] M. A. Gigosos and V. Cardeñoso, “New plasma diagnosis tables of hydrogen Stark broadening including ion dynamics,” *J. Phys. B At. Mol. Opt. Phys.*, vol. 29, no. 20, pp. 4795–4838, Oct. 1996, doi: 10.1088/0953-4075/29/20/029.
[60] A. Descoeudres, C. Hollenstein, G. Wälder, R. Demellayer, and R. Perez, “Time- and spatially-resolved characterization of electrical discharge machining plasma,” *Plasma Sources Sci. Technol.*, vol. 17, no. 2, p. 024008, May 2008, doi: 10.1088/0963-0252/17/2/024008.

[61] Nagahanumaiah, J. Ramkumar, N. Glumac, S. G. Kapoor, and R. E. DeVor, “Characterization of plasma in micro-EDM discharge using optical spectroscopy,” *J. Manuf. Process.*, vol. 11, no. 2, pp. 82–87, Jul. 2009, doi: 10.1016/j.jmapro.2009.10.002.
[62] A. Marotta, "Determination of axial thermal plasma temperatures without Abel inversion," J Phys. D: Appl. Phys., vol. 27, no. 2, pp. 268-272, Feb. 1994.
[63] M. Aula, “Optical emission from electric arc furnaces,” University of Oulu, Oulu (Finland), 2016.

CHAPTER III
EXPERIMENTAL SETUPS AND METHODOLOGY

3. Experimental setups and methodology

3.1 Introduction

The purpose of this chapter is to describe the experimental approach chosen for diagnostics of the underwater electric discharge plasma in the present work.

As it was mentioned in the previous chapters, foundation for this thesis has been laid in the National University of Life and Environmental Sciences of Ukraine, where Lopatko K. G. has been leading extensive investigations of the electric spark dispersion of conducting materials in liquid media [1]–[4]. With the main purpose of studying the biological functionality of nanomaterials obtained via impulse electric erosion processing, a setup for synthesis of colloidal solutions of ultra-disperse metal powders [5] has been designed. Its operation is based on the volumetric electric spark erosion of conducting materials, and follows the same principles as preceding impulse systems developed and studied in the Institute of Electrodynamics of National Academy of Sciences of Ukraine by Shcherba A. A. and his colleagues [6]–[10]. Specifics of the process lies in the possibility of a direct synthesis of colloidal solutions with potential of controlling the degree of nanomaterials' dispersion. In such electric erosion systems, granules of the precursor material are located in several planes forming a volume, wherein tens - hundreds of spark channels occur simultaneously. The high number of current passages existing in parallel leads to their high drift velocities and overall process stability.

Investigations of biological functionality of colloidal solutions carried out by Lopatko K. G. show that results of interaction of biological objects with NPs depend directly on concentration, size and shape of the latter, their chemical, structure and phase composition, overall interaction time, and synthesis parameters. Since final properties of NMs are formed during their synthesis, it is important to consider the nature of the synthesis process, as well as its most determinative aspects, such as temperature, heating and cooling rates, frequency and duration of any physical impacts.

In order to build a complete comprehension of correlations between the electrophysical synthesis parameters and characteristics of the resulting NMs, it is crucial to understand the thermal destruction process occurring at the surface of granules. Setup in [5] employs energies of the spark discharge channels to erode the material, which attributes such method to a plasma-assisted synthesis. Therefore, investigations of the underwater electric spark discharge plasma were undertaken by Veklich A. N. and his research team in Taras Shevchenko National

University of Kyiv, specializing in thermal multi-component plasma with metal admixtures. This was the starting point that subsequently constituted the subject of this thesis.

The setup for the synthesis of metal colloids (otherwise, setup for multiple-pulse underwater electric discharge generation) is presented in detail in section 3.2. It allows to study the underwater electric discharge plasma under 'real' operational conditions, meaning that the experimental parameters correspond to that employed during the actual process of synthesis. It is not easy to study plasma in such configuration. Among the main reasons, one can distinguish variable discharge position and duration, resulting from the stochastic nature of the current passing through the layers of metal granules, and from the fact that the input energy supplied to the discharge chamber eventually splits into multiple sub-pulses (micro-discharges). In terms of the plasma diagnostics, the impossibility of "isolation" of a discharge generated between two metal granules independently of the overall synthesis process also presents a challenge. Since the emission entering the spectrometer in such case corresponds to the spectrum of integrated plasma radiation from dozens of micro-discharges occurring within the 100 μs acquisition time, there is no possibility to obtain information about a separate discharge. Therefore, this setup is used for the qualitative investigation of the multiple-pulse underwater electric discharge in relation to other aspects of the synthesis process, such as final properties of the synthesized NMs and their biological functionality.

In order to enable quantitative plasma characterization, a complementary experimental apparatus was designed in the LAPLACE laboratory within the framework of the joint international PhD programme between Taras Shevchenko National University of Kyiv and University Toulouse III – Paul Sabatier. Aiming to "model" or, in somehow, "simulate" the behavior of two separately taken granules and discharge between them, this setup allows to control certain parameters in order to enable more advanced plasma diagnostics. The chosen experimental configuration is intended as a compromise between "realistic" operation of the setup for synthesis of colloidal solutions (i.e. staying as close as possible to the operating process parameters) and overcoming the constraints associated to plasma investigation (fixed location and controlled duration of discharge, controlled position of electrodes). This "academic" setup for single-pulse underwater electric discharge generation is presented in section 3.3.

Section 3.4 gives the overview of the OES techniques used for characterization of underwater electric discharge plasma. Section 3.5 summarizes the chapter.

3.2 Experimental setup for multiple-pulse underwater electric discharge investigation

3.2.1 Electric spark dispersion of metals

For more than 30 years, impulse generators with capacitive energy storage have been proving to be highly effective. In particular, for their application in spark-erosion systems for powders' manufacturing by means of volumetric electric spark dispersion. The sizes of particles resulting from such process vary from 30 nm to 100 μm.

According to the empirical data [6], impulse discharge generator must meet a number of requirements. Apart from the necessary impulse energy and current rise rate, it is also essential to ensure the dynamic balance of input and dissipated energies at occurring spark channels when value of the equivalent electric resistance changes during one pulse. Arguably, this is the most important requirement since those are the electric parameters of granulated conducting media that predominantly define the operating conditions of a generator. Control over the discharge impulse parameters can be achieved by regulating the capacitor's load voltage or by changing the structure of a discharge circuit. Duration of the discharge impulses can vary from several microseconds up to milliseconds, depending on technical characteristics of the utilized element base.

The distinguishing feature of the volumetric electric spark dispersion is presence of the conducting layer of granules between two main electrodes. The principal element of the electric circuit is a discharge chamber where the dispersion process occurs. Usually, the chamber is filled with a weekly-conductive liquid, such as water, ethanol, glycerin, etc. Voltage supply to the main electrodes causes the current flow through the layer of freely-deposited granules in a stochastic commutation mode. Low voltage and small inter-electrode gaps allow to ensure that 85% of all accumulated energy from the capacitor goes to the local heating of electrode surface [6], [11].

3.2.2 Experimental setup description

Processing unit for implementation of the electrical spark dispersion regime for synthesis of metal colloidal solutions is shown in Figure 3.1. The arrangement consists of impulse generator, discharge chamber and auxiliary devices for registration of electric parameters, such as Rogowsky coil, voltage divider and oscilloscope.

Simplified schematics of the impulse generator's power circuit can be also seen in Figure 3.1. Generator feeds from the single-phase 220 V

alternating current network of 50 Hz frequency. The supply voltage is being rectified, filtered and regulated by the controlled phase rectifier consisting of power diodes (VD_1 and VD_2), power thyristors (VD_3 and VD_4) and working capacitor C_1. The control board regulates periodical charging and discharging of the working capacitor that has a discretely variable capacity from 25 to 650 μF.

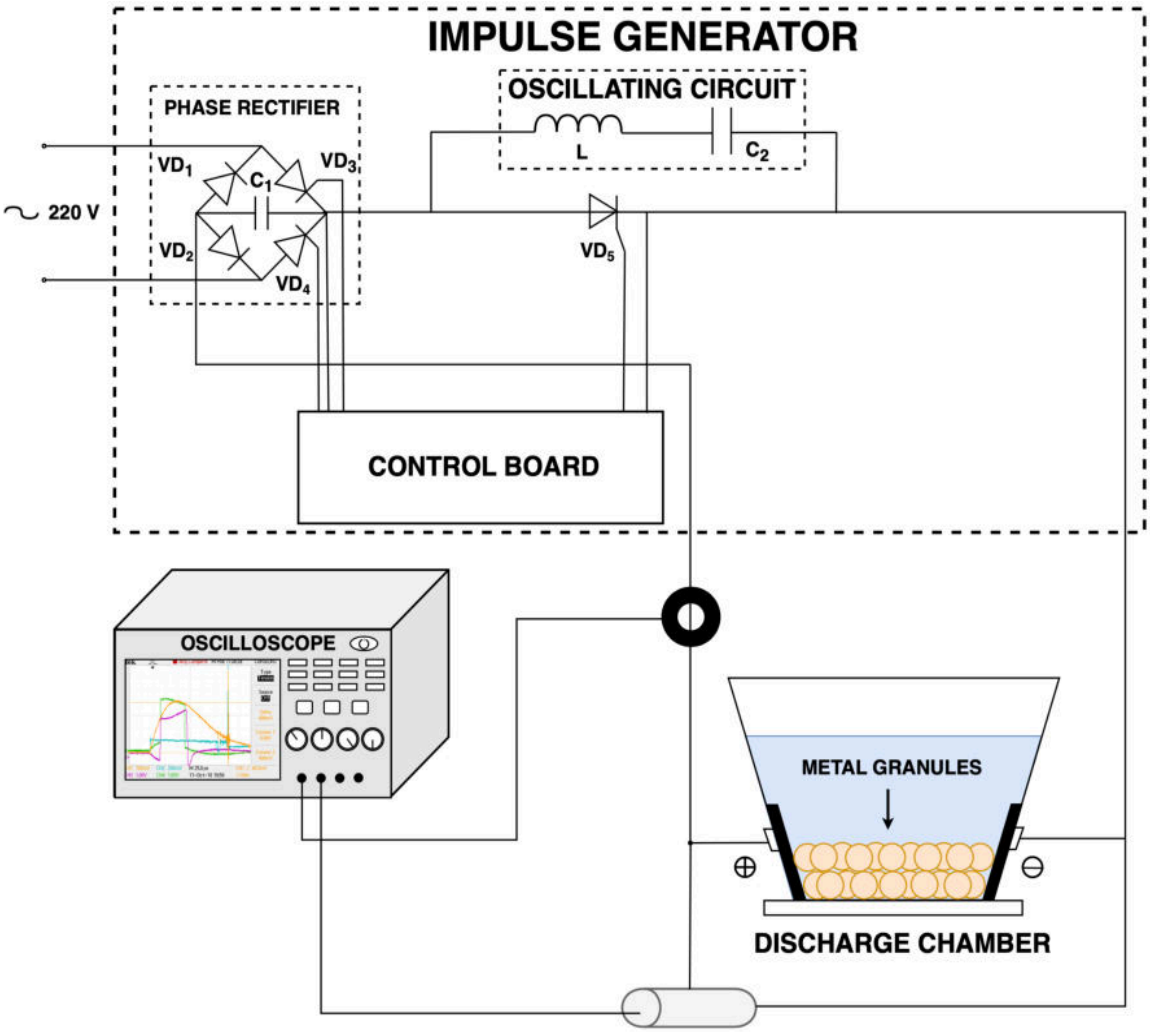

Figure 3.1: Experimental arrangement for multiple-pulse underwater electrical discharge investigation.

Commutation of the discharge chamber with metal granules is achieved via thyristor VD_5. The switching moment of that thyristor is regulated by the control board. Switching of thyristor occurs rapidly and thus leads to the steep edge of the impulse. This, in turn, contributes to a higher dispersion degree of the spark erosion particles. Since the given setup arrangement employs common non-controlled thyristors, there is an LC_2 oscillating circuit connected in parallel to VD_5. It is the semiperiod of free oscillations of this LC_2 circuit that defines the impulse duration. The inductance L and capacity C_2 are controlled parameters that allow to

change the impulse duration over a wide range of values. Such parameter regulation has a great significance, given that the trailing edge of the impulse will be elongated without it. This does not contribute to the dispersion degree of particles.

Control board allows to regulate the voltage, frequency and the duty cycle of impulses through power thyristors. Phase-shifting algorithm in the control circuit is used in order to control the voltage level supplied to the electrodes of the discharge chamber: depending on the set value of a phase shift (rectifier phase, %), the impulse is supplied to the transformer of a control board after a sinusoid zero-crossing point. Then, the impulse goes to thyristors in the rectifying scheme. Consequently, the higher the value of a rectifier phase, the lower is the load voltage of working capacitor in a phase rectifier. The diagram of a phase-shift control over thyristors in rectifier is presented in Figure 3.2.

After the capacitor, the current is supplied to the discharge chamber through the third thyristor. The control circuit of the latter generates impulses of set frequency and duty cycle value (see Figure 3.3). Control over thyristors in rectifier and VD_5 thyristor is realized through pulse-width modulation (PWM) microcontroller.

Investigations and experimental results previously obtained by research group of the National University of Life and Environmental Sciences of Ukraine of the electric spark dispersion of metals allow to make certain conclusions on regularities occurring in the process [1]–[3].

Influence of process parameters on dispersion and morphology of the erosion products of metal granules formed as a result of the local electric spark channels was studied at various electric parameters, such as load voltage U_0, capacitance C, and resistance of the discharge chamber R_{DC} (see Table 3.1). These investigations allowed to distinguish load voltage and capacitance as main factors of influence.

Table 3.1. Parameters of the discharge circuit

Inductance L, μH	Load voltage U_0, V	Capacitance C, μF	Electrical conductivity of purified water σ, mS/cm	Resistance of discharge chamber R_{DC}, Ohm	Impulse frequency f, kHz
~ 1	40 – 270	25 – 1000	0.001 – 0.02	0.15 – 1.5	0.2 – 2.0

The equivalent scheme of resistance of the conducting layer of granules is shown in Figure 3.4.

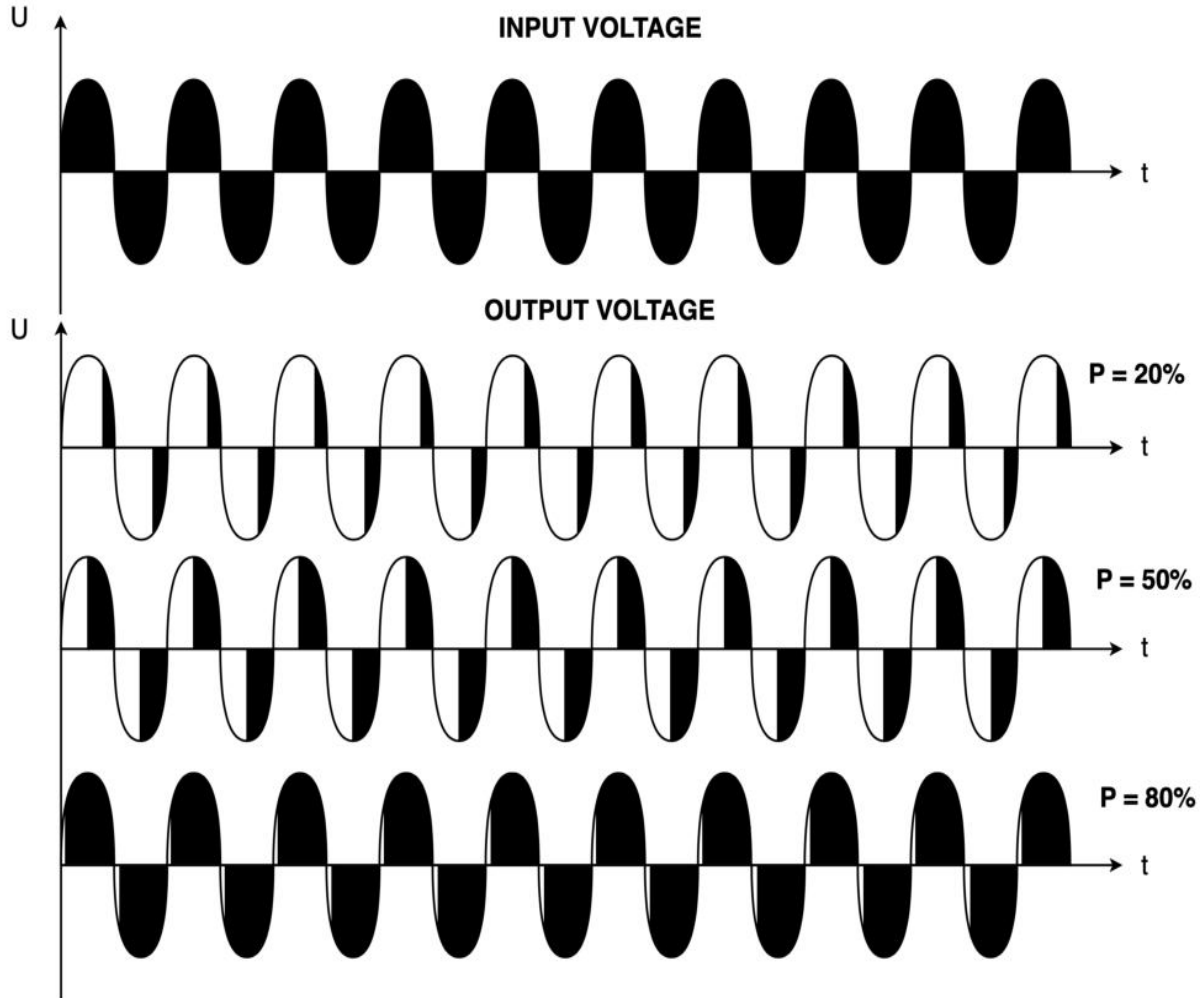

Figure 3.2: Phase-shifting diagram of the control board (P – duty cycle).

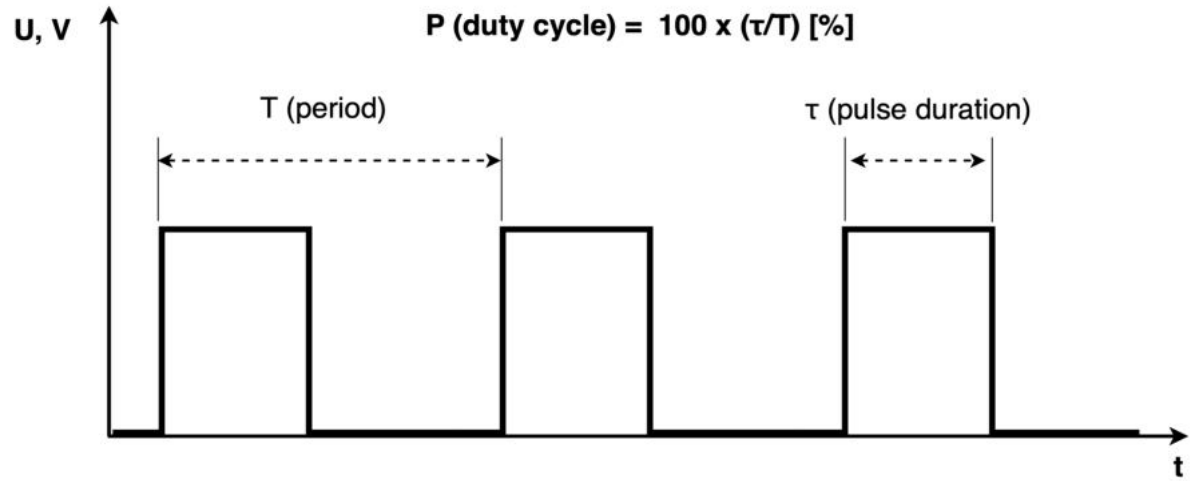

Figure 3.3: The schematic diagram explaining the duty cycle parameter.

Instantaneous value of equivalent resistance of the discharge chamber rapidly increases at the end of the impulse and is around several

Ohms, while in the middle of the impulse (in its active phase) this value does not exceed a fraction of an Ohm.

The equivalent resistance of the discharge chamber tends to change stochastically within the dynamic range of values. In case of an aperiodic discharge, the discharge duration usually resides within the range of 50 – 150 μs. Increase of the impulse duration leads to decrease of highly-dispersed particles in a bulk erosion product mass.

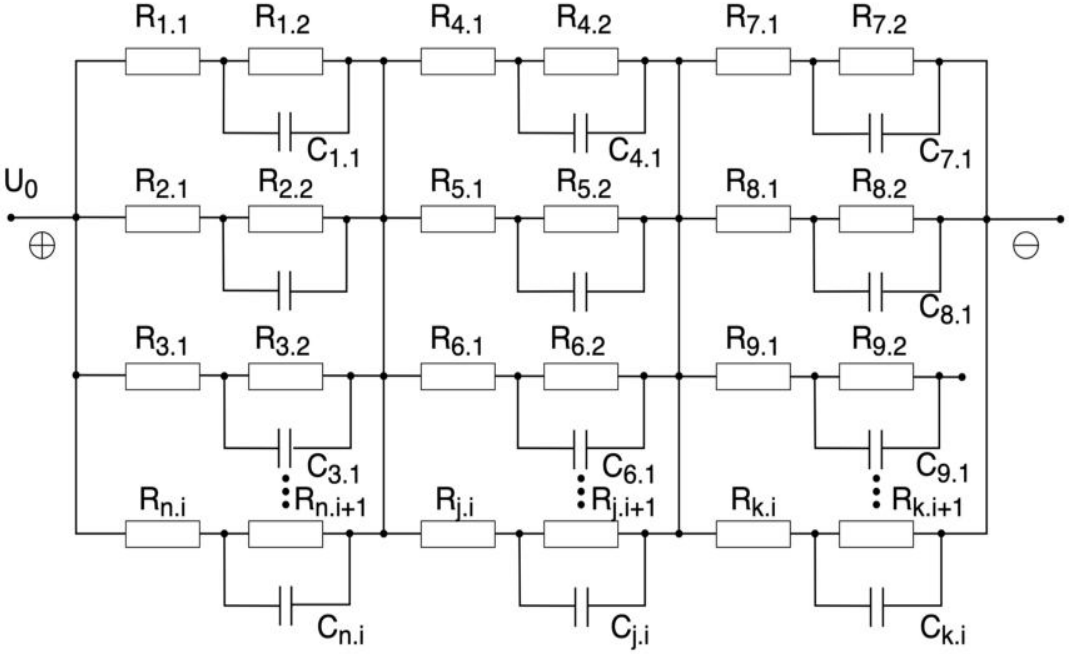

Figure 3.4: The equivalent scheme of resistance of the conducting layer of granules: $R_{1.1}$, $R_{2.1}$, $R_{3.1}$... – resistance of the granules; $R_{1.2}$, $R_{2.2}$, $R_{3.3}$ ... – resistance of the spark channels; $C_{1.1}$,... $C_{4.1}$,... $C_{7.1}$,.... – capacitance of the spark channels.

Electrical parameters of the conducting layer of granules to the fullest can be described by the equivalent active layer resistance during one impulse:

$$R_E = (\sum_{j=1}^{m} i_j \cdot u_j) / \sum_{j=1}^{m} i_j^2, \quad (3.1)$$

where i_j – the value of current at a moment of time t_j, A; u_j – value of the voltage at a moment of time t_j, V.

The mean impulse power can be calculated from the averaged oscillograms of the discharge current and voltage using the formula:

$$P_P = \frac{1}{n} \sum_{j=1}^{n} u_j \cdot i_j. \quad (3.2)$$

Taking into account the specifics of the conducting layer of granules, positioning of the metal granules plays an important role since it influences the integral resistance of the reaction chamber R_{DC}. Ensuring the minimal

resistance of the chamber and condition that $R_{DC\,MIN} > 2\sqrt{L/C}$ allows to avoid the critical regime of energy input. At the same time, the value of $R_{DC\,MIN}$ must ensure that the open-circuit operation will be avoided. Obviously, increase of the U_0 leads to increase of energy accumulated in the working capacitor:

$$W_C = 0.5\,U_0^2 C, \tag{3.3}$$

where U_0 is the load voltage of a working capacitor, V; C – its capacitance, F.

Transformation of the accumulated electric energy into the thermal energy is a characteristic phenomenon for electric spark processes with small inter-electrode gaps (l), when l ≤ 1 mm. The plasma channel input energy W_K equals to:

$$W_K = \int i(t) \cdot u(t) dt, \tag{3.4}$$

where i(t) – current flow, A; u(t) – voltage flow, V.

W_K is the bigger part of energy accumulated in the capacitor that increases proportionally to W_C, and part of which transforms into the thermal energy (W_E). Therefore, increase of the load voltage U_0 leads to increase of the thermal effect on surfaces of conducting granules. This, in turn, causes facilitated erosion of the latter due to the melting process.

It should be noted that the current and voltage waveforms of an actual pulse occurring between two granules (otherwise, a single micro discharge) are unknown: one can only have access to the electric parameters of the pulse generated by the power supply.

3.2.3 Plasma emission registration

The arrangement for the registration of the electric spark discharge plasma emission is shown in Figure 3.5. The setup consists of a discharge chamber, the bottom of which has been adjusted for the spectroscopic diagnostics through the quartz window. The spectrometer used in all the experiments is the high-aperture compact SDH IV spectrometer by Solar LS. The spectrometer is equipped with a four-position manually switch grating turret, consisting of diffraction gratings of 300, 400, 600 and 900 lines/mm. The technical specifications of the spectrometer are presented in Table 3.2. Plasma emission is registered using all four diffracting gratings. The exposure time for every measurement is 100 μs. The spectrometer was placed below the discharge chamber, with the entrance slit pointed directly at the quartz window in order to increase the possibility of capturing the light from the plasma channels.

The discharge chamber used in the experiments is shown in Figure 3.6. It is designed specifically for these experiments and is made of polycarbonate. The outer surface of the chamber's walls is coated with a layer of silver paint and another layer of black paint on top of it, in order to reduce the dissipation of plasma emission through it. The length of the side of the chamber's foundation is 5 cm, while the length of the top is 15 cm. Main electrodes embedded into the discharge chamber are flat carbon electrodes of 5 mm thickness. Carbon is used in order to avoid the necessity of replacing the main electrodes after every set of measurements.

Table 3.2. Parameters of the discharge circuit

Spectral range, nm	200 – 1100			
Linear image sensor	TCD1304 Toshiba			
Detectable spectral range, nm	200 - 390	300 - 600	450 - 900	600 - 1100
Diffraction gratings, lines/mm	900	600	400	300
Reciprocal linear dispersion (average), nm/mm	7.0	10.5	15.8	21.1
Spectral resolution (FWHM, average), nm	0.18	0.28	0.42	0.54

In order to study the electric spark dispersion of a conducting materials, the layer of metal granules is placed at the bottom of the chamber in quantity of around 100 g. The chamber then is filled with a non-purified water. The average diameter of granule is 1.5 mm. The measurements are carried out involving the granules of copper, aluminum, molybdenum, chromium, manganese, magnesium, argentum, cobalt, iron, zinc and silicon (with addition of 2% of iron).

The plasma emission registration is performed in regime of a constant water flow through the discharge chamber in order to avoid the excessive contamination of liquid with erosion products.

It should be mentioned that no high-speed imaging of the discharge was performed due to the fact that the current setup was oriented to operational unit study on the application point of view (production of colloidal solution) and not designed for on-line thorough diagnoses such as high-speed imaging.

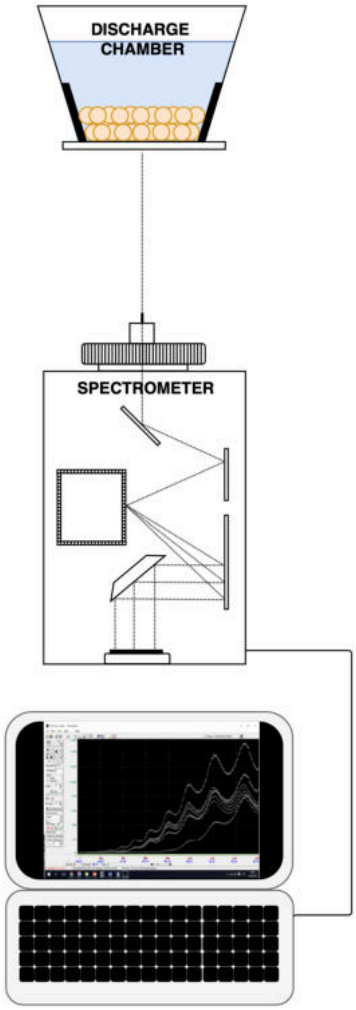

Figure 3.5: Experimental arrangement for registration of plasma emission of multiple-pulse underwater electrical discharges.

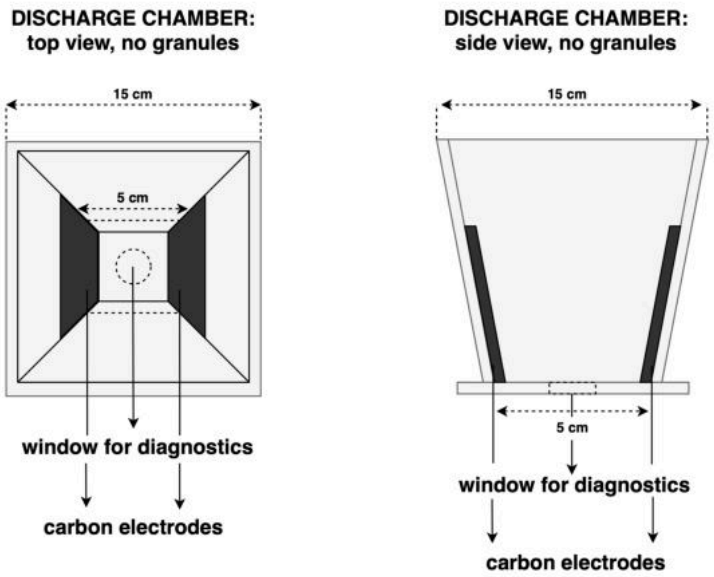

Figure 3.6: Experimental arrangement for registration of plasma emission of multiple-pulse underwater electrical discharges.

3.3 Experimental setup for single-pulse underwater electrical discharge investigation

3.3.1 General description

Figure 3.7 shows a general setup developed for investigation of an underwater single-pulse electric discharge in Laplace laboratory. In this configuration, the electric discharge is generated between the tips of two metal electrodes immersed into dielectric liquid. The liquid used in this study is water (both, deionized and non-purified). The latter was chosen for several reasons. Primarily, for the sake of simplicity, but also due to its ubiquity and being one of the most versatile solvents. Stochastic movement of metal granules occurring during the operation of setup from section 3.2 is replaced by an electrode mounting allowing pendulum-like motion of one of the electrodes, while another electrode remain in a fixed position.

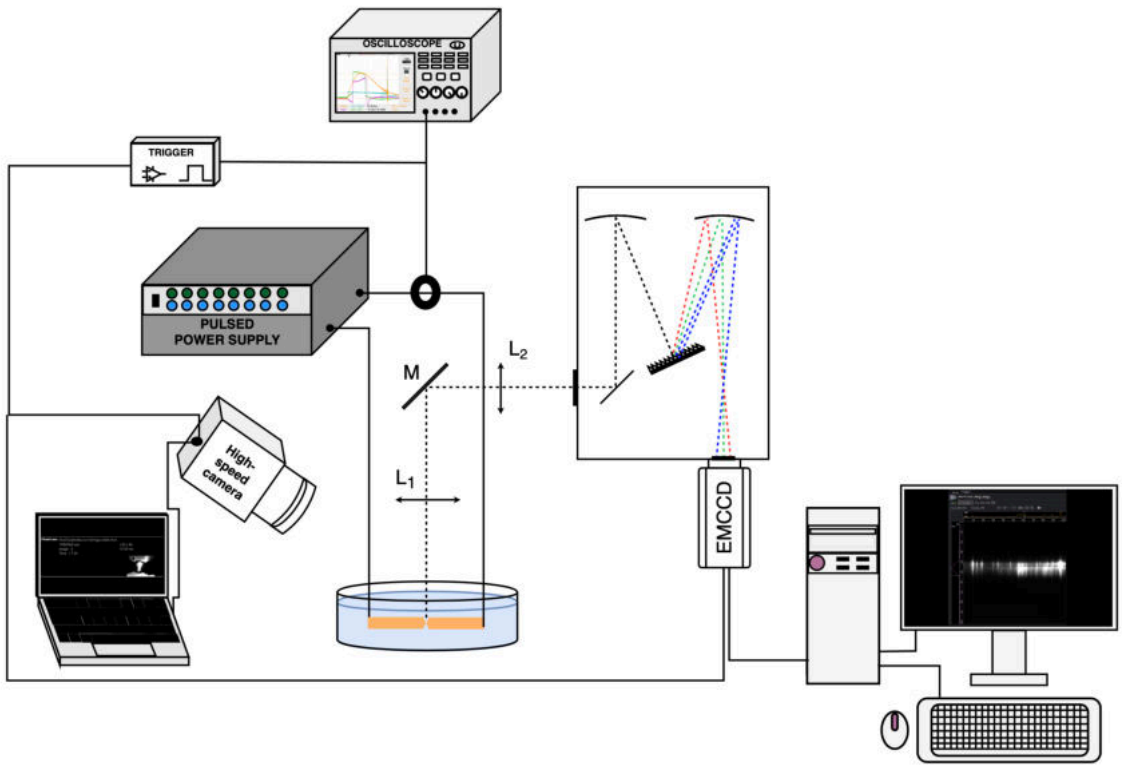

Figure 3.7: Experimental arrangement for single-pulse underwater electrical discharge investigation.

In the setup for multiple-pulse underwater electric discharge generation, metal granules are initially in contact. However, during the setup's operation one can observe the movement of the metal granules. Discharge ignites from the short circuit and molten bridge mechanism [12], [13]. This allows to work with relatively low voltages (below 1 kV), unlike

in the majority of the studies, wherein the voltage of several kV and higher is applied in order to achieve the breakdown of dielectric liquid in inter-electrode gap. After some time of setup's operation, granules begin to erode and, occasionally, contact points disappear. In such case, the discharge occurs directly in liquid between the eroded granules, which is possible due to the water's contamination with conductive particles of eroded metal. Additionally, it is assumed that discharge itself causes granules to move apart as a result of the electrostatic repulsion and/or the effect of the plasma channel expansion [14]. The breakdown and the bubble growth are associated with a pressure shockwave that can push apart two "electrodes" represented by granules. The idea behind using mobile electrodes in setup in Fig. 3.7 is to allow motion of the electrodes in order to stay as close as possible to the real synthesis process. It is not known how exactly the granules move in setup from Fig. 3.1 in terms of the rate or displacement values, since it depends not only on the discharge energy input but also on the friction with other granules.

It should be noted that the choice of a pendulum was made in order to place all the mechanical parts away from the water tank and the optical path towards the spectrometer. The rotation axis of the pendulum is insulated in order to avoid power up of the holding structure during experiments. Connection of the moving electrode to the power supply was sure to be not too rigid to avoid impeding the motion.

3.3.2 Impulse generator and electrical measurements

The schematic diagram of the modular impulse generator is illustrated in Figure 3.8. It is built on the base of thyristor-switched capacitors. Consisting of 8 capacitors connected in parallel, capacitor bank allows for generation of up to 8 consecutive pulses with the shortest delay of 1 ms between two pulses. Capacitors used are EPCOS/TDK Electronics aluminum electrolytic capacitors of 1000 μF capacitance and 450 V maximal load voltage. Thyristors used are thyristor modules VSKT162/12PBF by Vishay Intertechnology. They have a switching time of 50 - 100 μs, maximum average on-state current of 160 A, and maximum repetitive peak reverse voltage of 1200 V. Such arrangement allows for a maximum pulse frequency of 1 kHz with peak pulse current of 4 kA and pulse duration of 250 μs.

Once the capacitors are loaded, the discharge is triggered manually by pressing a button on the control board that activates the trigger of the thyristors. This leads to the discharge of capacitors in a "RC circuit" exponential decay mode. The resistance corresponds to the total resistance of cables, connectors, and the arc.

Additionally, there is a possibility to manually discharge each capacitor channel in two lamps using switches. This allows to reduce the

load voltage to the wanted value or to secure the power supply by eliminating remaining voltage after one test.

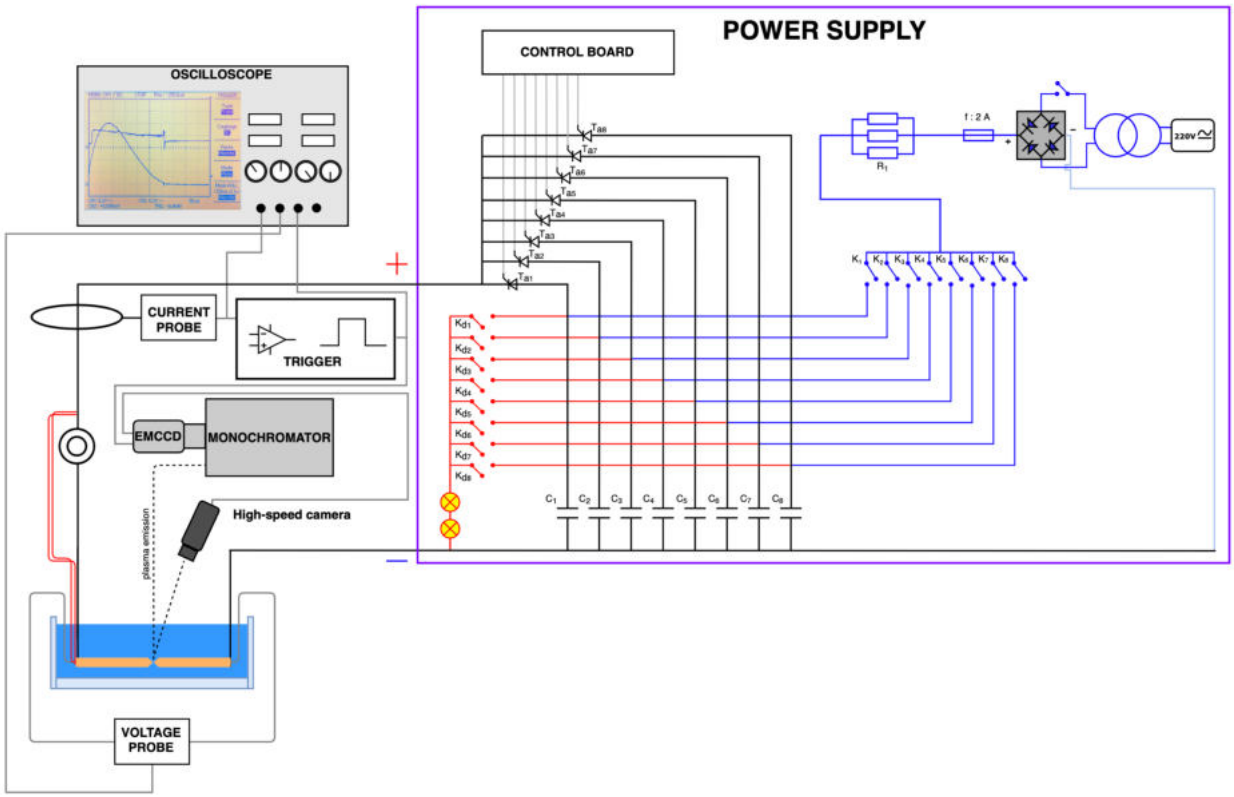

Figure 3.8: Schematic diagram of the initial version of impulse generator for investigation of single-pulse underwater electrical discharge: T_{a1}, T_{a2},… – thyristors; C_1, C_2,…– capacitors; K_{d1}, K_{d2}, …– switches to discharge the capacitors.

Electrical measurements are made using voltage and current probes. The first probe is a Rogowski Current Waveform Transducer by Power Electronic Measurements (PEM). It has a measurement range from 300 mA to 300 kA and typical bandwidths from 0.1 Hz to 16 MHz. The second probe is ELDITEST Electronic differential probe GE8115. It allows for attenuation factors of 100 and 1000 and a bandwidth of 30 MHz. All experiments are carried out with attenuation factor 100. The maximum input voltage is 1500 V. The roles of these probes are to measure the evolution of the current and voltage over time, respectively.

The electrical characteristics obtained by the probes are visualized and recorded by a digital oscilloscope. In the earlier experiments, Française d'Instrumentation FI 3208 oscilloscope is used. Its maximum acquisition frequency is 100 MS/s (for 2 channels simultaneously) and 200 MS/s (for 1 channel) for a bandwidth of 80 MHz. It should be noted that in first experiments the electric data was not recorded on any electronic data storage device, and only snapshots of the oscilloscope screen were saved after every experiment (see Figure 3.9).

This can be explained by a simple need for an initial general overview of the process characteristics prior to a thorough investigation. The subsequent more detailed studies were carried out using a four-channel digital storage oscilloscope Tektronix TDS2024C. The maximum acquisition frequency of this oscilloscope is 2 GS/s for a bandwidth of 200 MHz. The reproducibility of the experimental discharge current and voltage drop on the electrodes can be seen in Figures 3.10 and 3.11, respectively.

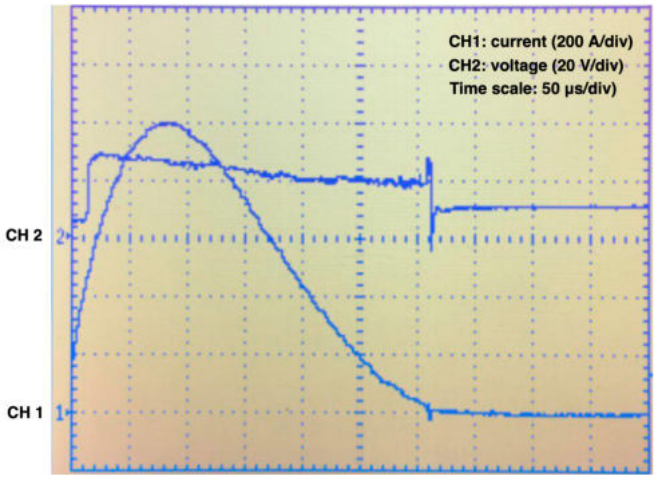

Figure 3.9: Sample oscillogram registered for the experimental regime of 1000 A peak current and 220 V load voltage.

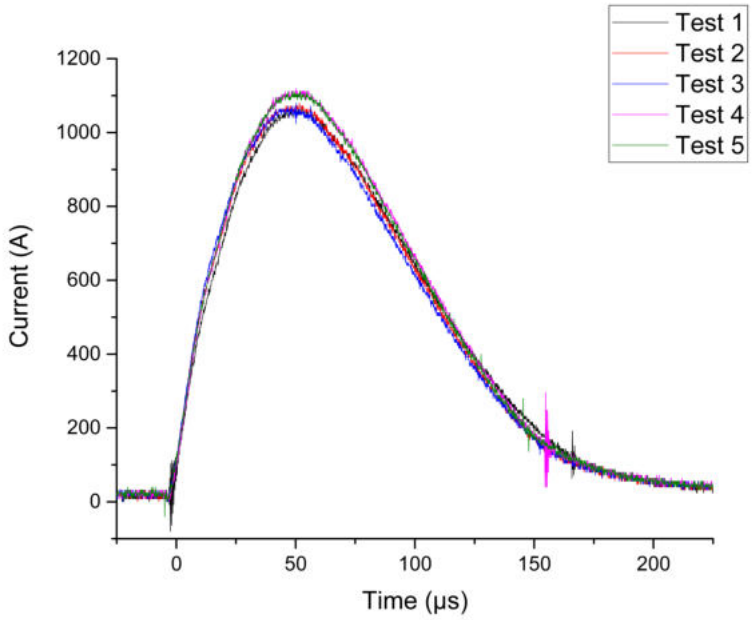

Figure 3.10: Reproducibility of the discharge current within experiments for the experimental regime with peak current of ~ 1000 – 1100 A and load voltage of ~ 320 V.

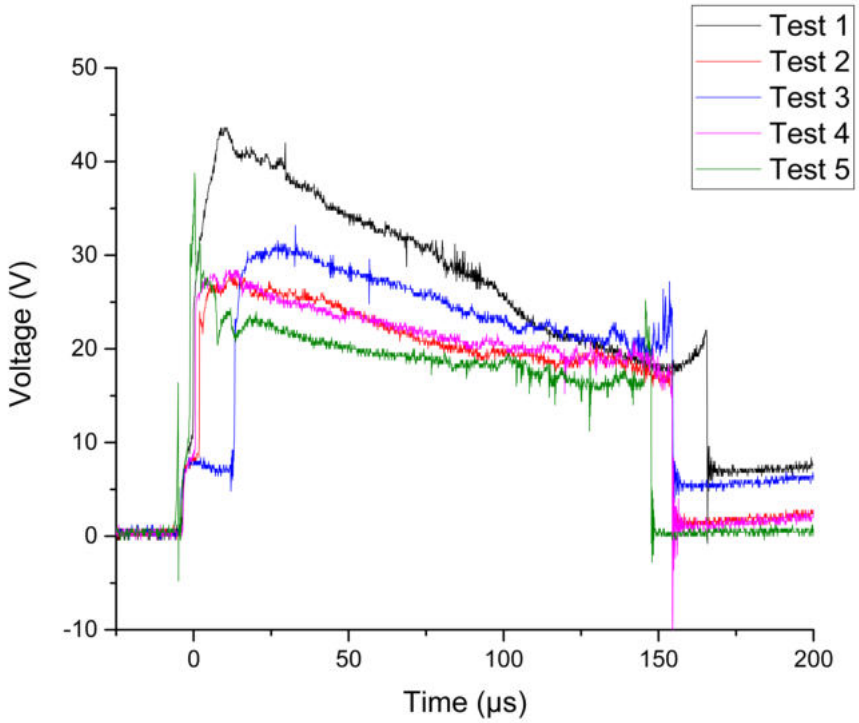

Figure 3.11: Reproducibility of the electrode voltage drop within experiments for the experimental regime with peak current of ~ 1000 – 1100 A and load voltage of ~ 320 V.

The fact that current waveform in Fig. 3.10 remains almost unchanged from one experiment to another is due to the fact that the electrodes and the discharge present only a part of the electrical circuit. The impedance of the main circuit (with cables and connectors), where the other part of voltage is dissipated, remains unchanged in all tests. It is only the arc voltage drop that changes from one measurement to another (Fig. 3.11). For an initial load voltage of 320 V (and a voltage of about 175 V after 50 µs since the beginning of the pulse), the voltage that is being measured between the two electrodes (including voltage drop at the electrodes, and arc voltage) constitutes a relatively small part (20 V in case of test 5, and, for instance, about 45 V in case of test 1) of total voltage. Therefore, the total impedance variation is limited, which could explain the better reproducibility observed for current.

As for the voltage waveform, the strongest difference in voltage for all the 5 tests presented in Fig. 3.11 is observed at the beginning of the pulse. The final value (about 20 V) is quite similar for all the tests. As can be seen, the voltage measured in test 2 and test 4 are almost identical.

One can assume that reason for these differences is that the arc ignition pattern is not the same for all experiments. If the contact area between the electrodes is large, the plasma column will be initially larger than in the case of a sharp contact. The "molten bridge" ignition mode involves very small contact area (< 100 µm), and it is difficult to ensure

constant configuration in all tests. Alternative option would be to use sharp electrodes, placed tip to tip. However, such configuration would be too much different from the actual operation of the setup in section 3.2 (with large and blunt metal granules). This represents one of the main issues related to the experimental configuration: a "controllable" and simplified arrangement that still has to remain "realistic".

Additionally, it should be noted that the current corresponds to an exponential decay, according to a RC-circuit discharge model. In case if the thyristor commutation is instantaneous, the current should rise to the maximal value (defined by the load voltage divided by the circuit impedance) and then follow exponential decay. But the thyristor switching time is "long" in comparison to the overall pulse duration (50 - 100 μs for a 150 – 200 μs pulse). This means that the maximal value observed on the curves in Fig. 3.10 is slightly lower than the one obtained from dividing the load voltage by the resistivity. During the switching of the thyristor, capacitors start to discharge but not as fast as in the case of an exponential decay: it is the thyristor that limits the current flow. Therefore, it is difficult to deduce the circuit resistivity from the measurements of voltage and current. The best approach would be to fit the shape of the decay (rather considering the maximal value) by adjusting the resistance, considering the given capacity.

3.3.3 Optical characterization: high-speed imaging and spectroscopy

The arrangement for high-speed imaging of discharge and its photo are shown in Figures 3.12 and 3.13, respectively. The halogen lamp (iodine high-pressure projector lamp) is placed below the water tank with electrodes allowing to study the shape and size of the bubble formed around the discharge. The lamp is placed about 40 cm below the electrodes. Similarly, the high-speed camera lens is placed about 40 cm above the electrodes.

Discharge visualization is performed with Photron FASTCAM Mini AX100. The camera allows to acquire images in the optical wavelength range within 400 – 1000 nm (in monochrome). The maximum acquisition rate of 540,000 frames per second (fps) for a resolution of 128 × 16 pixels. The discharge has a lifetime ~150 – 340 μs and therefore working at the maximum speed is not necessary for general characterization of the discharge behavior. Besides, the frame resolution corresponding to the maximum acquisition rate is too small to capture the whole discharge. In Chapter 4, high-speed imaging of the discharge is performed with rate that varies from 75,000 to 100,000 fps depending on the peak current value being studied. Exposure time for all experiments is 0.95 μs. In some

cases, imaging is performed with 1/100 ND filter to avoid an overexposure.

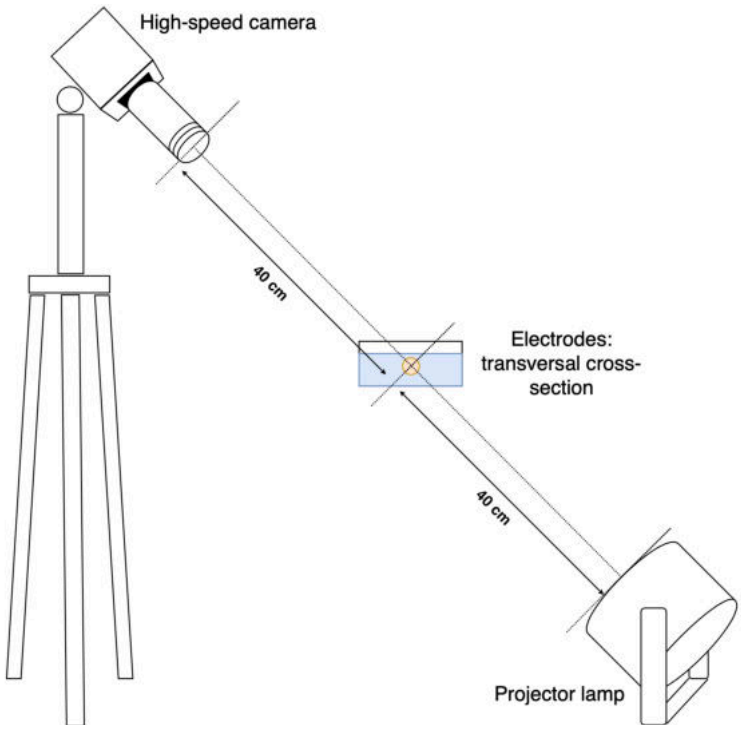

Figure 3.12: Schematic diagram of the experimental setup for high-speed imaging of the single-pulse underwater electrical discharge.

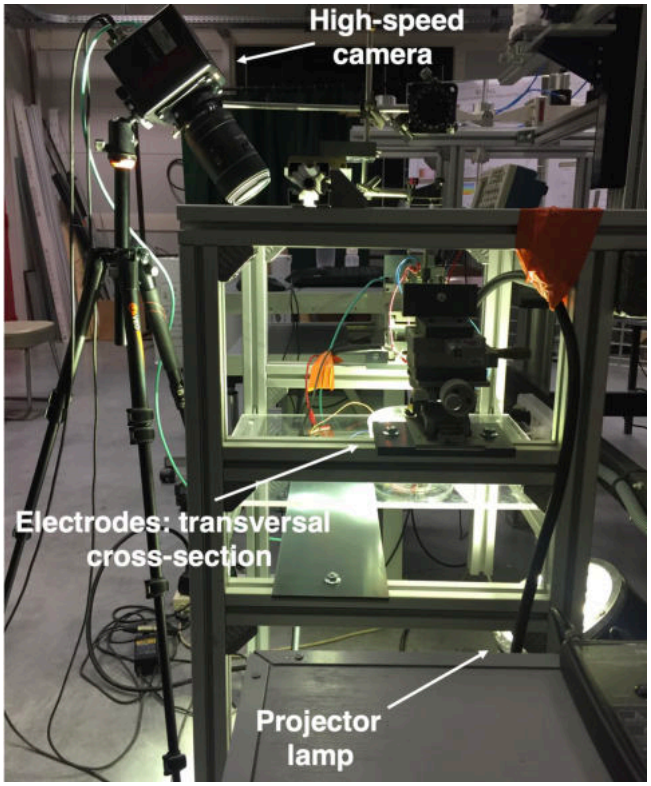

Figure 3.13: Photo of the experimental setup for high-speed imaging of the single-pulse underwater electrical discharge.

Optical emission spectroscopy is essential to characterize the radiation emitted by the plasma. For this, we use Princeton Instruments Acton SpectraPro SP-2750 750 mm triple grating imaging spectrometer, which is fitted with three diffraction gratings 300, 1200 and 1800 lines/mm. The light emitted by the plasma is collected and transported to the entrance slit of spectrometer by an optical arrangement (see Figure 3.14) consisting of 2 biconvex lenses (L_1 and L_2) and a flat mirror (M). Both lenses are made of fused silica, allowing observation of the light from ultraviolet to infrared. Besides, since the experiments are made in air in which only light with a wavelength superior to 200 nm is visible, it might be better to indicate (200 - 3000 nm). The lens L_1 is placed horizontally above the electrodes, producing a parallel beam from the discharge that is situated at its focal plane. The lens L_2 is placed vertically in front of the entrance slit of the spectrometer and focuses the beam on it. The focus lengths of L_1 and L_2 are 25 and 35 cm, respectively.

The diffracted light is collected by an EMCCD (Electron Multiplying Charge Coupled Device) detector PROEM-HS 1024BX3 from Princeton Instruments allowing the analysis of low intensity light signals.

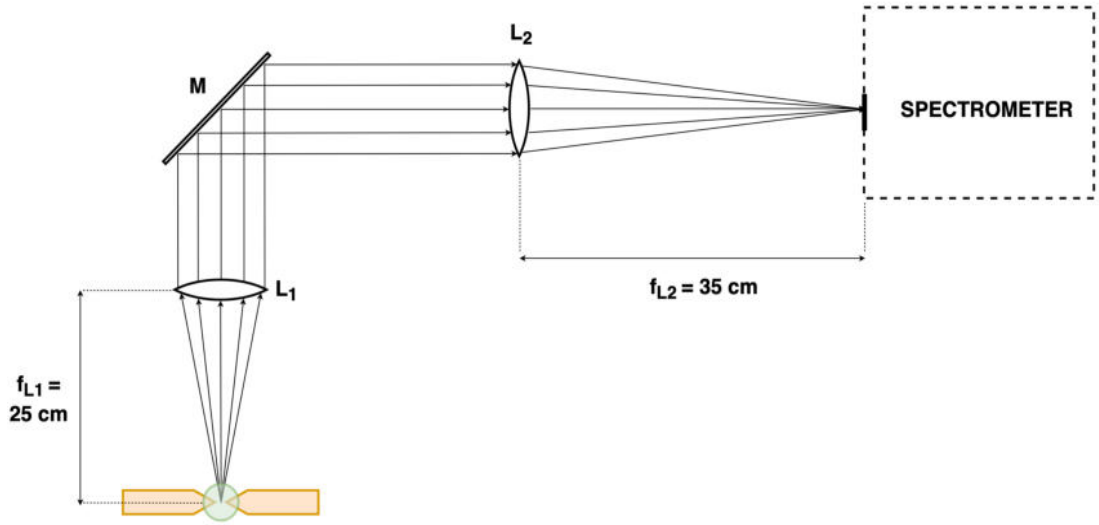

Figure 3.14: Schematic diagram of the optical arrangement for single-pulse underwater electrical discharge plasma investigation.

Registration of the spectra is performed using 300 lines/mm grating (for hydrogen H_α and atomic copper lines with central wavelength set on λ = 616.5 and 515.0 nm, correspondingly) and 1800 lines/mm grating (for hydrogen H_β line with central wavelength set on λ = 486.1 nm). The spectral resolution of the system is 0.056 nm for the 300 lines/mm grating and 0.0078 nm for 1800 lines/mm grating. In all the experiments carried out using the initial impulse generator arrangement (see Figure 3.8), the exposure time of the EMCCD camera varies from 50 to 200 μs. Optical

emission spectra are often averaged a number of times (from 1 to 10) to increase the signal-to-noise ratio.

The start of the spectroscopic acquisition and high-speed camera recording are both triggered by the trigger unit. The signal from the current probe is recorded on Channel 1 of the oscilloscope. As soon as the value of current rises above the set value, the comparator of a trigger unit generates a TTL signal that is used to trigger the EMCCD camera. The output trigger of the latter, in turn, is used to trigger the high-speed camera.

The trigger unit is based on a comparator that trigs when the signal from the current probe crosses a given set threshold. This device was built in the lab (i.e. not a commercial product), and has a very simple design with an operational amplifier arranged as a comparator. The trigger of the oscilloscope, on the other hand, is internal and is different from the trigger device controlling the camera. It is as well based on the current measurement but is chosen on the trigging parameters of the oscilloscope.

3.3.4 Electrodes and liquid media

The electrodes in all the experiments have point-to-point configuration. Two metal cylindrical electrodes of 6 mm diameter each are installed using a specially designed electrode support that allows anode to move in a horizontal plane, while cathode remains fixed. In this work, two types of electrode materials are studied: copper (Cu – Cu electrodes) and molybdenum (Mo – Mo electrodes). The electrodes are sharpened to have a tip with a radius of curvature of about 1 mm in case of copper electrodes, and about 2 mm in case of molybdenum electrodes.

The copper electrodes are provided by “Comptoir Général des métaux” (CGM) and have a purity of ~ 99%. The purity of molybdenum electrodes is ~ 99.99%.

Two types of liquid media are studied: non-purified and deionized water. Non-purified water being simply tap water of pH ~ 6.5, conductivity ~ 5–50 mS/m and temperature of 20–25 °C. Deionized water has pH ~ 7, conductivity ~ 0.05 mS/m and t = 20–25 °C.

The container for liquid is a borosilciate glass dish with an ellipse base. The height of the dish is 4.7 cm, while the semi-major and semi-minor axes of ellipse are 10.25 and 6.75 cm, respectively. After the dish is filled with liquid, the electrodes are immersed in it. The effect of liquid pollution by the eroded electrodes during the study is not taken into account. Two cases are to be specified:

(i) when studying the interaction of the discharge with the electrode surface, the maximum number of discharges is set at 20-30 (depending

on the electrode material) before the liquid is changed and the electrodes are re-sharpened and new series of measurements can be realized.
(ii) when diagnosing plasma by optical emission spectroscopy, the liquid is not changed during an acquisition. The study of bubble is also performed on a few tens of discharges before changing the liquid.

3.4 Optical emission spectroscopy of the underwater electric discharge plasma

Optical emission spectroscopy (OES) is a classical tool for plasma diagnostic. Generally, OES consists in the spectral analysis of the light emitted in the visible region by the plasma. The light is dispersed in a spectrograph by a grating, and detected by a CCD camera. Finally, the signal is digitalized and treated with a computer.

3.4.1 Sensitivity calibration

The various components of optical system for plasma emission registration have a different intensity response to each wavelength. Therefore, prior to any experimental measurements, a sensitivity calibration of spectroscopic system must be carried out. It is best done for the complete system and not separately for the individual components. The standard source of known radiance should be placed in such a way that the radiation fills the full solid angle of the spectroscopic system and that the identical part of the entrance slit, preferably the total slit, is illuminated as in the measurements.

One distinguishes primary and secondary radiance standards. Primary standards are the blackbody radiator for the infrared to the visible region, and synchrotrons for the short wavelength range. The spectral radiance of a blackbody $\mathrm{L}_{\lambda}^{\mathrm{B}}(\lambda, \mathrm{T})$ is determined by Planck's law and it is a function of temperature and wavelength only:

$$L_{\lambda}^{B}(\lambda, T) = \frac{2hc^2}{\lambda^5} \frac{1}{e^{h\nu/k_B T} - 1} \tag{3.5}$$

which may be written as numerical value equation

$$L_{\lambda}^{B}(\lambda, T) = \frac{1.1910 \times 10^{20}}{\lambda^5} \frac{1}{e^{h\nu/k_B T} - 1} \left[\frac{\mathrm{W}}{\mathrm{m^2 \cdot nm \cdot sr}}\right]. \tag{3.6}$$

The precision of the temperature determines the uncertainty of the spectral radiance. Fixed-points of the International Temperature Scale ITS like the melting temperatures of gold (1337.33 K) and platinum (2041.4 K) are the most commonly used reference standards. Most

national metrological laboratories maintain a series of blackbody sources and provide calibration services.

In principle, a blackbody is realized by a suitably designed furnace ("hohlraum") with a small hole from which the radiation escapes. The hole has to be small enough not to disturb the radiation inside the hohlraum, which is in thermodynamic equilibrium with the walls.

In contrast to the thermal radiation of a blackbody the synchrotron radiation is completely polarized in the plane of the electron orbits with the **E**-vector parallel to the orbital plane. Outside this plane vertical polarization components exist. Drawbacks for the calibration of a complete spectroscopic system are certainly the facts that the synchrotron radiation is emitted into a small cone and that the system has to be moved to the location of the synchrotron [15], [16].

Secondary standard sources are readily available for UV to near-infrared spectral region and have usually been calibrated against a primary standard source. The most commonly used secondary standard is the tungsten strip lamp: a strip of tungsten is mounted in a glass envelope with a window of fused silica or of sapphire in some cases. Vacuum lamps are usually for temperatures from 1100 to 2000 K; lamps filled with argon are used for temperatures from 1600 to 2700 K, since the gas slows down evaporation of tungsten. Heating of the strip is by a highly stabilized current. Because the temperature varies considerably along the filament, calibration is done nominally for a small central part, maybe of 1 mm height, which hence should be used in the measurements only. This is certainly a restriction in some cases. It is also advised to mount especially gas-filled lamps in the same position as the calibration was done, because changing heat conduction in the lamp may change the temperature.

The spectral radiance $L_\lambda(\lambda, T)$ is obtained by multiplying the blackbody radiance with the spectral emissivity $\varepsilon(\lambda, T)$ of tungsten and with the spectral transmittance $T(\lambda)$ of the window:

$$L_\lambda(\lambda, T) = T(\lambda) \cdot \varepsilon(\lambda, T) \cdot L_\lambda^B(\lambda, T). \tag{3.7}$$

T is the true temperature at the center of the strip. The emissivity is a rather weak function of wavelength and temperature: it varies between 0.41 and 0.48 in the wavelength range from 250 to 700 nm and temperatures from 1600 to 2700 K [17], [18]. Uncertainties of the spectral radiance of calibrated lamps are typically around ±1%.

Tungsten strip lamps age and re-calibration becomes necessary after some use. In cases where high precision is not striven for, one may calibrate a lamp in the laboratory employing a pyrometer. This is usually done at the wavelength λ_0 = 650 nm. The procedure yields a temperature called brightness temperature T_b, defined in the following way: a

blackbody at T_b has the same spectral radiance at λ_0 = 650 nm as the tungsten strip lamp at T:

$$\varepsilon(\lambda_0, T) \cdot L_\lambda^B(\lambda_0, T) = L_\lambda^B(\lambda_0, T_b). \quad (3.8)$$

The true temperature T is thus readily obtained from the brightness temperature. In the limit $h\nu_0 \gg k_B T$ the relation between the two temperatures becomes

$$\frac{1}{T_b} = \frac{1}{T}\left\{1 - \frac{k_B T}{h\nu_0} ln[\varepsilon(\lambda_0, T)]\right\}. \quad (3.9)$$

The relative sensitivity calibration is the one most commonly used. It gives the true relative peak intensities and corrects for all instrument properties on a relative basis. An absolute calibration, however, allows to measure spectral data in absolute irradiance units from which absolute power levels can be calculated. Both types of sensitivity corrections require the measurement of the relative response function of the spectroscopic system. The relative response is defined as the ratio of the data obtained with the standard source or detector to the calibration data for the standard; i.e., the ratio of observed intensity to true intensity:

$$Sensitivity\ of\ spectroscopic\ system\ [S(\lambda)] = \frac{Measured\ spectrum\ of\ calibrated\ lamp}{Theoretical\ spectrum\ of\ lamp}, \quad (3.10)$$

S(λ) is also known as responsivity of the detector.

Multiplying spectroscopic data by the inverse of the relative sensitivity function yields accurate wavelength position and true relative intensity of spectral peaks; spectra corrected with different multiples of the function will differ only by a uniform vertical expansion factor. For most applications, a relative correction is sufficient.

3.4.2 Abel inversion

The end goal of plasma diagnostics is to obtain local values of plasma parameters. The latter, as well as the plasma radiance, vary not only in axial (from cathode to anode) but also in radial (from axis of discharge to its periphery) directions.

In case of an axially symmetric plasma columns, and in assumption of plasma being optically thin, the transversal plasma cross-section, so-called plasma “slice” can be displayed as sum of coaxial circles (see Fig. 3.15) [19]. Plasma emission coefficients $\varepsilon(r_i)$ vary along the radius, meaning from layer to layer, but are considered to be constant within the

limits of one circular layer. Discharge is being observed along the chords parallel to y axis. This being said, the observed emission intensity is the integration of the emission coefficient along the line of sight $I_{obs}(\lambda, x)$. Radius of the plasma column defines the external limit of discharge r_0, where there is no emission: $\varepsilon(r_0) = I_{obs}(r_0) = 0$.

If one positions zero of coordinate system on the discharge axis, and takes the axial symmetry ($x^2 + y^2 = r^2$) into account, observed intensity $I_{obs}(x)$ at a distance x can be expressed as

$$I_{obs}(x)\Delta x = \sum_{-r_0}^{r_0} \varepsilon(r)\Delta y \Delta x, \tag{3.11}$$

where ε(r) – local value of plasma emission.

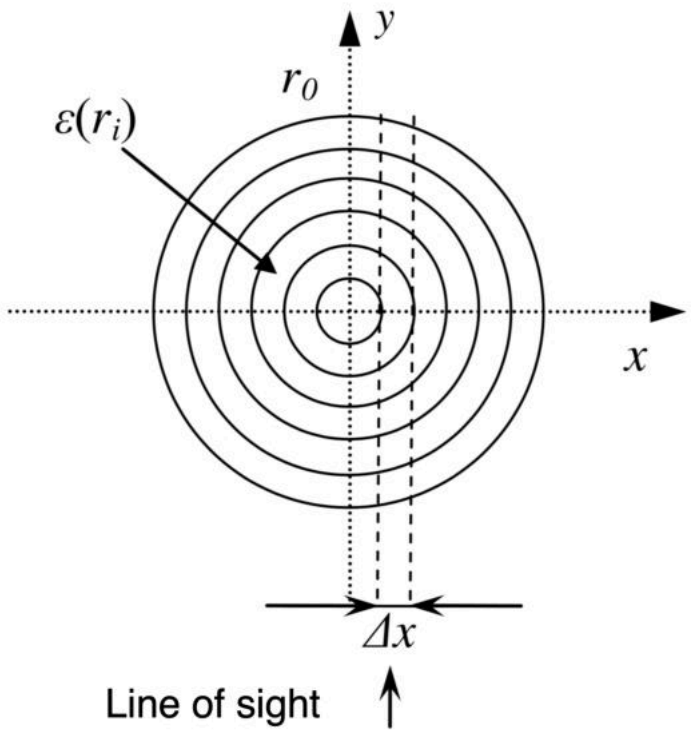

Figure 3.15: A slice of plasma, axially symmetric with respect to the z axis, which is normal to the paper [19].

In approximation to infinitively small volume elements:

$$I_{obs}(x) = 2\int_0^{r_0} \varepsilon(r)dy. \tag{3.12}$$

The substitution $y = (r^2 - x^2)^{1/2}$ introduced into (3.9) gives the integral Abel equation:

$$I_{obs}(x) = 2\int_x^{r_0} \frac{\varepsilon(r)}{(r^2 - x^2)} r dr, \tag{3.13}$$

Determination of local plasma characteristics (in our case, emission coefficients $\varepsilon(r_i)$) from the observed intensity is called an inverse Abel transform:

$$\varepsilon(r) = \frac{1}{\pi}\int_r^{r_0} \frac{I'_{obs}(x)}{(x^2-r^2)}\,dx, \qquad (3.14)$$

where $I'_{obs}(x)$ – spatial derivative of intensity, r_0 – external radius of an axially-symmetrical emitting object.

An algorithm proposed in [20] allows to calculate $\varepsilon(r_i)$ avoiding differentiation and integration of the experimental data. This method uses matrix of transforming coefficients a_{jk} for calculation of radial emission distribution:

$$\varepsilon_j = \frac{1}{r_0}\sum_k a_{jk} \cdot (I_{obs})_k, \qquad (3.15)$$

where j and k – indexes of local and observed values.

Index j has a physical significance of number of the circular layer with an emission coefficient ε_j, while index k denotes a chord number along the line of sight (see Fig. 3.16). In such a manner, matrix of transforming coefficients a_{jk} describes contribution of j-th layer's emission with length and position of k-th chord into observed emission intensity.

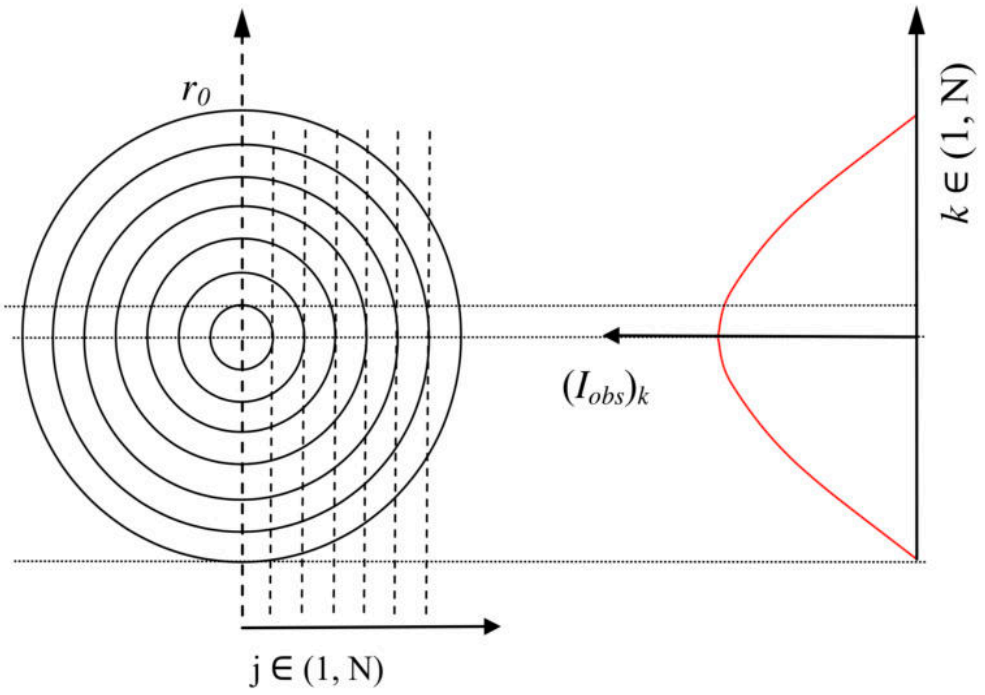

Figure 3.16: Illustration of method proposed in [20] for calculation of radial distribution of plasma emission [19].

3.4.3 Determination of plasma parameters

Plasma as an aggregation state of matter exists in an extremely vast range of parameters: pressure, temperature and concentration of its components. Moreover, dominating processes that define plasma's state and characteristics also vary. Therefore, a number of models has been proposed in order to adequately describe plasma under certain conditions.

One of the most general models is the one that assumes the state of a complete thermodynamic equilibrium (CTE). It is considered that in such plasma particles follow Maxwell velocity distribution, while population of energy levels obey the Boltzmann distribution. Additionally, ratio of concentrations of particles with different degrees of ionization is defined by Saha ionization equation. Another inherent characteristic of a CTE system is equilibrium of matter and plasma emission following Planck's law of blackbody radiation.

However, situations where plasma resides in CTE are limited to plasmas in inner shells of stars and some cases of dense magnetically-insulated plasmas. Main factors that limit application of the CTE model are the presence of spatial gradients of plasma parameters and radiation losses. This concerns most of the laboratory plasmas [107].

Taking this into account, a local thermodynamic equilibrium (LTE) model has been introduced. Plasmas in LTE can be described with the same laws as those in CTE with an exception of radiation [21].

Thermal plasma presents the main example of LTE realization. In such plasma, collision processes between particles are dominating the radiative processes. That means that population of energy levels and ratio of concentrations of particles with different degrees of ionization are maintained at equilibrium values as a result of particle collisions. It is also considered that since electrons have the highest mobility among plasma particles, the main mechanism of energy transfer and LTE establishment is due to collisions with electrons. Therefore, electron number density N_e presents a crucial parameter that defines the existence of LTE in plasma.

3.4.3.1 Plasma temperature

In this work, for the temperature determination of the underwater electric discharge plasma, two approaches are used: Boltzmann plot and two-line (otherwise, method of relative intensities) methods. In fact, the latter is a particular case of the Boltzmann plot method. Both of them are based on measurements of the intensities of spectral lines, emitted by atoms or ions of the same element [22], [23]. Since it is a relative and not an absolute intensity measurement, the calibration of the absolute spectral sensitivity of the optical arrangement is not necessary.

If we assume that the plasma is in a state of LTE (the validity of this assumption for the underwater electric discharge plasmas will be discussed in section 4.3.2 of Chapter 4), the distribution of atoms and ions in the different excited states is described by the Boltzmann distribution. Thus, the density n_i of a certain type particle, atom or ion, in an excited state i is given by:

$$n_i = \frac{n_0 g_i}{Z} \cdot \exp\left(-\frac{E_i}{k_B T_e}\right), \tag{3.16}$$

where n_0 is the total density of the considered particles in the plasma, g_i the statistical weight of the excited level and E_i its energy, Z the total partition function, k_B the Boltzmann constant and T_e the electron temperature In case of LTE, T_e is also equal to the ion temperature and to the gas temperature; T_e could thus be replaced in (3.16) with a unique plasma temperature T.

The intensity of the line emitted by the transition from the upper state i to a lower state j is [21]:

$$I_{ij} = \frac{1}{4\pi} n_i A_{ij} h\nu, \tag{3.17}$$

where n_i – population of the upper state i, A_{ij} –probability for spontaneous radiative emission from the state i to the state j, h – Planck's constant, ν – emission frequency. In practice, oscillator strength f_{ji} is often used instead of transition probability A_{ij} in SI units (A in s^{-1}, λ in m) [24]:

$$A_{ij} = \frac{g_j}{g_i} \frac{2\pi^2 e^2 \nu^2}{\varepsilon_0 m_e c^3} f_{ji}, \tag{3.18}$$

where g_i and g_j – statistical weights of the upper and lower states, e – electron charge, m_e – electron weight, ε_0 – vacuum permittivity, c – speed of light in vacuum.

Replacing n_i in (3.17) by its expression given in (3.16), we obtain:

$$I_{ij} = \frac{1}{4\pi} g_i A_{ij} h\nu_{ij} \frac{n_0}{Z} exp\left(-\frac{E_i}{k_B T_e}\right). \tag{3.19}$$

Expression (3.19) can be rewritten as:

$$\ln\left(\frac{I_{ij}}{g_i A_{ij} h\nu_{ij}}\right) = \ln\left(\frac{1}{4\pi}\frac{n_0}{Z}\right) - \frac{E_i}{k_B T_e}. \tag{3.20}$$

Plotting the intensity logarithm simultaneously for group of spectral lines with different E_i yields a so-called Boltzmann diagram (i.e. Boltzmann plot). The experimental data on this diagram should form a line, slope of which corresponds to the temperature T_e (T in LTE) in a certain spatial point of plasma.

If the resulting Boltzmann plot presents a scatter of experimental points it may signify that

- plasma is non in equilibrium and/or
- values of spectroscopic constants used for temperature calculations are not appropriate and should be reconsidered.

Now considering only two lines λ_1 and λ_2 emitted by the same species, i.e. by atoms or even charged ions of the same element, the ratio of their intensities is given by:

$$\frac{I_1}{I_2} = \frac{g_1 A_1}{\lambda_1} \cdot \frac{\lambda_2}{g_2 A_2} exp(-\frac{E_2 - E_1}{k_B T_e}), \tag{3.21}$$

where g_i, A_{ij} and E_i for the line k (k = 1,2) are noted g_k, A_k and E_k respectively. Extracting T_e from the preceding equation, one can obtain

$$T_e = \frac{E_2 - E_1}{k_B} \cdot [\ln(\frac{I_1 \lambda_1 g_2 A_2}{I_2 \lambda_2 g_1 A_1})]^{-1}. \tag{3.22}$$

The ratio I_1/I_2 is experimentally determined from an emission spectrum. The electron temperature can be thus calculated with equation (3.22) if E_k, λ_k, g_k and A_k are known values for the two lines.

Practically, the choice of the two lines is of importance. Since the relative error on the temperature is

$$\frac{\Delta T_e}{T_e} = \frac{k_B T_e}{|E_2 - E_1|} \cdot \frac{\Delta({}^{I_1}/_{I_2})}{{}^{I_1}/_{I_2}}$$

according to (3.22), it is crucial to choose two lines with a difference $|E_2 - E_1|$ as large as possible. Moreover, the chosen lines have to be intense and isolated from other lines, in order to avoid overlapping and to minimize $\Delta (I_1/I_2)$. It is also desirable that λ_1 and λ_2 are close to each other. In this case, the absorption by the dielectric and the spectral sensitivity of the optical arrangement can be considered equal for the two lines. No spectral correction is then required for the calculation of I_1/I_2. Finally, the lines have to be non-resonant ones, to avoid self-absorption.

It has to be emphasized that with the two-line method, a minimum error of 10% on T_e is expected [23].

Additionally, it should be noted that to calculate the line intensities from a spectrum, the continuous plasma emission has to be subtracted

first. Then the line shapes are deconvolved if there are adjacent lines. The line intensity I_{ij} is not simply the maximum value of the peak, but the whole area under the line contour. The simplest way is to integrate directly the "line" formed by the experimental data, and more advanced approach would be fitting the experimental data with Lorentz or Voigt functions, following by calculation of the integral of the obtained profile.

Finally, the lines have to be not self-absorbed. In particular one has to avoid resonant lines, and lines with level close to fundamental level.

3.4.3.2 Electron number density of plasma

Apart from the temperature, the electron number density (hereinafter, electron density) N_e is another important physical parameter characterizing a plasma, which can also be determined with OES. Several methods for N_e calculation can be distinguished: based on measurements of line and continuum intensities, and based on measurements of line profile [23], [25]. The electron density has a direct influence on line shapes, while they are relatively insensitive to electron and ion temperatures. Spectral lines are broadened and shifted from their theoretical position, proportionally to values of the electron density. The influence of the density on line broadening can be qualitatively explained as follows: the collision frequency will increase with density, and so the lifetime of atoms in excited states will decrease due to collisions. By the Heisenberg principle, this will increase the uncertainty on the energy levels, i.e. the uncertainty on the emitted wavelength. Spectral lines are thus more broadened in plasma with high (~ 10^{17} cm^{-3}) electron number density.

In this work, the H_α and H_β lines emitted by atomic hydrogen at 656.28 nm and 486.13 nm, respectively, are used to determine the electron density. These lines are the classical candidates for density measurement, because the hydrogen atom is particularly sensitive to the Stark effect. Additionally, for the purposes of completeness and comparison, the electron density was also determined from the line profiles exposed to the quadratic Stark effect: Cu I 515.3 nm.

Whenever the contribution of other broadening mechanisms compared to Stark broadening is not negligible, the deconvolution procedure must be employed to determine Stark width — w_S, which is used to determine N_e from the comparison with theoretical widths at the same electron temperature (T_e).

One should consider the following mechanisms contributing to the spectral line profile and width:

- instrumental broadening;
- natural broadening;
- Doppler broadening;

- pressure broadening (resonance broadening, Van der Waals broadening Stark broadening).

The deconvolution of the various contributions in the line broadened profile can be carried out based on the fact that, in many cases, the experimentally measured line profiles can be fitted with the Voigt function which is the convolution of the two functions: Gaussian and Lorentzian with the full width at half maximum (FWHM) given by w_G and w_L. The Voigt function can be represented through the combination of the Gauss and Lorentz components as follows [26]:

$$w_v = \frac{w_L}{2} + ((w_L/2)^2 + w_G^2)^{\frac{1}{2}}, \tag{3.23}$$

where w_V is the full half width at half maximum (FWHM) of the Voigt profile.

The broadening contributions with a Gaussian shape will lead to a profile with w_G determined as:

$$w_G = (\sum_i (w_{Gi})^2)^{1/2}. \tag{3.24}$$

Whereas for Lorentzian broadening components the final contribution to the line profile will also be Lorentzian, with FWHM determined as:

$$w_L = \sum_i w_{Li}. \tag{3.25}$$

Instrumental broadening is an important quantity in particular at low N_e and low emitter's temperature when line profile is narrow, i.e. when Stark broadening is small or comparable with other broadening mechanisms.

Natural broadening is a consequence of the Heisenberg uncertainty principle applied to the energies of the initial and the final states of the transition. It is the largest when one of the two states is dipole-coupled to the ground state. Even in this case, it is usually negligible (of the order of 10^{-4} nm). However, it may be of some importance for low electron density plasmas generated in low-pressure gas discharges.

Resonance broadening is manifested as perturbations of atomic levels resulting from the interaction between pairs of neutral atoms of the same kind (atom A + atom A). If r is the separation between the absorber and the perturbing particle, the change in energy induced by the collision is proportional to r^{-3}. When the perturber is of a different species (atom A + atom B), the interaction is called van der Waals interaction, and the energy perturbation is proportional to r^{-6}. Resonance broadening is important for the hydrogen lines in the spectra of F-type and later stars, while van der Waals broadening is important in the atmospheres of cool stars where both the absorbers and the perturbing particles are mainly

neutral. Both, resonance and van der Waals profiles have Lorentzian form. Apart from broadening, Van der Waals interaction shifts the spectral line in the red, approximately 1/3 of the FWHM [23]. Resonance and van der Waals broadening are usually negligible compared to Stark broadening within the range of N_e considered in this work (~ 10^{23} m^{-3} and higher). However, for atmospheric air plasmas with plasma densities $n < 10^{21}$ m^{-3} Van der Waals broadening can be significant.

The relative motion of an emitter to the detector leads to a shifted line. In plasma with gas temperature T_g the line profile due to the presence of Doppler effects can be well described by a Gaussian profile with a FWHM (nm):

$$w_D = (1/2)\lambda_0 \sqrt{\frac{8k_B T_g ln2}{m_a c^2}}, \quad (3.26)$$

where k_B is the Boltzmann constant, T_g – gas temperature, and m_a – the mass of the emitter.

Stark broadening results from Coulomb interactions between the radiator and the charged particles present in the plasma. Both ions and electrons induce Stark broadening, but electrons are responsible for the major part because of their higher relative velocities. The line shape can be approximated by a Lorentzian except at the line center where electrostatic interactions with ions cause a dip [113], [114]. Both the linear and the quadratic Stark effects are encountered in spectroscopy. However, only the hydrogen atom and H-like ions exhibit the linear Stark effect, whereas all other atoms exhibit the quadratic Stark effect. In the case of linear Stark effect, the relation between electron density and the line width is given by a simple relation [23]:

$$N_e = C(n_e, T_e) \times (w_S)^{3/2}, \quad (3.27)$$

where w_S is the «true» FWHM and the parameter $C(n_e,T_e)$ depends (only weakly) on N_e and T_e, which can normally be treated as being constant. The constant C for Balmer lines is available in the literature [23]. Usually, the first choice for the electron density determination is H_β line (with an error of 5%) [23] because of its large intensity and sufficiently large line broadening, which can be measured precisely using spectrometer of moderate resolution. The possibility of self-absorption in this case is relatively small. The second-best choice among the Balmer series is the H_Y line. The H_α line is suitable for electron densities with upper limit of ~ 10^{23} m^{-3} because at higher electron densities this strong line is quite susceptible to self-absorption, which severely distorts the line profile.

In the case of non-H-like atoms, where the quadratic Stark effect is dominant, the relation between the electron density and the line width [23] is:

$$w_S \approx 2[2 + 1{,}75 \times 10^{-4} N_e^{\frac{1}{4}} \alpha (1 - 0{,}068 N_e^{\frac{1}{6}} T^{-1/2})] \times 10^{-16} w N_e. \quad (3.28)$$

The first term in the brackets gives the contribution from the electron broadening, and the second term stems from ion broadening. Here *w* is the electron impact parameter at $N_e = 10^{22}$ m^{-3}, and α is the ion broadening parameter. These parameters can be found easily from the literature [23]. Since the second term after opening the brackets in (3.28) is normally small, so the expression reduces to

$$w_S \approx 4 \times 10^{-16} w N_e. \quad (3.29)$$

It has been reported in [29] that the electron density derived from the H_β and H_γ lines using (3.29) were in good agreement with each other, while the electron density estimated from the H_α line is not purely Stark broadened. The additional broadening might be due to the onset of self-absorption.

Therefore, in section 4.4 of this work, values of electron density were obtained using H_β, H_α lines from the following equations presented in [26]:

for H_β: $$N_e\ [m^{-3}] = 10^{23} \times (w_S[nm]/4{,}8)^{1{,}46808}, \quad (3.30)$$

for H_α: $$N_e\ [m^{-3}] = 10^{23} \times (w_S[nm]/1{,}098)^{1{,}47135}. \quad (3.31)$$

Electron density for Cu I 515.3 nm line is obtained from the linear interpolation from the table presented in [30], whereas the theoretical and experimental Stark widths of Cu I lines are listed for $N_e = 10^{23}$ m^{-3} and $T_e = 10000$ K.

3.4.4 Plasma coupling parameter

Natural plasmas and artificially-produced plasmas are both very diverse. Generally, they are classified according to their temperature and density, because the properties of a plasma depend mostly on these two parameters.

In particular, the density N_e and temperature T_e (T in case of LTE) define whether a plasma is ideal or not. In an ideal plasma, the particles are almost free, i.e. their movement is only weakly influenced by other

particles. In this case, the mean kinetic energy of particles is much higher than the mean Coulomb potential energy between them.

Knowing N_e and T_e for a given plasma, one can calculate its coupling parameter Γ, which quantifies its "degree of ideality". This parameter represents the ratio of the potential energy of Coulomb interaction at the mean inter-particle distance divided by the mean thermal energy of the charged particles in the plasma. It is defined by

$$\Gamma = \frac{Z^2 e^2}{4\pi\varepsilon_0 a k_B T_e}, \tag{3.32}$$

where Z is the charge of the particles (Z = 1 for hydrogen ions, for example), e – the elementary charge, ε_0 – the vacuum permittivity, and a – the mean inter-particle distance given by:

$$\mathrm{a} = \left(\frac{3}{4\pi N_e}\right)^{1/3}. \tag{3.33}$$

Therefore, it can be seen that

$$\Gamma \propto \frac{{N_e}^{1/3}}{T_e}. \tag{3.34}$$

The plasma is called:
- ideal if $\Gamma \ll 1$;
- weakly non-ideal if $\Gamma \leq 1$;
- strongly coupled if $\Gamma > 1$.

According to equation (3.34), ideal plasmas are characterized by a low density and a high temperature. It should be noted that Γ is linked to the Debye length λ_D, defined by

$$\lambda_D \doteq \sqrt{\frac{\varepsilon_0 k_B T_e}{e^2 N_e}}, \tag{3.35}$$

by the relation

$$\Gamma^{3/2} \propto \frac{1}{N_e \lambda_D^3}. \tag{3.36}$$

Therefore, one can see that, in an ideal plasma, a very large number of particles is contained in a Debye sphere. Nevertheless, the higher the number of particles in a Debye sphere, the less the particles interact with each other.

On the other hand, non-ideal and strongly coupled plasmas are dense and/or cold. In such plasmas, the inter-particle distance is short enough, and the particle velocity small enough, to produce significant electrostatic interactions between the charged particles. For a given particle, the microfields created by the others have a significant influence on it.

3.5 Conclusions

This chapter describes an experimental approach chosen for diagnostics of the underwater electric discharge plasma. The subject of this thesis originated from investigations of the electric spark dispersion of conducting materials in liquid media carried out in the National University of Life and Environmental Sciences of Ukraine. For the initial purpose of studying the biological functionality of nanomaterials obtained via impulse electric erosion processing, a setup for synthesis of colloidal solutions of ultra-disperse metal powders has been designed. Within the framework of this research, it is positioned as setup for multiple-pulse underwater electric discharge generation. Specifics of its operation are discussed in section 3.2. Such electric erosion systems use the volumetric electric spark erosion of conducting materials in liquid for a direct synthesis of colloidal solutions.

In order to build a complete comprehension of correlations between the electrophysical synthesis parameters and characteristics of the resulting NMs, it is crucial to understand the thermal destruction process occurring at the surface of granules. While the setup for the synthesis of metal colloids allows to study the underwater electric discharge plasma under ‘real’ operational conditions, it imposes certain amount of experimental difficulties in terms of the plasma diagnostics. These difficulties include variable discharge position and duration, resulting from the stochastic nature of the current passage through the granules, and from splitting of the input energy into multiple sub-pulses (micro-discharges). The impossibility of “isolation” of a discharge generated between two metal granules independently of the overall synthesis process also presents a challenge. Therefore, this setup can be used for the qualitative investigation of the multiple-pulse underwater electric discharge in relation to other aspects of the synthesis process, such as final properties of the synthesized NMs and their biological functionality.

Therefore, a complementary “academic” experimental apparatus was designed in in Laplace laboratory of University Toulouse III – Paul Sabatier in order to enable quantitative plasma characterization. Section 3.4 gives the overview of this so-called setup for single-pulse underwater electric discharge generation. Aiming to reproduce the behavior of two separately taken granules and discharge between them, this setup allows

to control certain parameters in order to enable more advanced plasma diagnostics. The chosen experimental configuration is intended as a compromise between "realistic" operation of the setup for synthesis of colloidal solutions and overcoming the constraints associated to plasma investigation. The main advantages of this setup are the fixed position of the discharge and ability to control certain parameters, such as, for instance, discharge duration.

Optical emission spectroscopy diagnostic was used for characterization of underwater electric discharge plasma. Section 3.4 presents the techniques employed for determination of the most crucial plasma parameters, such as temperature and electron density. Boltzmann plot method chosen for temperature estimations is used under assumption of plasma residing in the state of LTE. The validity of this assumption for the underwater electric discharge plasmas will be discussed later in Chapter 4, along with other experimental results.

The Stark broadening of the spectral lines for which it is the dominant broadening mechanism was chosen for the electron density estimations. Hydrogen Balmer limes, namely H_α and H_β were selected for calculations as the most sensitive lines to electron density variations. Additionally, broadening of copper spectral lines (Cu I at 515.3 nm) exposed to the quadratic Stark effect were also used to verify the obtained values of N_e.

Calculation of the plasma coupling parameter allows to estimate the degree of non-ideality of the underwater electric discharge plasma. The majority of natural and artificial plasmas are ideal. Besides extremely dense astrophysical objects, few non-ideal plasmas exist. From the physical point of view, their extreme properties make them particularly interesting to study. The physics of non-ideal plasmas is more complex, differing from “classical” plasma physics theories.

References to chapter III

[1] S. N. Zakharchenko, I. P. Kondratenko, A. Ye. Perekos, V. P. Zalutsky, V. V. Kozyrsky, and K. G. Lopatko, “Influence of duration of discharge pulses in a layer of iron granules on the sizes and a structurally-phase state of its electro-eroded particles,” *East Eur. J. Enterp. Technol.*, vol. 6, no. 5, pp. 66–72, 2012.
[2] K. G. Lopatko *et al.*, “Obtaining of metallic nanoparticles by plasma-erosion electrical discharges in liquid mediums for biological application,” *Ann. Wars. Univ. Life Sci. - SGGW Agric.*, no. 61, pp. 105–115, 2013.
[3] N. Taran *et al.*, “Colloidal Nanomolybdenum Influence upon the Antioxidative Reaction of Chickpea Plants (Cicer arietinum L.),” *Nanoscale Res. Lett.*, vol. 11, no. 1, p. 476, Dec. 2016.
[4] N. Taran, V. Storozhenko, N. Svietlova, L. Batsmanova, V. Shvartau, and M. Kovalenko, “Effect of Zinc and Copper Nanoparticles on Drought Resistance of Wheat Seedlings,” *Nanoscale Res. Lett.*, vol. 12, no. 1, p. 60, Dec. 2017.
[5] K. G. Lopatko, E. H. Aftandilyants, A. A. Scherba, S. M. Zakharchenko, and S. A. Yatsuk, “Setup for synthesis of colloidal solutions of ultra-disperse metal powders,” u200810312, 10-Dec-2009.
[6] A. A. Shcherba and S. N. Zakharchenko, “Stabilization and control of parameters of discharge impulses in volumetric electric spark systems for processing of heterogeneous conducting media,” *Works NASU Inst. Electrodyn. Top. Issue Electrodyn.*, pp. 30–35, 2001.
[7] A. A. Shcherba and N. I. Suprunovska, “Cyclic transients in the circuits of electric discharge installations taking into account the influence of magnitude and rate of discharge currents rise on resistance of electric spark load,” *Tech. Electrodyn.*, no. 2, pp. 3–10, 2018.
[8] A. A. Shcherba, A. D. Podoltsev, S. N. Zakharchenko, I. N. Kucheryavaya, N. I. Shevchenko, and N. I. Suprunovskaya, “Progress in spark-eroded particle production: Development of technological system for high-yield electrical-spark dispersion of metal granules in liquid,” *Tech. Electrodyn.*, no. 6, pp. 3–13, 2005.
[9] A. A. Shcherba, S. N. Zakharchenko, N. I. Suprunovskaya, and N. I. Shevchenko, “The influence of repetition rate of discharge pulses on electrical resistance of current-conducting granular layer during its electric-spark treatment,” *Tech. Electrodyn.*, no. 2, pp. 10–14, 2006.
[10] A. A. Shcherba, N. I. Suprunovskaya, and D. S. Ivashchenko, “Modeling of nonlinear resistance of electro-spark load for synthesis of discharge circuit of capacitor by time parameters,” *Tech. Electrodyn.*, no. 3, pp. 12–18, 2014.

[11] A. E. Berkowitz and J. L. Walter, “Spark erosion: A method for producing rapidly quenched fine powders,” *J. Mater. Res.*, vol. 2, no. 2, pp. 277–288, Apr. 1987.
[12] M. J. Price and F. L. Jones, “The electrical contact: the properties and rupture of the microscopic molten metal bridge,” *J. Phys. Appl. Phys.*, vol. 2, no. 4, pp. 589–596, Apr. 1969.
[13] W. Ren, H. Wang, C. Chang, S. Xue, and Y. Chen, “Experimental Investigation and Understanding of the Intermittent Molten Bridge Phenomena and Mechanism of Contacts With Superlow Opening Speed,” *IEEE Trans. Compon. Packag. Manuf. Technol.*, vol. 6, no. 3, pp. 418–423, Mar. 2016.
[14] S. Kharin, H. Nouri, and M. Bizjak, “Effect of Vapour Force at the Blow-Open Process in Double-Break Contacts,” *IEEE Trans. Compon. Packag. Technol.*, vol. 32, no. 1, pp. 180–190, Mar. 2009.
[15] D. L. Ederer, E. B. Saloman, S. C. Ebner, and R. P. Madden, “The use of synchrotron radiation as an absolute source of VUV radiation,” *J Res Natl Bur StandUS 79a*, vol. 761, 1975.
[16] G. Ulm, “Radiometry with synchrotron radiation,” *Metrologia*, vol. 40, no. 1, pp. S101–S106, Feb. 2003.
[17] J. C. De Vos, “A new determination of the emissivity of tungsten ribbon,” *Physica*, vol. 20, no. 7–12, pp. 690–714, 1954.
[18] R. D. Larrabee, “Spectral Emissivity of Tungsten†,” *JOSA*, vol. 49, no. 6, pp. 619–625, Jun. 1959.
[19] A. V. Lebid, “Spectroscopy of electric arc discharge plasma between Cu-based composite electrodes,” Taras Shevchenko National University of Kyiv, Kyiv (Ukraine), 2015.
[20] K. Bockasten, “Transformation of Observed Radiances into Radial Distribution of the Emission of a Plasma*,” *J. Opt. Soc. Am.*, vol. 51, no. 9, p. 943, Sep. 1961.
[21] W. Lochte-Holtgreven, *Plasma Diagnostics*. Moscow (USSR): Mir, 1971.
[22] H. R. Griem, “Validity of Local Thermal Equilibrium in Plasma Spectroscopy,” *Phys. Rev.*, vol. 131, no. 3, pp. 1170–1176, Aug. 1963.
[23] H. Griem, *Plasma Spectroscopy*. Moscow (USSR): Atomizdat, 1969.
[24] S. E. Frisch, *Spectroscopy of gas discharge plasma*. Leningrad (USSR): Nauka, 1970.
[25] H. R. Griem, *Spectral line broadening by plasmas*. New York: Academic Press, 1974.
[26] N. Konjević, M. Ivković, and N. Sakan, “Hydrogen Balmer lines for low electron number density plasma diagnostics,” *Spectrochim. Acta Part B At. Spectrosc.*, vol. 76, pp. 16–26, Oct. 2012.

[27] J. M. Luque, M. D. Calzada, and M. Saez, “Experimental research into the influence of ion dynamics when measuring the electron density from the Stark broadening of the Hα and Hβ lines,” p. 13.
[28] M. A. Gigosos and V. Cardeñoso, “New plasma diagnosis tables of hydrogen Stark broadening including ion dynamics,” *J. Phys. B At. Mol. Opt. Phys.*, vol. 29, no. 20, pp. 4795–4838, Oct. 1996.
[29] D. C. S. Beddows, “Application of laser-induced breakdown spectroscopy to in situ analysis of liquid samples,” *Opt. Eng.*, vol. 39, no. 8, p. 2248, Aug. 2000.
[30] N. Konjević and R. Konjević, “Stark broadening and shift of neutral copper spectral lines,” *FIZIKA*, no. 18, pp. 327–335, 1986.

CHAPTER IV
RESULTS AND DISCUSSION

4. Results and discussion

4.1 Introduction

This chapter aims to present the main results on the experimental characterization of the underwater electric discharge plasma carried out within the frame of this thesis.

Two different configurations of pulsed discharge in water are investigated: the electric discharge occurring between the metal granules of the operational unit in Kiev (see section 3.2 of Chapter 3) and the electric discharge generated between two tips of metal electrodes in setup designed in Toulouse (see section 3.3 of Chapter 3). All the results shown in this chapter have been obtained following the procedures and methodology described in section 3.4 of this work.

Second section of the chapter describes the standard procedures of the data treatment that must be performed before any calculations. This involves the sensitivity calibration of the optical system employed for the plasma emission registration, and the inverse Abel transformation allowing to operate with local values of the plasma emission, not the intensity integrated along the line of sight.

Third section shows typical spectra of the underwater electric discharge plasma, including the time- and spatially-integrated spectra registered using setup in Kiev, and time-integrated spatially resolved spectra registered with the setup in Toulouse. The effects of the electrode material and experimental current on the plasma emission are discussed.

Section four presents the first estimations of the plasma parameters, namely temperature and electron number density. Knowing these parameters allowed to verify that the LTE assumption is a reasonable hypothesis for plasma in studied configuration and conditions. Calculation of plasma coupling parameter constituted that the underwater electric discharge plasma is a cold and weakly non-ideal plasma.

Fifth section describes the procedure used for estimation of the sub-pulse duration in the operational unit in Kiev (i.e. duration of the discharge between two granules). This was performed in order to achieve more accurate correlation between the two studied experimental arrangements. Knowing this parameter allowed to adjust the schematics of the setup in Toulouse to match the value of the corresponding discharge duration.

Comparative and parametric investigation of plasma temperature and electron number density calculated for two different setups is presented in section 6. The time- and spatially integrated characteristics of the underwater discharge plasma are qualitatively and quantitatively

compared to the radial distribution profiles of plasma temperature and electron density.

The seventh section of this chapter presents results of the high-speed imaging of the underwater electric discharge generated between two metal electrodes. Analysis of the obtained images allowed to identify two stages in the discharge lifetime: plasma in liquid and plasma in bubble. Temporal size evolution of bubble and plasma depending on the experimental conditions, such as electrode material, type of the liquid, and discharge current, allowed to establish main correlations between these parameters.

Analysis of the electrode erosion behavior and energy analysis is discussed in the eighth section. The latter mostly focuses on the part of the energy transferred to the electrodes and its dissipation on different mechanisms resulting in metal ablation.

The general summary of the underwater discharge plasma physical properties, measured in this work is presented in the concluding Chapter 5.

4.2 Pre-treatment of data

4.2.1 Sensitivity calibration

The spectral sensitivity of the optical system used in Kiev (see Figure 3.5, Chapter 3) has been measured with tungsten ribbon and commercial halogen lamps [1]. The supplied filament current of the ribbon lamp varied within the range 21.87-22.12 A. According to manufacturer, the brightness temperature of the tungsten filament T_b lies within the values from 2176.78 to 2202.66 K. For calculations, the average brightness temperature of 2189.22 K was used. With that in mind, true temperature of the tungsten filament was derived from (3.9): T_{true} = 2410 K.

In case of halogen lamp, true lamp temperature is provided by manufacturer T_{true} = 2854 K, and lamp emission can be approximated to the electromagnetic radiation emitted by a blackbody.

Figures 4.1 and 4.2 show the spectra of tungsten and halogen lamps registered by the second channel of spectrometer covering the wavelength range 345-605 nm, respectively.

The spectra were interpolated within the set spectral range in order to smooth the dependences and take account of background noises, background emission was subtracted.

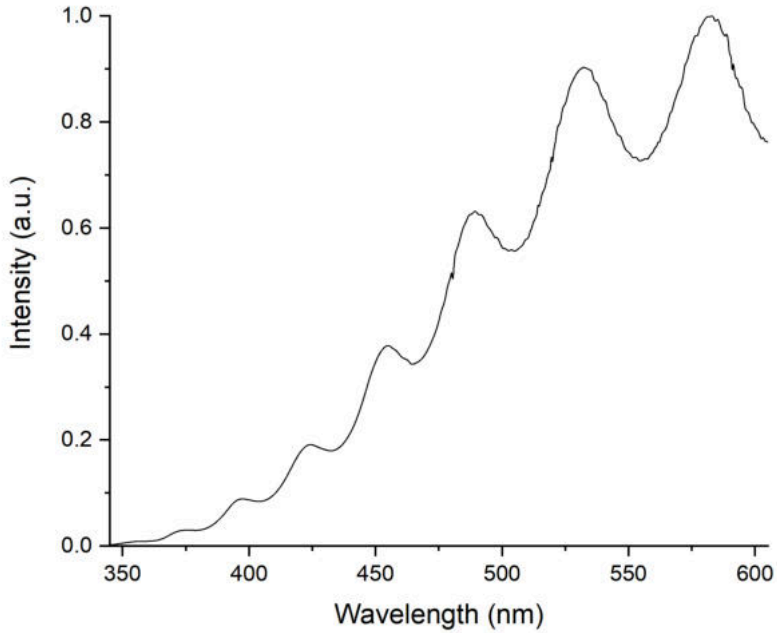

Figure 4.1: Registered emission of a tungsten ribbon lamp in spectral range λ = 345 – 605 nm.

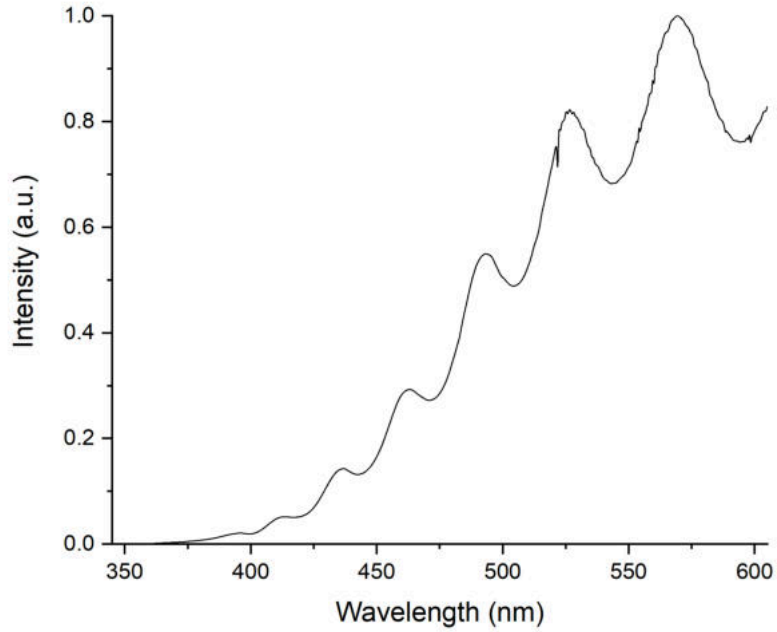

Figure 4.2: Registered emission of a commercial halogen lamp in spectral range λ = 345 – 605 nm [1].

Spectral response of the system S (see Fig. 4.3) was estimated as a ratio between tungsten emissivity and registered intensity of tungsten ribbon lamp emission.

In real laboratory experiments, it is not always reasonable to use the tungsten ribbon lamp every time for calibration of optical system prior to conduction of experiments. Therefore, application of a low-cost commercial halogen lamp would be more convenient. With that in mind,

emission of a halogen lamp can be calibrated using previously obtained spectral response of the optical system. Figure 4.4 shows calibrated intensity of a halogen lamp emission, calculated as a ratio of experimentally registered intensity of halogen lamp emission and spectral response obtained by using of the tungsten ribbon lamp.

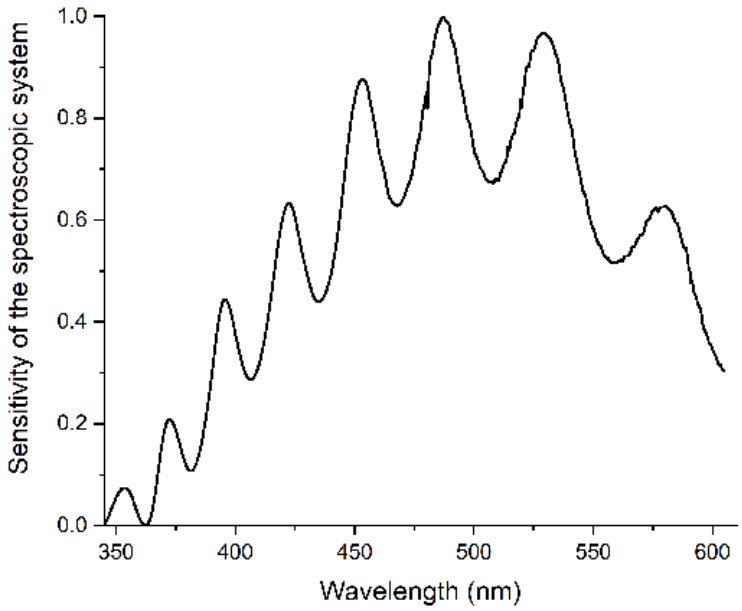

Figure 4.3: Normalized sensitivity of the spectroscopic system in spectral range λ = 345 - 605 nm measured with a tungsten ribbon lamp [1].

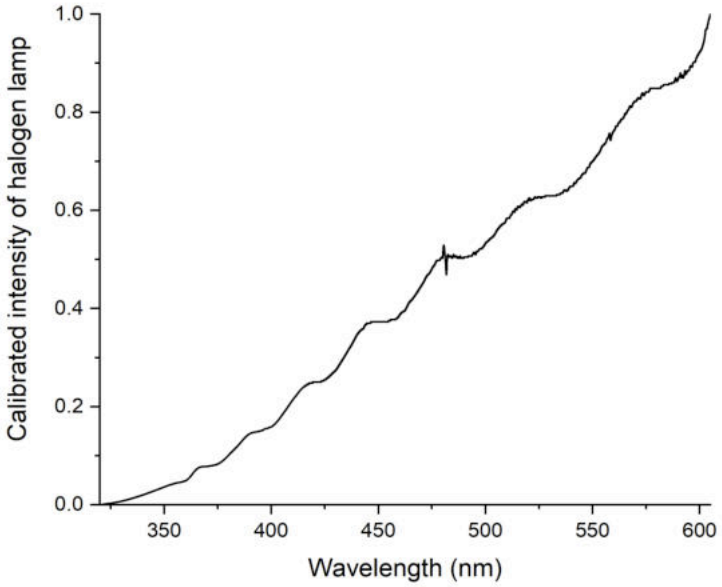

Figure 4.4: Intensity of a halogen lamp emission, calibrated with previously obtained spectral response of a spectroscopic system calculated using a tungsten ribbon lamp [1].

Similarly, the spectral sensitivity of the spectroscopic system used in setup in Toulouse (see Fig. 3.15, Chapter 3) has been measured with a tungsten ribbon lamp WI 17/G by OSRAM. However, unlike in the previous case, it is the color, not the brightness temperature that is provided by manufacturer for the nominal current and voltage values. The color temperature T_c of a light source is the temperature of an ideal black-body radiator that radiates light of a color comparable to that of the light source. The true temperature T of the tungsten strip can then be calculated from

$$\frac{1}{T} = \frac{1}{T_c} + \left(\frac{\ln\frac{L_\lambda(\lambda_1,T)}{L_\lambda^B(\lambda_1,T)} \div \frac{L_\lambda(\lambda_2,T)}{L_\lambda^B(\lambda_2,T)}}{C_2\left(\frac{1}{\lambda_1}-\frac{1}{\lambda_2}\right)}\right), \qquad (4.1)$$

where $L_\lambda^B(\lambda_1, T)$, $L_\lambda^B(\lambda_2, T)$ – blackbody radiance at λ_1 and λ_2, respectively; $L_\lambda(\lambda_1, T)$ and $L_\lambda(\lambda_2, T)$ – spectral radiance of tungsten ribbon at λ_1 and λ_2, respectively; C_2 = 1.439 cm·K = 0.01439 m·K.

The EMCCD camera of the spectrometer used in the optical system features 1024 x 1024 eXcelon3 EMCCD image sensor with 13 μm pixel size. The major limitation of this CCD array-based spectrometer is the relatively narrow spectral range (≈ 60 nm with a focal length of 750 mm and a grating with groove density of 300 g/mm) that can be covered during one acquisition of a spectrum.

The observed wavelength range is determined by the grating orientation which sets the wavelength of light incident on the central pixel of the CCD array detector. For example, setting the grating orientation of a spectrometer to “630 nm” directs the photons of wavelength 630 nm to fall upon the central pixel of the CCD array detector (e.g., the 512th pixel for a CCD with 1024 pixels). The pixels on both sides of the central pixel respond to wavelengths in the range 600 nm to 660 nm (given a grating with a groove density of 300 g/mm) To obtain another range of wavelengths, the grating has to be rotated and another spectrum collected.

Therefore, to measure a spectrum over a larger range of wavelengths it is necessary to measure multiple partial spectra each associated with a different central wavelength. The multiple partial spectra then have to be spliced into a single extended spectrum. The splicing algorithm used for the acquisition, spectral correction and calibration was suggested in [2].

The partial spectra (PS) of the tungsten ribbon lamp emission were collected with the integration time set to 20 ms. The choice of this exposure time can be explained by the short exposure time of the experiments: the calibration should be close to the recording conditions of

the experiment. The response should be linear with integration time; however, some differences may occur if ratio is too high (e.g. 100 µs for the experiment, and 100 ms for the calibration).

The central wavelength of the partial spectra were calculated to cover the specified wavelength range with an overlap between the partial spectra. The central wavelengths were set sequentially in ascending order, the partial spectra acquired, and the accumulated partial spectra were displayed for preliminary evaluation before transfer to a file. Figure 4.5 shows the 15 partial spectra from the calibrated reference tungsten ribbon lamp used.

The number above each partial spectrum gives its place in the sequence of accumulation. The lamp emission was registered over the entire wavelength range from 450 nm to 900 nm.

The splicing of the partial spectra was carried out pair-wise starting with the partial spectra at lowest wavelengths. The same splicing procedure was carried out for all pairs of partial spectra. The splicing was accomplished by joining the partial spectra at a wavelength in the midpoint of the overlap region and adjusting the intensity of one of the partial spectra to match the intensity of the other.

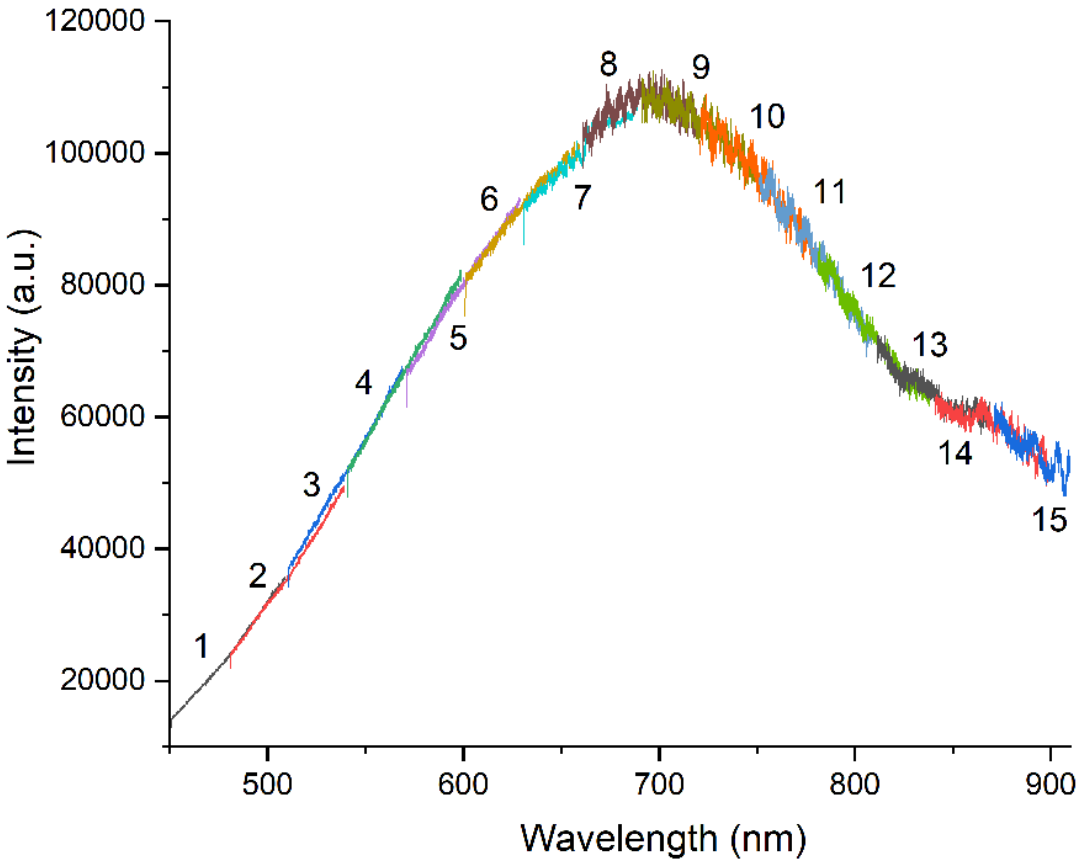

Figure 4.5: Partial spectra of tungsten ribbon lamp emission registered in separate acquisitions (number on the plot denotes the reference number of corresponding spectrum).

Similar to sensitivity shown in Fig. 4.3, spectral response of the spectroscopic system presented in Fig. 3.15 of Chapter 3 was calculated as a ratio between tungsten emissivity and registered intensity of tungsten ribbon lamp emission. The resulting curve can be seen in Fig. 4.6.

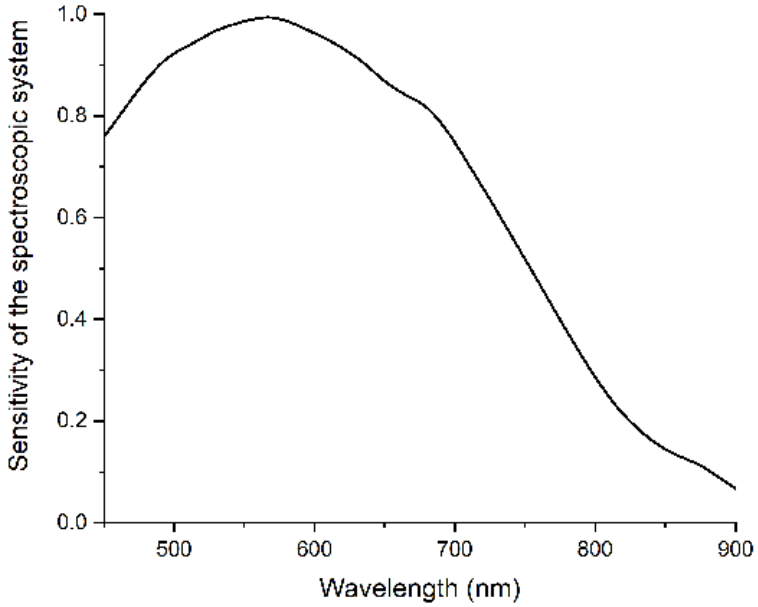

Figure 4.6: Normalized sensitivity of the spectroscopic system over a spectral range of λ = 450 - 900 nm measured with a tungsten ribbon lamp.

The spectral sensitivity is maximum between 500 and 650 nm, and falls off below 500 nm and above 700 nm, mainly due to the quantum efficiency of the EMCCD camera. Generally, for all spectrograph-detector configurations, the optical system is sensitive to light emitted roughly between 300 and 1000 nm.

4.2.2 Abel inversion

In experiments for single-pulse underwater electrical discharge plasma investigation, image of the plasma was focused on the entrance slit of the spectrometer by using an optical system shown in Fig. 3.15 (see Chapter 3). Emitted light was detected by using the EMCCD camera placed at the exit of spectrometer. In this way, a 1024 x 1024 data matrix was obtained in which the wavelength distributed along the horizontal axis while the line-of-sight light coming from different lateral positions in the plasma distributed along the vertical axis (Fig. 4.7).

Method of an inverse Abel transform described in [3] requires one to divide radius into N equidistant parts. The number of the parts can be chosen in an arbitrary fashion. In this work, N = 10 was chosen for calculations. Table 4.1 presents a matrix of corresponding a_{jk} coefficients. The size of the a_{jk} coefficients matrix increases with increase of N, as N^2.

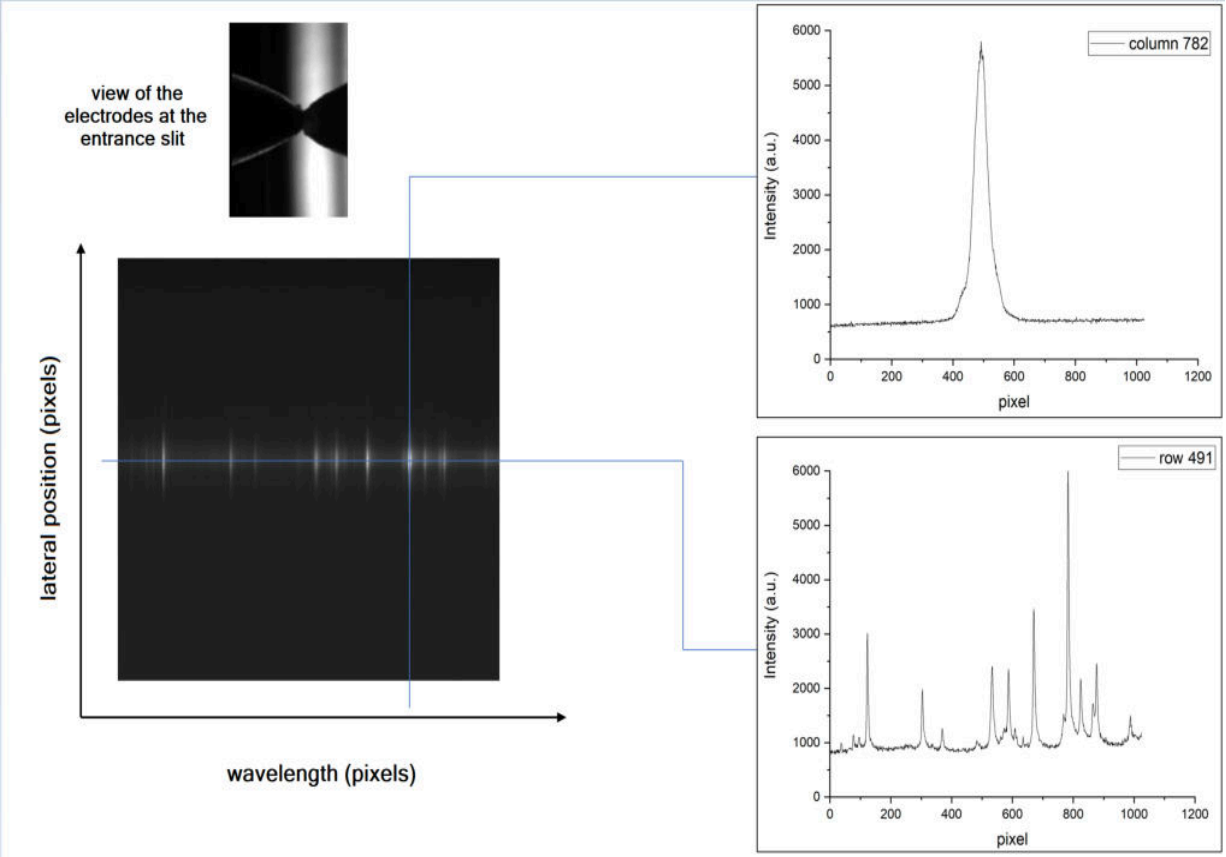

Figure 4.7: Description of a measurement made with single pulse setup with the EMCCD camera.

Usually, only relative values are of interest, and r_0 in (3.15) can be put equal to unity. However, if the absolute values of ε are wanted, the introduced readings $(I_{obs})_k$ must be absolute and the computed values should afterwards be divided by r_0.

It should be noted that since the spatial derivative $I'_{obs}(x)$ in (3.14) enters the inversion it is obvious that the results are very sensitive to noise and errors in the measured radiance I(x). Unfortunately, the errors in the derivative accumulate over the integration interval [r, r_0], and the resulting uncertainty is most severe on the axis r = 0. Hence, appropriate smoothing of the data is essential for the quality of the inversion.

As an example, Figure 4.8 shows a spatially-distributed observed intensity (curve 2) and calculated local values of plasma emission (curve 1) for a spectral line of atomic copper at wavelength 456.1 nm emitted by plasma between copper electrodes at 400 A.

Table 4.1. Coefficients a_{jk} for transforming observed radiances into radial distribution [3]

k	j = 0	j = 1	j = 2	j = 3	j = 4
0	7.625972	0.463415	0	0	0
1	-5.800962	3.6063	0.323954	0	0
2	-0.584698	-2.951278	2.653847	0.263182	0
3	-0.339474	-0.182401	-2.058371	2.198581	0.227286
4	-0.197038	-0.214891	-0.138728	-1.666071	1.918418
5	-0.126877	-0.134649	-0.162498	-0.112322	-1.434904
6	-0.088278	-0.092042	-0.105026	-0.133815	-0.095626
7	-0.064907	-0.066934	-0.073682	-0.087694	-0.115548
8	-0.04825	-0.04941	-0.053181	-0.060617	-0.074289
9	-0.044883	-0.045711	-0.048354	-0.053365	-0.061987
k	j = 5	j = 6	j = 7	j = 8	j = 9
0	0	0	0	0	0
1	0	0	0	0	0
2	0	0	0	0	0
3	0	0	0	0	0
4	0.202929	0	0	0	0
5	1.723807	0.18502	0	0	0
6	-1.278587	1.578512	0.171141	0	0
7	-0.084151	-1.164009	1.464693	0.159977	0
8	-0.100408	-0.072617	-1.070717	1.381857	0.251406
9	-0.076986	-0.104895	-0.086465	-1.03729	0.984158

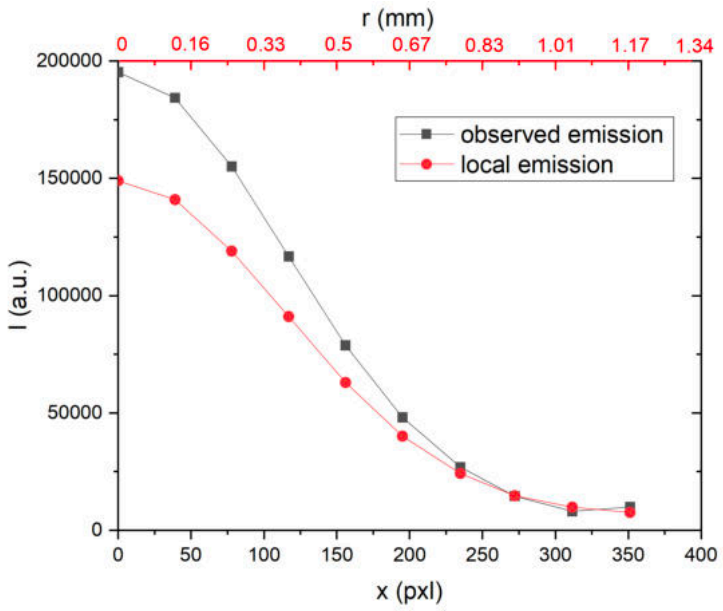

Figure 4.8: Radial profiles of observed intensity (2) and local values of plasma emission (1) for spectral line Cu I 465.1 nm

4.3 Emission of the underwater electric discharge plasma

4.3.1 Time- and spatially-integrated spectra

The example of optical spectra emitted by the underwater electric discharge plasma generated between copper and molybdenum granules are shown in Figures 4.9 and 4.10. As described before, spectrometer used for the spectroscopic diagnostics (see section 3.2.3, Chapter 3) allows to register plasma emission in four different spectral ranges: 200 – 390 nm, 350 – 600 nm, 450 – 850 nm and 605 – 1000 nm (ranges 1, 2, 3 and 4, respectively). With the main purpose to demonstrate how the various experimental parameters affect the plasma emission, most of the spectra presented in this section are those falling within the third spectral range (i.e. visible spectrum).

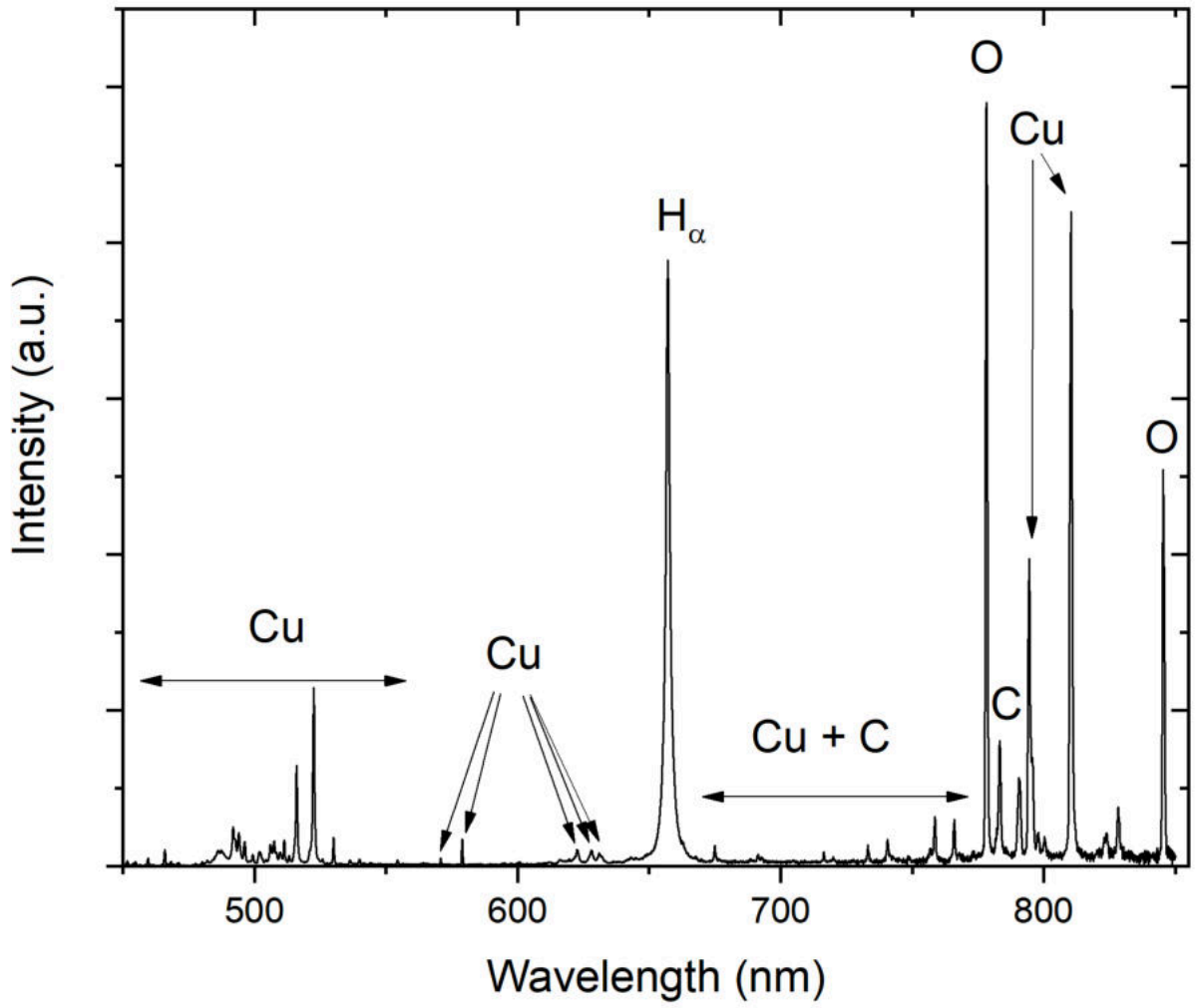

Figure 4.9: Typical emission spectrum of the underwater discharge plasma generated between copper granules: the peak pulse current of about ~ 520 A.

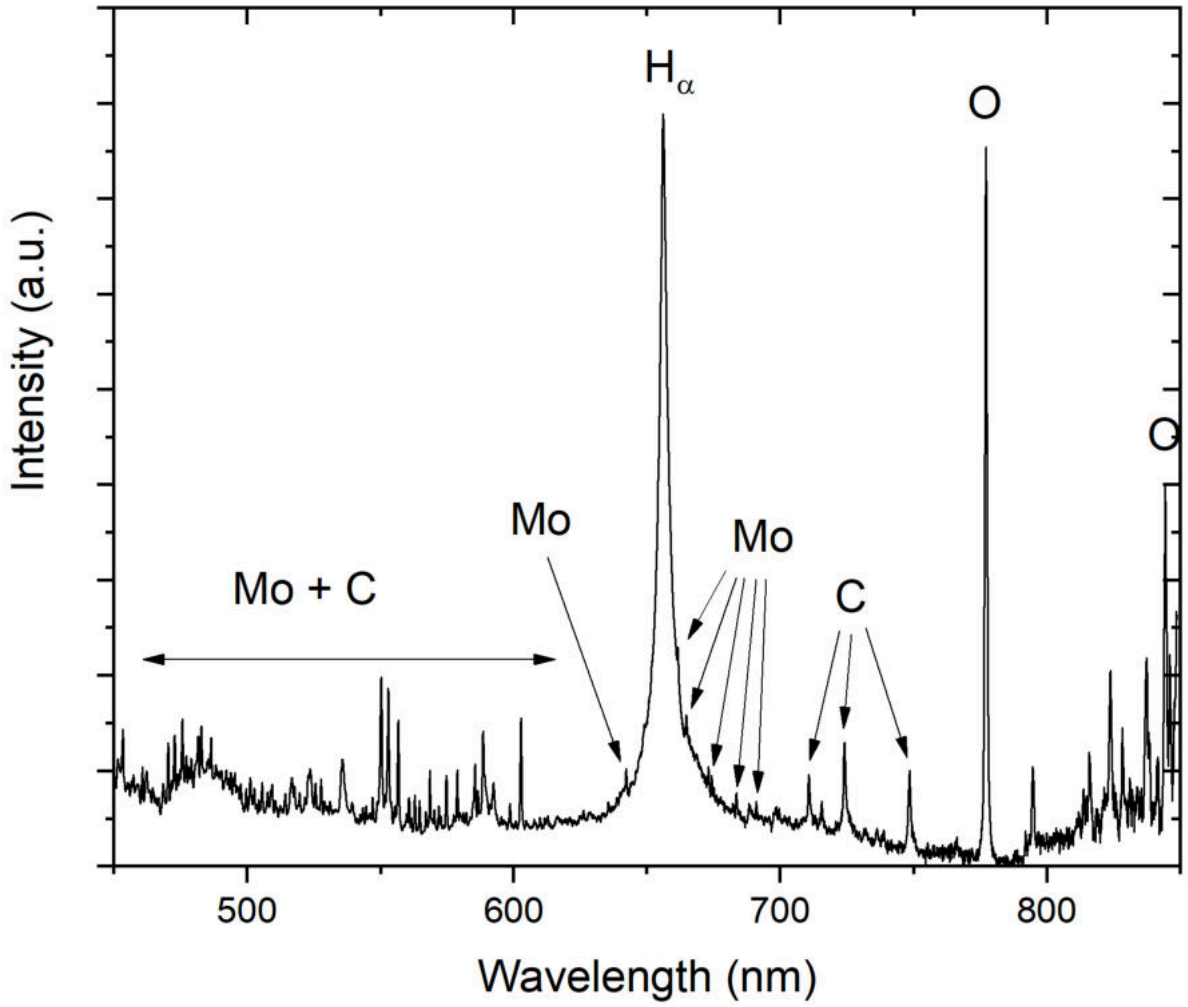

Figure 4.10: Typical emission spectrum of the underwater discharge plasma generated between molybdenum granules: the peak pulse current of about ~ 520 A.

As can be seen from the spectra above, the dominant line is the Balmer H_α line emitted by atomic hydrogen, which comes from the cracking of the water molecules. Some lines of atomic carbon from the main electrodes of the discharge chamber are also visible. Since the hydrogen source is the dielectric, hydrogen atoms are present everywhere in the plasma. Although the H_α line is dominant, the remaining Balmer series lines such as H_β (486.13 nm) or H_γ (434.05 nm) are not observed. This will be discussed in Chapter 5.

The plasma is contaminated by impurities from the electrode material: atomic copper (Fig. 4.9), and atomic molybdenum (Fig. 4.10).

The fact that all observed lines are atomic lines and that no ionic lines are visible, is a first indication that the plasma is cold. The excitation of ions requires indeed higher energy than the excitation of atoms. Furthermore, atoms and ions of metallic elements are easily excited, more easily than those of non- metallic elements. For example, the excited state energies of visible transitions of Cu atoms and of Cu^+ ions are respectively

around 6 and 16 eV (from the ground state of atoms and ions respectively), but for C atoms and for C+ ions they are respectively around 8 and 22 eV. Thus, the absence of ionic lines of copper or molybdenum indicates clearly that the plasma temperature is low (for the pressure around atmospheric). The energy balance at the cathode is strongly related to the electrode material properties [4]. This will be discussed in more detail later, in section 4.8.

The low excitation energy of metallic atoms explains the abundance and the relatively high intensity of their lines in the underwater discharge plasma emission. However, it should be noted that this abundance does not mean that a large amount of metal is present in the plasma. In electric arcs for example, the light emission is dominated by metallic lines already with a contamination of a few percent of metal. It is also well known that metallic impurities strongly cool down plasmas in gas-metal arc welding (GMAW) processes, because of their strong radiation. Thus, a quantitative estimation of the metallic contamination in the underwater electric discharge plasma is a prospective for the future research.

An intense broadband continuum radiation is also observed (see Fig. 4.11) in case of molybdenum granules. The origin of this radiation remains unclear. Water can also contribute to the continuum.

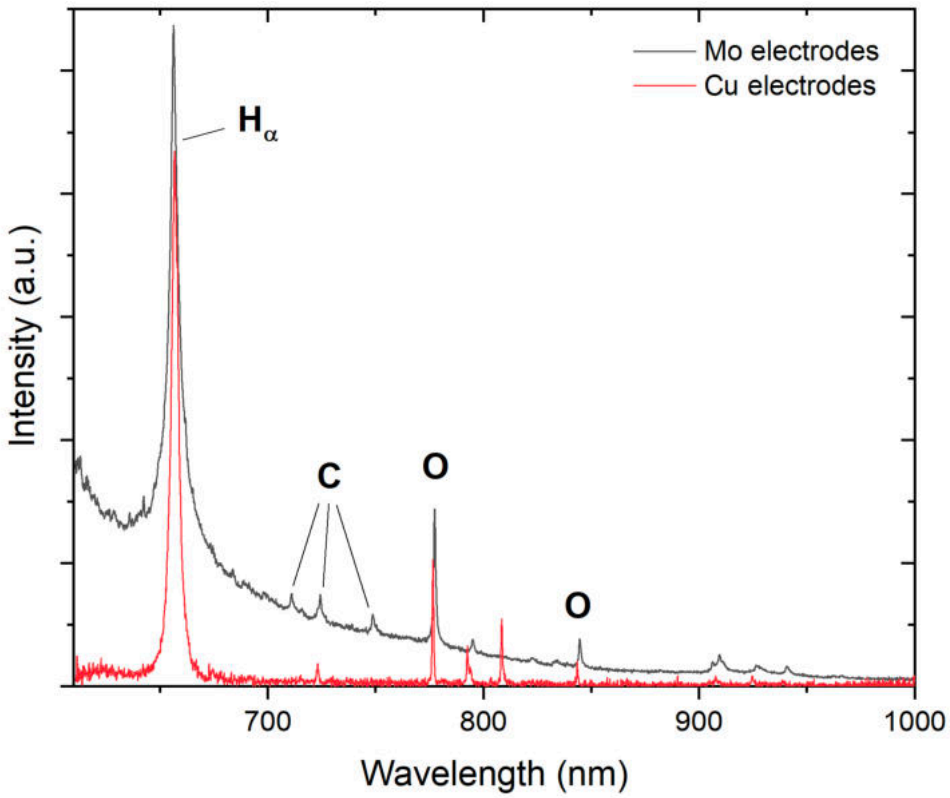

Figure 4.11: Continuum radiation in the emission spectrum of the underwater discharge plasma generated between molybdenum and copper granules: the peak pulse current of about ~ 520 A (fourth spectral range of the spectrometer).

Blackbody fit do not match well with these measurements. Thus, a continuous emission by heated electrodes or metal particles is unlikely. It is more probable that this continuum is due to free-bound transitions, i.e. radiation emitted during recombination processes. Free-free radiation is also another plausible source. Since molecules generally emit a broadband spectrum, molecules or fragments of molecules from the water may also participate to the continuum.

The emission spectra obtained with different discharge currents are presented in Figure 4.12.

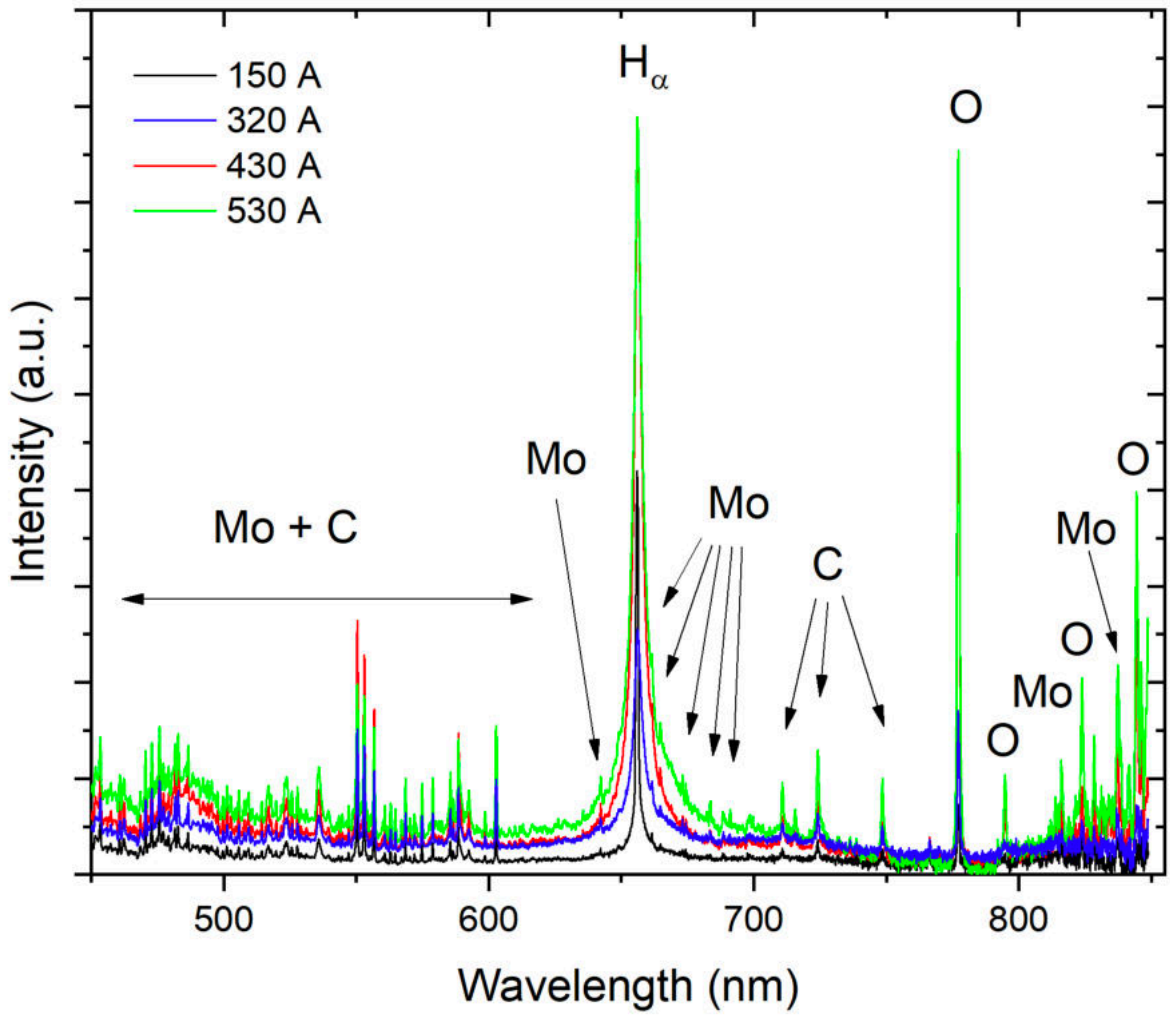

Figure 4.12: Emission spectrum of the underwater discharge plasma generated between molybdenum granules: effect of the peak pulse current.

Increasing the discharge current strongly enhances the intensity of the emitted light. But from the spectroscopic point of view, the increase in the current has little effect. It only increases the intensities of the metallic lines and continuum. This can be understood by considering that discharges with high current causes higher removal rate of material than low current discharges.

4.3.2 Spatially-resolved time-integrated spectra

Setup in Toulouse (see section 3.3 of Chapter 3) allows to register spatially-resolved spectra of the underwater electric discharge plasma emission.

Figures 4.13 and 4.14 show examples of spatially-resolved spectra of discharge generated, respectively, between copper and molybdenum electrodes along the vertical axis. The intensities of the spectra located in the center are higher, because the plasma is brighter in this region.

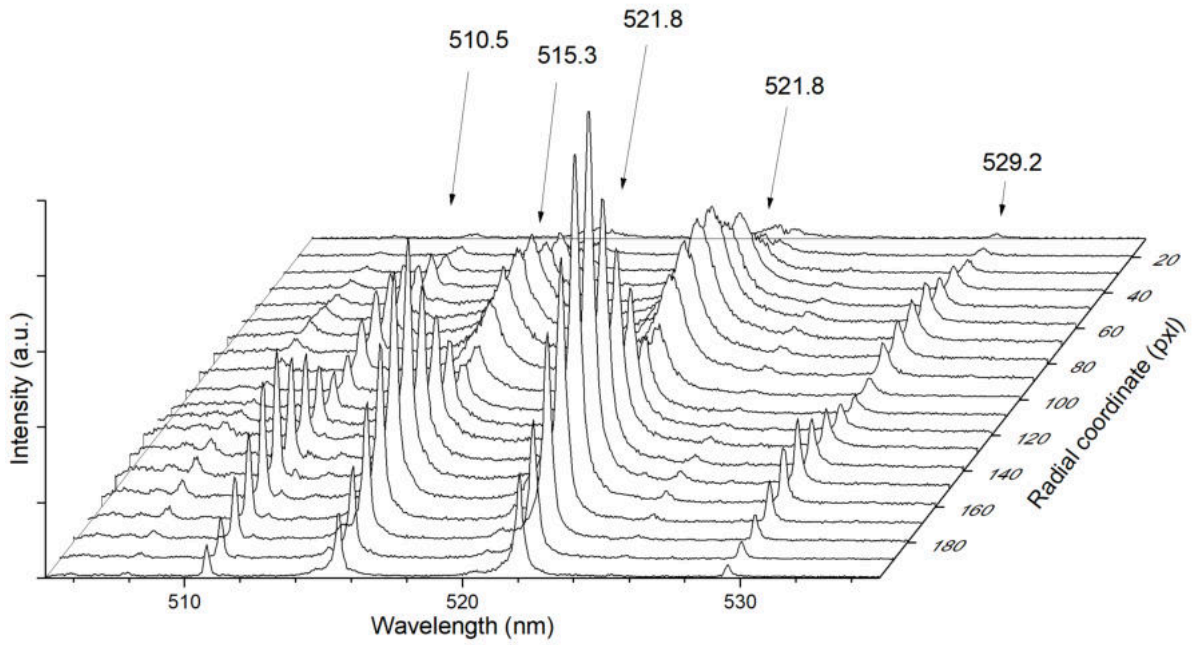

Figure 4.13: Spatially-resolved spectra of underwater discharge plasma emission: copper electrodes in tap water, peak pulse current of 400 A (exposure time 50 µs, grating 300 g/mm, spatially integrated data).

Note that the spatially-resolved axis in Fig. 4.13 and 4.14 is not calibrated in real distance, but simply shown as number of the row of the registered data matrix. In order to make the conversion into real distance, one has to know the spatial resolution of the system which depends on the optical arrangement. After each set of measurements (the successive acquisition of the 20-25 spectra), the electrodes have to be changed due to their erosion, and the optical arrangement has to be re-aligned. Thus, an exact calibration for each set of measurements is time-consuming and has not been systematically done. The spatial resolution was nevertheless estimated around 4.3 µm/pixel for all the measurements presented here.

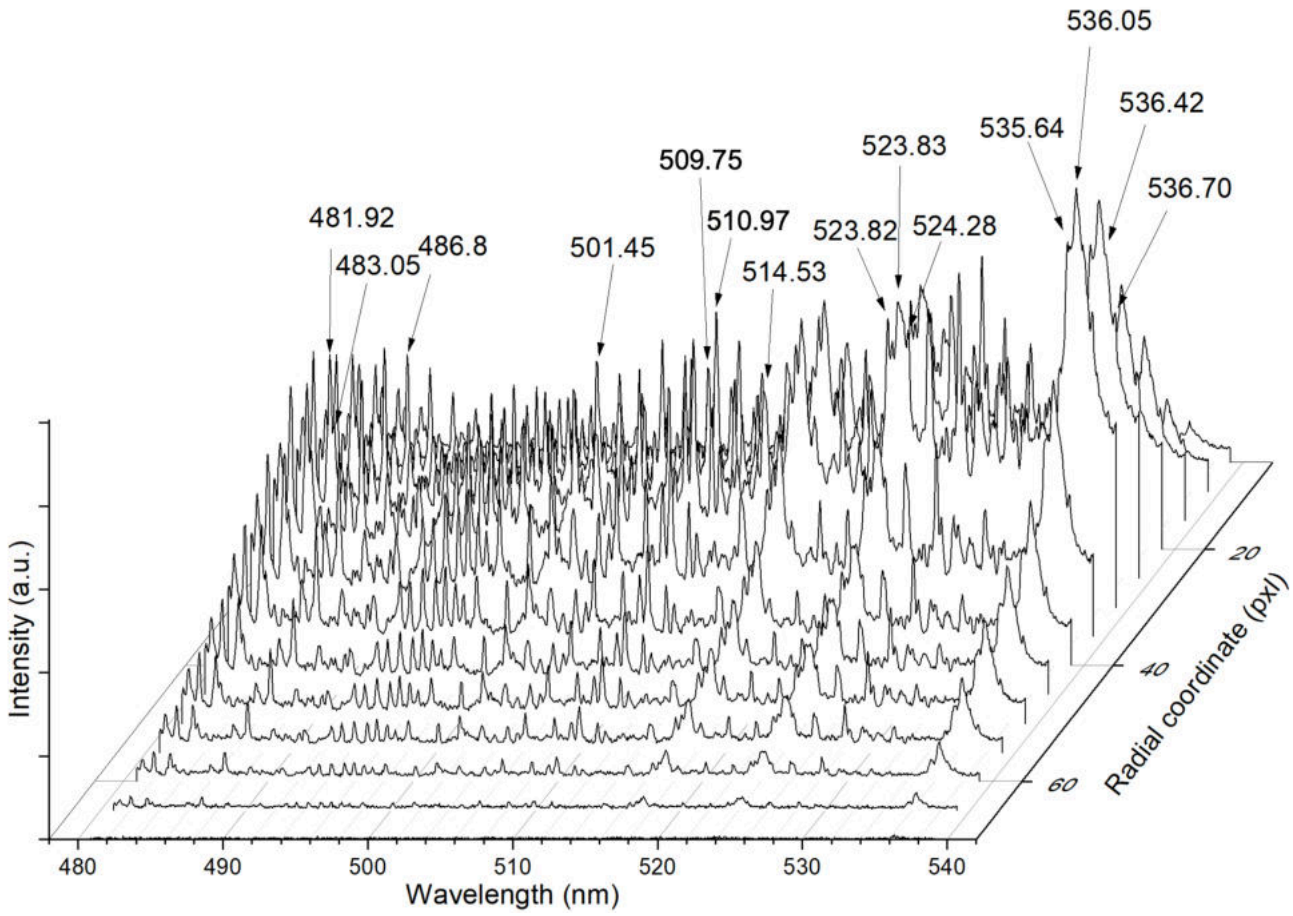

Figure 4.14: Spatially-resolved spectra of underwater discharge plasma emission: molybdenum electrodes in tap water, peak pulse current of 400 A (exposure time 50 μs, grating 300 g/mm, spatially integrated data).

Similar to the case displayed in Fig. 4.11, on can see that there is an intense continuum radiation in emission of plasma generated between the molybdenum granules in Fig. 4.14.

Figures 4.15 – 4.16 present the spatially-resolved spectra of the underwater electric discharge plasma generated between copper electrodes in non-purified (tap) and purified water at 600 A current. The increase of the discharge current results in increase of the emission intensity of atomic copper spectral lines. This is an expected behavior.

As for the effect of the type of the liquid, some remarkable differences can be observed in plots 4.15 and 4.16. Namely, the presence of the intense continuum radiation and broadening of spectral lines in Fig. 4.16. This correlates with the fact that plasma is much brighter when generated in deionized water, both for copper and molybdenum. Spatially-resolved spectra of the copper and molybdenum lines used for temperature calculations will be shown and discussed in section 4.6 of the present chapter, along with the radial temperature profiles calculated from them. The same goes for the spatially-resolved H_α spectra, along with the corresponding electron density profiles (see section 4.7).

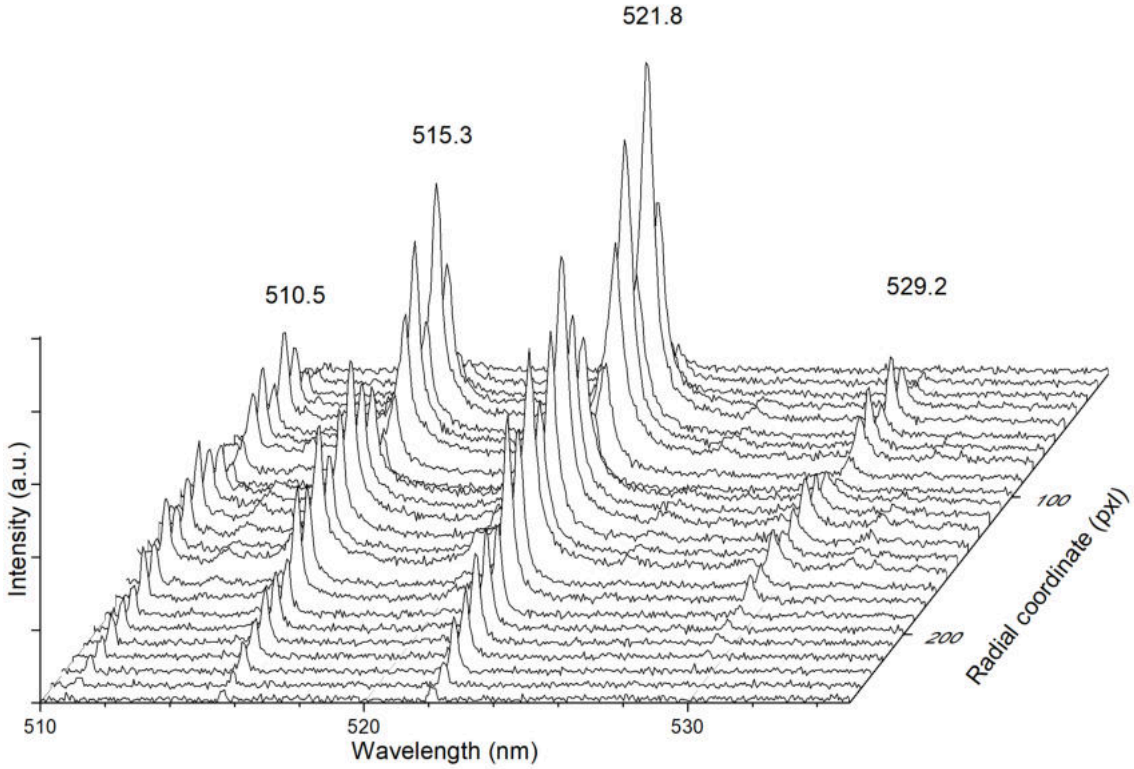

Figure 4.15: Spatially-resolved spectra of underwater discharge plasma emission: copper electrodes in tap water, peak pulse current of 600 A (exposure time 50 µs, grating 300 g/mm, spatially integrated data)..

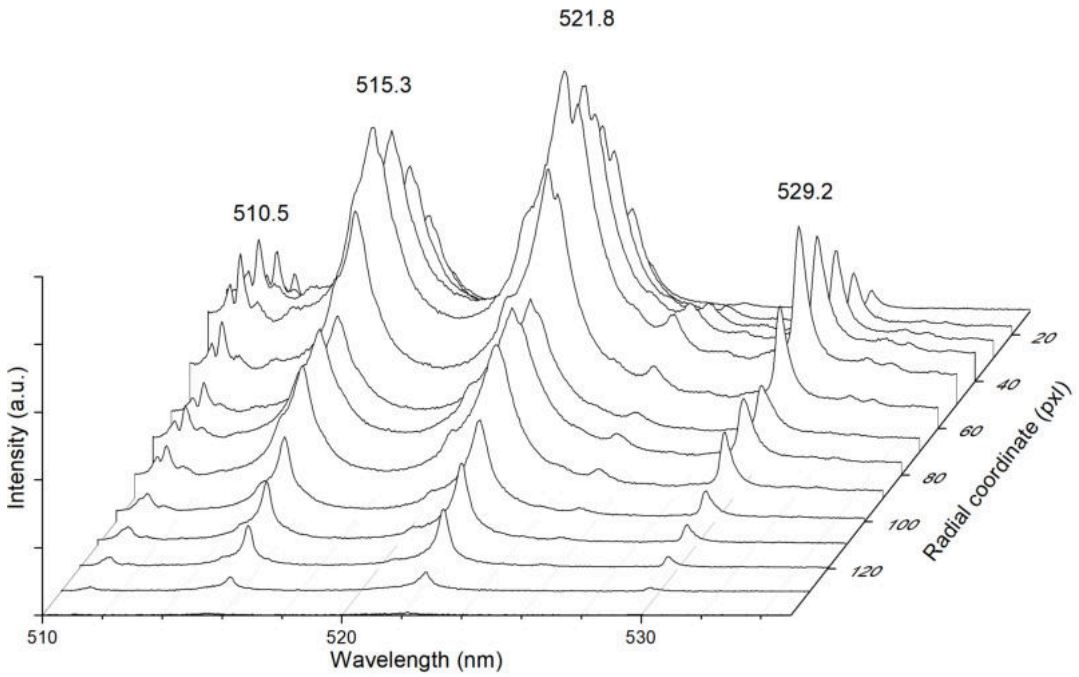

Figure 4.16: Spatially-resolved spectra of underwater discharge plasma emission: copper electrodes in deionized water, peak pulse current of 600 A (exposure time 50 µs, grating 300 g/mm, spatially integrated data)..

4.4 First estimations of plasma parameters

4.4.1 Time- and spatially-integrated values of temperature and electron number density

First estimations of the underwater pulsed discharge plasma parameters were carried out for the operational unit in Kiev (see section 3.2 of Chapter 3) [5]. As explained earlier, due to the experimental configuration and available diagnostics equipment, only the time- and spatially-integrated values of plasma temperature and electron density can be studied.

This section presents plasma parameters obtained only for discharge generated in the copper granules. Since copper has been thoroughly studied before, the spectral lines of neutral copper and their spectroscopic data recommended for diagnostics of plasma with addition of copper can be easily found in the literature.

The emission spectrum of the discharge between copper granules registered with the third channel of spectrometer (spectral range 3: 450 – 850 nm) is shown in Figure 4.17.

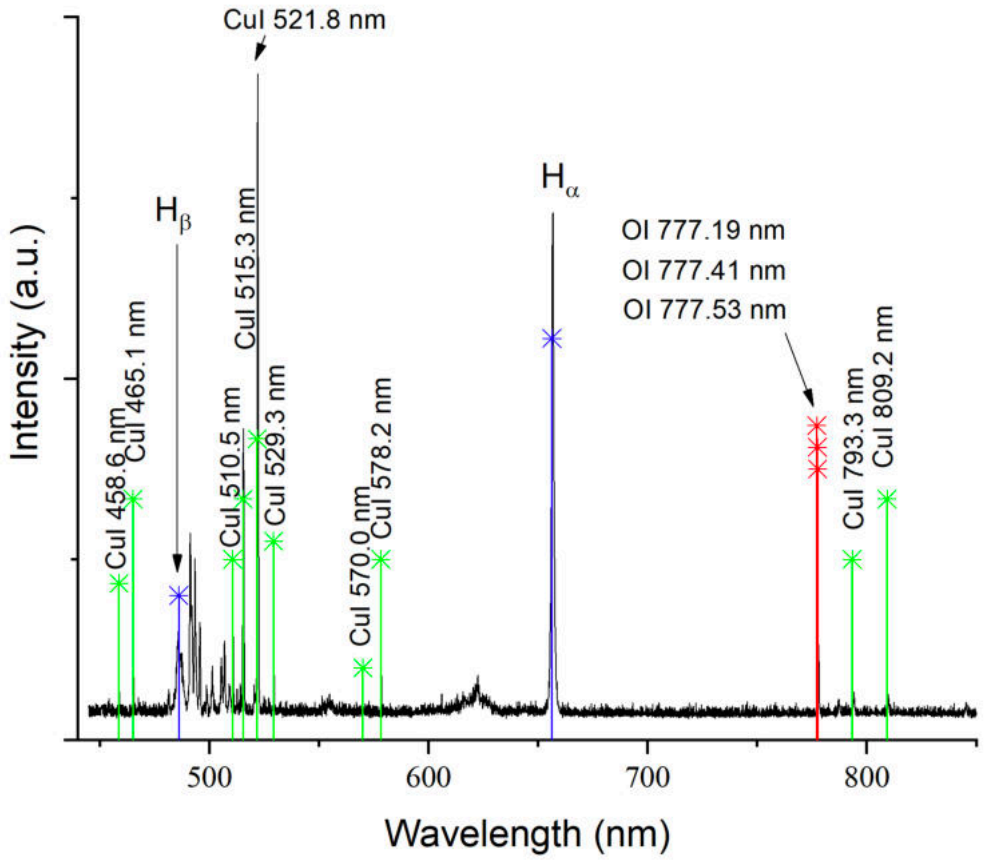

Figure 4.17: Plasma emission spectrum of the underwater electric pulsed discharge between copper granules: spectral range 450 – 850 nm [5].

It should be noted that while electrical parameters during the registration of the plasma emission resided within the range of setup's operational values (see Table 3.1 of Chapter 3) they were not recorded. This is due to the fact that these measurements were carried out primarily for the purposes of quantitative plasma characterization, not for establishment of a correlation between the parameters.

The excitation temperature of copper atoms in plasma was determined by Boltzmann plot technique (see section 3.4.3 of Chapter 3) using spectral lines of neutral copper. Table 4.2 summarizes the Cu I spectral lines and their spectroscopic constants used for the temperature calculations. The data was taken from [6].

Table 4.2. Selected spectral lines of copper atom (wavelength λ corresponding to transition from upper level i to lower j, statistical weights g, energy level E and oscillator strength f), max. uncertainty on $g_i f_{ji}$ – 18% [6]

λ, nm	Transition i ⟶ j	g_j	g_i	E_j, eV	E_i, eV	$g_j f_{ji}$
465.1	$4s5s'^4D \longrightarrow 4s4p'^4P^0$	10	8	5.07	7.74	1.4218
510.5	$4p^2P^0 \longrightarrow 4s^{22}D$	6	4	1.39	3.82	0.0197
515.3	$4d^2D \longrightarrow 4p^2P^0$	2	4	3.79	6.19	1.6466
521.8	$4d^2D \longrightarrow 4p^2P^0$	4	6	3.82	6.19	1.9717
570.0	$4p^2P^0 \longrightarrow 4s^{22}D$	4	4	1.64	3.82	0.0057
578.2	$4p^2P^0 \longrightarrow 4s^{22}D$	4	2	1.64	3.79	0.0130
793.3	$5s^2S \longrightarrow 4p^2\ P^0$	2	2	3.79	5.35	0.4246
809.2	$5s^2S \longrightarrow 4p^2P^0$	4	2	3.82	5.35	0.6120

Figure 4.18 presents the Boltzmann plot obtained for emission spectrum shown in Fig. 4.17. Therefore, the value of an excitation temperature averaged across the registered spectra was found to be 11600 ± 1930 K.

The spectroscopic data used for temperature calculation are known with uncertainties up to 18% (concerning transition probability). Errors come also from data treatment and overlapping of copper lines. Considering in addition experimental standard deviation, error bars have been set to 20% in Fig. 4.18. The value found is a moderate temperature, but consistent with previous studies (for instance, electron temperatures obtained for EDM plasmas [7] and other similar plasmas [8]).

Electron number density of plasma was determined from the half-width of H_α line following the procedure described in section 3.4.3 of Chapter 3. After the application of Voight fitting algorithm to the line profile (see Fig. 4.19), the Stark width w_S was obtained from the experimental

value of FWHM with corrections made for instrumental and Doppler contributions.

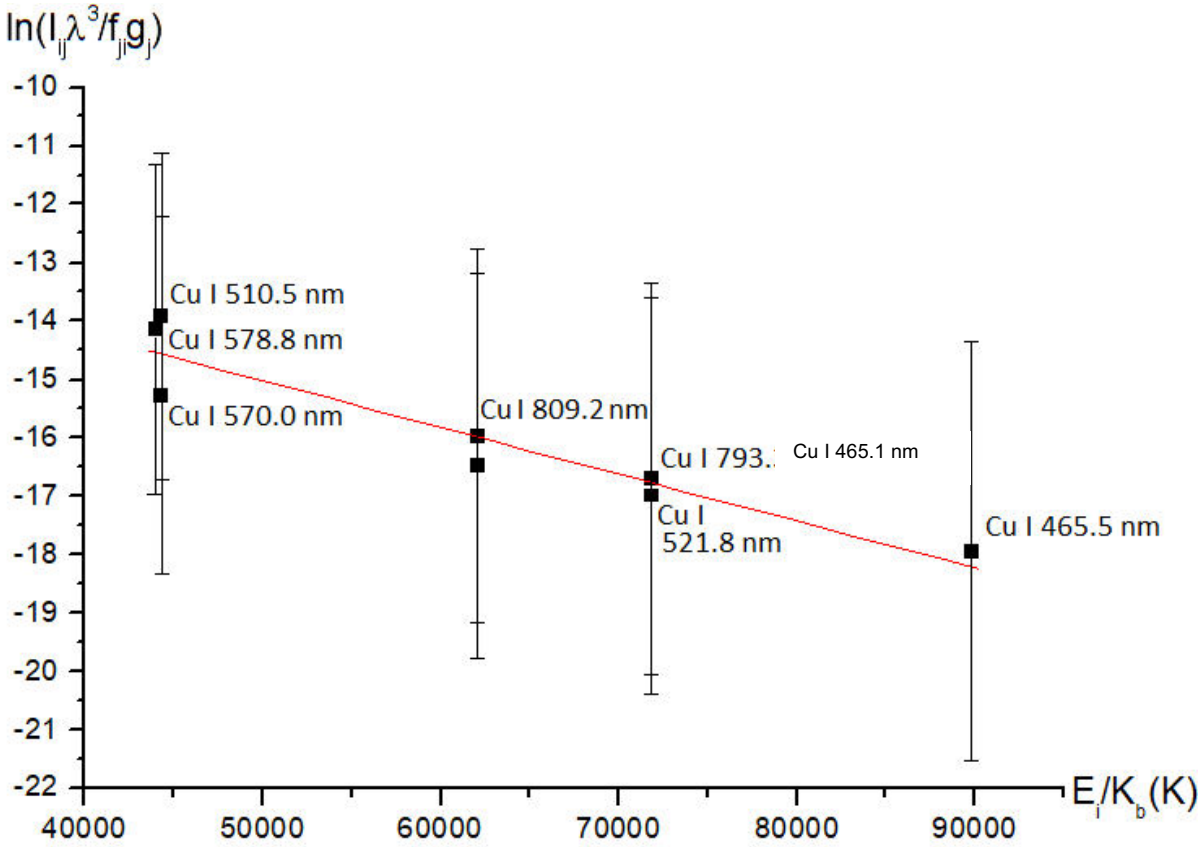

Figure 4.18: Boltzmann plot for neutral copper lines used for estimation of the spatially-integrated value of the plasma temperature [5].

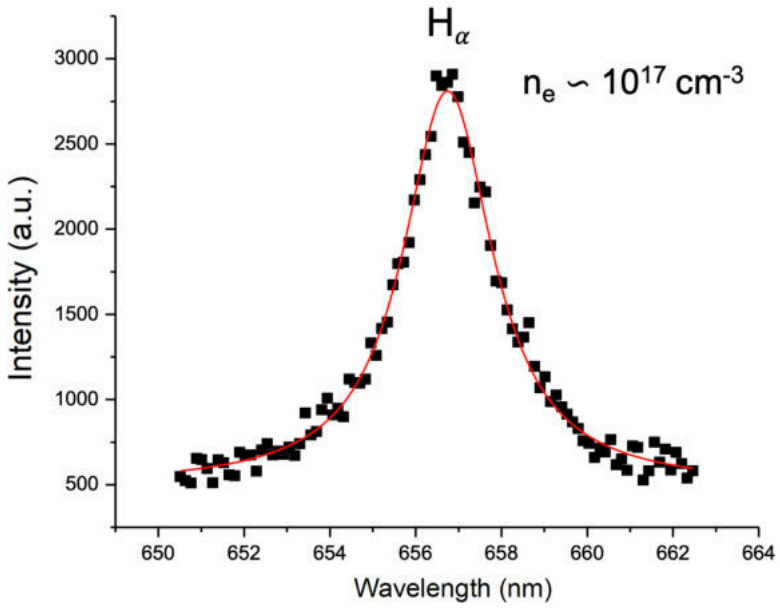

Figure 4.19: Voight fit of the H_α line profile [5].

The values of coefficients $C(n_e,T_e)$ (see formula (3.27) in Chapter 3) for Stark broadened hydrogen lines were calculated by interpolation from tables of half-widths presented by Griem [9]. With a H_α FWHM of almost 3 nm, the order of magnitude of the electron density is 10^{17} cm^{-3} (or 10^{23} m^{-3}), and corresponding average value of the electron density was found to be $4.3 \cdot 10^{17}$ cm^{-3}. This first estimation is in a good agreement with other studies on discharges in liquids (see section 2.5 of Chapter 2). The pressure imposed by the liquid surrounding the plasma is the cause of its high density.

4.4.2 Plasma non-ideality and the validity of LTE assumption

Knowing the values of electron number density and temperature allows to identify whether or not the considered plasma is ideal (see section 3.4.4 of Chapter 3). The first estimations of the underwater electric discharge plasma parameters show that the average temperature is around 11600 K, and average electron density of 10^{17} cm^{-3}. Thus, the typical coupling parameter of such plasma found from expressions (3.35) and (3.36) is around $\boldsymbol{\Gamma \simeq 0.25}$. This means that the underwater electric discharges produce plasmas with moderate temperatures and electron densities which are **weakly non-ideal**.

According to equation (3.35), the typical Debye length of such plasmas is around 12 nm. The mean inter-particle distance a is around 8.5 nm (equation (3.33)). Thus, a Debye sphere is containing roughly only one particle. This is another illustration of the plasma non-ideality.

Figure 4.20 shows the classification of the main types of natural and artificial plasmas in a log density−log temperature diagram. Ideal, weakly non-ideal and strongly coupled plasmas can easily be distinguished in such a log-log diagram, because Γ iso-contours are straight lines. It can be seen that underwater electric discharge plasma falls into the same position as the EDM and high-pressure arc plasmas.

As mentioned before, the Boltzmann plot method is based on the assumption of LTE. It is not an obvious assumption, especially for non-ideal plasmas such as in our case, where Coulomb interactions are comparable to thermal interactions. The evolution to the equilibrium state by thermal interactions is thus perturbed by Coulomb effects. However, due to the high plasma density, one can assume that the numerous collisions between particles thermalize them rapidly.

A density criterion giving the validity of LTE can be derived theoretically [10]. A plasma of temperature T is in complete LTE if its electron density N_e is higher than:

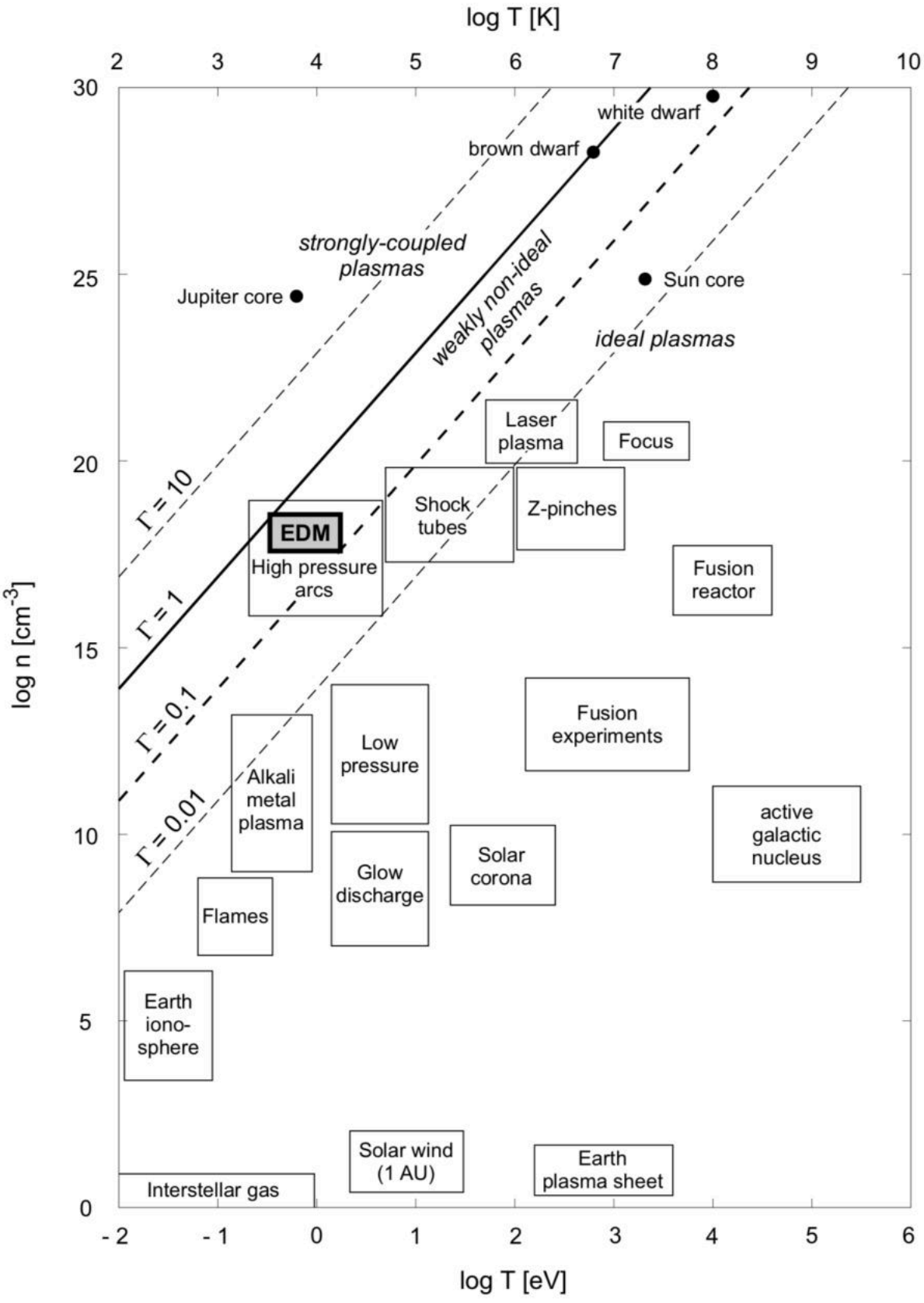

Figure 4.20: Classification of plasmas according to their density and temperature (adapted from [7]).

$$N_e \geq 9.2 \cdot 10^{17} \cdot \sqrt{\frac{k_B T}{E_H}} \cdot \left(\frac{E_2 - E_1}{E_H}\right)^3 \text{ [cm}^{-3}\text{]} \quad (4.2)$$

where E_H is the ionization energy of the hydrogen atom, E_1 the ground state energy of the atoms present in the plasma and E_2 the energy of their first excited state. For instance, according to this criterion, a hydrogen plasma at 1 eV is in LTE if $N_e \geq 8.6 \cdot 10^{16}$ cm−3.

If one assumes that the underwater electric discharge plasma is mainly composed by hydrogen (which is not the case), its electron density is sufficiently high for the assumption of LTE to be reasonably accepted. Therefore, even if it has not been measured separately, the ion temperature can be estimated to be of the same order as the electron temperature.

4.4.3 Spatially-resolved electron number density

First estimations of the underwater pulsed discharge plasma parameters performed using setup in Toulouse (see section 3.3 of Chapter 3) include time-resolved high-speed imaging, investigations of the electrical characteristics, and corresponding optical emission spectroscopic data [11]. However, this section presents and discusses only the spatially-resolved electron density calculations. Analysis of the high-speed imaging and electrode erosion will be addressed in sections 4.7 and 4.8, respectively. It should be noted that no estimations of the plasma temperatures were made for this set of experiments. This is due to fact that at the moment of measurements spectral sensitivity calibration has not been performed yet, making any possible temperature calculations of low relevance. However, the assumption was made that this does not affect the line shapes.

Analogically to the experiments discussed in 4.4.1, the underwater pulsed electric discharge was generated between copper electrodes in non-purified water by applying a pulsed voltage of ~ 120, 150, 180 and 220 V, corresponding to the values of current 450, 660, 800 and 1000 A. The average duration of the discharge was 320 – 360 μs. Copper is selected mainly to allow and simplify the comparison between results obtained for two different experimental setups.

Following the procedure described in section 3.4.3 of Chapter 3, radial distributions of the electron density were estimated from the analysis of profiles and widths of H_α and H_β hydrogen lines (registered with the 300 lines/mm and 1800 lines/mm gratings, respectively), and neutral copper 515.3 nm line (registered with the 300 lines/mm grating), exposed to the Stark mechanism of spectral lines broadening.

Profiles of the selected lines were fitted with a Voigt function, whereas the Gaussian part is presented by deconvolution of the instrumental and Doppler broadening, giving the average values of 0.02-0.04 nm, and the Lorentzian part of the profile is considered to be only the Stark FWHM.

Line shapes and Voigt fit of the studied lines are shown in Figure 4.21. Figure 4.22 presents the radial profiles of electron number density for 1 mm diameter plasma. It can be seen in Fig. 4.21 c that there is a large uncertainty concerning the maximum of the line (between 875 a.u. and 975 a.u.) and, therefore, the FWHM. Higher maximum leads to FWHM larger than 0.6 nm and, therefore, larger electron density, but the Voigt fit was performed according with the fixed Gaussian "contribution" into the line's width, which resulted in the profile shown in Fig. 4.21c.

The error bars in Fig. 4.22 correspond to the estimated error of 20% on Ne calculation.

Calculation of the electron density shows (Fig. 4.22) disagreement the values of N_e calculated using the Cu I 515.3 nm, H_α and H_β lines. While N_e determined from the widths of Cu I 515.3 and H_α line are of the same order of magnitude for all the studied current regimes, values of N_e obtained from the width of H_β line are by two orders of magnitude lower for cases of I = 660 and 800 A, and by one order of magnitude lower for the case of I = 1000 A.

Normally, the use of the H_α line can lead to the following problems:

- it could present a non-negligible self-absorption and it is necessary to evaluate how it affects the line broadening;
- it has a strong broadening by ion dynamics, an effect that can be evaluated by using some computational methods recently developed which allow us to simulate the profiles of the spectral lines [12].

Taking into account the fact that self-absorption effects were not considered in the present study, one can conclude that the inconsistency between the values of N_e is caused by overestimation of the H_α line width. However, at the same time, values of N_e obtained from H_α line and Cu I 515.3 nm line show good agreement leading to the conclusion that the suggested value of the electron temperature T_e = 10000 K and $N_e \sim 10^{23}$ m^{-3} are close to the experimental values of the electron density and electron temperature in our discharge.

It was shown in [13] that the expression connecting the Stark width of Balmer lines with N_e, which has been derived from the Kepple–Griem theory (KG) [14], in case of use of H_α line, overestimates the electron density by about 80% with respect to the N_e obtained from the H_β line.

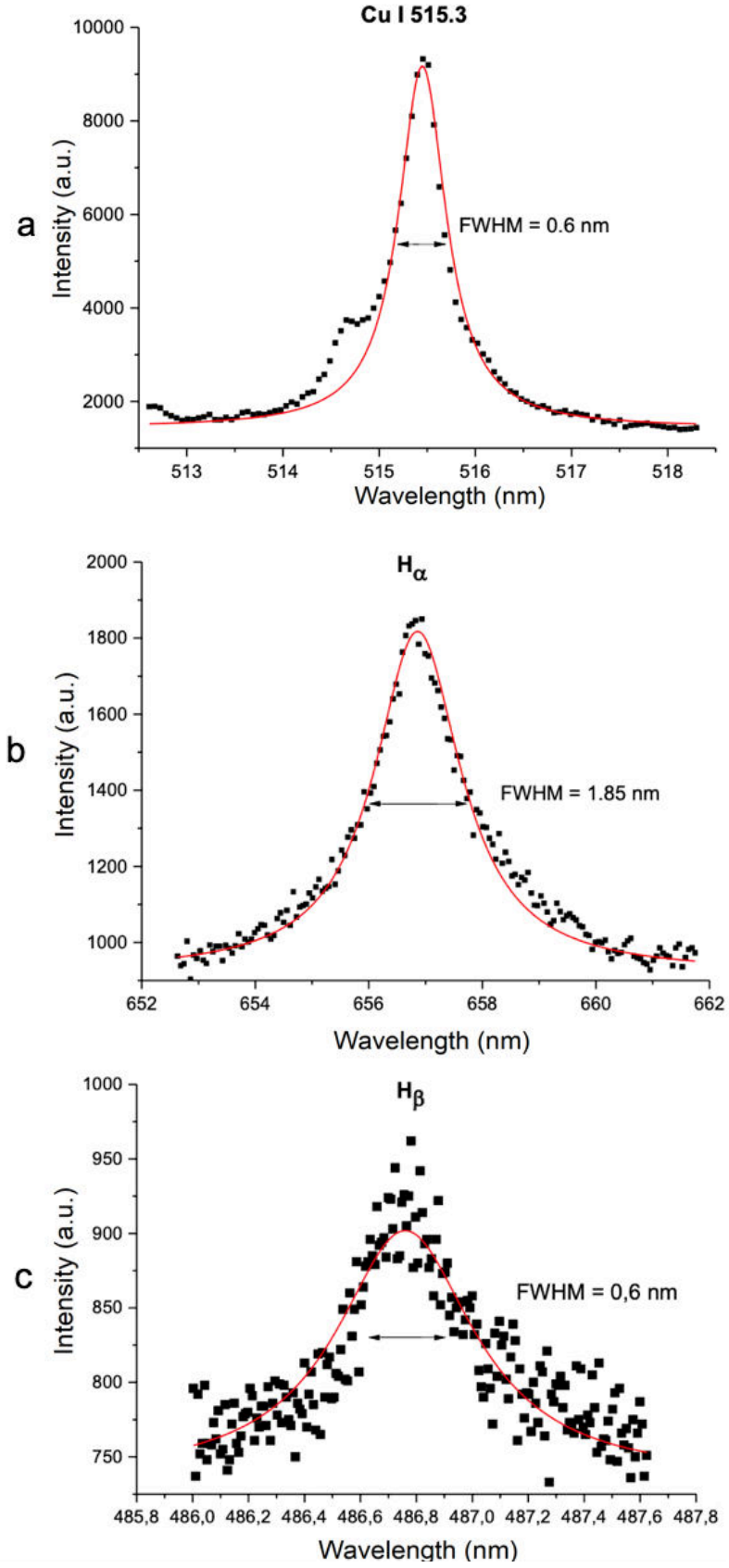

Figure 4.21: Line profiles and Voigt fit of the registered lines for current regime I = 1000 A, radial position r = 0 mm (discharge axis): (a) Cu I 515.3 nm line; (b) H_α line; (c) H_β line [11].

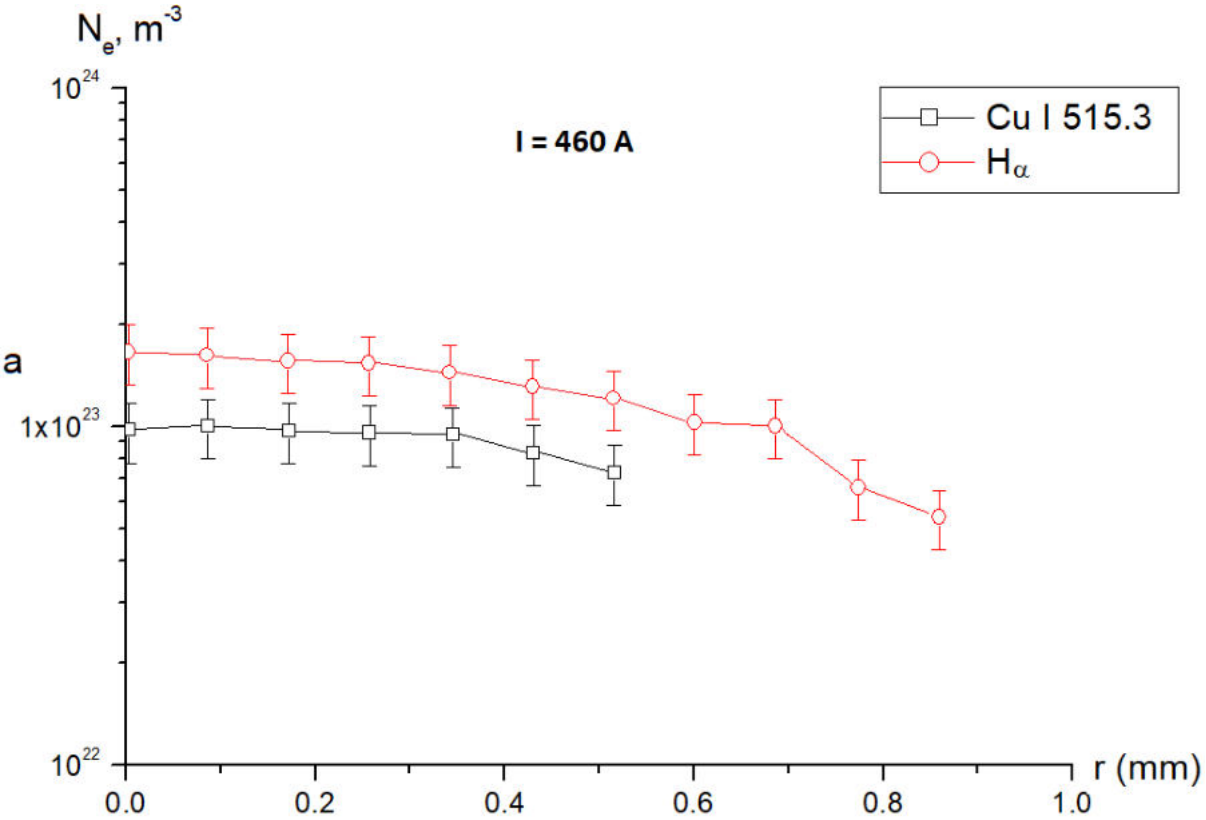
a
N_e, m^{-3}
10^{24}
$1x10^{23}$
10^{22}
I = 460 A
Cu I 515.3
H_α
0.0
0.2
0.4
0.6
0.8
1.0
r (mm)

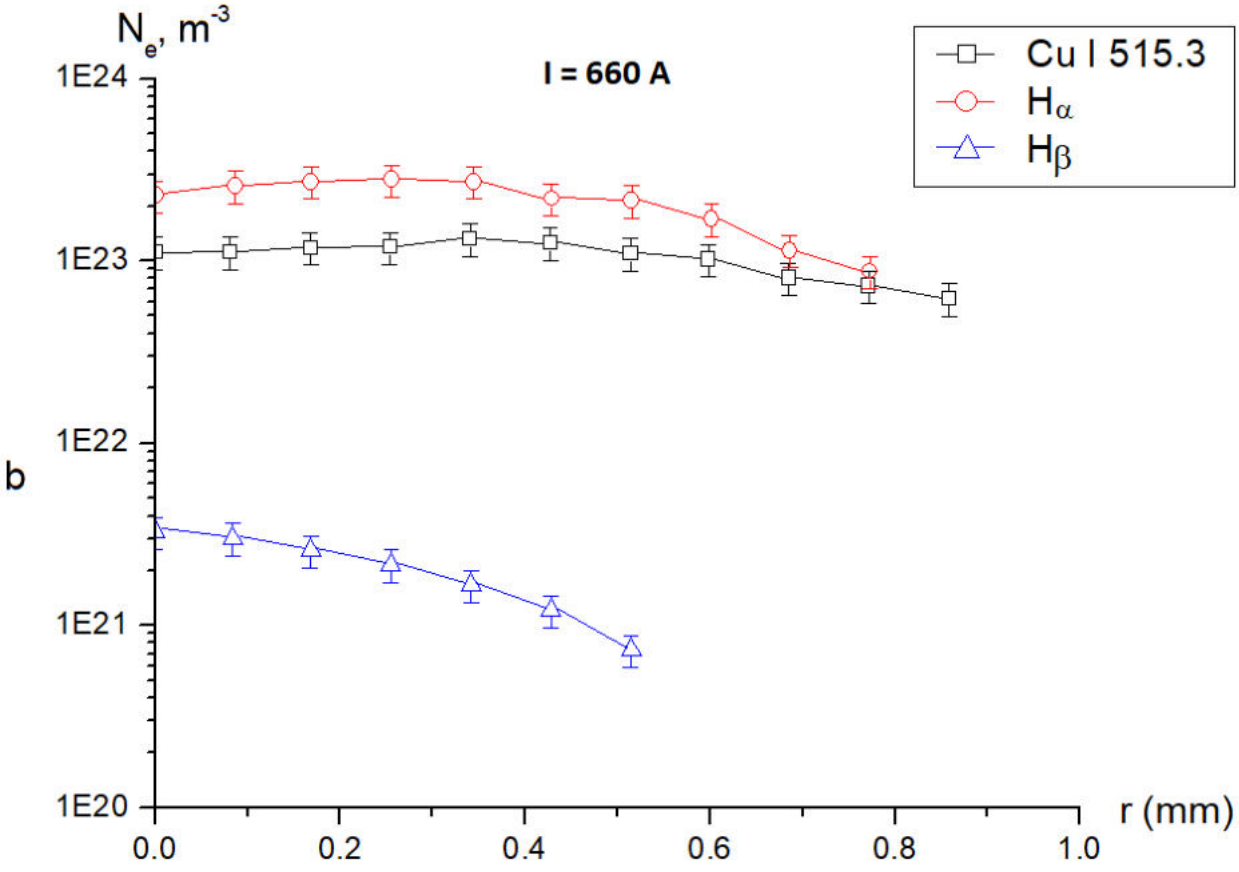
b
N_e, m^{-3}
1E24
1E23
1E22
1E21
1E20
I = 660 A
Cu I 515.3
H_α
H_β
0.0
0.2
0.4
0.6
0.8
1.0
r (mm)

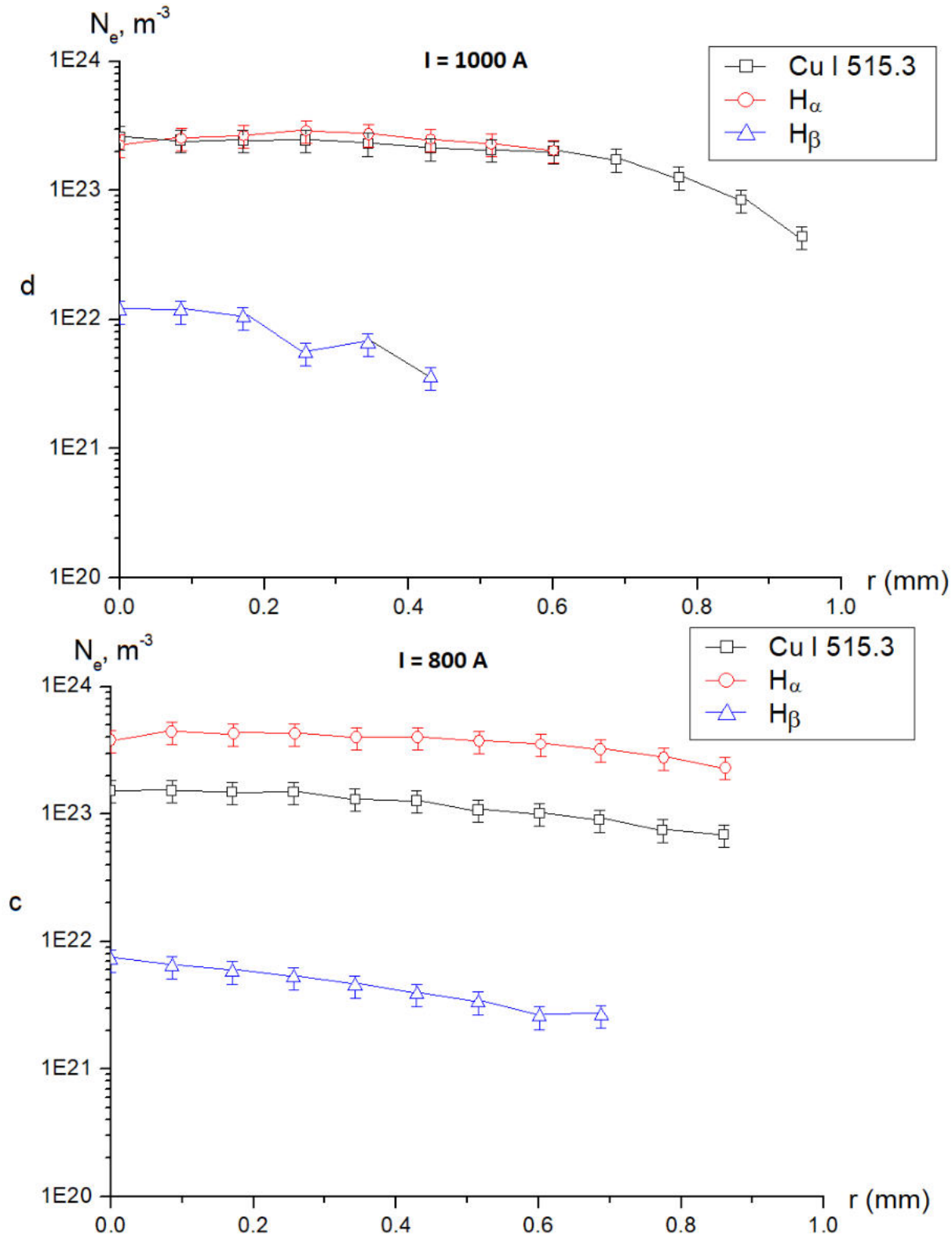

Figure 4.22: Radial profiles of the electron density calculated using broadening of the selected registered lines for different experimental current regimes: (a) I = 450 A, N_e calculated using Cu I 515.3 nm line and H_α line; (H_β line was not registered for this regime); (b) I = 660 A, N_e calculated using Cu I 515.3 nm, H_α and H_β lines; (c) I = 800 A, N_e calculated using Cu I 515.3 nm, H_α and H_β lines; (d) I = 1000 A, N_e calculated using Cu I 515.3 nm, H_α and H_β lines [11].

This overestimation is due to the KG theory not taking into account the influence of the ion dynamics on the spectral profiles of the Balmer series lines. Computational methods taking into consideration these ion dynamic effects have been developed, among them the Gigosos–Cardenoso model (GC) [15] permitting the use of a line different from H_β for measuring the electron density, obtaining in this way the same value of density as the one obtained from H_β.

Values of the FWHM of H_α and H_β lines with the corresponding N_e and $T_e = 10000$ K for the case of $\mu = 0,9$ (reduced perturber mass corresponding to the hydrogen emitter and any perturbing atom or ion) are showed in Table 4.3.

Table 4.3. FWHM (in nm) of H_α and H_β lines for $\mu = 0,9$ ($T_e = 10000$ K) [14]

$\log N_e (m^{-3})$	FWHM (nm) for H_α	FWHM (nm) for H_β
20.00	0.0142	0.0424
20.33	0.0244	0.0741
20.67	0.0404	0.129
21.00	0.064	0.217
21.33	0.102	0.361
21.67	0.16	0.601
22.00	0.25	0.999
22.33	0.393	1.67
22.67	0.621	2.80
23.00	1.01	4.70
23.33	1.68	7.77
23.67	2.84	1.27
24.00	4.86	2.05
24.33	8.31	3.25

It can be seen from the Table 4.3 that in order to get the same N_e at $T_e = 10000$ K, FWHM of H_β line must be between 3 and 4 times greater than that of H_α, while the experimentally obtained values of FWHM of H_β line are around 2 - 6 times smaller than that of H_α. (see Table 4.4), which,

to our beliefs, leads to the correspondingly lower values of the estimated N_e. Another possible reason for the obtained FWHM of H_β values being several times smaller than those of H_α can be bad signal-to-noise ratio during measurements.

Table 4.4. Experimentally obtained values of FWHM of H_α and H_β lines (in nm)

Line	FWHM (nm) at I = 660 A	FWHM (nm) at I = 800 A	FWHM (nm) at I = 1000 A	Average $\log N_e$ (m^{-3})
H_α	1.13	2.60	2.40	23.36
H_β	0.40	0.39	0.57	21.51

It can be seen from Tables 4.3 and 4.4 that the obtained results of FWHM of H_α line are in the 30-33% agreement with the data given by GC in [14] in terms of N_e/FWHM ratio.

4.5 Determination of a sub-pulse duration in setup for synthesis of colloidal solutions

The experimental results obtained from the first sets of experiments carried out on setup in Toulouse (section 3.3 of Chapter 3) and presented in 4.3.3 allowed to understand that the adjustment of the electrical operation parameters must be done in order to achieve the correspondence between the characteristics of the two experimental setups. The first step for this being determination of a sub-pulse duration in setup for synthesis of colloidal solutions (section 3.2 of Chapter 3).

Therefore, to align the experimental parameters of both setups employed in the present work it was required to know the typical discharge duration between two metal granules occurring in the process of colloid synthesis. For this purpose, the discharge chamber from the electrospark dispersion generator was connected to the experimental setup in Toulouse, replacing the electrodes. By doing so, the sought discharge duration was estimated from the high-speed imaging [16].

The top view of the discharge chamber filled with copper granules and the schematics of the arrangement are shown in Figures 4.23 and 4.24, respectively. The process was visualized using a Photron high-speed camera used in section 3.2.1. As in the case of single-pulse discharge between the electrodes, the acquisition of a high-speed camera was synchronized to the discharge triggering.

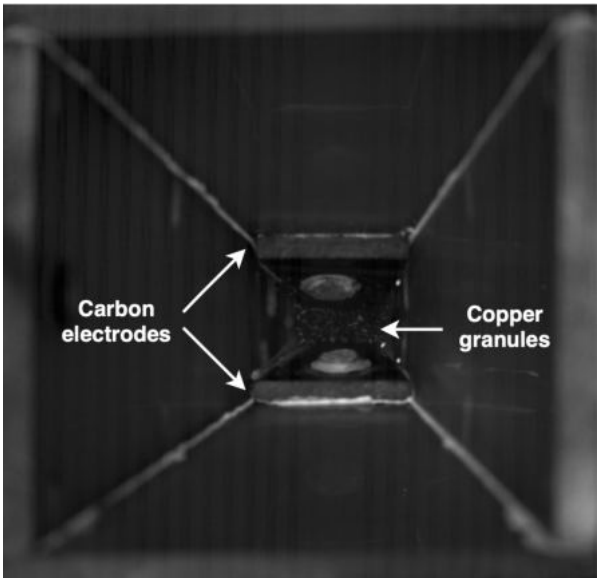

Figure 4.23: The top view of the discharge chamber used for the estimation of the spark duration between two metal granules; no water, granules of 1 mm diameter.

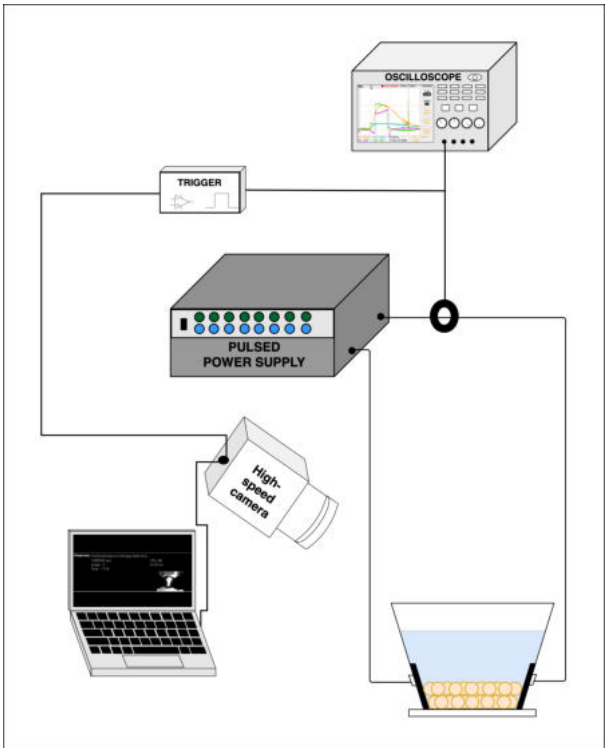

Figure 4.24: The experimental setup used for the estimation of the spark duration between two metal granules.

Three configurations were investigated aiming to study the patterns of current passage and sparking process, differing in sizes of the granules placed in the chamber: small granules of around 1 mm diameter, medium granules of around 2 mm diameter and large of 3-4 mm diameter. In all cases, high-speed imaging rate was 127,500 fps with 128 x 64 pixels image resolution for regime of 550 A peak current, corresponding to load voltage of 150 V.

From the high-speed imaging data, it was concluded that independently of the layer configuration or size of the granules, the average duration of a separate spark discharge varies within 150-180 μs (see Figure 4.25). It was also noted that sparks tend to occur mostly along the carbon electrodes mounted into the chamber's walls rather than in its central region.

Based on the results obtained from the high-speed imaging of the discharge chamber with copper granules, the adjustment of the experimental setup in Toulouse was carried out. The newly arranged version of the impulse generator is presented in Figure 4.26.

Replacement of the feeding cables by shorter and thicker ones contributed to the decreased total resistance of the experimental setup. Changing the 8 parallelly-connected capacitors by parallel connection of capacitors connected in series of 3 allowed to decrease the overall capacity from 1000 µF to 330 µF. In such a manner, the average duration of a single discharge between the tips of two electrodes was set up to 150 µs, meeting the required value. The electrical components used in the rearranged version of the impulse generator are the same as in the initial version (see Figure 3.6 of Chapter 3).

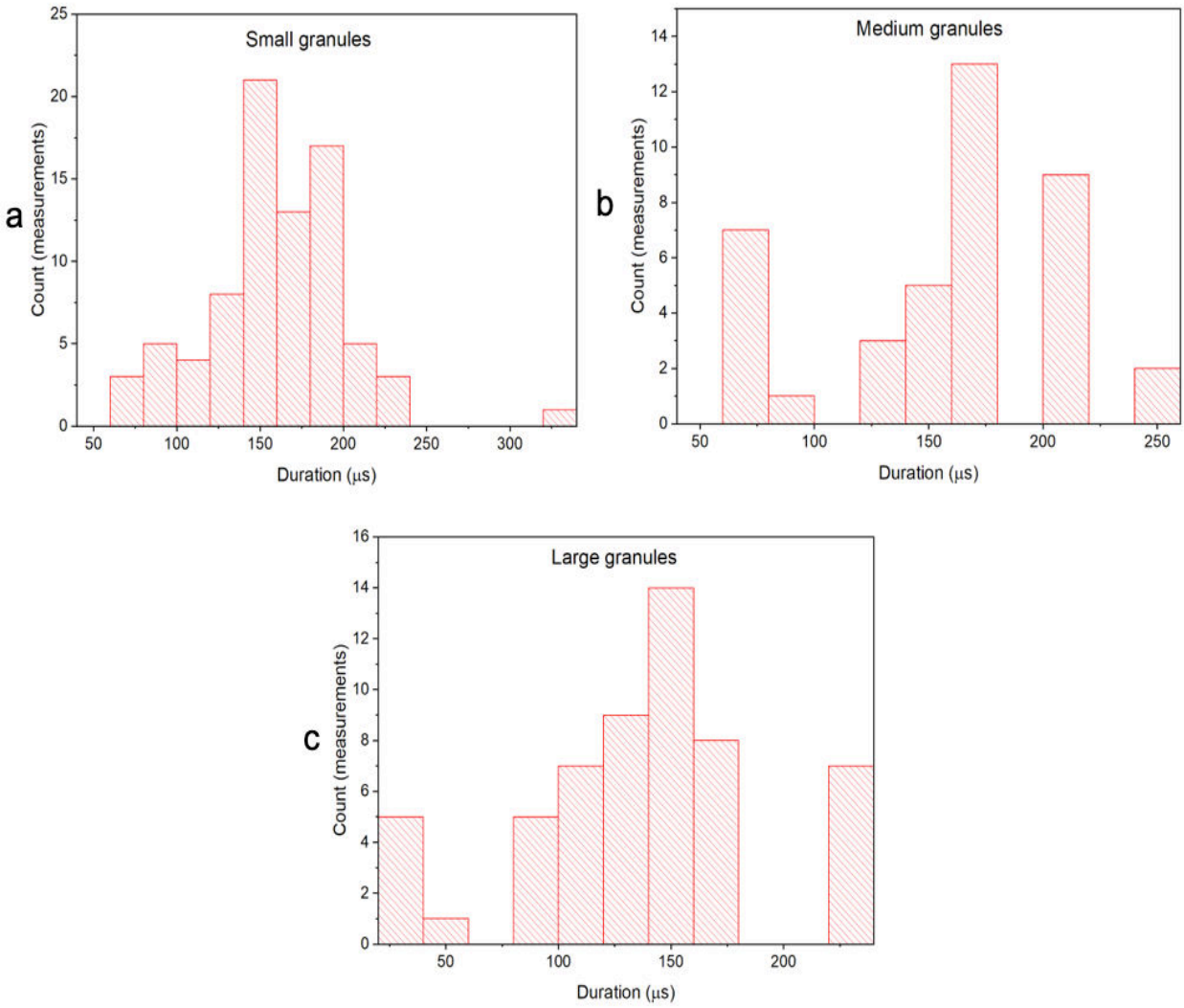

Figure 4.25: Distribution of sub-pulse discharge duration determined from the high-speed imaging: (a) small granules (1 mm diameter); (b) medium granules (2 mm diameter); (c) large granules (3-4 mm diameter).

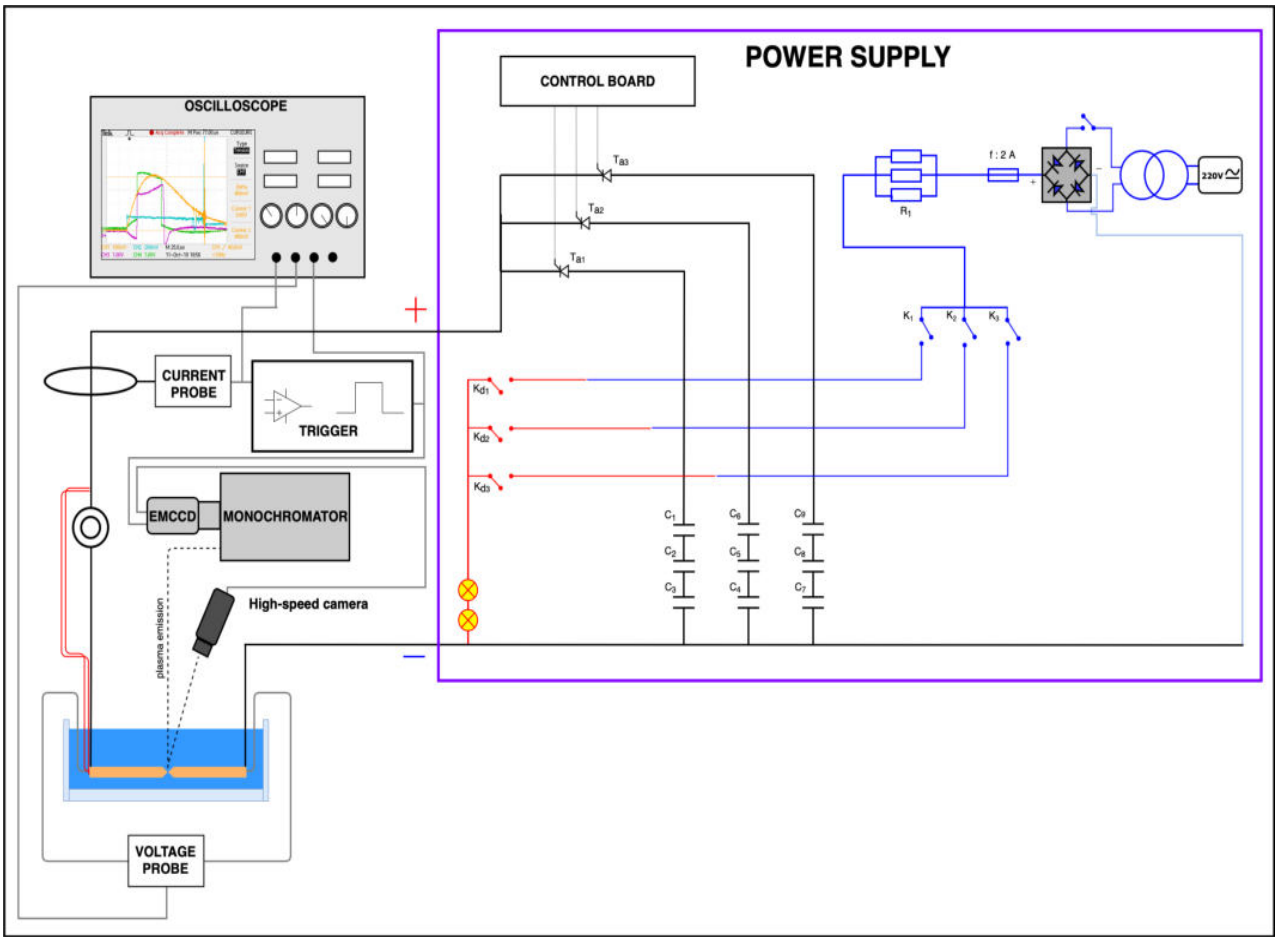

Figure 4.26: Schematic diagram of the rearranged version of impulse generator for investigation of single-pulse underwater electrical discharge: T_{a1}, T_{a2},… – thyristors; C_1, C_2,…– capacitors; K_{d1}, K_{d2}, …– switches to discharge the capacitors.

4.6 Plasma temperature and electron number density of the underwater pulsed discharge

As it has been mentioned before, spectral lines of neutral copper suitable for diagnostics of plasmas with metal admixtures and the corresponding spectroscopic constants are well-studied in the literature [6]. However, the list of the atomic copper lines (see Table 4.2) used for the first estimations of the plasma parameters in section 4.4 summarizes the data obtained and recommended for free-burning arc generated at 3.5 and 30 A current in air and argon.

It is expected that with the increase of the discharge current, and, respectively, proportion of copper vapor, the self-absorption of spectral lines will occur. That means that the light emitted by the very center of plasma could be absorbed within the plasma and not be measured. The opacity can be a problem for spectroscopic diagnostics, since the core of an opaque plasma cannot be characterized with such diagnostics.

Without performing the corresponding measurements to identify plasma opacity, one must avoid using the spectral lines which can be absorbed with higher probabilities. First and foremost, these include the resonant lines. In [17], author has studied interferograms of Cu I lines emitted by free-burning arc in air and argon at current of 100 A. It was shown that compared to the results obtained for the same experimental conditions at 3.5 and 30 A, at 100 A most of the investigated line profiles are self-absorbed, thus cannot be used for plasma diagnostics of discharge generated at higher current. However, the contours of atomic copper lines emitted at 448.0, 465.1, 570.0, 793.3 and 809.3 nm did not show any signs of reabsorption, and can be considered as suitable candidates for plasma parameters determination.

Additionally, analysis of the theoretical emission of the atomic copper lines emitted by a pure copper plasma at atmospheric pressure at temperatures 10 – 15 kK shows that the absorption is moderate (about 10% or less) for lines emitted at 522, 570, 578 and 793 nm. Which is consisted with the results from [17].

Of course, plasma temperature changes as a function of the radial position, and some absorption will always occur at the edge of the plasma where temperature drops. But the choice of the lines that theoretically present lower absorption could help yielding better results. In addition, one can consider that copper rich plasma remains at the center of plasma volume, and that absorption will be low in the copper-poor colder outer parts.

For diagnostics of plasma with molybdenum vapors, spectral lines and corresponding spectroscopic constants were taken from [18]. It should be noted that Boltzmann plots used for selection of the spectral lines in [18] were obtained for an electric discharge plasma generated between composite Cu-Mo electrodes at 3.5 and 30 A current, similarly to [17]. Therefore, self-absorption issue was not addressed in the case of the spectral lines of atomic molybdenum.

Table 4.5 summarizes spectral lines of neutral copper and molybdenum used for plasma diagnostics in this work.

Table 4.5. Selected spectral lines of Cu I and Mo I and their corresponding spectroscopic constants for diagnostics of the underwater electric discharge plasma (max. uncertainty on $g_i f_{ji}$ – 18%)

λ, nm	g_j	g_i	E_j, eV	E_i, eV	$g_j f_{ji}$
Cu I 427.5	6	8	4.84	7.74	0.9097
Cu I 465.1	10	8	5.07	7.74	1.4218

Cu I 793.3	2	2	3.79	5.35	0.4246
Cu I 809.2	4	2	3.82	5.35	0.6120
Mo I 473.1	9	11	2.62	5.24	1.551
Mo I 476.0	11	13	2.65	5.25	2.031
Mo I 550.6	5	7	1.34	3.59	0.854
Mo I 553.3	5	3	1.34	3.58	0.460

Values of the time- and spatially-integrated, as well as spatially-resolved plasma parameters of the underwater pulsed electric discharge plasma were calculated for the values of the discharge current of ~ 400 and 600 A (430 and 530 A in case of setup in Kiev). These values are within the range of working parameters of the operational unit in Kiev (see section 3.2), therefore ensuring the “realistic” configuration of the discharge generated at roughly the same conditions using setup in Toulouse (see section 3.3). Following the same reasoning, the results are presented for the discharge generated in tap water only.

Electron number density was obtained from the FWHM of hydrogen H_α line using the formula [7]:

$$N_e = 8.3808 \cdot 10^{16} \cdot (\Delta\lambda_W)^{1.6005}, \quad (4.3)$$

where $\Delta\lambda_W$ is the FWHM in nm and N_e is the electron number density in cm^{-3}.

It should be mentioned that formulas used for estimations of the electron density from Stark broadening of H_α and H_β in section 4.4 are different (see section 3.4.3). Since the previous results (see Fig. 4.22) have demonstrated sufficient inconsistencies, the used approach required reconsidering. Taking into account that underwater electric discharge is a high-pressure phenomenon, the values of the electron density presented in section 4.4 are underestimated due to the fact that corresponding formulas used for their calculations are derived for plasmas with lower electron number density values (for the H_β line, this limit is at $N_e \approx 10^{15}$ cm^{-3} while for the H_α, it is close to 10^{16} cm^{-3}) [112].

Time- and spatially integrated temperature of plasma generated between the copper granules at 430 and 530 A discharge current was calculated using the ratio of relative intensities of the two Cu I spectral lines emitted at 427.5 and 809.3 nm. This resulted in the average plasma temperature values of ~ 7400±1300 K and 9700±1800 K for I = 430 and 530 A, respectively.

Temperature of the plasma generated between molybdenum electrodes was obtained from the Boltzmann plot using Mo I lines listed in

Table 4.5 (see Fig. 4.27). Corresponding average temperatures at I = 430 and 530 A were found to be 13300±2400 K and 14600±2700 K, respectively. The spectroscopic data used for temperature calculation are known with uncertainties from 3% (Mo I lines at 550.6 and 553.3 nm) to 5% (Mo I lines at 473.1 and 476 nm). Considering errors from data treatment and experimental standard deviation, error bars in Fig. 4.27 have been set to 5% and 10%, respectively.

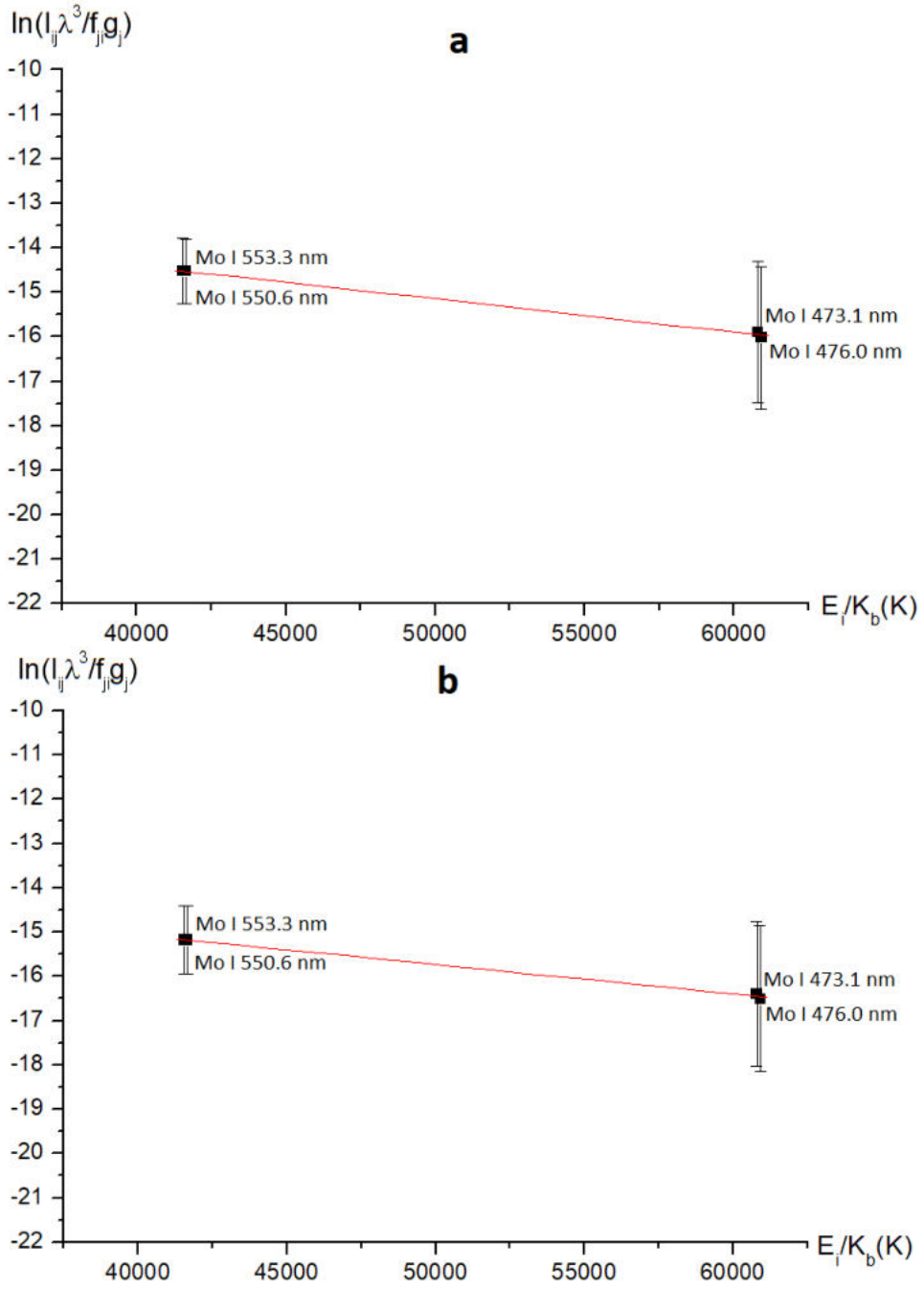

Figure 4.27: Boltzmann plots for temperature calculation of the underwater electric discharge plasma generated between molybdenum granules (Mo I spectral lines): a) at current of 430 A and b) 530 A.

FWHM of the H_α line was obtained from fitting the line profile with a Lorentzian function, as the one giving the best fit. This is the evidence that Stark broadening is the dominant mechanism of this line's broadening, and other contributions (instrumental and Doppler broadening) are negligible in our case. Figure 4.28 shows an example of fitting the H_α line profile registered for the discharge generated between copper (Fig. 4.28a) and molybdenum (Fig. 4.28b) granules at 530 A. Intensity of the hydrogen line emission is normalized in Fig. 4.28. The resulting values of the electron density obtained for plasma between cooper granules are $(2.2\pm0.44) \cdot 10^{17}$ cm^{-3} and $(3.8\pm0.76) \cdot 10^{17}$ cm^{-3} for I = 430 and 530 A, respectively. And in case of molybdenum granules: $(7.6\pm1.52) \cdot 10^{17}$ cm^{-3} and $(8.45\pm1.69) \cdot 10^{17}$ cm^{-3} for I = 430 and 530 A, respectively.

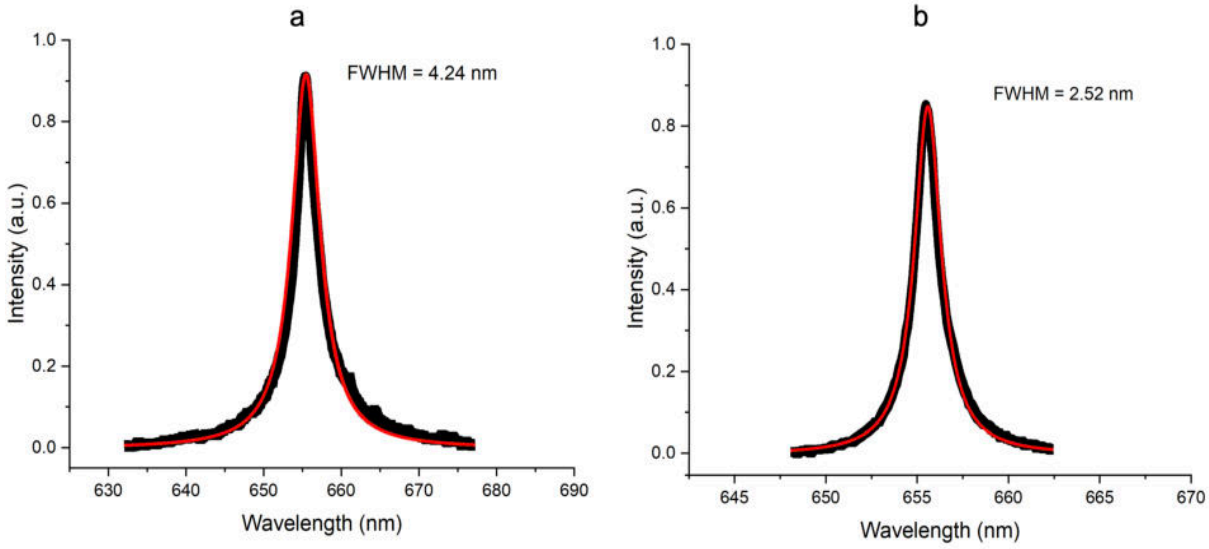

Figure 4.28: Lorentz fit and corresponding FWHM of H_α line for electron density calculation of the underwater electric discharge plasma generated at current of 530 A between: a) molybdenum granules and b) copper granules.

Spatially-resolved spectra of the neutral Cu and Mo lines used for temperature calculations are shown in Figures 4.29 and 4.30, respectively. Plasma emission was registered using 300 g/mm spectral grating for all the spatially-resolved spectra presented in this section.

Fig. 4.29 – 4.30 show spectral lines emitted by the underwater discharge plasma generated at 400 A. As previously shown in section 4.3, increase of the discharge current results in the increased emission intensity in the experimental spectra. Therefore, spatially-resolved spectral lines of copper and molybdenum registered at 600 A current are not very different. However, as discussed before, emission spectra registered in case of discharge generated between molybdenum

electrodes do have a distinctive continuum radiation, that is not observed for copper electrodes (Fig. 4.30).

As an example, Figure 4.31 show Boltzmann plots used for calculation of the radial distribution of plasma temperature for the case of discharge generated between molybdenum electrodes at 400 A current. Error bars are similar to those of Fig. 4.27 (5% for Mo I lines at 550.6 and 553.3 nm and 10% for Mo I lines at 473.1 and 476 nm). Fig. 4.31a shows Boltzmann plot obtained for the discharge axis (r = 0 mm), and Fig. 4.31b – for the discharge periphery (r = 0.7 mm). Corresponding radial temperature profiles calculated using Cu I and Mo I lines are presented in Figure 4.32 for I = 400 and 600 A, respectively.

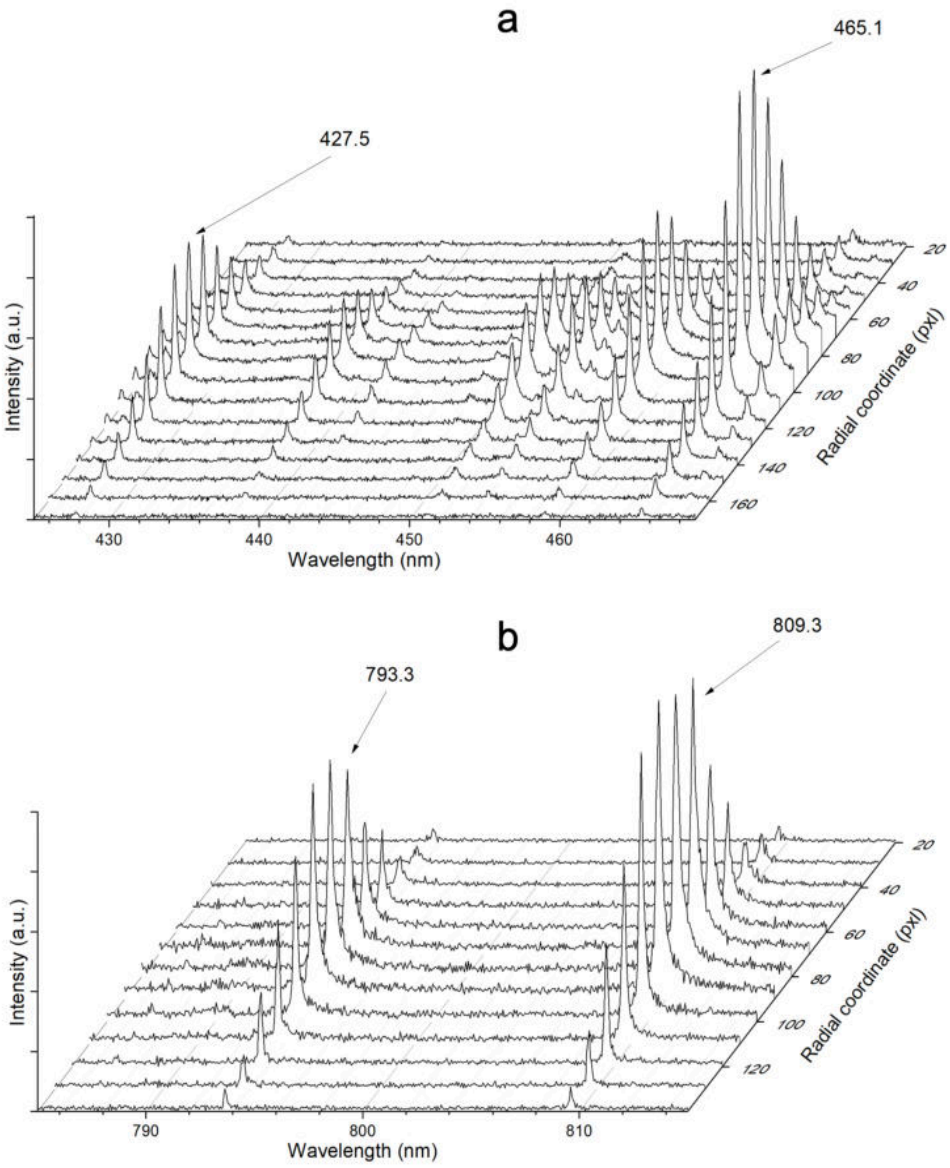

Figure 4.29: Spatially-resolved lines of atomic copper used for plasma temperature calculations (copper electrodes in tap water, I = 400 A, grating 300 g/mm): a) Cu I at 427.5 and 456.1 nm, and b) Cu I at 793.3 and 809.3 nm.

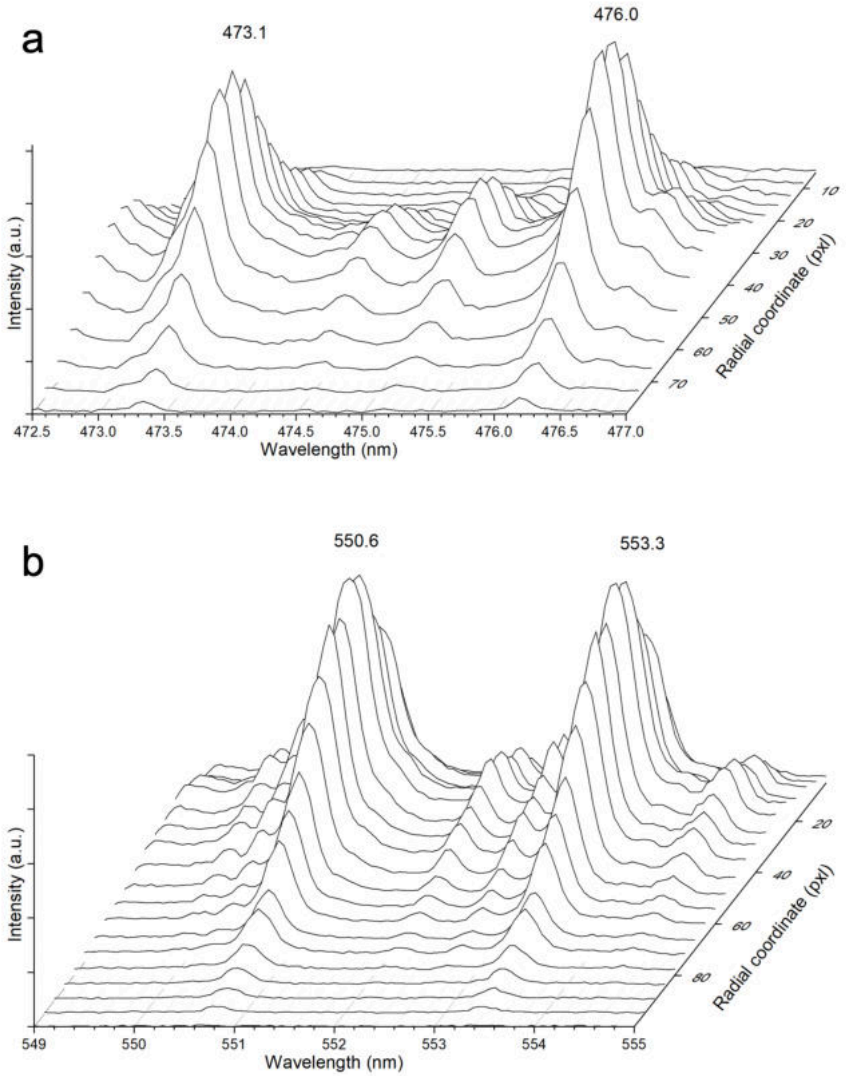

Figure 4.30: Spatially-resolved lines of atomic molybdenum used for plasma temperature calculations (molybdenum electrodes in tap water, I = 400 A, grating 300 g/mm): a) Mo I at 473.1 and 476.0 nm, and b) Mo I at 550.6 and 553.3 nm.

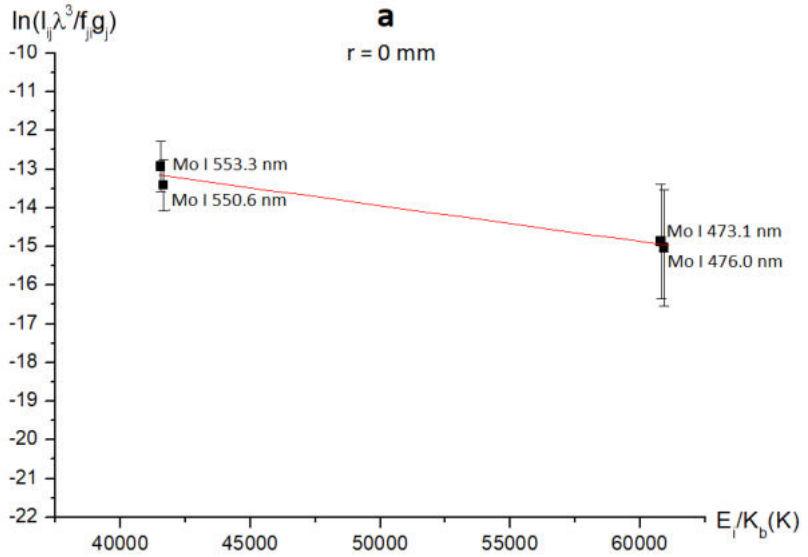

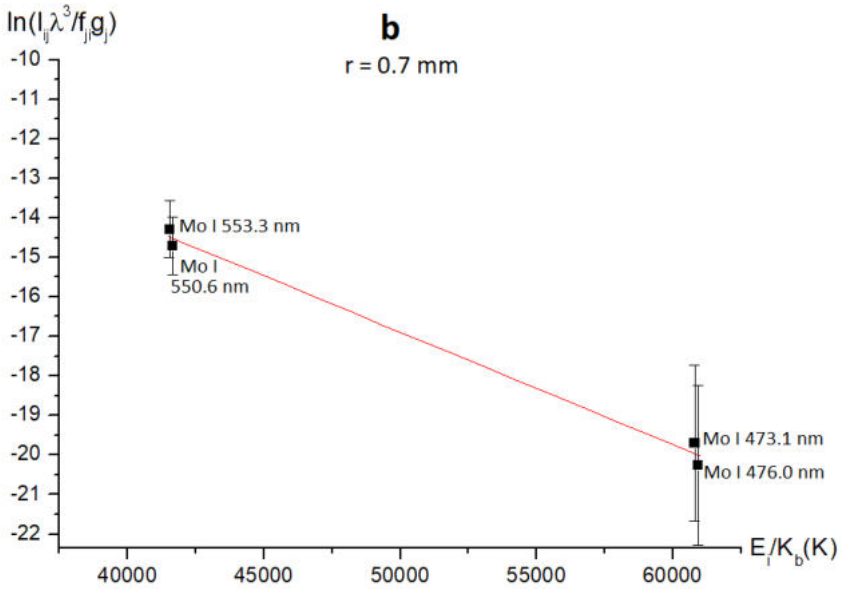

Figure 4.31: Boltzmann plots for temperature calculation of the underwater electric discharge plasma generated between molybdenum granules at 400 A: a) at the discharge axis (r = 0 mm) and b) at the discharge periphery (r = 0.7 mm).

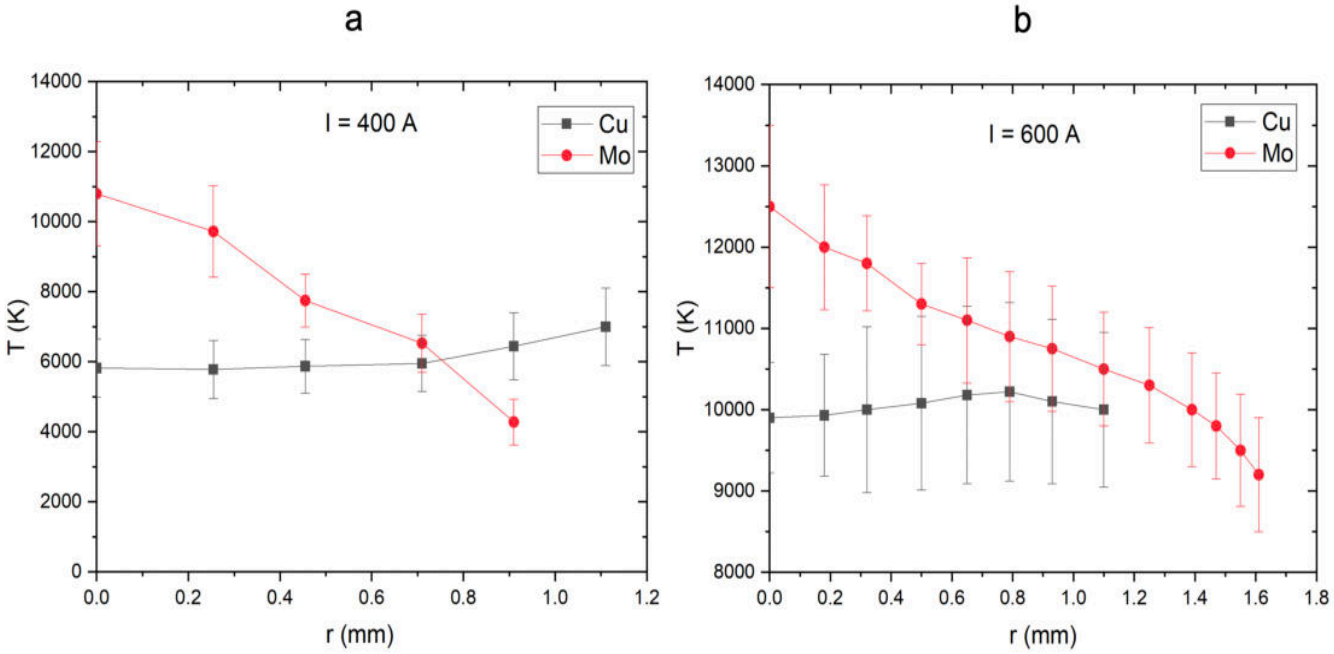

Figure 4.32: Radial profiles of temperature of the underwater electric discharge plasma generated between molybdenum and copper electrodes: a) at 400 A and b) at 600 A.

It can be seen from Fig. 4.32 that while temperature of plasma generated between copper electrodes remains fairly constant, in case of molybdenum electrodes temperature decreases at the periphery with its maximum at the discharge axis. This is an expected result, since one can consider that “core” of discharge is composed mostly of metal vapor while

its proportion decreases at higher radii. Temperature of plasma with molybdenum vapors is higher than that with copper vapors. This is due to the lower thermal conductivity of molybdenum. The latter means that lower proportion of the input energy is transferred to the electrodes (and, respectively, lower proportion of the energy contributes to metal erosion), thus, energy deposited in the plasma column is higher, resulting in the higher plasma temperature and emission intensity, compared to the case of plasma generated between copper electrodes.

The values of the time- and spatially-integrated plasma temperature estimated for the setup in Kiev are consistent with the values in Fig.4.32 for the copper and molybdenum electrodes, within the margin of error. However, an overestimation of plasma temperature in case of molybdenum electrodes may be accounted for the fact that no previous selection of the spectral lines based on the probability of their self-absorption was carried out.

Figure 4.33 shows spatially-resolved H_α line registered for the discharge generated between copper electrodes at current of 400 A (Fig. 3.33a) and 600 A (Fig. 3.33b). Corresponding radial electron density profiles calculated from the FWHM of H_α line under different experimental conditions are presented in Figure 4.34.

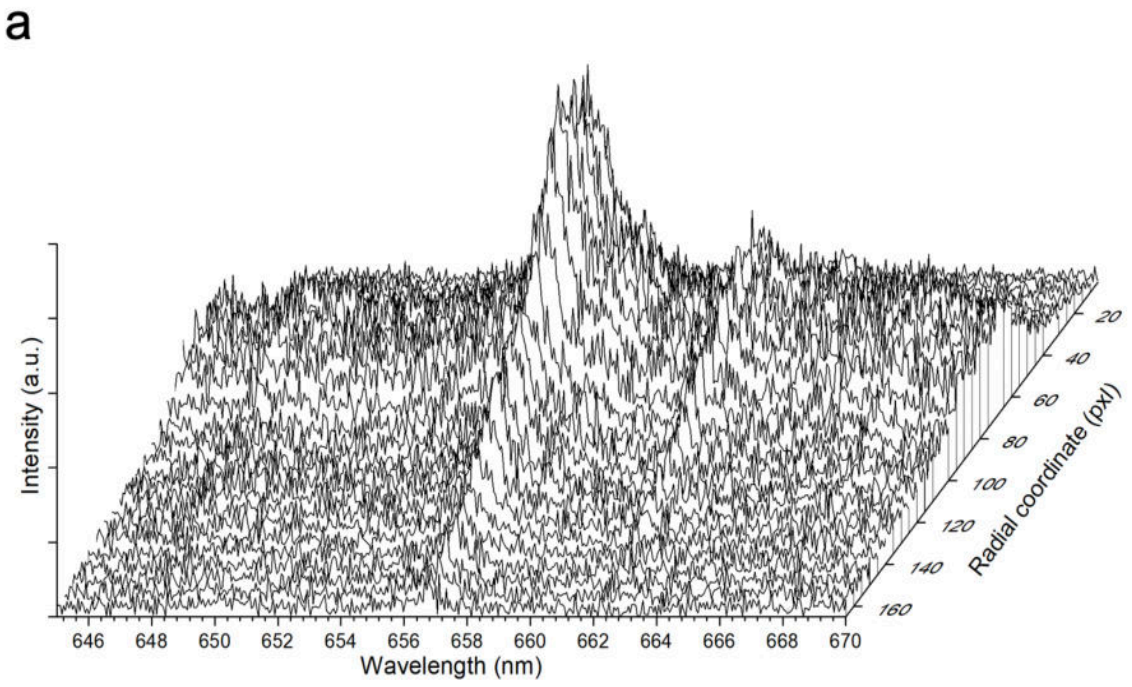

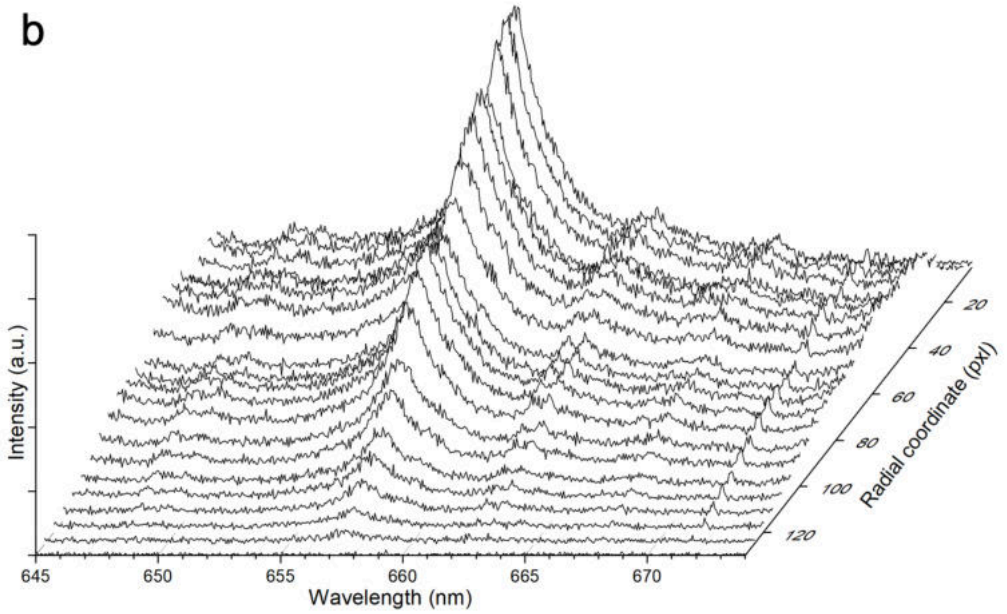

Figure 4.33: Spatially-resolved H_α line used for plasma electron density calculations (copper electrodes in tap water, grating 300 g/mm): a) at 400 A, and b) at 600 A.

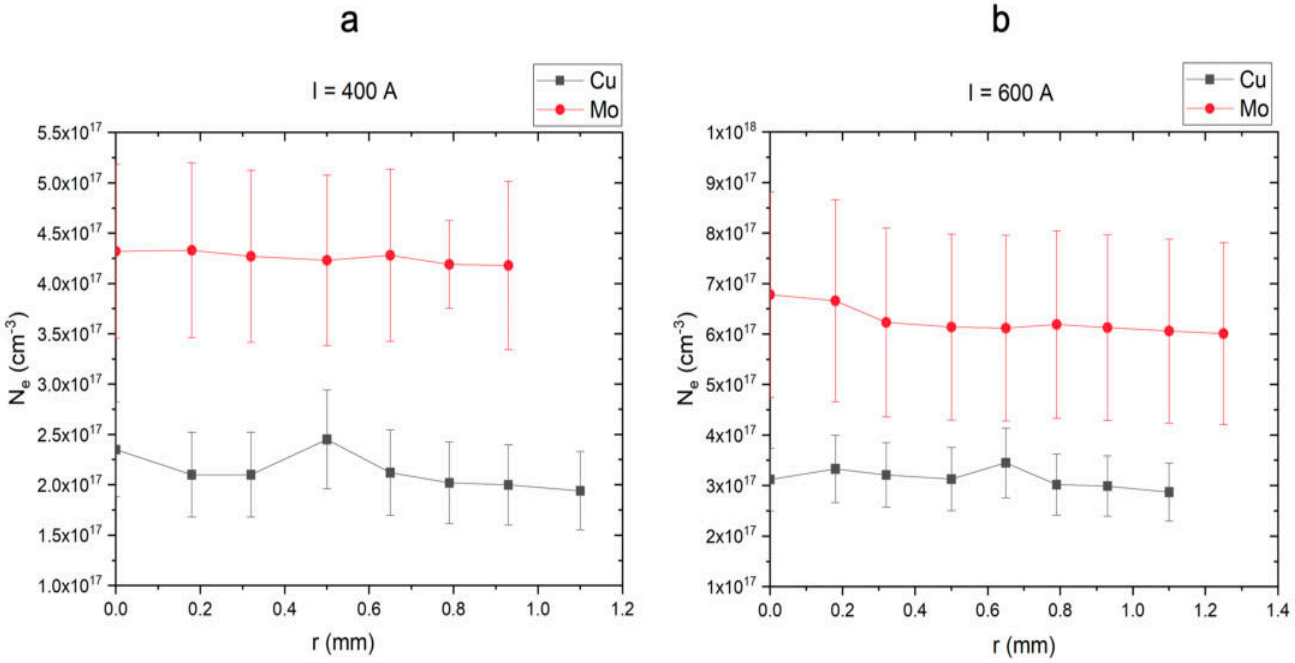

Figure 4.34: Radial profiles of electron number density of the underwater electric discharge plasma generated between molybdenum and copper electrodes: a) at 400 A and b) at 600 A.

One can see from Fig. 4.34 that electron density is higher in case of discharge generated between molybdenum electrodes in cases of both current regimes. This is consistent with the time- and spatially-integrated values within the margin of error.

It should be noted that plasma radii obtained from the spectral diagnostics are different from those derived from the high-speed imaging (see section 4.7). While no images of plasma were collected for the discharge current of 400 A, for measurements at 600 A it can be concluded that plasma diameter obtained from the imaging is overestimated in the case of molybdenum electrodes. This results from the increased brightness of the discharge that makes it difficult to estimate plasma sizes. This issue will be discussed in section 4.7.

4.7 Imaging of the underwater pulsed electric discharge

This section summarizes some observations made about the plasma and bubble created during the underwater pulsed electric discharge. Due to the small size of the plasma channel and electrodes, close images of the discharge region show details that might give useful information about the whole process: behavior of vapor bubble, localization of the discharge, behavior of eroded particles, etc. Imaging of the plasma itself is also interesting, particularly to see the evolution of the plasma size and shape, from the its beginning to the afterglow.

These results are certainly not exhaustive, but they give a first insight into the phenomena of the underwater pulsed electric discharge of the given configuration.

4.7.1 Bubble dynamics

Generation of an electric discharge in water leads to the formation of a plasma channel between the electrodes. The lifetime and temperature of the plasma are a few hundred microseconds and a few thousand Kelvin, respectively. The inhomogeneity of the plasma creates an inhomogeneity in the spatial distribution of temperature and pressure in the inter-electrode region.

The high temperature leads to a local heating and then to a vaporization of the liquid which, from a thermodynamic point of view, causes a dynamic variation of the temperature and the pressure. The dynamic variation of pressure (and temperature) gives rise to a dynamic movement of the gas pocket created in the volume of the liquid.

Electrical discharges in liquids resemble underwater explosion processes whose basic physics has been extensively studied by Kirkwood and Bethe [19] and by Cole [20]. The analysis of underwater explosions employs the properties of acoustic waves and shock waves.

Independently of the considered initiation mechanism (existence of a gaseous phase before the plasma or not, i.e. direct breakdown in liquid, gaseous phase or other), the discharge leads to the formation of a

gaseous pocket. Transition from the liquid state to the gaseous state of a body corresponds to the thermodynamic phenomenon of evaporation. The transition from a liquid initial state to a gaseous final state can follow an infinite number of reversible thermodynamic paths, but as in majority of phase-change situations (liquid-gas), one can distinguish two main processes: boiling and cavitation. The boiling phenomenon is a process which is established at constant pressure while the cavitation phenomenon is established at a constant temperature.

The spectral analysis of the luminous intensity emitted shows a significant emission of the radiation during the existence of plasma (~ 150 µs). Therefore, the main mechanism of bubble formation is evaporation induced by Joule heating. Indeed, the plasma temperature (thousands of Kelvins) is sufficient to heat the liquid and form a gas bubble of an initial size comparable to that of the plasma at start-up. The high pressure generated causes bubble expansion, which lasts long after the extinction of the arc (~ 500 µs). Then the bubble collapses and some decaying oscillations take place. This means that the part during which the discharge, i.e. the energy source, is present is not negligible considering the bubble lifetime.

This subsection aims to experimentally investigate the bubble dynamics occurring during a pulsed electric discharge in water.

Following local deposition of energy into a liquid, it is dissipated in different ways:

- first of all, a pressure shock wave is generated as a result of the development of a plasma channel in the water,
- a part of the energy is dissipated on the initiation and expansion of the channel itself,
- a part of the energy is dissipated on the erosion of metal electrodes,
- the rest of the energy is used to develop a gas bubble.

In the first moments of its formation, the bubble is under conditions of high temperature and high pressure. These extreme conditions originate the observed expansion-implosion dynamics.

High-speed imaging enables to trace bubble dynamics over time with a resolution of ten microseconds. Figure 4.35 below presents a series of images from a high-speed video measurement showing the temporal evolution of the bubble.

The bubble appears right after the plasma grows to its maximum diameter and then, due to the pressure of surrounding water, implodes to reach a minimum volume. Decreasing of the bubble’s volume causes increasing of pressure, which in turn leads to the bubble’s expansion until the pressure of the surrounding water results in a new implosion and so on. In our case, these oscillations are observed clearly in all measurements but involve only primary explosion and following implosion of the bubble.

Starting from a certain moment of time, the wall of the bubble undergoes modifications due to development of various instabilities at the gas-liquid interface. After the implosion, the bubble collapses. Upon collapse and for some time afterwards, some minor oscillations in liquid can be seen.

Figure 4.36 schematically shows the physical processes that dominate bubble dynamics at each time interval.

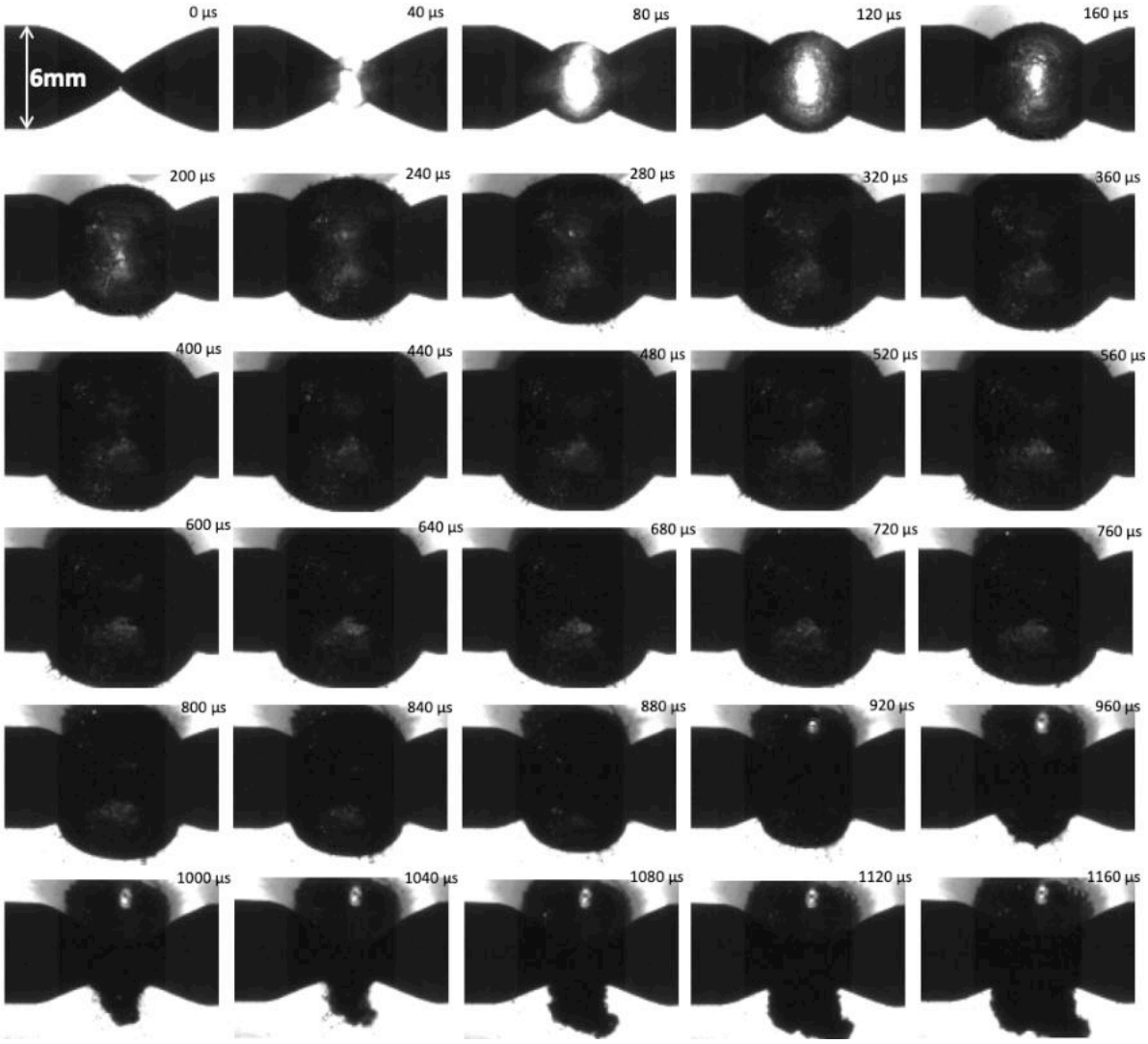

Figure 4.35: Time evolution of bubble: high-speed imaging of discharge generated between Cu electrodes in deionized water, peak pulse current of 1000 A.

It can be seen from Fig. 4.35 that bubble has quite good spherical shape during its growth, but for the latest parts of its collapse (after 720 µs) it seems to be compressed. The shape evolves to a toroidal configuration, or to two separate bubbles (920 µs). This can be explained by the presence of the electrodes that disturb the "natural" evolution of the bubble. On the other hand, the features observed from 960 to image 1160 µs (and of collapse and beginning of next oscillation's growth) can

be related to the presence of eroded material in the liquid (in particular the "cloud" on the lower part the images starting from 1000 µs).

For the future outlook, it would be interesting to estimate the value of pressure from the amplitude of bubble growth oscillation. This could be done using models of bubble growth and collapse (for instance, Rayleigh-Plesset), by finding the pressure yielding the best fit to the temporal evolution of bubble. The attempts were made to use a cavitation bubble model for this purpose, but with little success. This can be explained by the fact that cavitation model does not consider energy input during the growth of the bubble, only a punctual energy input causing the bubble formation (not after the bubble growth has started). In these experiments, the arc is present in a part of the bubble lifetime that is not negligible. That means that an adequate model should be find suitable for this case.

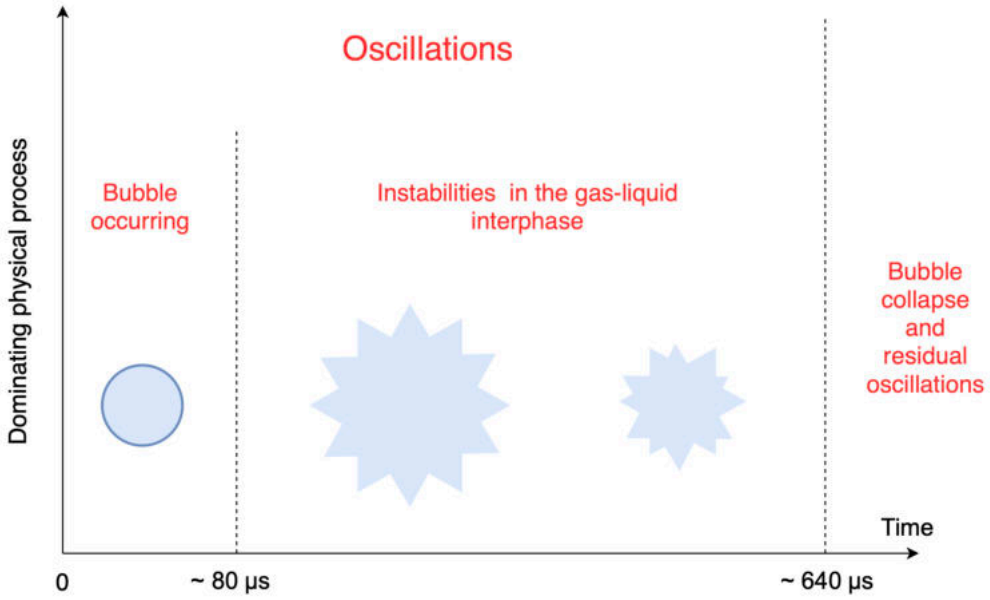

Figure 4.36: Observed dynamics of a bubble created in water as a result of pulsed electric discharge.

The instabilities related to material flows at the interface are known as instabilities of Landau-Darrieus (LD). They appear when there is a phenomenon of a mass transfer across the interface that can contribute to its distortion.Instabilities of LD and KH types have negligible effects on the interface, therefore the RT type instabilities that appear when the bubble is imploding [21] dominate [22], [23].

However, it is visible from Fig. 4.37 that instabilities on the gas-liquid interface occur already during the explosion phase of the bubble (around 80 µs after bubble generation) and undergo development until its collapse. Additionally, it has been observed that in some experiments, a

small bubble can be created and separated from the volume of main bubble surrounding the plasma (Fig. 4.38).

The visible instabilities distorting the gas-liquid interface of the bubble can be seen in Figure 4.37. Generally, several types of the hydrodynamic instabilities can be distinguished:

- Rayleigh-Taylor instabilities (RT) occurring during the implosion phase when the densest fluid (liquid) is accelerated towards the least dense fluid (gas bubble).
- Kelvin-Helmholtz instabilities (KH) occurring due to the presence of a shear force at the gas-liquid interface.

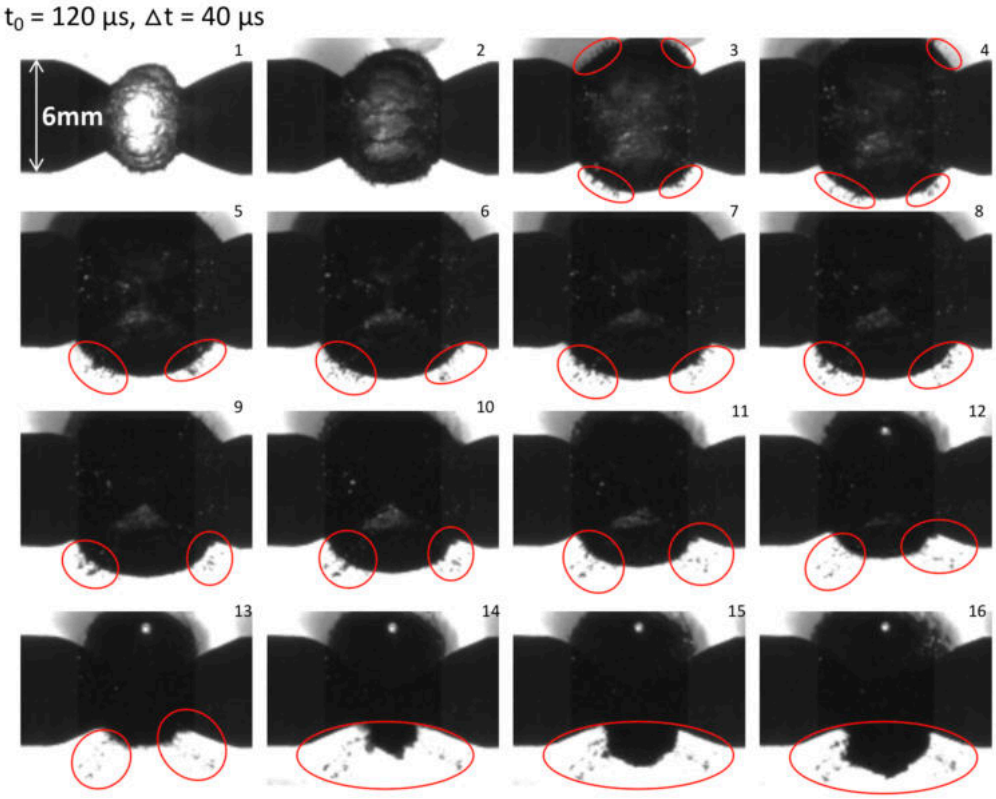

Figure 4.37: Time evolution of instabilities at gas-liquid interphase: high-speed imaging of discharge generated between Cu electrodes in deionized water, peak pulse current of 1000 A.

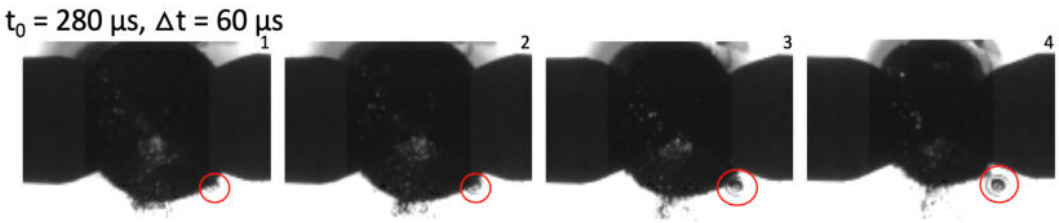

Figure 4.38: Creation of a small gas bubble and its separation from the main bubble surrounding the plasma: high-speed imaging of discharge generated between Cu electrodes in deionized water, peak pulse current of 600 A.

Figure 4.39 shows a temporal diameter evolution of a bubble formed during an electric pulsed discharge generated between molybdenum electrodes as a function of the energy injected (i.e. value of a peak impulse current) and a type of the liquid media. The bubble's diameter was estimated from the high-speed images of the discharge. It should be mentioned that the error bars indicated in Fig. 4.39 – 4.41, correspond to averaging across several series of experiments.

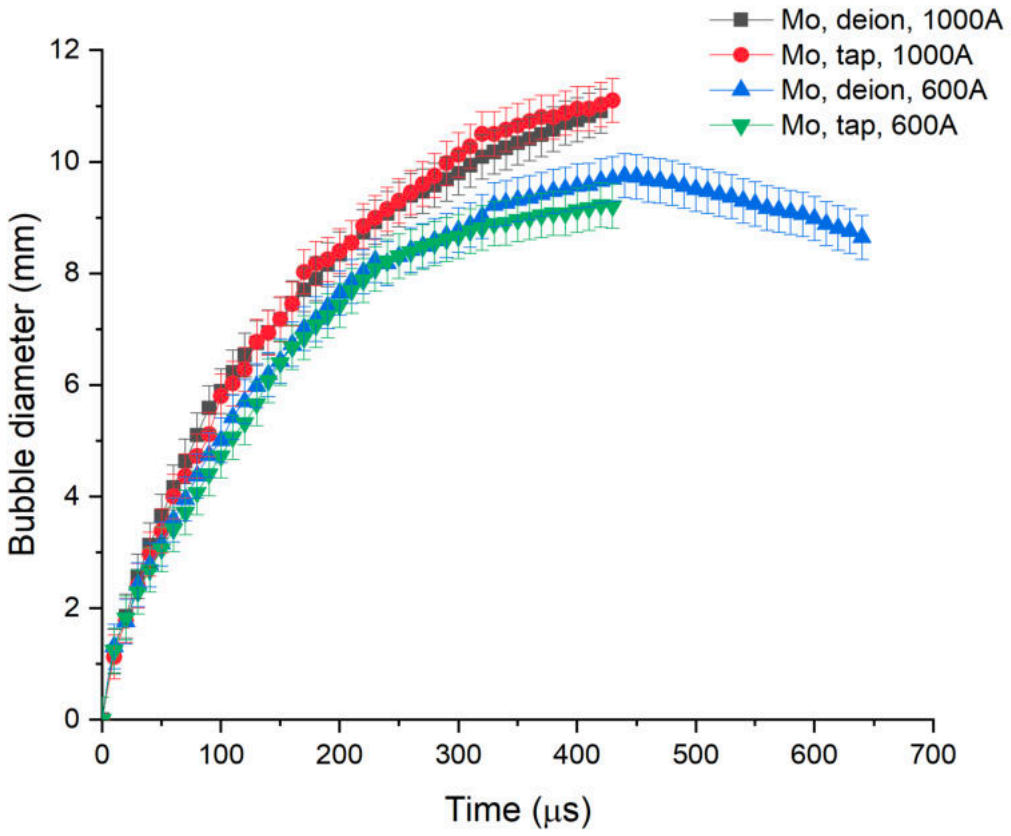

Figure 4.39: Bubble diameter as a function of time for a discharge generated between molybdenum electrodes: effect of the peak impulse current and type of a liquid.

The procedure for estimating the diameter is quite straightforward and easy when bubble is spherical. But, as can be seen in Fig. 4.37, it is not always the case, and the shape of the bubble can be elongated. In such case, measurements of the plasma and bubble diameters are estimated as an average between larger and smaller bubble dimension (along two perpendicular directions). It should be noted that bubble size is difficult to estimate in case of the discharge generated between molybdenum electrodes. This is due to the fact that the bubble becomes larger than the view area, and due to the stronger contamination of water by "particles" originating from electrode erosion.

It can be clearly seen from Fig. 4.39 that whether discharge has been generated in tap or deionized water, it does not have a remarkable

effect on the bubble's diameter. It is also obvious that the higher energy input leads to the bubble of a bigger diameter. It should be noted that in case of the discharge between molybdenum electrodes it is not possible to follow the explosion-implosion cycle of a bubble completely. This is due to the fact that bubble grows beyond the set size of a camera frame. This can be improved by decreasing the resolution of a high-speed imaging, which will not allow to get the same amount of details of the discharge process. Figure 4.40 confirms that the similar correlation between the energy input and the bubble diameter is observed in the discharge generated between copper electrodes in tap water.

However, no effect at all can be concluded if the maximal diameter of the bubble would have been achieved at the same time. From Fig. 4.39 one can deduce that the maximum diameter of the bubble in deionized water is reached at the moment corresponding to around 600 µs, while Fig. 4.40 displays a plateau at 400-450 µs. This can possibly be considered as the effect of the liquid dielectric.

While the type of the liquid has no effect on the oscillation of the bubble, the different electrode material used, as can be seen in Figure 4.41, cause certain variation in bubble's diameter. Bubble formed during discharge generated between molybdenum electrodes has a bigger diameter and a longer lifetime.

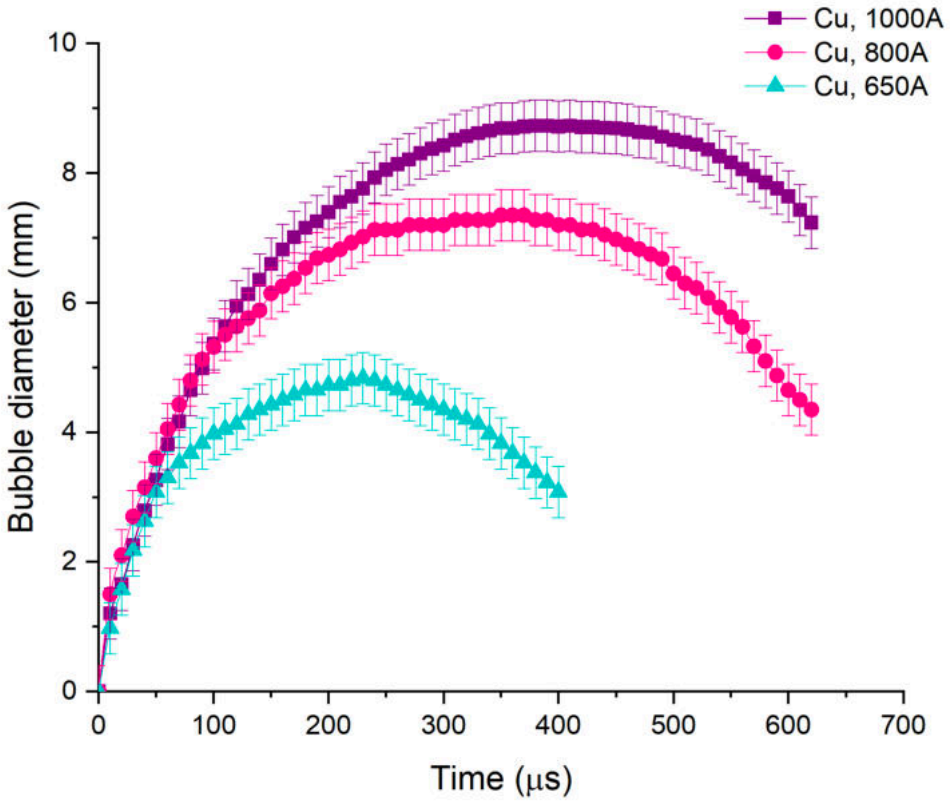

Figure 4.40: Bubble diameter as a function of time for a discharge generated between copper electrodes: effect of the peak impulse current.

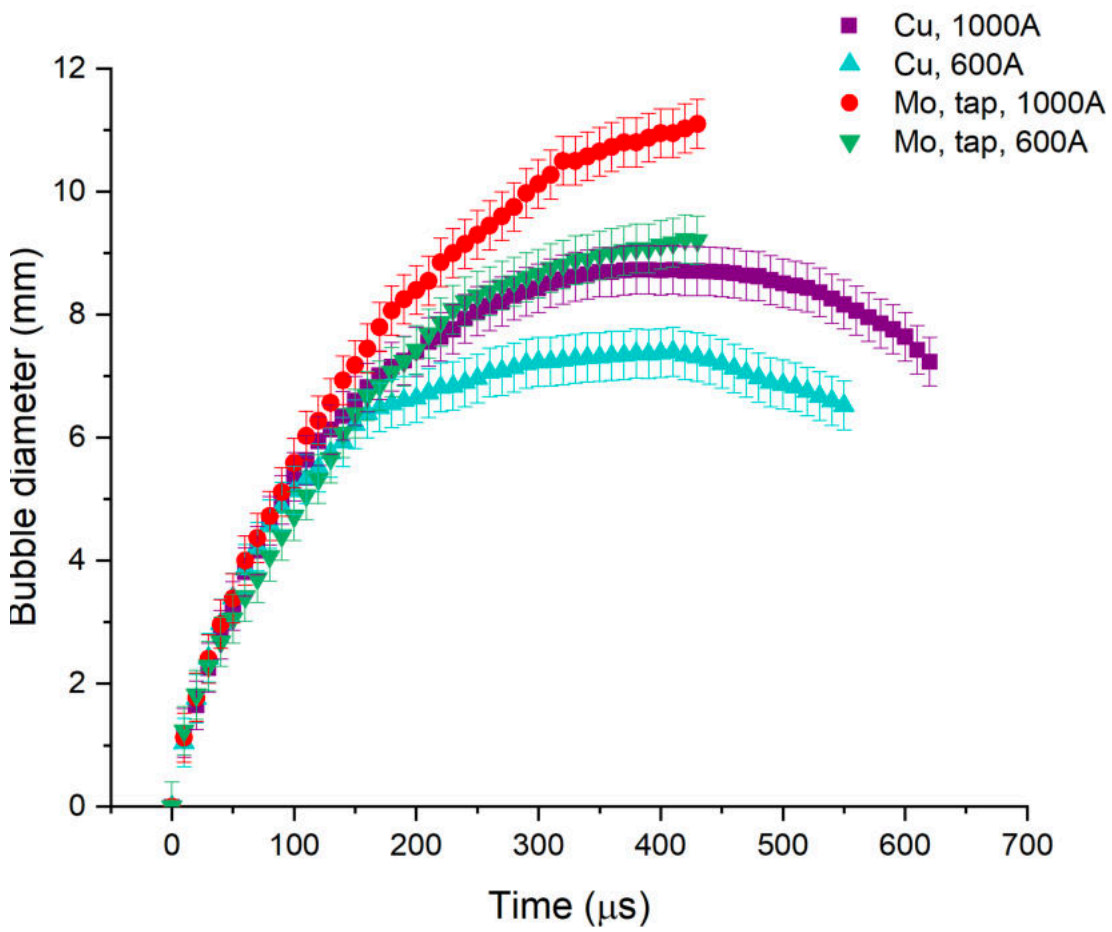

Figure 4.41: Bubble diameter as a function of time: effect of electrode materials.

Results in Fig. 4.39 - 4.41 confirm that bubble dynamics is a phenomenon that mostly depends on how energy is dissipated.

It can be seen from Fig. 4.41 that bubble maximal size is greater for molybdenum than for copper: about twice larger at low current, and 25% larger at high current. There are two possible explanations. First one being that the part of power dissipated in the formation of the bubble (and formation of plasma that emits more intensely) is greater in the case of molybdenum, meaning that the remaining part, dissipated for electrode erosion and heating is lower. The second possible explanation can be a presence of an additional energy input (for instance, oxidation).

The bubble maximal size in case of copper electrodes seems to increase linearly with current (this is analogical to dependence of a discharge diameter, see Fig. 4.49). At least for the considered current range of 650 – 1000 A, a linear fit seems then a reasonable approximation for the given current range (see Fig. 4.42). It yields to a proportionality coefficient of 10 μm/A (with a fitting error of about 20%) for the maximal size as a function of current. A fit with a second-degree polynomial would yield to $y = - 17.34762 + (0.04986) \cdot x – (2.38095e^{-5}) \cdot x^2$. Having only 3 experimental points making it difficult to conclude which is the best fit: 1st

order linear or 2nd order polynomial. Therefore, a higher number of experimental working conditions would be helpful to get more precise results. The error bars are comparable to the size of the data points in Fig. 4.42, considering the scale, therefore they are not indicated.

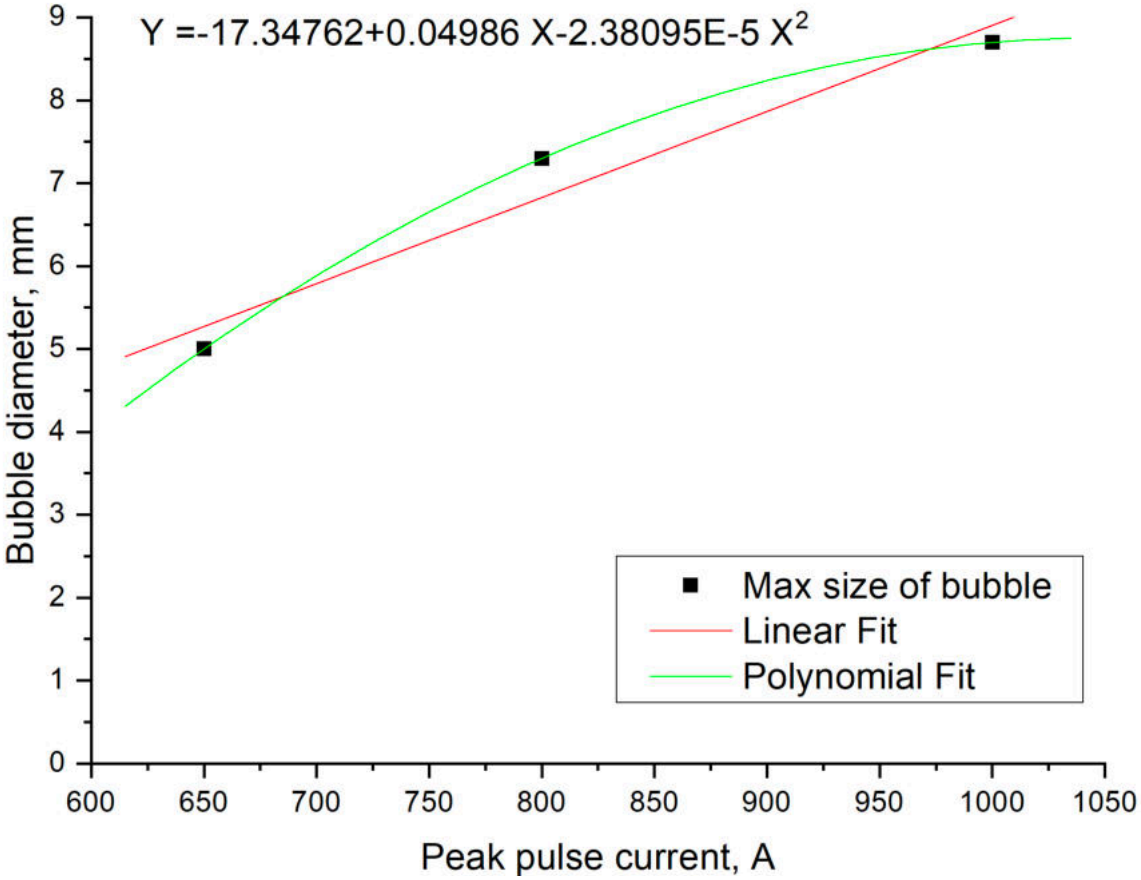

Figure 4.42: Linear and polynomial fitting of the maximal bubble's diameter on the peak pulse current value: discharge between copper electrodes.

For molybdenum the ratio of maximal size as a function of current is lower than with copper: the linear fit yields to a coefficient of 4 µm/A.

Considering the bubble growth speed, the various parameters (liquid, electrode material and current) seems to have little influence: it remains always close to 20 µm/A. Differences do not exceed 5%, which is negligible considering uncertainties. Bubble has a bigger maximal diameter and a longer lifetime with Mo electrode, but the growth speed is similar to the case of copper.

For the previously carried out experiments, the results were different. The bubble maximal diameter was reached at about 330 µs at 400 A and 350 µs at 600 A. In both cases, the maximal diameter was similar (8.5 mm) and twice higher than for the results presented in Fig. 4.41 (about 4.5 mm). The experiments with molybdenum also yielded to higher diameter: about 9.5 mm at 200 µs, and 10.2 mm at 220 µs for a

current of 426 A, which is higher than what is presented in Figure 4.14 for a current of 1000 A (about 8.5 and 9 mm at 200 and 220 μs, respectively).

4.7.2 Plasma imaging

Figure 4.43 shows a typical example of the underwater electric pulsed discharge generated between molybdenum electrodes.

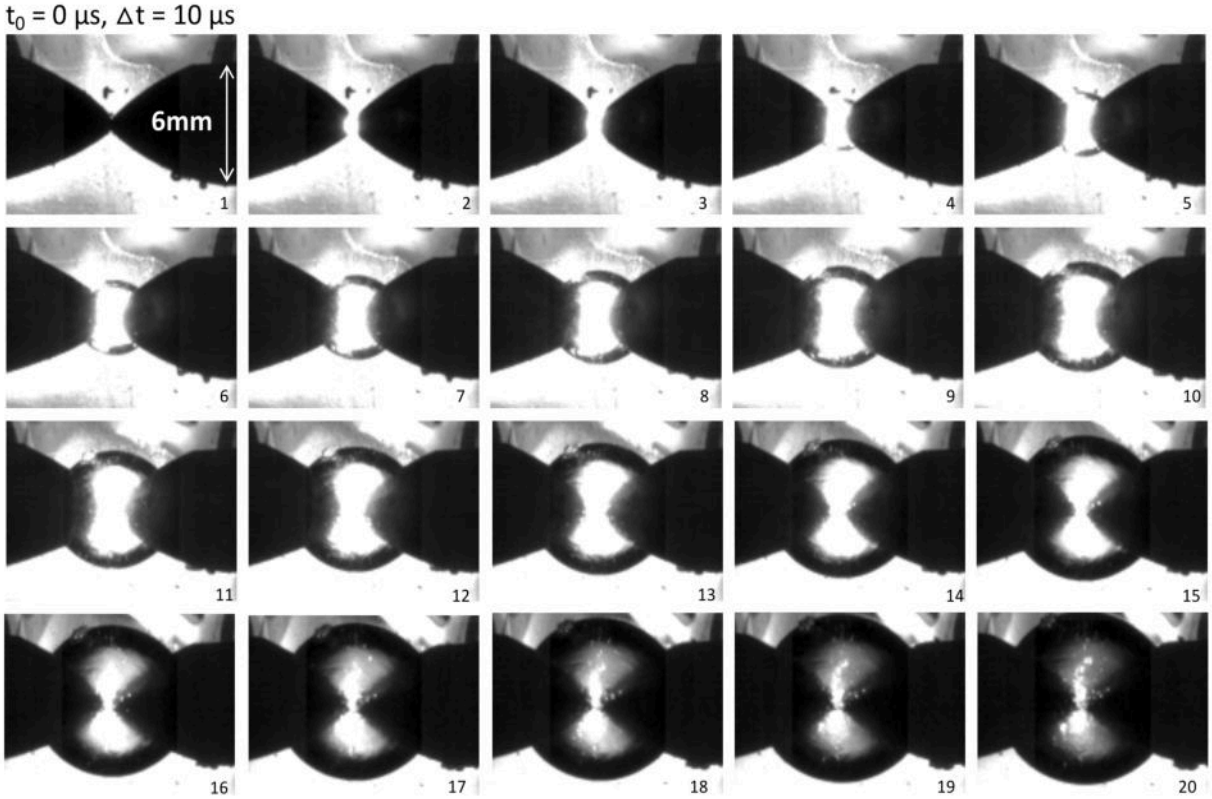

Figure 4.43: Time evolution of plasma channel: high-speed imaging of discharge generated between Mo electrodes in deionized water, peak pulse current of 600 A.

As it can be seen from Fig. 4.43, two phases of the discharge can be distinguished: plasma in water, i.e. approximately during the first 30 – 70 μs, and plasma in bubble formed afterwards. Figures 4.44 -4.47 show the temporal evolution of bubble and plasma diameters during the discharge generated between copper and molybdenum electrodes. The corresponding moment of time when diameter of bubble “outgrows” the plasma diameter is indicated in each graph. While there seems to be no remarkable effect of the peak impulse current value, the time threshold in case of discharge between molybdenum electrodes is higher compared to that in case of copper.

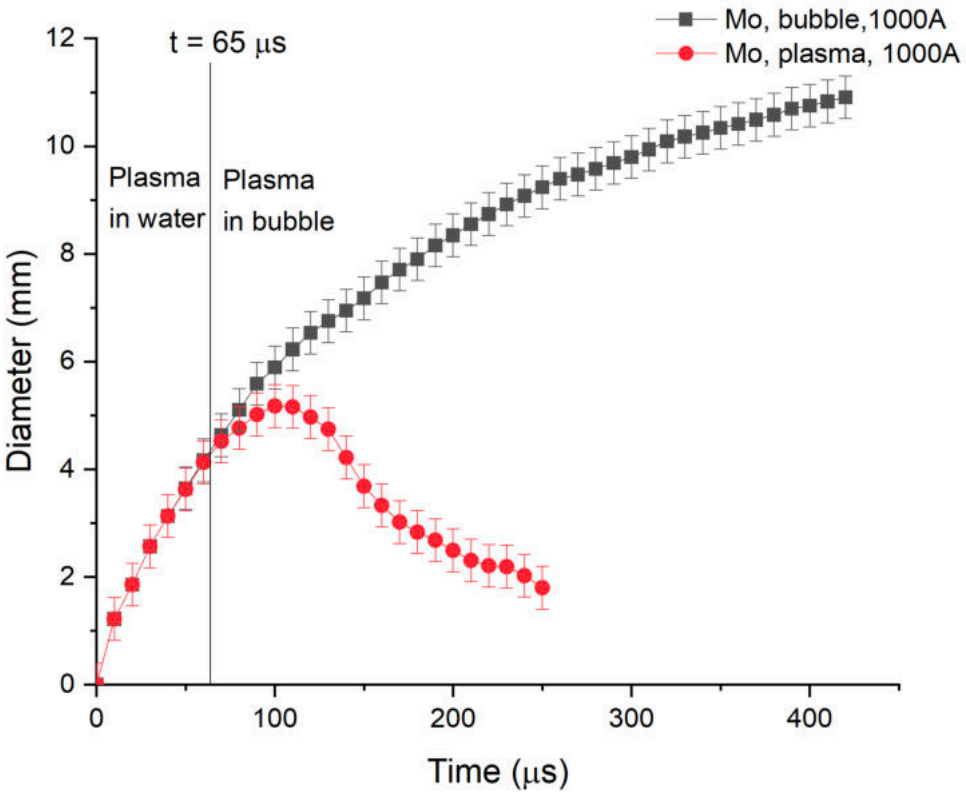

Figure 4.44: Time evolution of bubble and plasma diameters: discharge generated between Mo electrodes in deionized water, peak pulse current of 1000 A.

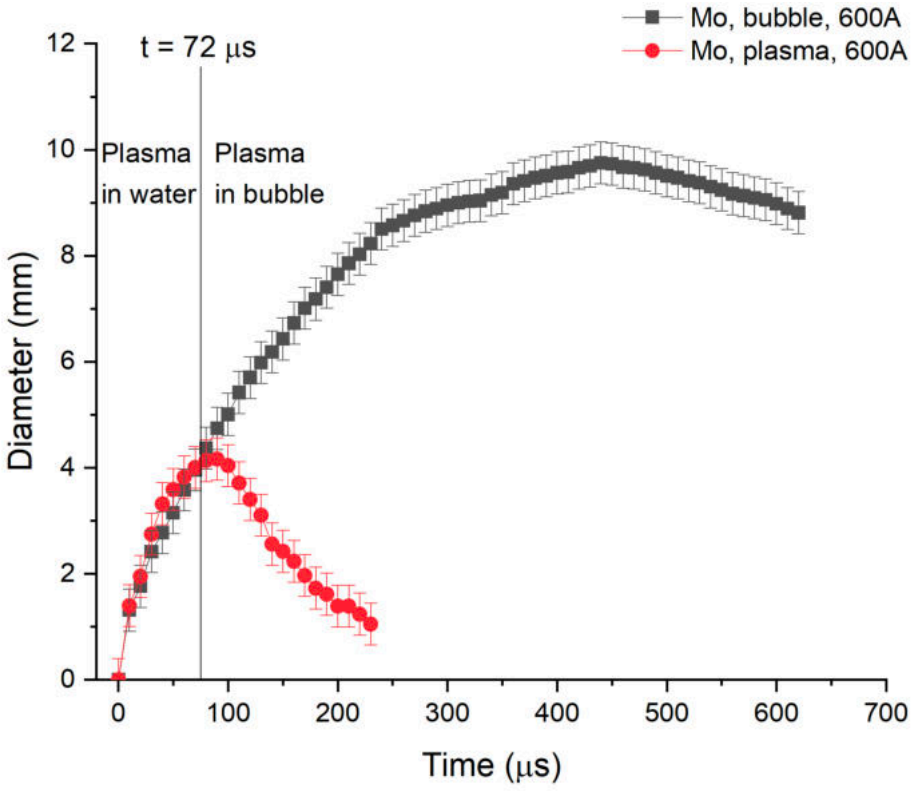

Figure 4.45: Time evolution of bubble and plasma diameters: discharge generated between Mo electrodes in deionized water, peak pulse current of 600 A.

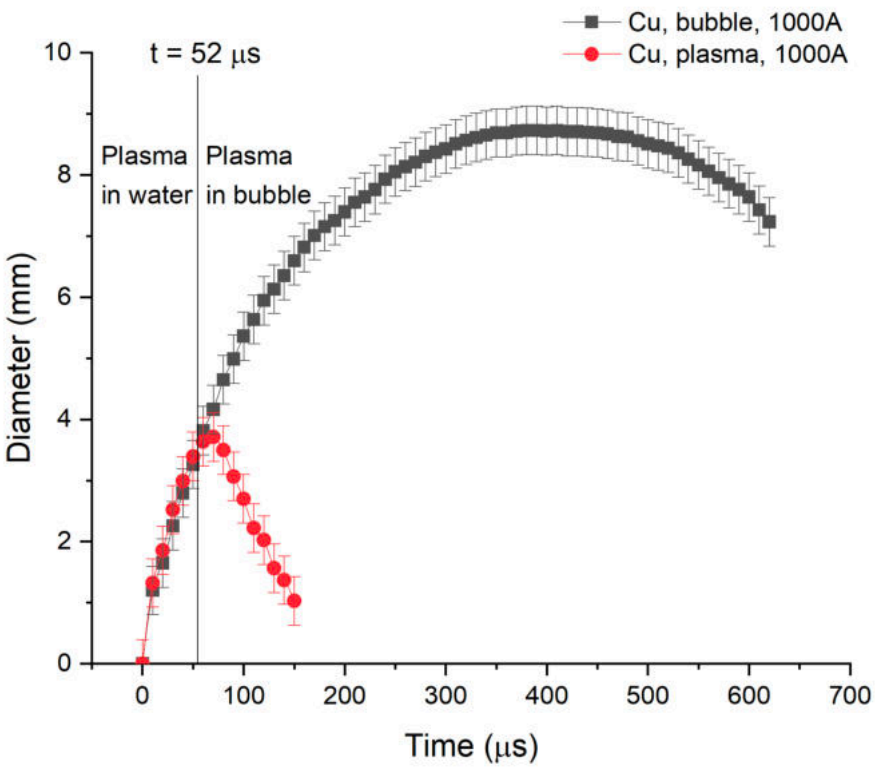

Figure 4.46: Time evolution of bubble and plasma diameters: discharge generated between Cu electrodes in deionized water, peak pulse current of 1000 A.

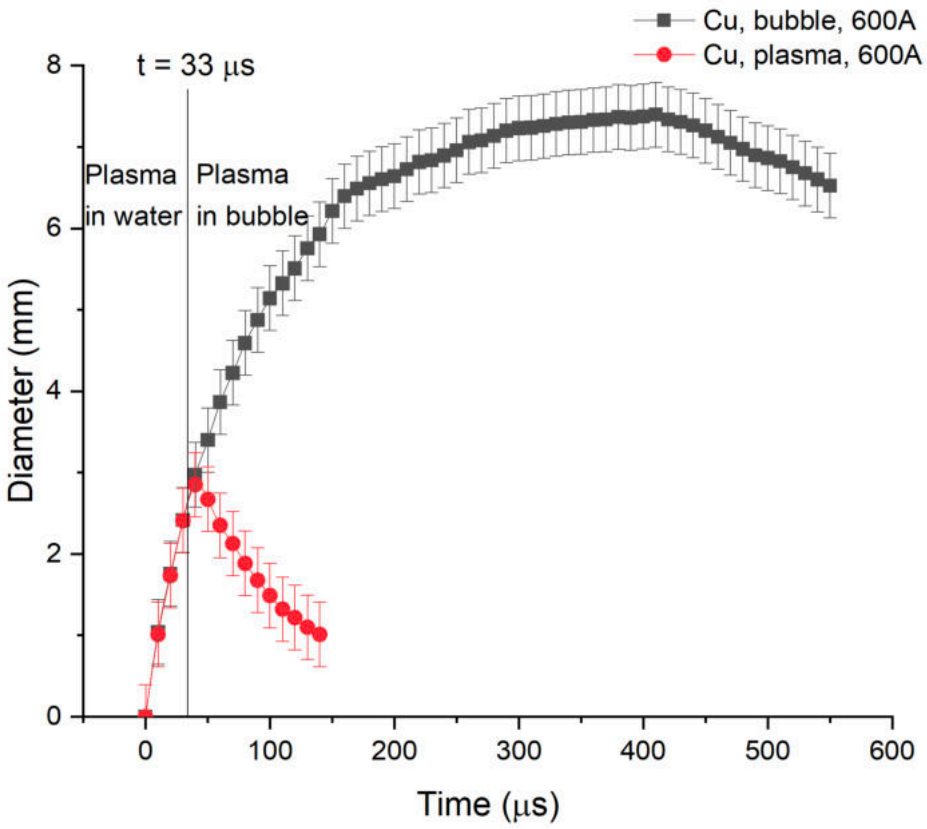

Figure 4.47: Time evolution of bubble and plasma diameters: discharge generated between Cu electrodes in deionized water, peak pulse current of 600 A.

In Fig. 4.45, the plasma size is greater than the diameter of the bubble at the beginning of the discharge (before 72 µs). Normally, they should match if there is no visible bubble around the arc. This could come from the fact that the two measurements have been made for two different tests, and the difference corresponds to the uncertainties of the data.

One can consider that the ignition of the arc creates a pressure shockwave responsible of bubble formation and growth. Then the pressure gradually decreases from that instant, until it reaches the value of the surrounding media (water). Due to inertia, the bubble grows a little further and the pressure becomes even lower, which causes its collapse and further oscillation.

The plasma inside the bubble will provide heating, helping the bubble growth. This appears clearly on Fig. 4.47, there is an inflection point in the curve of bubble diameter when arc extinction occurs (at t = 150 µs), the bubble growth becomes slower. This can also be seen in Fig. 4.45 for t = 250 µs.

From the erosion point of view, the two phases of the discharge should presumably lead to different quenching conditions, and, consequently, to the different synthesis conditions. The high intensity of plasma emission during the first tens of microseconds suggests that a massive flow of energy is brought to the electrodes during this phase. Due to the relatively short duration of this event, it is probable that only the electrode surface is affected by this energy flow, while the bulk metal remains unaffected [127].

A burst of energy will in such case directly evaporate only the very superficial layers of the electrode. The bulk electrodes will be heated by the plasma during the further discharge phase.

The plasma diameter is correlated to the current value. The plasma size evolution curve quite well follows the current waveform (see Fig. 4.48).

However, the curve of discharge diameter has its maximum after the current maximum. For time greater than 20 µs, there is a delay of about 20 µs that remains up to the end of the discharge. Since the two curves are initially superposed, this is not a synchronization problem. The delay of 20 µs is not negligible in terms of plasma physical phenomena (nanosecond time scale). One can consider that due to power losses, the plasma cannot grow as fast as the current rise. The time lag seems indeed to increase with time. On the other hand, the size of the bright zone (associated to the plasma) might not be directly dependent on plasma energy. If the global input energy is lower, the plasma can be more expanded but with a lower temperature. If the pressure decreases inside the bubble, a lower pressure may lead to a larger plasma diameter.

Figure 4.49 shows the correlation between the plasma size evolution and current evolution for the case of discharge between molybdenum electrodes. It can be seen that the same “delay” as in Fig. 4.48 is observed between the current and the plasma diameter reaching maximum. The fact that this delay is lower may indicate the presence of the additional heating (for instance, from the oxidation reactions) that helps the plasma growth.

In general, Fig. 4.48 and 4.49 illustrate that the current amplitude and plasma diameter are unsurprisingly interdependent. The volume of plasma depends on the energy input and since voltage evolution is low during the discharge, most of power evolution is due to current evolution. Figure 4.50 shows the linearity of dependence of the maximal plasma diameter on peak impulse current for the considered range of currents.

It should be noted, however, that the evolution of the plasma size is a delicate point. The plasma diameter presented in Fig. 4.44 – 4.47 have been estimated directly from the high-speed images of the discharge. Care has to be taken for the image treatment and interpretation. The light emitting region (excited region) could be broader than the plasma itself (ionized region), and the light could partly be scattered from the liquid in the surrounding of the electrodes, therefore the overestimation is unavoidable for the given experimental conditions. As can be seen from Fig. 4.50, the diameter of the light emitting region increases with the discharge current, being roughly from 2.1 to 3.7 mm for a current increase from 400 to 1000 A. The error bars are comparable to the size of the data points in Fig. 4.50, considering the scale, therefore they are not indicated. Thus, the plasma size most likely also increases with the discharge current. This can be correlated with the fact that discharges with high current produce larger craters than discharges with low current.

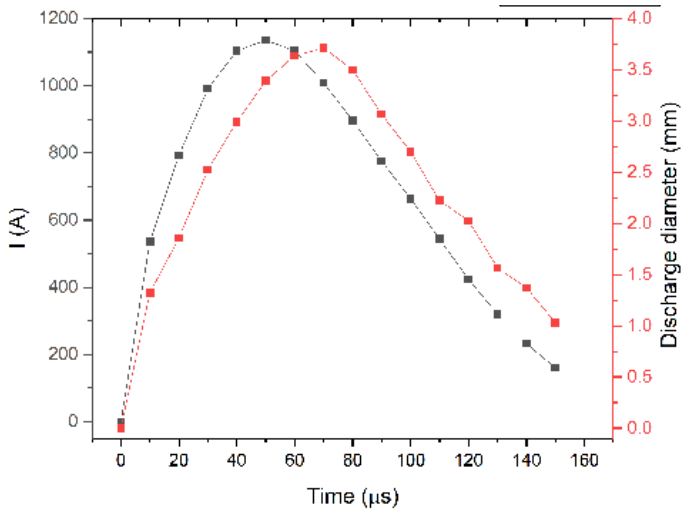

Figure 4.48: Time evolution of current and radius of a plasma channel for discharge initiated between Cu electrodes in deionized water.

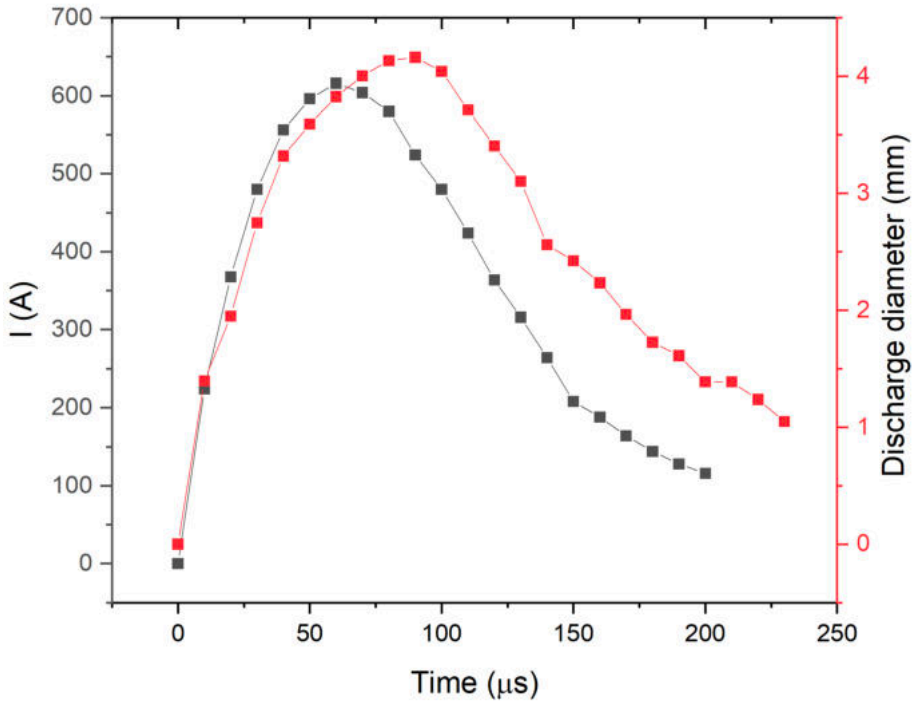

Figure 4.49: Time evolution of current and radius of a plasma channel for discharge initiated between Mo electrodes in deionized water.

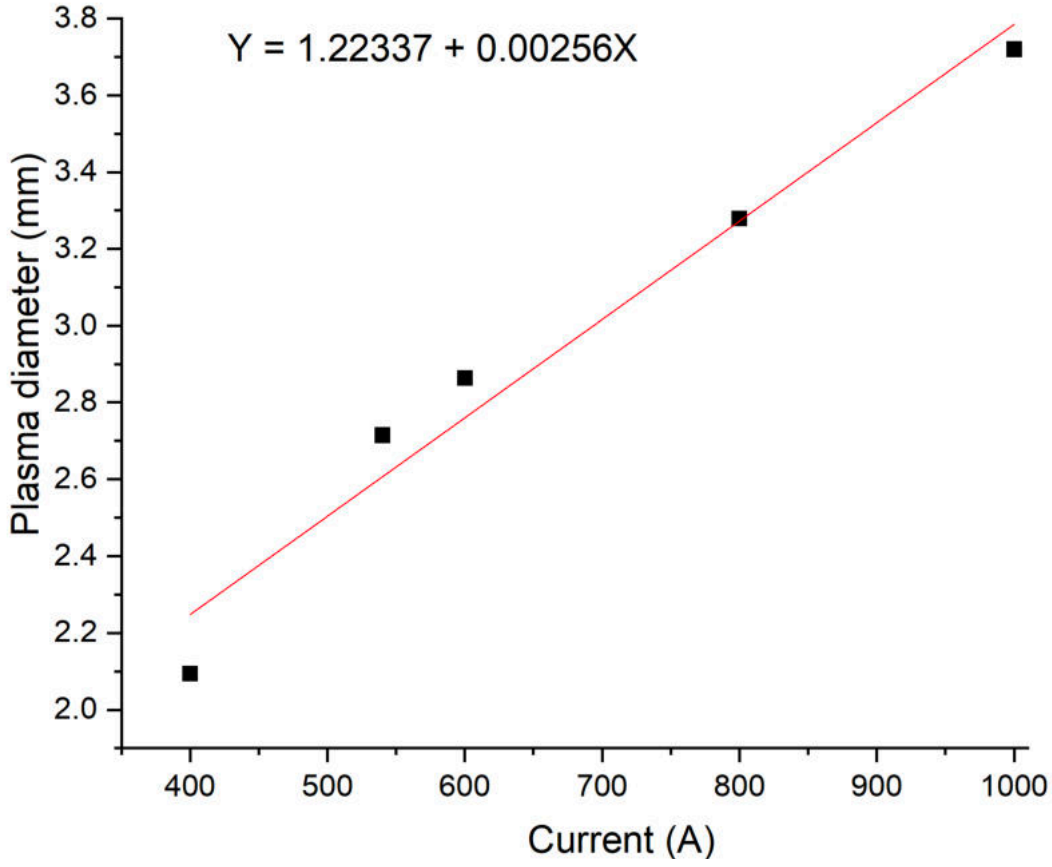

Figure 4.50: Linear fit of the dependence of the maximal plasma diameter on maximal discharge current: discharge generated between copper electrodes.

The transition from the discharge to the post-discharge is particularly interesting to study. Drawing an analogy with the EDM process, where the major part of the workpiece material is removed at the end of the discharge when the plasma collapses, one can say that this stage in the EDM process is certainly crucial for the optimization of the material removal rate. The same considerations can be applied for the underwater pulsed discharge used in NM synthesis.

As soon as the current is shut down, it drops rapidly to zero, and the light intensity is simultaneously also dropping fast. But in the case of discharge generated between molybdenum electrodes, there is still a weak slowly-decaying light emission, typically until 400 -500 µs after the end of the discharge. The corresponding images of the transition are given in Figure 4.51.

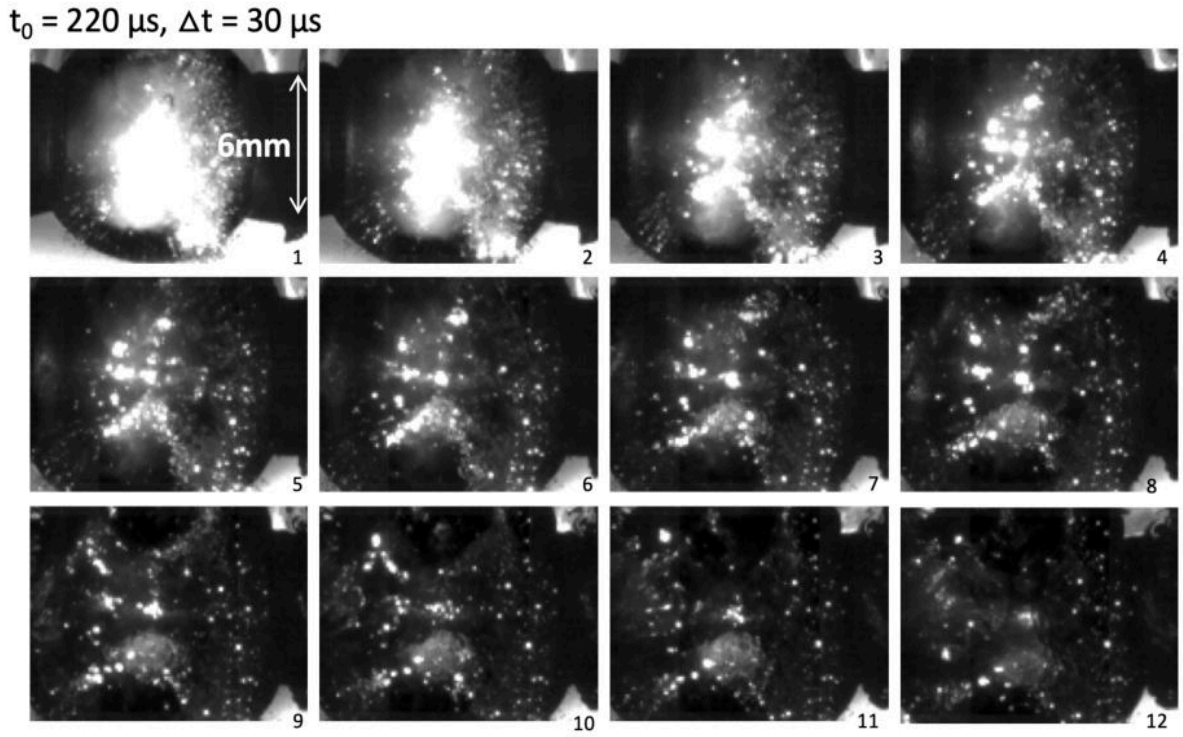

Figure 4.51: Post-discharge emission: high-speed imaging of discharge generated between molybdenum electrodes in deionized water, peak pulse current of 1000 A.

As long as the discharge current is established, the plasma is visible as a bright area. When the current drops down, the disappearance of the plasma is almost immediate in case of discharge generated between copper electrodes. The plasma collapse is thus a very fast phenomenon. However, this is not the case for discharge generated between molybdenum electrodes. Apart from the fact that disappearance of plasma takes longer, the interpretation of objects which are emitting light in Fig. 4.51 is not obvious. They could be attributed to bubbles for example,

which would scatter the light of the spark or the backlight. On the other hand, these particles may come from the molten metal pool created in the electrode during the discharge, and are then removed from its surface and ejected in the dielectric when the discharge is shut down.

This hypothesis of the metal particles can be confirmed with optical emission spectroscopy of the post-discharge light. If the post-discharge light emission is close to a blackbody radiation, that will mean that the emitters are hot metal particles. In this work no spectroscopy of the post-discharge emission was carried out. Therefore, it is impossible to state that the light emitted after the discharge is due to particles of heated metal. Besides, it is difficult to observe light from these "bright spots" since their position and amplitude is rather randomly distributed, with a short lifetime. Comparison of measurement with and without backlighting could be a better approach: with no backlighting, bubbles should be far less visible (with fewer light to scatter) while hot particles will still emit comparable amount of light.

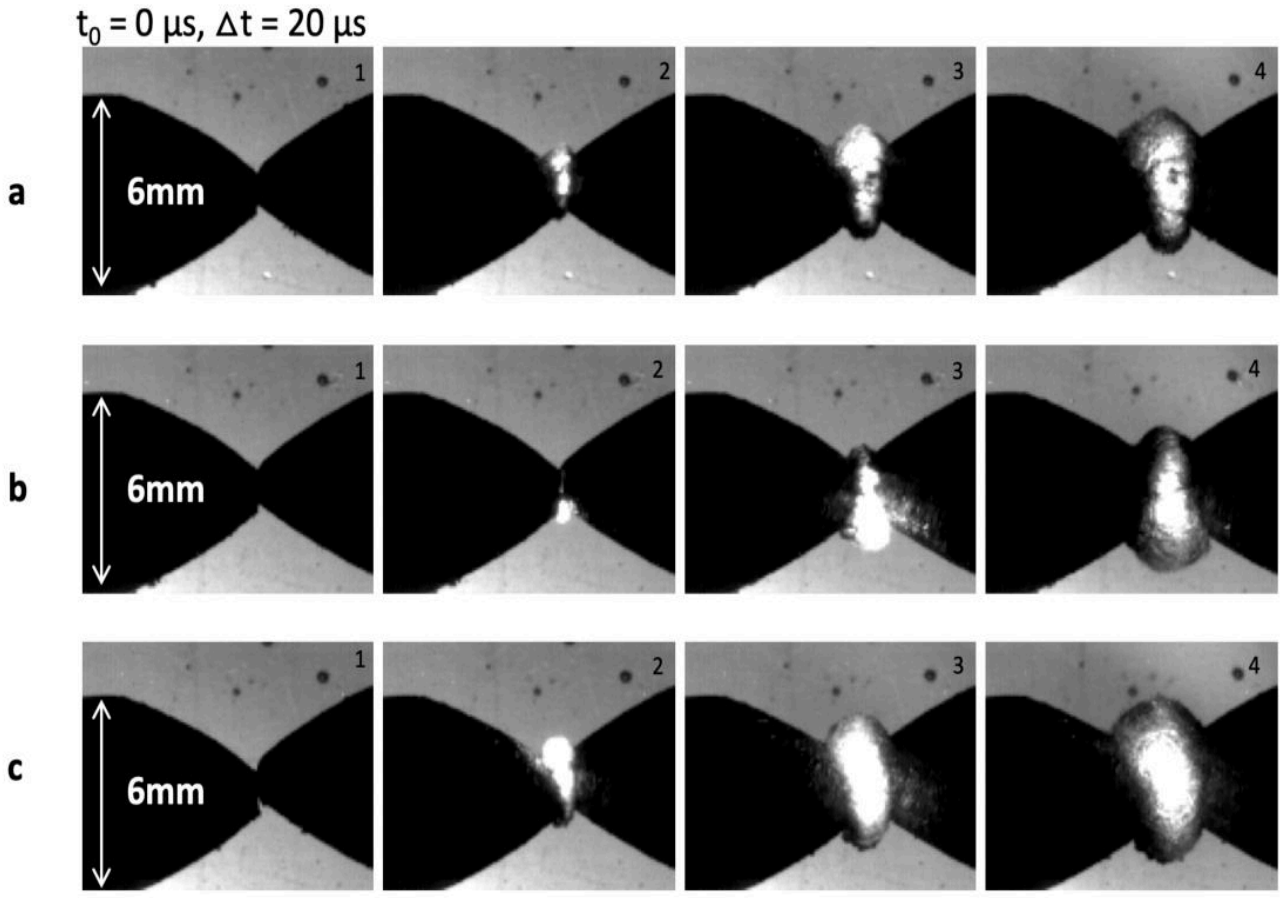

Figure 4.52: Images of similar discharges, illustrating the problem of reproducibility: high-speed imaging of discharge generated between copper electrodes in deionized water, peak pulse current of 600 A.

To address the problem of the reproducibility of the discharges, Figure 4.52 shows several images of discharges with the same parameters. It can be seen that even with a point-to-point geometry, the plasma localization strongly changes from one discharge to another. Furthermore, the size of the plasma channel, and consequently their physical properties, also vary.

Additionally, even though the experimental conditions are the same for discharges showed in Fig. 4.35 and 4.37, the images show some differences. 120 μs after beginning of discharge (first image in Fig. 4.37), the size of plasma bubble is different in these two presented samples: it is spherical (with a diameter of ~ 4.9 mm) in Fig. 4.35, and more elongated in Fig. 4.37 (with maximal size being close to 6 mm). This is yet another indication of lack of reproducibility.

However, the case in Fig. 4.52 corresponds to rather “extreme” case, and since the measurements in this work were repeated several times, numerous plasma images were acquired, and the averaged results are presented in this section.

4.8 Electrode erosion and energy balance calculation

Concerning the physical processes associated with the results in the section 4.7, the purpose of the setup in Kiev (see Chapter 3, section 3.2) is to evaporate material from the metal granules using the electric discharge that later will condensate into NPs. Taking into consideration that setup in Toulouse (see Chapter 3, section 3.3) was designed for the same purpose, it is reasonable to study the energy dissipation paths, and their relative proportion.

Due to the complexity of the processes taking place during the spark erosion process, the description of the mechanisms leading to and controlling NPs’ formation are mostly phenomenological and qualitative.

The initial step of particle formation is the production of an atomic vapor by means of the erosion of the electrode material [25]. The term “erosion” or “ablation” is used partly because the exact process of material removal from the electrode is not fully explored. The surface of the electrodes is heated at the so called “hot spots” where the plasma channel interacts with the electrode surfaces and hence the eroded material of the electrodes forms a vapor plume [25], [26]. In addition to this, ions of the surrounding media, as well as those of the anode and the cathode bombard the electrodes that may lead to further removal of electrode material [27].

Recently, it was reported that the experimentally determined mass-loss of the electrodes can be fairly well explained by a first principle theoretical model which takes into account evaporation only [28]. This suggests that

evaporation might be the dominant mechanism of material removal. The evaporation of the electrode material in such case is usually described by the simple model assuming a single tiny spot created by the spark plasma channel [25], [26]. By calculating the energy balance, i.e. the energy delivered to the electrode material by the plasma channel is equal to the energy output represented by thermal conduction and radiation loss, the evaporated mass from such a spot can be calculated [29]. This is the so-called Jones model (see Figure 4.53).

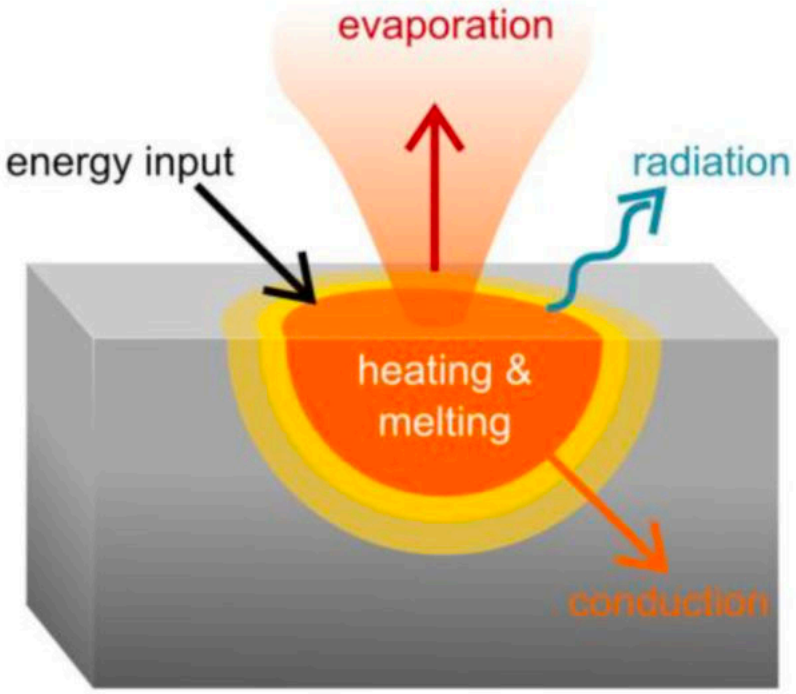

Figure 4.53: Schematic representation of the simplified picture of electrode erosion, called the Jones model [26].

Naturally, not all the input power is used for NMs production, and one can consider that the part of the energy will be deposited in the arc column, and the power that will be transferred to the electrodes, the most important being the part responsible for the electrode erosion. The mass measurements can give an indication of this through thermodynamic calculations of the corresponding energies required for heating, melting and vaporizing the metal. The electrical data registered by the oscilloscope allows to estimate the “efficiency” of the process.

However, not all ablated mass from the electrodes will result as NPs. Only vaporized material can possibly condensate into nanosized particles, while solid or liquid phase will mostly form a micro fraction.

With all that said, the energy balance can be considered as shown in Figure 4.54.

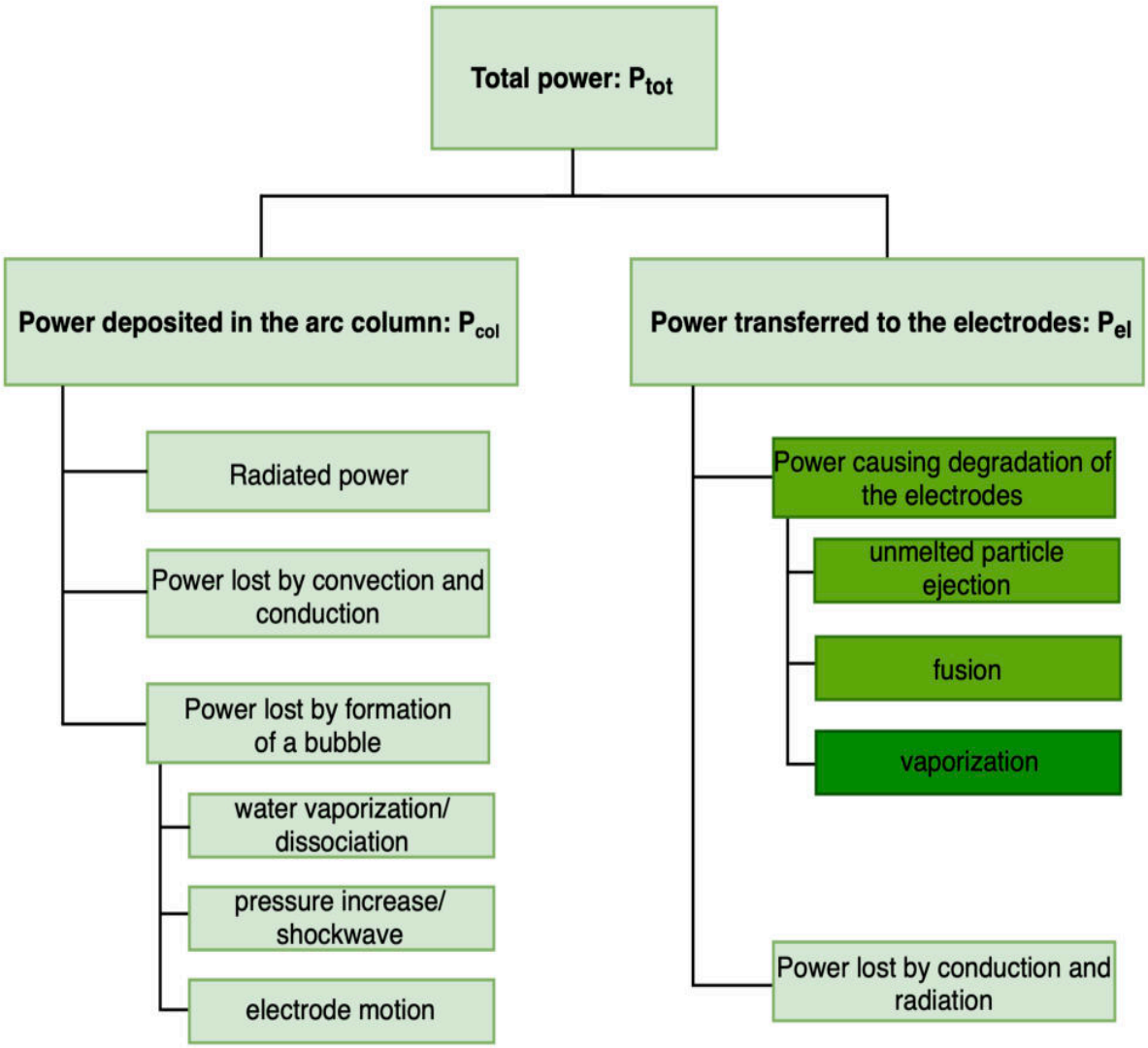

Figure 4.54: Scheme illustrating the energy dissipation paths in the studied system.

Energy input comes from electrical power. The electrical data recording allows calculating the total average power, as expressed in the following equation:

$$P_{tot} = \frac{1}{t_{arc}} \int u(t)i(t)dt = P_{col} + P_{el}, \qquad (4.2)$$

where t_{arc} is the duration of discharge. Instantaneous power at moment of time t_1 can be calculated simply as $U(t_1)$ x $I(t_1)$.

If exothermic chemical reactions occur (for instance, alumina formation when working with aluminum), additional energy input can be considered. In the case of working with copper and molybdenum, this

factor can be neglected, considering the energy and the duration of the pulse.Fig. 4.54 shows that part of the energy is deposited in the arc column, and the other part is dissipated at the electrodes. As for the energy deposited in the arc column, a part of it is radiated, part is lost by conduction/convection, and another part is lost due to the formation of the bubble. As for the energy transferred to the electrodes, a part of it causes the electrode ablation (ejection, fusion and vaporization), and part is lost through conduction in the electrodes and another is radiated from the electrodes.

Additionally, part of the energy also leads to a presumable motion of the anode. This part can equally be referred to as the part "transferred to the electrodes" or as a part of the energy lost due to the formation of a bubble (as in Fig. 4.54). It should be noted that none of the experimental imaging results performed within the scope of this work have clearly confirmed that the motion of the electrode is actually taking place during the expansion of the plasma channel and, consequently, the surrounding bubble.

The only values that can readily be calculated are the total electrical input and ablated electrode mass. The other quantities have to be estimated from available in the literature models predicting behavior of discharges with similar parameters or experimental studies.

While it is challenging to identify the average power transferred to the electrodes, it is known that it causes metal melting and vaporization, which can be expressed as:

$$P_{melt-vap} = P_{melt} + P_{vap}, \tag{4.3}$$

where P_{melt} is the energy required for the melting of the metal, and P_{vap} is the energy required for its vaporization. Not all of the ablated metal is melted, and not all of the melted metal part is vaporized. However, the energies for melting and vaporization can be expressed as in the following equations (4.4) and (4.5):

$$P_{melt} = m \cdot L_{melt} + \int_{T_{sol}}^{T_{melt}} m \cdot C_{sol}(T)dT, \tag{4.4}$$

$$P_{vap} = m \cdot L_{vap} + \int_{T_{melt}}^{T_{vap}} m \cdot C_{liq}(T)dT = m \cdot L_{vap} + m \cdot C_{liq}(T_{vap} - T_{melt}), \tag{4.5}$$

where T_{sol}, T_{melt}, and T_{vap} are the solid initial, melting and vaporizing temperatures, respectively; L_{melt} and L_{vap} are the latent heats of melting and vaporization respectively, C_{sol} and C_{liq} are the heat capacities at solidand liquid state, respectively, and m is the ablated metal mass.C_{sol}

varies with temperature, but C_{liq} remains constant [30]. Table 4.6 summarizes the thermodynamic data used to calculate the energy required for melting and vaporizing copper and molybdenum. It should be noted that the values in Table 4.6 are given at atmospheric pressure, therefore they will be different with the pressure increase.

Table 4.6. Thermodynamic data of copper and aluminum

	Copper	**Molybdenum**
Melting point (K)	1358	2896
Boiling point (K)	2843	4913
Melting latent heat (J/g)	206.15	375.15
Boiling latent heat (J/g)	4725	6231
Specific heat capacity of solid ($J \cdot g^{-1} \cdot K^{-1}$)	0.385	0.251
Specific heat capacity of liquid ($J \cdot g^{-1} \cdot K^{-1}$)	0.517	0.377
Energy to melt 1 g of metal (kJ)	0.653	1.050
Energy to vaporize 1 g of metal (kJ)	5.493	6.991
Energy to melt and vaporize 1 g of metal (kJ)	6.146	8.041

The power $P_{el,\ cond\text{-}rad}$, which is transferred to the electrodes but not involved in melting and vaporization, is lost by conduction and radiation. In case if P_{el} is known, $P_{el,\ cond\text{-}rad}$ can be calculated as follows in equation:

$$P_{el,cond-rad} = P_{el} - P_{melt-vap} \,. \tag{4.6}$$

Only a small part of the ejected metal is vaporized, but the exact proportion is unknown. For instance, in plasma processes involving electric spark discharges and transient arcs (such as arc tracking [31], low voltage circuit breaker or lightning impact [24]), the amount of molten

matter that vaporizes is ~ 1%. For instance, investigations of the spark discharge generator for nanomaterial synthesis [32] showed that energy consumed for evaporated mass gives a value of only about 0.2% of the energy stored in a capacitor. In this work the amount of the vaporized metal was assumed to be 10% of the molten matter.

Power lost by conduction and radiation in the electrode is considered to be negligible.

Tables 4.7 and 4.8 present synthesis of energy balance for part of the power transferred to the electrodes for the considered electrode materials and peak pulse current regimes. While Table 4.7 shows values of the total input energy, calculated energy required for the electrode ablation and their proportion, Table 4.8 gives more detailed information about energy dissipation of the power transferred to the electrodes. The uncertainties given for erosion rate (in μg/μs), and the associated power $P_{melt\text{-}vap}$ arise from uncertainties associated to the electrode weigh loss measurements. The uncertainties concerning total power P_{tot} (10 to 15%) result from the uncertainties associated to voltage measurements.

Table 4.7. Power balance of the energy transferred to electrodes

Electrodes	I, A	Erosion rate, μg/μs	P_{total}, J	$P_{el,heat\text{-}melt\text{-}vap}$, J	P_{el}/P_{total}, %
Mo	400	0.872±0.12	1.063±0.12	0.181±0.02	17.05
Mo	600	1.214±0.21	2.072±0.23	0.251±0.03	12.11
Mo	1000	2.131±0.21	4.573±0.50	0.442±0.05	9.68
Cu	400	1.433±0.14	1.224±0.13	0.200±0.02	16.53
Cu	600	4.228±0.42	2.109±0.23	0.593±0.07	28.27
Cu	1000	8.339±0.83	4.730±0.52	1.171±0.14	24.76

Table 4.8. Energy dissipation of power causing electrode ablation

Electrodes	I, A	Energy to heat 1/3 of ablated mass, J	Energy to melt 2/3 of ablated mass and vaporize 10% of it, J	Total energy for electrode ablation, J
Mo	400	0.028±0.003	0.153±0.02	0.181±0.02
Mo	600	0.039±0.004	0.212±0.02	0.251±0.03
Mo	1000	0.069±0.007	0.373±0.04	0.442±0.05
Cu	400	0.029±0.003	0.172±0.02	0.200±0.02
Cu	600	0.085±0.009	0.507±0.06	0.593±0.07
Cu	1000	0.169±0.002	1.002±0.11	1.171±0.14

Without analysis of the erosion products it is difficult to quantitatively estimate the proportion of non-melted particles, melted and vaporized metal. As mentioned before, results presented in Table 4.7 are made under assumption that proportion of vaporized metal from the melted quantity is 10%. Another hypothesis is related to the non-melted particles ejection, assuming that macro-fraction particles are formed when non-molten metal detaches from the bulk electrode, i.e. being heated but not melted. For the presented calculations, we considered a proportion of one third of all the ablated mass being ejected without melting. From the high-speed imaging it can be seen that in some cases considerably large dark spots are ejected from the anode, which could correspond to such "macro particles". Therefore, the total energy going to the ablation of the electrode mass is $P_{el,heat\text{-}melt\text{-}vap}$.

For example, one can see from Table 4.7 that in case of discharge generated between copper electrodes with a peak pulse current of 400 A, the average erosion rate is ~ 1.433 μg/μs. Taking into consideration that discharge duration is 150 μs (the same for all tests), the eroded metal weights up to ~ 216 μg. Thermodynamic data (see Table 4.6) indicate a required energy of 0.653 kJ for melting 1 g of copper, meaning that one needs ~ 0.14 J to melt the measured ablated mass. This represents roughly 12% of the available energy. On the other hand, energy required for complete copper vaporization is 6.146 kJ/g, and one would need 1.32 J to vaporize entirely 216 μg of copper. This exceed available energy, and confirms that not all ablated metal is vaporized. Moreover, this is also consistent with the observed particle ejection on high speed

imaging of the discharge. Analysis of the presented results shows that erosion rate expectedly increases with increase of the current (see Fig. 4.55). For both, copper and molybdenum electrodes this dependence is linear within considered range of currents.

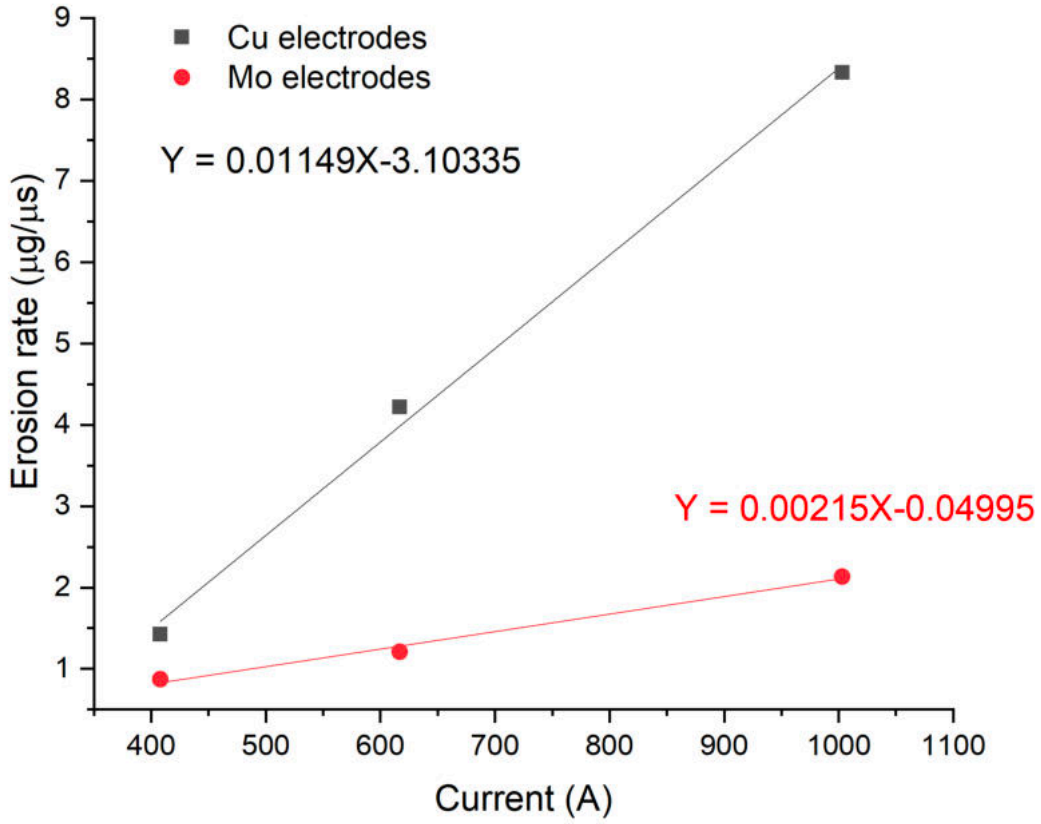

Figure 4.55: Linear fit of the dependence of the average electrode erosion rate on maximal discharge current: discharge generated between copper and molybdenum electrodes.

It can be seen from Fig. 4.55 that erosion of the copper electrodes occurs at higher rates than that of molybdenum. The error bars are comparable to the size of the data points in Fig. 4.55, considering the scale, therefore they are not indicated. This is due to the fact that latent melting and boiling heat values for molybdenum are higher, i.e. more energy is required to melt and vaporize 1 g of molybdenum than 1 g of copper. Additionally, molybdenum has lower thermal conductivity than copper, which results in the different energy dissipation behavior. This point will be discussed further.

Figures 4.56 – 4.57 show proportion of the energies needed for heating without melting, melting and vaporizing of the corresponding portions of the ablated electrode mass for the considered experimental conditions.

These plots allow to clarify the difference of energy dissipation in case of discharge generated between copper and molybdenum electrodes.

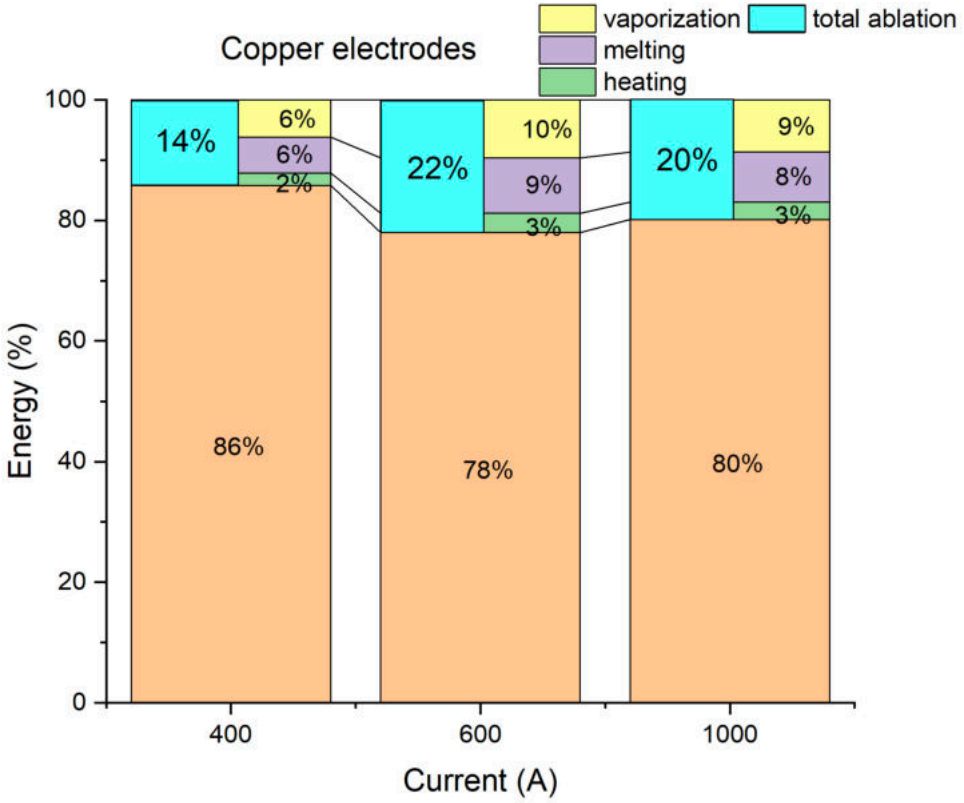

Figure 4.56: Ratio of energies dissipated on ablation of the copper electrode (for peak pulse current values of 400, 600 and 1000 A).

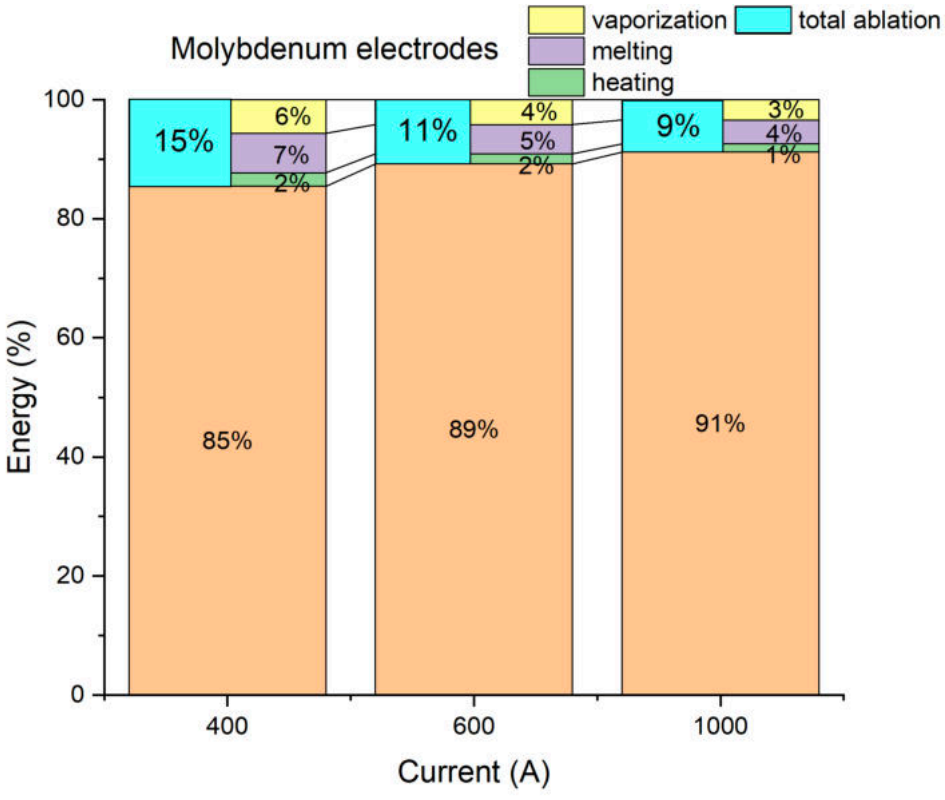

Figure 4.57: Ratio of energies dissipated on ablation of the copper electrode (for peak pulse current values of 400, 600 and 1000 A).

One can see that in case of copper electrodes the proportion of the energies contributing to the electrode ablation, and, consequently, their total increase with increase of the peak pulse current. The decrease in the amount of the energy needed for the electrode ablation by 2% at 1000 A compared to that at 600 A (Fig. 4.56) can be explained by the fact that at higher currents more experiments end up with electrode tips being melted to one another (as a result of short-circuit), rather than occurrence of the discharge. This is due to the high erosion rates that cause faster degradation of the electrode surface and, consequently, more points of contact for current just to pass through the electrodes without formation of the plasma channel. Since these “short-circuit” tests also contribute to the total number of tests, the average erosion value is lower.

In case of discharge generated between molybdenum electrodes, one can clearly see in Fig. 4.57 that the amount of the energy causing the electrode degradation decreases with the current increase. This constitutes the principal difference between these two experimental regimes (Fig. 4.58).

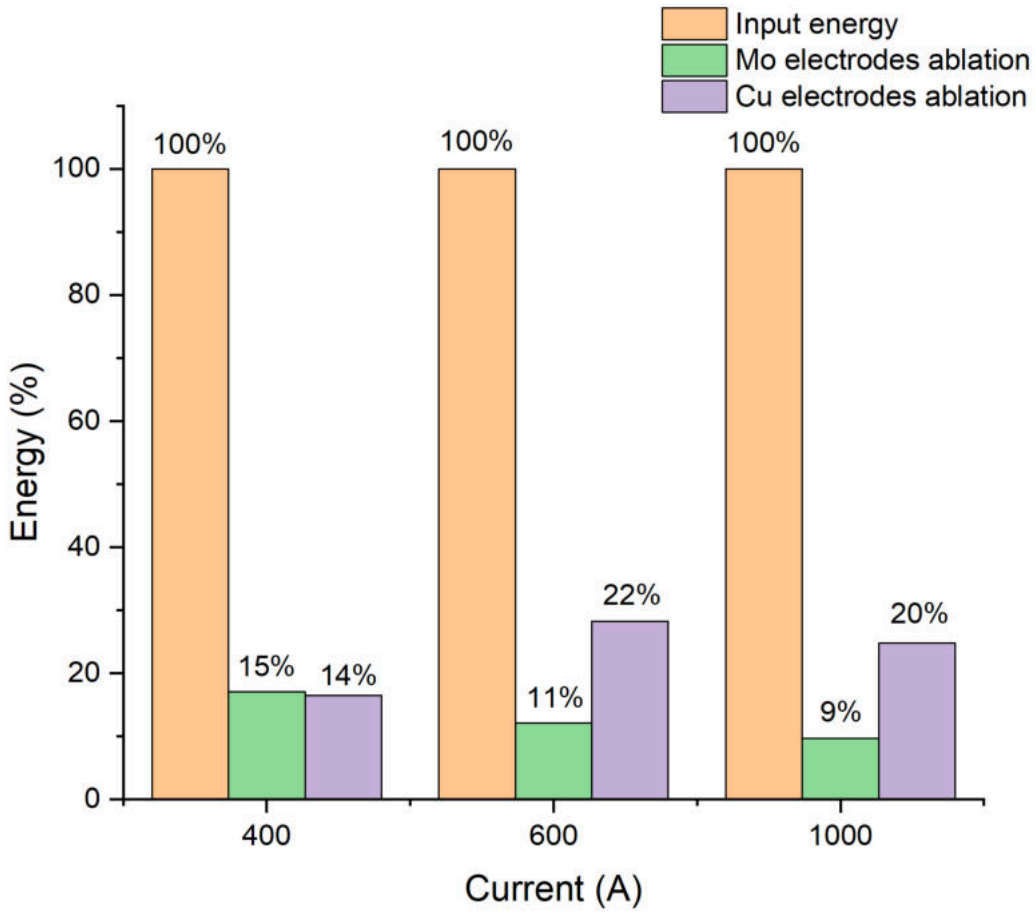

Figure 4.58: Comparison of ratio of the total available energy and total energy causing the electrode ablation for discharge generated between molybdenum and copper electrodes (for peak pulse current values of 400, 600 and 1000 A).

One can conclude that while in case of the discharge between copper electrodes, biggest part of the energy transferred to the electrodes is causing the electrode ablation, in case of discharge between the molybdenum electrodes the decreasing proportion of this energy indicates that the portion of energy deposited in the arc column should increase proportionally. Indeed, more intense plasma emission in case of molybdenum electrodes (see section 4.7) can be associated to a higher part of energy dissipated in the arc. This could be explained by a lower thermal conductivity of molybdenum: energy cannot be dissipated as easily in the bulk electrode as in the case of copper, and, therefore, remains available for the arc. On the other hand, some chemical reactions (for instance, oxidation) can also be involved in case of molybdenum vapors, meaning that power feeding the arc may come not only from the power supply, but also from the triggered chemical reactions.

It should be noted that in all of the measurements, erosion of anode is higher than that of cathode. This correlates with the previously obtained results (see section 4.3), and with the available literature [33]. During the pulse, the cathode remains at negative potential and the anode at ground potential. The externally imposed field makes the ions in the plasma to move towards cathode and the electrons move towards anode. Electrons being much lighter than ions move much faster and impart their energy to the anode. While both electrodes start melting as they are exposed to the high heat flux, the anode melts faster as it receives the fast electrons during discharge. Since cathode acts like a point source for emission of electrons, part of the cathode in contact with the plasma is much smaller compared to the same of the anode. Once voltage pulse is over, the discharge stops and the plasma channel undergoes a violent collapse leading to a burst of the superheated molten material on the surface of the electrodes into the dielectric liquid. The molten material is, thus, partly carried away by the liquid dielectric as debris material and partly solidified on the electrode surface.

For the purposes of extension of the present work in the future, energy balance calculations can be further improved by considering and estimating the part of the energy deposited in the arc column, including the fine measurements of the electrode motion, determination of the radiated power and pressure determination.

Electrode motion can be estimated from the acceleration needed to move the electrodes by a given distance, during a given time. This allows to deduce the value of speed from acceleration and duration, and, consequently, estimate the kinetic energy (considering the electrode

mass). In the framework of the present work, no electrode motion has been observed during the high-speed imaging of discharge. This can either be a result of plasma and bubble creating “obstacles” for such observation, or due to the setup design (perhaps, the motion is not free enough and the mechanical energy provided by the arc is not sufficient to move the electrodes).

Determination of the electrode motion would require a dedicated setup for fine displacement measurements (better than the "mobile electrode" device we used for this thesis, see section 3.3 of Chapter 3). However, this might affect the arcing conditions, and move them further from the “realistic” configuration of the operational unit (see section 3.2 of Chapter 3).

Currently, no results were obtained allowing to distinguish the power repartition from what is deposited in the column. However, knowing the plasma composition will allow to calculate the radiated power for the given temperature and pressure. Pressure measurements could be made using piezo sensor.

References to chapter IV

[1] T. A. Tmenova, A. N. Veklich, and V. F. Boretskij, “Calibration of spectral response of SDH-IV spectrometer,” *Bull. Taras Shevchenko Natl. Univ. Kyiv*, vol. 1, no. 24, pp. 54–59, 2016.

[2] A. K. Gaigalas, L. Wang, H.-J. He, and P. DeRose, “Procedures for Wavelength Calibration and Spectral Response Correction of CCD Array Spectrometers,” *J. Res. Natl. Inst. Stand. Technol.*, vol. 114, no. 4, p. 215, Jul. 2009.

[3] K. Bockasten, “Transformation of Observed Radiances into Radial Distribution of the Emission of a Plasma*,” *J. Opt. Soc. Am.*, vol. 51, no. 9, p. 943, Sep. 1961.

[4] R. Perez, H. Rojas, G. Walder, and R. Flükiger, “Theoretical modeling of energy balance in electroerosion,” *J. Mater. Process. Technol.*, vol. 149, no. 1–3, pp. 198–203, Jun. 2004.

[5] T. A. Tmenova *et al.*, “Optical emission spectroscopy of plasma of underwater electric spark discharges between metal granules,” *Probl. At. Sci. Technol.*, vol. 1, no. 23, pp. 132–135, 2017.

[6] I. L. Babich, V. F. Boretskij, A. N. Veklich, and R. V. Semenyshyn, “Spectroscopic data and Stark broadening of Cu I and Ag I spectral lines: Selection and analysis,” *Adv. Space Res.*, vol. 54, no. 7, pp. 1254–1263, Oct. 2014.

[7] A. Descoeudres, “Characterization of electrical discharge machining plasmas (Thesis),” EPFL, Lausanne (Switzerland), 2006.

[8] V. S. Burakov, E. A. Nevar, M. I. Nedel’ko, N. A. Savastenko, and N. V. Tarasenko, “Spectroscopic diagnostics for an electrical discharge plasma in a liquid,” *J. Appl. Spectrosc.*, vol. 76, no. 6, pp. 856–863, Nov. 2009.

[9] H. Griem, *Plasma Spectroscopy*. Moscow (USSR): Atomizdat, 1969.

[10] H. R. Griem, “Validity of Local Thermal Equilibrium in Plasma Spectroscopy,” *Phys. Rev.*, vol. 131, no. 3, pp. 1170–1176, Aug. 1963.

[11] R. Venger, T. Tmenova, F. Valensi, A. Veklich, Y. Cressault, and V. Boretskij, “Detailed Investigation of the Electric Discharge Plasma between Copper Electrodes Immersed into Water,” *Atoms*, vol. 5, no. 4, p. 40, Oct. 2017.

[12] N. Konjević, M. Ivković, and N. Sakan, “Hydrogen Balmer lines for low electron number density plasma diagnostics,” *Spectrochim. Acta Part B At. Spectrosc.*, vol. 76, pp. 16–26, Oct. 2012.

[13] H. R. Griem, *Spectral line broadening by plasmas*. New York: Academic Press, 1974.

[14] J. Torres *et al.*, “The Stark-crossing method for the simultaneous determination of the electron temperature and density in plasmas,” *J. Phys. Conf. Ser.*, vol. 44, pp. 70–79, Jul. 2006.
[15] M. A. Gigosos and V. Cardeñoso, “New plasma diagnosis tables of hydrogen Stark broadening including ion dynamics,” *J. Phys. B At. Mol. Opt. Phys.*, vol. 29, no. 20, pp. 4795–4838, Oct. 1996.
[16] V. F. Boretskij *et al.*, “Plasma of underwater electric discharges with metal vapors (Thesis),” vol. 1, no. 25, pp. 237–242, 2019.
[17] V. F. Boretskij, “Physical properties of multi-component electric arc discharge in gas flow,” Taras Shevchenko National University of Kyiv, Kyiv, Ukraine, 2011.
[18] A. N. Veklich, A. V. Lebid, and T. A. Tmenova, “Spectroscopic Data of W I, Mo I and Cr I Spectral Lines: Selection and Analysis,” *J. Astrophys. Astron.*, vol. 36, no. 4, p. 0, Dec. 2015.
[19] J. G. Kirkwood and H. A. Bethe, “The pressure wave produced by an underwater explosion, Part I,” Office of Scientific Research and Development, National Defense Research Committee, May 1942.
[20] R. H. Cole, *Underwater explosions*. New York: Dover Publications, 1965.
[21] S. Menon and M. Lal, “On the dynamics and instability of bubbles formed during underwater explosions,” *Exp. Therm. Fluid Sci.*, vol. 16, no. 4, pp. 305–321, 1998.
[22] J. E. Shepherd, “Interface effects in underwater explosions (Thesis),” Georgia Institute of Technology, USA, Dec. 1988.
[23] A. B. Arons and D. R. Yennie, “Energy Partition in Underwater Explosion Phenomena,” *Rev. Mod. Phys.*, vol. 20, no. 3, pp. 519–536, Jul. 1948.
[24] P. Teulet *et al.*, “Energy balance and assessment of the pressure build-up around a bolt fastener due to sparking during a lightning impact,” *Eur. Phys. J. Appl. Phys.*, vol. 77, no. 2, p. 20801, Feb. 2017.
[25] T. V. Pfeiffer, J. Feng, and A. Schmidt-Ott, “New developments in spark production of nanoparticles,” *Adv. Powder Technol.*, vol. 25, no. 1, pp. 56–70, Jan. 2014.
[26] A. Muntean, M. Wagner, J. Meyer, and M. Seipenbusch, “Generation of copper, nickel, and CuNi alloy nanoparticles by spark discharge,” *J. Nanoparticle Res.*, vol. 18, no. 8, p. 229, Aug. 2016.
[27] J. P. Borra, A. Goldman, M. Goldman, and D. Boulaud, “Electrical discharge regimes and aerosol production in point-to-plane DC high-pressure cold plasmas: aerosol production by electrical discharges,” *J. Aerosol Sci.*, vol. 29, no. 5, pp. 661–674, Jun. 1998.
[28] A. Voloshko, “Nanoparticle formation by means of spark discharge at atmospheric pressure (Thesis),” Université Jean Monnet - Saint-Etienne, Saint-Étienne, France, 2015.

[29] F. L. Jones, “Electrode Erosion by Spark Discharges,” *Br. J. Appl. Phys.*, vol. 1, no. 3, pp. 60–65, Mar. 1950.
[30] M. W. Chase, Jr., *NIST-JANAF Thermochemical Tables. Part I, Al-Co*, 4th edition. New York: American Chemical Society and American Institute of Physics for the National Institute of Standards and Technology, 1998.
[31] T. André, F. Valensi, P. Teulet, Y. Cressault, T. Zink, and R. Caussé, “Arc tracking energy balance for copper and aluminum aeronautic cables,” *J. Phys. Conf. Ser.*, vol. 825, p. 012001, Apr. 2017.
[32] D. A. Mylnikov, A. A. Efimov, and V. V. Ivanov, “Investigation of the Energy Balance in the Spark Discharge Generator for Nanoparticles Synthesis,” *J. Phys. Conf. Ser.*, vol. 830, p. 012162, Jul. 2017.
[33] S. Bhattacharya, N. Tiwari, A. Mishra, S. Mitra, G. K. Dey, and S. Ghorui, “Underwater Electrical Discharges: Temperature, Density and Basic Instability Features with Different Anode Materials,” *Plasma Chem. Plasma Process.*, pp. 1019–1048, Feb. 2019.

CHAPTER V
GENERAL CONCLUSIONS

5. General conclusions

Although electric spark dispersion processes have been known for a while, the plasma created during this process is not well-studied and understood. The lack of knowledge in this field is mainly due to complexity of the phenomena occurring during the underwater electric discharges. Additional obstacles encountered during characterization of such plasmas are imposed by the experimental difficulties, such as small sizes of plasma and their often-short duration, difficult environment of the discharge, its stochastic nature and poor reproducibility.

The main objective of this thesis was set on the investigation of the plasma occurring during the synthesis of metal colloids by an electrospark dispersion generator. To the best of our knowledge, as of today there are no complete and systematic investigations of the electric dispersion process plasma with various diagnostics. Therefore, considering the significant experimental challenges related to the discharge configuration for the volumetric plasma-assisted destruction of metal granules, the first success of this work is simply to show the applicability of optical emission spectroscopy diagnostics to such discharges. The efforts made for the development of the effective experimental approach in order to meet this research objective have been well rewarded. The results obtained in this work allow to draw interesting conclusions about the physical properties of the underwater pulsed electric discharge plasma of the considered configuration.

In the setup for the synthesis of metal colloids metal granules are initially in contact. Discharge ignites from the short circuit and molten bridge mechanism. This allows to work with relatively low voltages (below 1 kV), unlike in the majority of the studies, wherein the voltage of several kV and higher is applied in order to achieve the breakdown of dielectric liquid in inter-electrode gap.

The plasma is established very rapidly. During the discharge, the intensity of the emitted light depends mostly on the discharge current (more intense with higher current). Imaging shows that the discharge excites a broad volume around the electrodes, typically around 2 mm in diameter, brighter in its center. This volume also clearly increases with the discharge current. Ignition of the arc is characterized by formation of bubble resulting from a pressure shockwave. The plasma inside the bubble will provide heating, helping the bubble growth. Then the pressure gradually decreases from that instant, until it reaches the value of the surrounding water. Due to inertia, the bubble grows a little further and the pressure becomes even lower, which causes its collapse and further oscillation. From the analysis of the discharge imaging, this appears

clearly as an inflection point in the curve of bubble diameter when arc extinction occurs (at t = 150 µs), the bubble growth becomes slower.

The diameter of the light emitting region increases with the discharge current, thus, the plasma size most likely also increases with the discharge current. This is correlated with the fact that high current discharges produce larger craters on the electrode surfaces than low-current discharges.

High-speed imaging allowed to distinguish two phases in the discharge lifetime: plasma in water, i.e. approximately during the first 30 – 70 µs, and plasma in bubble formed afterwards. From the erosion point of view, these two phases presumably lead to different quenching conditions, and, consequently, to the different synthesis conditions. The high intensity of plasma emission during the first tens of microseconds suggests that a massive flow of energy is brought to the electrodes during this phase. Due to the relatively short duration of this event, it is probable that only the electrode surface is affected by this energy flow, while the bulk metal remains unaffected. A burst of energy will in such case directly evaporate only the very superficial layers of the electrode. The bulk electrodes will be heated by the plasma during the further discharge phase.

The transition from the discharge to the post-discharge is particularly interesting for the optimization of the material removal rate. As soon as the current is shut down, it drops rapidly to zero, and the light intensity is simultaneously also dropping fast. But in the case of discharge generated between molybdenum electrodes, there is a slowly-decaying light emission, typically until 400 -500 µs after the end of the discharge. This can be attributed to the ejection of eroded metallic particles out of the bursted bubble, and can be observable with imaging during the post-discharge.

The initial step of understanding the mechanisms leading to and controlling NPs' formation is calculating the energy balance. However, due to complexity of the processes taking place during the electric spark dispersion process, the estimations are mostly phenomenological and qualitative. Naturally, not all the input power is used for NMs production: the part of the energy is deposited in the arc column, and another part is transferred to the electrodes, As for the energy dissipates to the arc column, a part of it is radiated, part is lost by conduction/convection, and another part is lost due to the formation of the bubble. As for the energy transferred to the electrodes, a part of it causes the electrode ablation (ejection, fusion and vaporization), and part is lost through conduction in the electrodes and another is radiated from the electrodes. One can assume that 70% of the input power is deposited in the arc column, meaning that 30% is transferred to the electrodes.

Without analysis of the erosion products it is difficult to quantitatively estimate the proportion of non-melted particles, melted and vaporized metal. In this work, we considered a proportion of one third of all the ablated mass being ejected without melting (which “backs up” the hypothesis of the molten metal ejection observed during the imaging of discharge), and that proportion of vaporized metal from the melted quantity is 10%.

The energy dissipation on the electrodes depends on the metal. In case of copper electrodes, biggest part of the energy transferred to the electrodes is causing the electrode ablation. Higher discharge current leads to higher amount of the input energy going to the erosion of copper electrodes. However, in case of discharge between the molybdenum electrodes, increasing current results in the decreasing proportion of this energy. This indicates that the portion of energy deposited in the arc column increases proportionally. Indeed, this is confirmed by more intense emission of plasma generated between molybdenum electrodes, thus higher part of energy dissipated in the arc. Due to the lower thermal conductivity of molybdenum, energy cannot be dissipated as easily in the bulk electrode as in the case of copper, and, therefore, remains available for the arc. On the other hand, some chemical reactions (for instance, oxidation) can also be involved in case of molybdenum vapors, meaning that power feeding the arc may come not only from the power supply, but also from the triggered chemical reactions.

For the underwater electric discharge plasma of the given configuration, erosion of anode is higher than that of cathode. During the pulse cathode remains at negative potential and the anode at ground potential. The externally imposed field makes the ions in the plasma to move towards cathode and the electrons move towards anode. Electrons being much lighter than ions move much faster and impart their energy to the anode. While both electrodes start melting as they are exposed to the high heat flux, the anode melts faster as it receives the fast electrons during discharge. Since cathode acts like a point source for emission of electrons, part of the cathode in contact with the plasma is much smaller compared to the same of the anode.

The spectroscopic analysis of emission of the underwater electric discharge plasma gives information about its composition. It is mostly composed by species coming from the electrodes and from cracking of the dielectric molecules, mainly hydrogen from water. Since the plasma is formed from the dielectric, the H_α line is emitted by plasma in all observed measurements. Some contamination from the graphite electrode is also present. All the spectral lines observed are atomic lines and not ionic lines, which indicates that temperature of plasma is moderate.

Studied discharges produce spectra with strongly-broadened lines, especially the H_α line, and with an intense continuum radiation.

The electron number density of the underwater discharge plasma is high (~ $10^{17}cm^{-3}$) because it is formed from a liquid, which is a dense medium, and because it is constantly submitted to the pressure imposed by the surrounding liquid. The strong intensity of the continuum radiation can be related to the high electron density. Free-bound and free-free radiations are indeed more likely in a dense plasma. The high electron density also indicates that the plasma is in LTE.

Due to its high density, the underwater electric discharge plasma could be not completely optically thin. The opacity of a plasma increases in fact with the density. Consequently, the light emitted by the very center of plasma could be absorbed within its volume and not be measured. The opacity can be a problem for spectroscopic diagnostics, since the core of an opaque plasma cannot be characterized with such diagnostics. Therefore, resonant and other spectral lines of atomic copper that are known to be easily self-absorbed were not used for the calculations of plasma parameters.

As previously mentioned, the emission spectra of the underwater electric discharge plasma give a hint that plasma is cold and dense. The average plasma temperatures were found to be around 7000 K for plasma with copper admixtures, and 11000 K for plasma with molybdenum admixtures, and increase with increase of the discharge current (from 400 A to 600 A) up to 10000 K and 12000 K, respectively.

Spatial distributions show that plasma with molybdenum vapors is colder at the periphery, while temperature of the copper plasma remains fairly constant throughout the radius. The electron density N_e is high: around $2.2 – 3 \cdot 10^{17}$ cm^{-3} for plasma with copper, and $4.2 – 7 \cdot 10^{17}$ cm^{-3}, showing that pressure is above the atmospheric. The radial profiles of electron density show that plasma maintains fairly constant values of this parameter along. The assumption of LTE can be accepted due to the high plasma density.

Good correlation between the plasma parameters obtained with two different experimental setups confirm the relevance of the selected experimental approach, and “realistic” simplified representation of the electric dispersion process plasma.

The higher temperature of plasma with molybdenum vapors validates the conclusion derived from the energy balance calculations that in such plasma lower proportion of the input energy is transferred to the electrodes (and, respectively, lower proportion of the energy contributes to metal erosion), thus, energy deposited in the plasma column is higher, resulting in the higher plasma temperature and emission intensity, compared to the case of plasma generated between copper electrodes.

The plasma has a high density and moderate temperature, and therefore presents several non-ideal effects. With typical temperatures of 0.6 – 0.95 eV and a typical electron density of ~ 10^{17} cm^{-3}, its coupling parameter Γ is around 0.3, meaning that underwater electric discharge plasma is weakly non-ideal.

Moreover, this conclusion can be confirmed from the spectroscopic measurements. The broadening and the asymmetrical shape of the H_α line are characteristic signs of the non-ideality of the plasma [1]. Additionally, absence of H_β line in some experiments are other demonstrations of this fact [1].

In general, physical properties of the underwater electric discharge plasma are quite interesting. It is interesting that the general plasma properties are relatively insensitive to most of the discharge parameters, such as the discharge current or the type of liquid. The main differences in the energy transfer and mass transfer processes are related to the thermophysical properties of the electrode materials. It should be highlighter that these parameters certainly have a significant influence on the quality and efficiency of the NMs synthesis but they roughly change the plasma densities and so not significantly affect plasma temperatures.

Even with many interesting insights that this work has brought, further studies are required in order to get a complete understanding of the electric dispersion process plasma in water. For example, more thorough plasma diagnostics can be performed, including plasma opacity calculations and determination of plasma composition. Electron density can be carried out with interferometry, and information about bubble and eroded particles could be obtained with the scattering techniques.

In order to bring better understanding of physical processes occurring during the synthesis of metal colloids by an electrospark dispersion generator, it is crucial to know precisely how the energy is distributed between the plasma, electrodes and the metal granules, and how it is transferred to them during the discharge.

Energy balance calculations can be further improved by considering and estimating the part of the energy deposited in the arc column, including the fine measurements of the electrode motion, determination of the radiated power and pressure determination.

Determination of the electrode motion would require a dedicated setup for fine displacement measurements (better than the "mobile electrode" device we used for this thesis, see section 3.3 of Chapter 3).

Currently, no results were obtained allowing to distinguish the power repartition from what is deposited in the column. However, knowing the plasma composition will allow to calculate the radiated power for the given temperature and pressure. Pressure measurements could be made using piezo sensor.

To summarize, this thesis presents an important insight into fundamental aspects of the underwater electric discharge plasma. We believe that such research is a necessary component for the further development and optimization of the process, and that other studies should be carried on. Obviously, this work cannot yet provide answers to all the questions related to the electric dispersion process, and that no immediate industrial improvements and direct applications can be obtained from it. Nevertheless, this work presents a first step towards it.

References to chapter V

[1] A. Descoeudres, C. Hollenstein, R. Demellayer, and G. Wälder, “Optical emission spectroscopy of electrical discharge machining plasma,” *J. Phys. Appl. Phys.*, vol. 37, no. 6, pp. 875–882, Mar. 2004.